Dynamics of Rigid Bodies and Flexible Beam Structures

Nielsen, Martin Bjerre

Publication date:
2013

Document Version
Publisher's PDF, also known as Version of record

Dynamics of Rigid Bodies and Flexible Beam Structures

PhD Thesis

$$(EIv'')'' = q - \rho A\ddot{v}$$

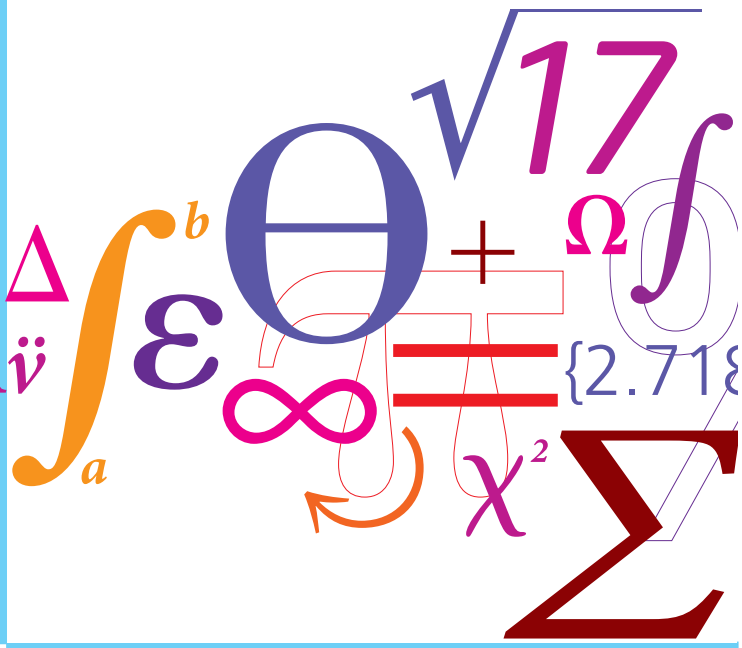

Martin Bjerre Nielsen
DCAMM Special Report No. S156
September 2013

DTU Mechanical Engineering
Department of Mechanical Engineering

Dynamics of Rigid Bodies and Flexible Beam Structures

Martin Bjerre Nielsen

Technical University of Denmark
Department of Mechanical Engineering
Section of Solid Mechanics
September 2013

Published in Denmark by
Technical University of Denmark

Section of Solid Mechanics
Department of Mechanical Engineering
Technical University of Denmark
Nils Koppels Alle, Building 404, DK-2800 Kgs. Lyngby, Denmark
Phone +45 4525 4250, Telefax +45 4593 1475
E-mail: `info@mek.dtu.dk`
WWW: `http://www.mek.dtu.dk/`

Publication Reference Data
Nielsen, M. B.
Dynamics of Rigid Bodies and
Flexible Beam Structures
PhD Thesis
Technical University of Denmark,
Section of Solid Mechanics.
September, 2013
ISBN 978-87-7475-373-5
Keywords: Finite rotations, conservative time integration, structural dynamics, constrained mechanics, beam elements, quaternions, cosine directors, wind turbines

Preface

This thesis is submitted in partial fulfillment of the Danish Ph.D. degree from the Technical University of Denmark. The work has primarily been performed at the Department of Mechanical Engineering at the Technical University of Denmark, in the period September 2010 to August 2013 under the supervision of Professor, Dr. Techn. Steen Krenk, to whom I owe my deepest gratitude for his excellent guidance and support throughout the entire project.

The part of the work on multi-level optimization of wind turbine blades has been carried out at the Department of Aerospace Engineering at Politecnico di Milano in the period October to December 2011. I am grateful to Professor Carlo L. Bottasso for making the stay possible and for his supervision during the stay.

Furthermore, I would like to thank my colleagues at the department for fruitful discussions and a pleasant and inspiring working environment.

Finally I would like to express my most sincere thanks to my family for their patience and support during the process. Especially Marie for always being encouraging and understanding.

Kgs. Lyngby, September 2013

Martin Bjerre Nielsen

Resumé

Roterende bevægelse er et ofte forekommende fænomen indenfor mange ingeniørmæssige anvendelser såsom biler, roterende maskineri og vindmøllerotorer. Denne afhandling består af fire dele, der alle omhandler udvikling af effektive beregningsmetoder til modellering af den dynamiske opførsel af stive legemer og fleksible bjælkekonstruktioner med hovedvægt på den roterende bevægelse.

Den første del vedrører bevægelse i en roterende referenceramme. En ny fremgangsmåde, hvor bevægelsesligningerne er formuleret i et hybridt tilstandsformat, er præsenteret. Det er vist, at betragtelige simplificeringer kan opnås, hvis de samme interpolationsfunktioner anvendes for begge tilstandsvariable, hvorved alle inertieffekter kan repræsenteres via den klassiske konstante massematrix. Det hybride tilstandsformat danner grundlaget for udviklingen af et konservativt tidsintegrationsskema samt en tilhørende algoritmisk dæmpning, der kun påvirker den lokale bevægelse.

I den anden del præsenteres et konservativt integrationsskema for stiftlegemebevægelse i en global referenceramme. En fuldtud algebraisk repræsentation af den roterende bevægelse er opnået ved anvendelse af enten fire quaternion parametre eller ni konvekterede basisvektor komponenter. I begge tilfælde er bevægelsesligningerne udledt via Hamilton's ligninger, hvori de kinematiske bindinger, der følger af den redundante rotationsbeskrivelse, er inkluderet ved brug af Lagrange multiplikatorer. En særlig egenskab ved formuleringen er, at disse kan erstattes af en projektionsoperator anvendt på gradienterne af det ydre potential og eventuelle ydre bindinger.

Den tredje del præsenterer et nyt to-knude bjælkeelement, der er i stand til at undergå vilkårligt store flytninger og endelige rotationer. Elementet er udtrykt eksplicit ved brug af globale komponenter af positionsvektorer og tilhørende konvekterede basisvektorer for elementets knuder. Kinematikken er beskrevet i en homogen kvadratisk form, og den konstitutive stivhed er udledt ved brug af komplementær energi for et sæt af ligevægtsformer, der hver repræsenterer en tilstand svarende til konstant indre kraft eller moment. Denne fremgangsmåde undgår lokal interpolation af kinematiske størrelser, hvilker leder til en formulering, der både er fri for låsningsmekanismer og invariant i forhold til valg af referenceramme.

I den sidste del af afhandlingen præsenteres en multi-level optimeringsprocedure for vindmøllevinger. Beregningsprocedurer svarende til dem, der er præsenteret i denne afhandling, udgør grundlaget for en foreløbig optimering ved brug af en multilegeme-baseret bjælkemodel af den fulde vindmølle. De nye aspekter, der her betragtes, vedrører automatisk generering af en 3D FE-model af en enkelt vinge til brug for detaljerede spændings og stabilitetsberegninger, der ikke kan udføres på bjælkemodellern samt anvendelse af resultaterne til opdatering af bjælkemodellen for et efterfølgende iterationsskridt. Det er demonstreret, at konvergens mellem de to modeller kan opnås ved ganske få iterationer.

Abstract

Rotational motion is a frequently occurring aspect in many engineering applications such as automobiles, rotating machinery or wind turbine rotors. The present thesis is organized in four parts - all concerning development of efficient computational methods for modeling the dynamic behavior of rigid bodies and flexible beam structures with emphasis on the rotational motion.

The first part deals with motion in a rotating frame of reference. A novel approach where the equations of motion are formulated in a hybrid state-space in terms of local displacements and global velocities is presented. It is shown that particular simplifications are obtained when the same interpolation functions are used for both state-space variables, whereby all inertia effects can be represented via the classic constant mass matrix. The hybrid state-space constitutes the basis for developing a conservative time integration scheme and an associated algorithmic dissipation, that affects only the local motion.

In the second part a conservative integration scheme for rigid body motion in a global frame of reference is presented. A fully algebraic representation of the rotational motion is obtained by using either four quaternion parameters or nine convected base vector components. In both cases, the equations of motion are obtained via Hamilton's equations by including the kinematic constraints associated with the redundant rotation description by means of Lagrange multipliers. A special feature of the formulation is that these can be replaced by a projection operator applied to the external potential gradient and possible external constraint gradients.

The third part presents a novel two-node beam element capable of undergoing arbitrary large displacements and finite rotations. The element is expressed explicitly in terms of the global components of the position vectors and associated convected base vectors for the element nodes. The kinematics is expressed in a homogeneous quadratic form and the constitutive stiffness is derived from complementary energy of a set of equilibrium modes, each representing a state of constant internal force or moment. This approach avoids local interpolation of kinematic variables, which makes the formulation inherently locking-free and frame-invariant.

In the final part of the thesis a multi-level optimization procedure for wind turbine blades is presented. Computational procedures similar to the ones presented in this thesis constitute the basis for a preliminary optimization using a multibody beam model of the full wind turbine. The novel aspects considered here consist of automatic generation of a 3D FE-model of a single blade for detailed stress and buckling analysis which cannot be performed on the beam model, and utilization of the results for updating the beam model for a subsequent iteration step. It is demonstrated that convergence between the two models is obtained in very few iterations.

Publications

Appended papers

[P1] S. Krenk, M.B. Nielsen, Hybrid state-space time integration in a rotating frame of reference, *International Journal for Numerical Methods in Engineering*, **87**:1301–1324, 2011.

[P2] S. Krenk, M.B. Nielsen, Hybrid state-space time integration of rotating beams, *Computer Methods in Applied Mechanics and Engineering*, **213-216**:243–254, 2012.

[P3] M.B. Nielsen, S. Krenk, Conservative integration of rigid body motion by quaternion parameters with implicit constraints, *International Journal for Numerical Methods in Engineering*, **92**:734–752, 2012.

[P4] S. Krenk, M.B. Nielsen, Conservative rigid body dynamics by convected base vectors with implicit constraints, *Computer Methods in Applied Mechanics and Engineering*, **269**:437–453, 2014.

[P5] M.B. Nielsen, S. Krenk Explicit free-floating beam element, *International Journal for Numerical Methods in Engineering*, **98**:59–78, 2014..

[P6] C.L. Bottasso, F. Campagnolo, A. Croce, S. Dilli, F. Gualdoni, M.B. Nielsen, Structural optimization of wind turbine rotor blades by multilevel sectional / multibody / 3D-FEM analysis, *Multibody System Dynamics*. (in press)

Additional contributions

[A1] M.B. Nielsen, S. Krenk, Hybrid state-space time integration of rotating beams, Proceedings of the 23rd Nordic Seminar on Computational Mechanics, October 21–22, Stockholm, Sweden, 2010.

[A2] M.B. Nielsen, S. Krenk, Conservative time-integration of rigid body motion with implicit constraints by quaternion parameters, Proceedings of the 8th European Solid Mechanics Conference, July 9–13, Graz, Austria, 2012.

[A3] M.B. Nielsen, S. Krenk, A conservative quaternion-based time integration algorithm for rigid body rotations with implicit constraints, Proceedings of the 25rd Nordic Seminar on Computational Mechanics, October 25–26, Lund, Sweden, 2012.

[A4] S. Krenk, M.B. Nielsen, Rigid body time integration by convected base vectors with implicit constraints, Proceedings of the 4th International Conference on Computational Methods in Structural Dynamics and Earthquake Engineering (Keynote), June 12–14, Kos, Greece, 2013.

[A5] M.B. Nielsen, S. Krenk, Multibody motion in an implicitly constrained director format and links via explicit constraints, Proceedings of ECCOMAS Thematic Conference on Multibody Dynamics 2013, July 1–4, Zagreb, Croatia, 2013.

Contents

1. Introduction

Rotating parts occur within many engineering fields such as automobiles, aeroplanes and helicopters, space structures, robotics and wind turbines. Common for all of them is the need for efficient and reliable computational procedures for dynamic analysis of the rotational motion as this is often an important aspect in determining the optimal design.

This has led to remarkable developments within the fields of structural and multi-body dynamics in the last two decades. In particular conservative time integration schemes for integrating the equations of motion have been developed in terms of the so-called energy-momentum methods [41, 93, 98]. Contrary to classic collocation-based methods such as the Newmark scheme [81] and its various α-modifications [28, 43, 105], these methods can be designed such that they exactly represent the energy and momentum balance equations over a finite time step.

The key point in conservative schemes is to base the time integration on an integrated form of the equations of motion. It was demonstrated in [98] for rigid bodies and in [93] for linear elastic materials with non-linear kinematics that energy conservation can be obtained by a suitable discretization. Extensions to more general elastic materials are given in [41] via the notion of finite derivatives, while inclusion of constraints has been considered in e.g. [12, 70]. Traditionally, the conservative properties rely on evaluation of internal forces via combinations of mean values of stresses and strains on element level. However, as demonstrated for translation based solid elements with a quadratic strain representation, the representative internal force can be expressed in a particularly attractive form where the model non-linearity enters via a global term formed by the increment of the geometric stiffness [58].

For some applications such as wind turbines and rotating machinery where the overall rotational motion is rather well-described and the local deformations can be assumed moderate, it may be convenient to consider the motion in a rotating frame of reference. Hereby the gross overall motion can be accounted for by the rotating frame, while the local deformations within this frame can be modeled using simplified models [9, 34, 90]. However, a fundamental aspect of such analysis is the effect of inertial forces generated by the rotation; notably coriolis and centrifugal forces. In classic methods the inertial effects are expressed via local velocities obtained by time differentiation of interpolated displacements at a generic point [36, 77, 78].

This leads to a representation where the angular velocities appear inside the integrals defining the inertia contributions for the individual elements, and thus such methods require recalculation on element level at each time step. Alternatively a rearrangement in auxiliary sub-matrices can be performed [90]. However, this is associated with increased complexity and furthermore complicates the development of a conservative integration scheme in a rotating frame.

In other cases where the local deformations cannot be assumed small, it may be desirable instead to formulate the equations of motion with respect to an inertial frame of reference. However, this introduces a number of difficulties, mainly associated with proper handling of finite rotations. In particular the combination of finite rotations in three-dimensional space requires special measures that account for their non-commutative properties. Several suggestions for proper parameterizations can be found in the literature. These can be classified as either trigonometric representations based on e.g. three successive angles about different axis [39] or rotation pseudo vectors representing a rotation about a fixed axis [5, 14] or algebraic representations such as the use of quaternions (Euler parameters) [18, 80, 91, 102] or convected base vectors (directors) [19]. In particular the algebraic representations provide simple relations for the rotation increments, thus facilitating the development of conservative integration schemes.

Furthermore, the development of flexible elements accommodating finite rotations usually results in rather complex formulations. In particular numerous formulations for flexible beams can be found in the literature. A special role is taken by the so-called geometrically exact formulations, see e.g. [21, 27, 45, 46, 86, 87, 92, 95]. However, while the underlying kinematic description is well-defined according to Euler's elastica theory the spatial discretization may introduce a number of problems such as locking-related phenomena or lead to frame invariant strain descriptions. Additionally, the strain description commonly used in these formulations seems unable to be expressed within a homogeneous quadratic format that permits development of a conservative time scheme in attractive global format [58].

The objective of the present work is to formulate efficient computational methods for rigid body dynamics and flexible beam structures. Both rotating frame of reference approaches as well as inertial frame approaches are considered with the common aim of developing associated energy and momentum conserving integration schemes. The key to the attractive format described in [58] is the use of a quadratic deformation description, and thus a recurrent goal of all the formulations considered in the present project is to extend this property to models including finite rotations. For an elastic system with quadratic kinematics, the elastic potential is a quadratic form in strain variables, that in themselves are quadratic in the generalized displacements. This bi-quadratic form permits explicit relations for the finite potential increment via end-point based mean values and differences. Furthermore, a quadratic kinematic description is the minimum order of non-linearity capable of handling finite deformation, see e.g. [61]. Models where the kinematic

description can be represented in a homogeneous quadratic form is thus the scope of the present thesis.

The thesis consists of an extensive summary covering the main aspects of the theory and representative numerical simulations, followed by six journal papers, denoted [P1] to [P6], which cover the presented material in greater detail. The papers [P1]-[P2] present a novel procedure for conservative time integration in a rotating frame of reference. The equations of motion are formulated in a hybrid state-space, formed by *local* displacements and *global* components of the velocity. It is demonstrated that particular simplifications are obtained for the inertia effects associated with rotational motion when the same interpolation functions are used for both state-space variables. This facilitates the development of an energy and momentum conserving integration algorithm and a consistent algorithmic damping scheme. The basic procedure is developed for translation-based isoparametric elements in [P1] and extended to beam elements accommodating translations and rotations of moderate magnitude in [P2]. Motion with respect to an inertial frame is the scope of the papers [P3] and [P4], where conservative time integration schemes for constrained rigid body rotations are presented based on the four component quaternion description and the nine component director representation, respectively. In both cases kinematic constraints associated with the redundant parameterization are enforced initially via Lagrange multipliers. However, a common feature, demonstrated in [P3] for a single scalar constraint and in [P4] for a set of multiple constraints, is that the Lagrange multipliers can be embedded in the discrete equations of motion via an explicit projection operator applied to the external potential gradient. The paper [P5] presents an explicit free-floating beam element via global components of nodal position and attached convected base vectors similar to the ones presented in [P4]. These serve to define six generalized strain components in a homogeneous quadratic form, each associated with a local equilibrium mode. The constitutive stiffness is derived via complementary energy of the equilibrium modes, which leads to an inherently locking-free formulation. Finally the paper [P6] presents a typical application for computational tools similar to the ones developed in this thesis in terms of a multi-level optimization procedure for wind turbines. The procedure combines 'coarse'-level analysis of multibody beam models with 'fine'-level analysis of detailed three-dimensional FE-models, and it is demonstrated that a simple heuristic approach can be used for integrating both models in a unified multi-level optimization framework for wind turbine blades.

The extended summary is organized as follows: First the theoretical framework for hybrid state-space time integration in a rotating frame of reference presented in [P1]-[P2] is summarized in Section 2. Next the procedures for modeling of general rigid body motion with implicit constraints from [P3]-[P4] are presented in a common notation in Section 3, while the explicit flexible beam element developed in [P5] is the scope of Section 4. Finally the multi-level optimization procedure for wind turbine blades presented in [P6] is summarized in Section 5, while concluding remarks on the main results and suggestions for possible future extensions of the work are given in Section 6.

2. Time integration in a rotating frame of reference

The dynamics of rotating bodies, such as machine parts or wind turbine blades is often modeled in a rotating frame of reference. This may be considered as a special case of the floating frame approach widely used in multibody dynamics, see e.g. Shabana [89]. Floating frame formulations are particularly attractive as the gross overall motion can be described by a rigid body motion of the local frame while the deformations within this frame for many applications may be assumed small or moderate, [9, 34, 90]. Despite these simple kinematic simplifications an accurate representation of the geometric stiffening is crucial for balancing the effect from centrifugal forces, Kane et al. [50]. Geometric stiffness may be included to various level of sophistication ranging from initial stress-based formulations with respect to initial geometry [103, 104] to the use of fully non-linear strain measures [74,96]. Comparative studies of the effect of geometric stiffness are presented in e.g. Meijaard [76], Mayo et. al. [75] or Maqueda et. al. [72].

The classic state-space representation of dynamics in a rotating frame follows the format given by Meirovitch [77, 78] in terms of *local* displacements and *local* velocities. However, this does not provide a direct representation of the momentum equation, and thus the equations are typically supplemented by a stiffness relation in order to satisfy suitable symmetry properties, [36, 79]. Additionally the presence of centrifugal and Coriolis effects in a discretized model leads to time dependent inertia matrices as the angular velocities representing the convected velocity contribution, appear inside the integrals representing the contributions from the individual elements. Thus, the system matrices must be reassembled when the angular velocity changes or reorganized into several auxiliary matrices, Shabana [90].

In contrast, it is demonstrated in the papers [P1] and [P2] that all inertial terms associated with the dynamics in a rotating frame of reference can be expressed solely via the classic constant mass matrix, when stating from a hybrid state-space, in which the *local* displacements and *global* velocities are interpolated using the same shape functions. The resulting equations of motion then take a symmetric form and provide the basis for development of a conservative time integration scheme including possibly algorithmic dissipation that only affects the local motion. The main points are summarized in the following.

2.1. Kinematics and independent interpolation

Analysis of a rotating structure is commonly based on a discretized model where the body is represented by N nodes. The nodal positions can be expressed in local components $\mathbf{x}_1, \ldots, \mathbf{x}_N$ with respect to a local frame of reference that rotates with angular velocity $\boldsymbol{\Omega}$ about a fixed origin. The situation is illustrated in Fig. 2.1 where the origin of the rotating frame for simplicity of notation is selected to coincide with the global frame.

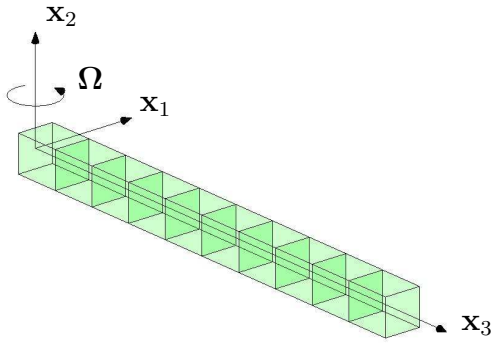

FIGURE 2.1. Body in a local frame $\{\mathbf{x}_1, \mathbf{x}_2, \mathbf{x}_3\}$ rotating with angular velocity $\boldsymbol{\Omega}$.

The positions of the nodes in the local frame serve to define the elastic energy, while the kinetic energy is a function of the corresponding global velocities, expressed via their local components $\mathbf{v}_1, \ldots, \mathbf{v}_N$. The transformation between the local components of the position of a node j given by $\mathbf{x}_j$ and its corresponding global components $\underline{\mathbf{x}}_j$ can be expressed by a rotation in the form

$$\underline{\mathbf{x}}_j \;=\; \mathbf{R}\mathbf{x}_j \,, \tag{2.1}$$

where the matrix $\mathbf{R}$ defining the current rotation of the local frame is a proper orthonormal rotation tensor, i.e. $\mathbf{R}^T\mathbf{R} = \mathbf{I}$. The local components of the absolute velocity $\mathbf{v}$ can be obtained by absolute time differentiation of (2.1) followed by pre-multiplication with $\mathbf{R}^T$. The result combines the contribution from the local velocity with the convective velocity from rotation of the frame and can be expressed in the generic form

$$\mathbf{v}_j \;=\; D_t\mathbf{x}_j \;=\; (\partial_t \,+\, \tilde{\boldsymbol{\Omega}})\,\mathbf{x}_j \,, \tag{2.2}$$

where $\tilde{\boldsymbol{\Omega}} = \boldsymbol{\Omega}\times$ is the skew-symmetric matrix representing the cross product with the angular velocity vector $\boldsymbol{\Omega} = [\Omega_1, \Omega_2, \Omega_3]^T$.

The choice of interpolation scheme for the motion of an internal point with material coordinates ξ constitutes a crucial step in obtaining a discretized form of the equations of motion. The assembled position vector, containing the local position of all the N nodes of the structure, is conveniently introduced as $\mathbf{x}^T = [\mathbf{x}_1^T, \ldots, \mathbf{x}_N^T]$. By using this notation, the position of a generic point with internal coordinate ξ can be expressed in the classic format via a suitable interpolation matrix $\mathbf{N}(\xi)$,

$$\mathbf{x}_\xi \;=\; \mathbf{N}(\xi)\mathbf{x} \,. \tag{2.3}$$

The main issue here is the representation of the corresponding velocity $\mathbf{v}_\xi$. Traditionally a Lagrangian approach has been used in the sense that the local components of the velocity $\mathbf{v}_\xi$ are obtained by absolute time differentiation of the interpolated values $\mathbf{x}_\xi$ according to (2.2). This will in general lead to a format where the convective terms accounting for rotation of the local frame are represented via the product $\tilde{\mathbf{\Omega}}\mathbf{N}(\xi)$, and thus the angular velocity $\mathbf{\Omega}$ appears inside the integral expression when forming the kinetic energy. In the particular case of isotropic interpolation, i.e. when the same interpolation functions apply to all displacement components associated with a node, the factors can be interchanged, i.e. $\mathbf{N}(\xi)\tilde{\mathbf{\Omega}}$, which allows the angular velocity to be extracted from the integral expression. In this way all inertia effects can be expressed solely via external matrix operations on the classic constant mass matrix [51]. However, in the general case of non-isoparametric interpolation, the attractive property of moving the angular velocity outside the integral requires a substantial substructuring of the mass matrix, [90]. Therefore, in cases with time-dependent angular velocity, the formulation involves reassembly of all matrices containing $\mathbf{\Omega}$ or its derivatives.

In the papers [P1] and [P2] a fundamentally different approach along the lines of Hamiltonian mechanics is adopted, see e.g. [39]. In Hamilton mechanics the equations of motions are represented by a symmetric set of first order differential equations in terms of a set of generalized displacements and their conjugate momentum variables. These are treated as independent variables, which suggests use of identical interpolation schemes for both variables. This approach is illustrated for translation-based elements in [P1]. When the mass matrix is constant, the momentum vector can be replaced by the nodal velocity vector, hence an interpolation scheme similar to (2.3) can be adopted for the velocity. The absolute velocity at a generic point ξ then takes the form

$$\mathbf{v}_\xi \;=\; \mathbf{N}(\xi)\mathbf{v} \;=\; \mathbf{N}(\xi)(\partial_t + \tilde{\mathbf{\Omega}}_D)\mathbf{x}\,. \tag{2.4}$$

In this format the velocity is interpolated from the nodal values obtained via the convected differentiation operator defined in (2.2). This is here extended to global form by introduction of the block diagonal matrix $\tilde{\mathbf{\Omega}}_D = \lceil \tilde{\mathbf{\Omega}}, \ldots, \tilde{\mathbf{\Omega}} \rfloor$.

In [P2] it is illustrated that extension to three-dimensional beam elements accommodating both translations and rotations of moderate magnitude is straight forward by inclusion of an additive term in the kinematic relation. The local configuration vector $\mathbf{x}_j$ is conveniently organized in a $2N$ block format where each nodal contribution includes three translational components $\boldsymbol{x}_j = [x_1, x_2, x_3\,]^T$ and three rotational components $\boldsymbol{\varphi}_j = [\varphi_1, \varphi_2, \varphi_3\,]^T$ expressed in the three-component rotation vector format, see e.g. [35]. Similarly an extended form of the absolute velocity vector $\mathbf{v}_j$ is introduced, whereby

$$\mathbf{x}_j \;=\; \begin{bmatrix} \boldsymbol{x}_j \\ \boldsymbol{\varphi}_j \end{bmatrix} \quad , \quad \mathbf{v}_j \;=\; \begin{bmatrix} \dot{\boldsymbol{x}}_j + \tilde{\mathbf{\Omega}}\boldsymbol{x}_j \\ \dot{\boldsymbol{\varphi}}_j + \mathbf{\Omega} \end{bmatrix}. \tag{2.5}$$

It is seen that the convective velocity contribution from rotating the frame of reference affects the translational velocity components according to (2.2), while the convective angular velocity enters as an additive contribution to the local angular velocity, which for moderate rotations is represented as $\dot{\boldsymbol{\varphi}}_j$. The interpolation of the velocity can therefore be expressed in a form similar to (2.4), by including an additive contribution to the rotational degrees of freedom:

$$\mathbf{v}_\xi \,=\, \mathbf{N}(\xi)\mathbf{v} \,=\, \mathbf{N}(\xi)\big[(\partial_t + \tilde{\boldsymbol{\Omega}}_D)\mathbf{x} \,+\, \boldsymbol{\Omega}_C\,\big]\,. \tag{2.6}$$

The block-diagonal matrix $\tilde{\boldsymbol{\Omega}}_D$ and the vector $\boldsymbol{\Omega}_C$ are here expressed via $\lceil\tilde{\boldsymbol{\Omega}}, 0\rfloor$ and $[\mathbf{0}^T, \boldsymbol{\Omega}^T]^T$, respectively, which are repeated for each node of the structure. It is seen that the shape-function matrix $\mathbf{N}(\xi)$ appears to the left of the combined time differentiation and convection terms in both (2.4) and (2.6), thereby permitting the simple representation of inertia forces as discussed above.

2.2. Equations of motion

The equations of motion can be obtained in several different ways using e.g. the variational principles of Lagrange or Hamilton, [39]. While the particular form may be of minor importance when considering the exact continuous case, the choice of format is a central issue in the development of discrete time integration schemes. For the current use Lagrange equations constitute a convenient means for obtaining the equations of motion from the derivatives of the kinetic energy T and the elastic energy G. These are expressed in terms of the displacements, here introduced as the difference between the current and the initial position $\mathbf{u} = \mathbf{x} - \mathbf{x}_0$, and their time derivatives $\dot{\mathbf{u}}$, in the form

$$\frac{d}{dt}\left(\frac{\partial T}{\partial \dot{\mathbf{u}}^T}\right) \,-\, \frac{\partial T}{\partial \mathbf{u}^T} \,+\, \frac{\partial G}{\partial \mathbf{u}^T} \,=\, \mathbf{f}\,, \tag{2.7}$$

where $\mathbf{f}$ represents the external generalized forces. The kinetic energy associated with the global motion follows from integrating the specific kinetic energy expressed via (2.4) or (2.6) over the volume of the body and yields the quadratic expression

$$T \,=\, \tfrac{1}{2}\mathbf{v}^T\mathbf{M}\mathbf{v}\,. \tag{2.8}$$

It is seen that the mass matrix is constant, since the interpolation refers to initial geometry. Furthermore, it is noted that the effect of rotating the local frame of reference is included implicitly via the absolute velocity vector. The internal forces $\mathbf{g}(\mathbf{u})$ are defined as the displacement derivatives of a potential function $G(\mathbf{u})$, hence the use of Lagrange's equations with the kinetic energy T expressed via the absolute velocity $\mathbf{v}$ then identifies the equations of motion in the well-known form, - as a set of second order differential equations in time. However, the effect of rotating the

local frame of reference is accounted for by replacing the partial time derivative ∂_t with the convected derivative $D_t = (\partial_t + \tilde{\mathbf{\Omega}})$, whereby

$$(\partial_t + \tilde{\mathbf{\Omega}}_D)\mathbf{M}\mathbf{v} \,+\, \mathbf{g}(\mathbf{u}) \,=\, \mathbf{f}\,. \tag{2.9}$$

This second-order differential equation typically constitutes the starting point for the development of collocation-based integration schemes such as Newmark [81] or generalized α-methods [28]. These methods are commonly based on matching the equations of motion at discrete points in time using approximate expressions for the local displacement and velocity increments, and thus they do not in general lead to exact conservation of energy and momentum as discussed in [56]. In contrast conservative integration schemes are typically developed from an integrated form of two first order state-space differential equations defining the momentum in terms of the displacement variables and the equations of motion via the momentum variables, respectively. In this context the application of a hybrid state-space format combining local displacements $\mathbf{u}$ and local components of the global velocities $\mathbf{v}$ appear as an obvious choice when observing that the momentum variables are given as $\mathbf{M}\mathbf{v}$. Following the procedure in [P1]-[P2], the hybrid state-space equations are obtained by combining the system format of the kinematic relation (2.2) and the equations of motion (2.9),

$$\begin{bmatrix} \mathbf{0} & \mathbf{M} \\ -\mathbf{M} & \mathbf{0} \end{bmatrix} \begin{bmatrix} \dot{\mathbf{u}} \\ \dot{\mathbf{v}} \end{bmatrix} + \begin{bmatrix} \mathbf{g}(\mathbf{u}) + \tilde{\mathbf{\Omega}}_D\mathbf{M}\mathbf{v} \\ \mathbf{M}\tilde{\mathbf{\Omega}}_D^T\mathbf{x} + \mathbf{M}\mathbf{v} \end{bmatrix} = \begin{bmatrix} \mathbf{f} \\ \mathbf{0} \end{bmatrix}. \tag{2.10}$$

The equations appear as a simple generalization of the classic state-space equations, see e.g. [61], where the effect of rotating the local frame are accounted for by two linear terms in the angular velocity. In the limit of vanishing angular velocity the classic state-space format is recovered, however with a sign change in the second equation in order to provide a symmetric set of equations. The change of sign is a trade-off, as symmetry is obtained by sacrificing the positive definite form of the second matrix. A main feature of the present format is that all convective contributions are represented solely via the matrix $\tilde{\mathbf{\Omega}}_D\mathbf{M}$ and its transpose, and thus neither the angular acceleration of the rotating frame nor the square of the angular frequency, associated with the centrifugal force, appear explicitly. In the classic format based on local displacements $\mathbf{u}$ and local velocities $\dot{\mathbf{u}}$ a similar anti-symmetric and symmetric structure is obtained by expressing the kinematic equation in a stiffness format and neglecting the angular acceleration, [36, 79]. The use of hybrid state-space variables therefore leads to a more general format, while preserving the interpretation of the kinematic equation as a momentum relation. Furthermore, as the angular velocity only enters linearly, the format lends itself easily to the development of a conservative integration scheme and the possible introduction of monotone algorithmic damping.

2.3. Conservative time integration algorithm

Conservative time integration algorithms are typically developed by considering an incremental form of the equations of motion, - in the present case (2.10). For a constant mass matrix the increments of the state-space variables $\Delta\mathbf{u}$ and $\Delta\mathbf{v}$ are obtained directly by integration over a time interval $h = t_{n+1} - t_n$. The striking point is therefore associated with representation of the remaining terms which now represent equivalent mean values over the considered time interval. It is well-known that use of the implicit mid-point rule leads to a conservative format in the case of non-rotating systems, [93,98]. It has been demonstrated in [P1]-[P2] via the discrete energy balance that conservative properties are achieved in a rotating frame when also the angular velocity is represented by the algebraic mean of its initial and final value in the interval $\bar{\mathbf{\Omega}}$. The internal forces $\mathbf{g}$ and external forces $\mathbf{f}$ can in general be represented via discrete derivatives [41], as denoted by an asterisk. In terms of this notation the discretized state-space equations take the form

$$\left[\begin{array}{cc} \mathbf{0} & \mathbf{M} \\ -\mathbf{M} & \mathbf{0} \end{array}\right]\left[\begin{array}{c} \Delta\mathbf{u} \\ \Delta\mathbf{v} \end{array}\right] + h\left[\begin{array}{c} \mathbf{g}(\mathbf{u})_* + \bar{\tilde{\mathbf{\Omega}}}_D\mathbf{M}\bar{\mathbf{v}} \\ \mathbf{M}\bar{\tilde{\mathbf{\Omega}}}_D^T\bar{\mathbf{x}} + \mathbf{M}\bar{\mathbf{v}} \end{array}\right] = h\left[\begin{array}{c} \mathbf{f}_* \\ \mathbf{0} \end{array}\right]. \tag{2.11}$$

This result is simple in the sense that all products are discretized by representing each factor by its mean value. This is a neat consequence of using the hybrid state-space format, where angular velocities only enter linearly, without explicit occurrence of either angular accelerations or centrifugal forces.

An important aspect when modeling rotating structures is a proper representation of the stress stiffening effect as this plays a central role in balancing the centrifugal forces which introduce a negative stiffness term of the form $-\tilde{\mathbf{\Omega}}_D^T\mathbf{M}\tilde{\mathbf{\Omega}}_D$. However, this requires a non-linear internal force relation, for which the conservative discretizations traditionally rely on evaluation of stresses and strains in mean states within the current time interval. When using a quadratic format for the generalized strains, which is the case for the solid elements based on Green strains in [P1] and beam elements with quadratic kinematics in [P2], the internal force term can be represented by a global term formed by its mean value at t_n and t_{n+1} plus an extra term involving the increment of the global geometric stiffness matrix $\Delta\mathbf{K}_g$ over the current step, [58],

$$\mathbf{g}(\mathbf{u})_* \;=\; \tfrac{1}{2}[\,\mathbf{g}_{n+1} + \mathbf{g}_n\,] - \tfrac{1}{4}\Delta\mathbf{K}_g\Delta\mathbf{u}\,. \tag{2.12}$$

This format is particularly attractive since the global increment of the geometric stiffness usually is directly available in standard finite element codes, hence special procedures for evaluating internal mean states - typically on element level - are avoided. Furthermore, the additional term permits a rather intuitive interpretation as a viscous damping term that ensures exact conservation of energy. Similarly, if a potential representation of the external force $\mathbf{f}$ is known, the discrete derivative $\mathbf{f}_*$ in (2.11) can often be expressed within a global difference/mean value format.

The local form of the energy balance can be obtained by pre-multiplication of the state-space equations (2.11) and expressing the absolute velocity $\mathbf{v}$ in terms of the local velocity $\dot{\mathbf{u}}$ via the kinematic relation (2.11b). The discrete energy balance equation hereby takes the form

$$\left[\tfrac{1}{2}\dot{\mathbf{u}}^T\mathbf{M}\dot{\mathbf{u}} - \tfrac{1}{2}\tilde{\boldsymbol{\Omega}}_D\mathbf{x}^T\mathbf{M}\tilde{\boldsymbol{\Omega}}_D\mathbf{x} + G(\mathbf{u})\right]_n^{n+1} \;+\; \overline{\mathbf{v}^T\mathbf{M}(\Delta\tilde{\boldsymbol{\Omega}}_D\mathbf{x})} \;=\; \Delta\mathbf{u}^T\mathbf{f}_* \,. \tag{2.13}$$

It is seen that the overall rotation of the local frame is accounted for by a modification of the local energy potential by a term that is quadratic in the angular velocity $\boldsymbol{\Omega}$ and a term containing the angular acceleration, - here expressed via its increment $\Delta\boldsymbol{\Omega} = h\dot{\boldsymbol{\Omega}}$. The contribution to the local energy potential is associated with the work performed by the centrifugal forces, and thus it leads to a negative contribution to the local stiffness, even in the case of stationary rotation.

2.4. Algorithmic damping

Discretized structures often include high-frequency components that are not representative for the underlying continuous system. Therefore it may be desirable to introduce a so-called algorithmic damping that monotonically increases the rate of dissipation with increasing frequency, while leaving the low-frequency range virtually unaffected. In [P1] a consistent algorithmic damping scheme is identified by applying the conservative algorithm to a decaying response, which is rendered stationary by an increasing exponential factor that compensates the decay. A more direct approach is used in [P2], where a suitable format for algorithmic damping is identified by selecting a desirable form of the dissipative contribution D to the energy balance. It has been demonstrated for a non-rotating system that a suitable dissipation is a quadratic form of the local state-space variables $\Delta\mathbf{u}$ and $\Delta\dot{\mathbf{u}}$ [7,60]. In the present context it is similarly desirable to formulate the dissipation in terms of the local velocity $\dot{\mathbf{u}}$ in order only to affect the local motion in the rotating frame of reference. Thus the dissipation is introduced as a suitable fraction of the local energy represented by the dissipation parameter α, in the form

$$D = \tfrac{1}{2}\alpha\Big\{\Delta\dot{\mathbf{u}}^T\mathbf{M}\Delta\dot{\mathbf{u}} + \Delta\mathbf{u}^T(\mathbf{K} - \bar{\tilde{\boldsymbol{\Omega}}}_D^T\mathbf{M}\bar{\tilde{\boldsymbol{\Omega}}}_D)\Delta\mathbf{u}\Big\}\,. \tag{2.14}$$

It is important to realize that the centrifugal potential gives a negative contribution to the local stiffness, here expressed by a representative value $\mathbf{K}$, as discussed in relation to the energy balance. As illustrated in [P2] this can be expressed via the increments of the state-space variables and the discrete state-space equations can then be recast into the following form:

$$\begin{bmatrix} \tfrac{1}{2}\alpha h\mathbf{K} & (\mathbf{I} + \tfrac{1}{2}\alpha h\bar{\tilde{\boldsymbol{\Omega}}}_D)\mathbf{M} \\ \mathbf{M}(-\mathbf{I} + \tfrac{1}{2}\alpha h\bar{\tilde{\boldsymbol{\Omega}}}_D^T) & \tfrac{1}{2}\alpha h\mathbf{M} \end{bmatrix}\begin{bmatrix}\Delta\mathbf{u}\\ \Delta\mathbf{v}\end{bmatrix} + h\begin{bmatrix}\mathbf{g}(\mathbf{u})_* + \bar{\tilde{\boldsymbol{\Omega}}}_D\mathbf{M}\bar{\mathbf{v}} \\ \mathbf{M}\bar{\tilde{\boldsymbol{\Omega}}}_D^T\bar{\mathbf{x}} + \mathbf{M}\bar{\mathbf{v}}\end{bmatrix} \;=\; h\begin{bmatrix}\mathbf{f}_*\\ \mathbf{0}\end{bmatrix}. \tag{2.15}$$

It is seen that the algorithmic dissipation is introduced via symmetric terms with the common factor $\frac{1}{2}\alpha h$ in the first matrix. Alternatively these could have been embedded in the second matrix by introduction of α-weighted mean values [P1]. The scheme may be generalized to high-frequency dissipation by using auxiliary variables representing the state-space variables via a first order filter relation [60]. Furthermore a higher order accuracy can be obtained by introducing off-diagonal block-matrices $-\frac{1}{12}h^2\mathbf{K}$ in the first matrix of (2.15) along with additional damping block matrixes $-\alpha h\mathbf{K}$ in the second term [57]. For frequencies well below the aliasing limit, the damping parameter α can be related to the modal damping ratio ζ_k [60]. This can be formulated as the asymptotic relation $\zeta_k \simeq \frac{1}{2}(\omega_k h)$, i.e. a modal damping ratio proportional to the associated modal frequency ω_k.

The state-space format (2.15) provide a convenient means for illustrating the structure of the algorithm as well as a clear interpretation of the term needed for ensuring energy conservation. However, from a numerical point of view it is advantageous to recast the equations into a displacement format by eliminating the explicit occurrence of the velocity $\mathbf{v}$. This is accomplished by using the second equation in (2.15), which after solving for the displacement increment $\Delta\mathbf{u}$ also serves as the recovery relation for obtaining the associated velocity increment $\Delta\mathbf{v}$. The details of the algorithm and explicit pseudo-codes are given in [P1] and [P2].

2.5. Numerical examples

The accuracy and performance of the present algorithm has been illustrated by several examples for isoparametric elements as well as beam elements with quadratic kinematics in [P1] and [P2]. Furthermore simulations based on a linearized beam theory are considered in [A1].

Kane's driver

A classic benchmark problem originally introduced by Kane et. al. [50] consists of a spin-up sequence of a beam rotating about a fixed axis. A crucial aspect in this example is the need for inclusion of a representative geometric stiffness. The parameters in common use were defined in [94,96] and have been adopted here. The angular velocity is increased over a period $T_s = 15\,\mathrm{s}$ to its final value $\Omega_s = 6\,\mathrm{rad/s}$. Results for the transverse and axial tip displacements are shown in Fig. 2.2(a) and 2.2(b), respectively. The response is characterized in terms of the maximum magnitude of the displacement components occurring at approx $t = 7\,\mathrm{s}$ and the behavior in the stationary state, i.e. $t \geq T_s$. Numerical results for these values are given in [P2] for elements based on a beam theory with quadratic kinematics, a linearized beam theory with initial stress-based geometric stiffness and a fully nonlinear isoparametric formulation with quadratic interpolation. In general a good agreement is found among the three formulations as well as with respect to results in Simo and Vu-Quoc [94], Downer et. al [31] and Meijaard [76]. However, a slight deviation is found for the quadratically interpolated isoparametric elements.

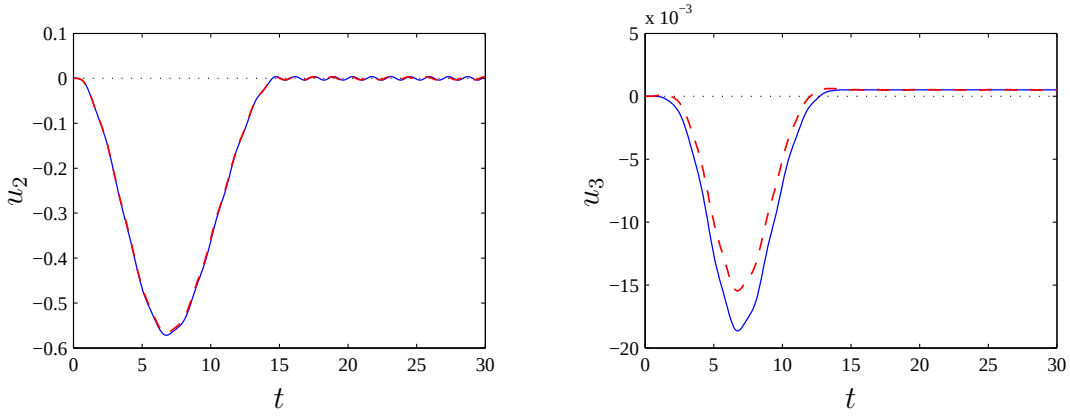

FIGURE 2.2. Kanes driver: (a) Transverse tip displacement. (b) Axial tip displacement. (—) 10 Beam elements with quadratic kinematics, (- -) 10 Isoparametric elements.

Vibration analysis in rotating frame

This example serves to illustrate how a frequency analysis can be performed within the hybrid state-space format. The details are given in [P1] and concerns a rotating U-frame discretized using 20-node isoparametric elements with quadratic interpolation. The natural vibration modes and the corresponding eigenfrequencies of the undamped frame can be determined from the eigenvalue problem

$$\left(\begin{bmatrix} \mathbf{K}_c + \mathbf{K}_g & \tilde{\mathbf{\Omega}}_D \mathbf{M} \\ \mathbf{M}\tilde{\mathbf{\Omega}}_D^T & \mathbf{M} \end{bmatrix} + i\boldsymbol{\omega}_j \begin{bmatrix} \mathbf{0} & \mathbf{M} \\ -\mathbf{M} & \mathbf{0} \end{bmatrix} \right) \begin{bmatrix} \mathbf{u} \\ \mathbf{v} \end{bmatrix}_j = \begin{bmatrix} \mathbf{0} \\ \mathbf{0} \end{bmatrix}, \tag{2.16}$$

which follows directly from the hybrid format (2.10) of the equations of motion, when the internal force is linearized. These equations are somewhat simpler than the traditional format proposed in [36, 79]. The first six natural vibration modes of the U-frame in a stationary frame of reference are shown in Fig. 2.3. It should be

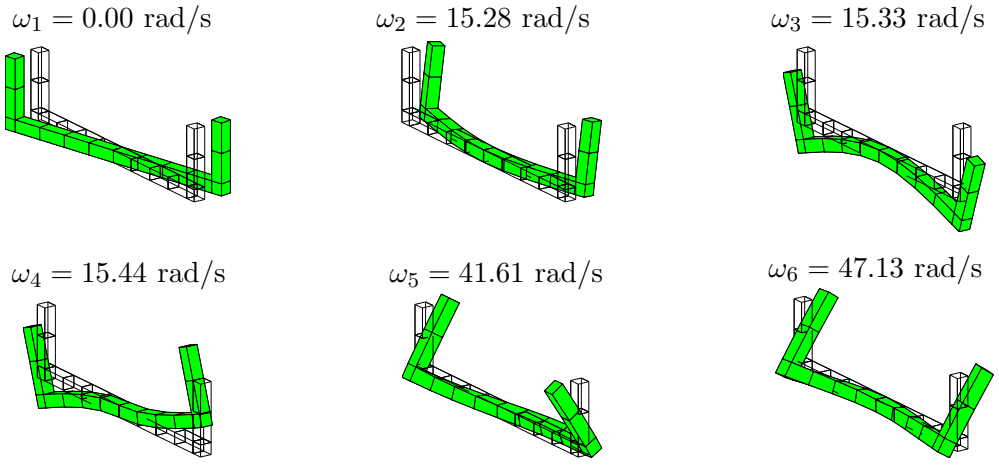

FIGURE 2.3. Solid U-frame: Vibration modes in stationary frame.

noted that the mode-shapes and frequencies change slightly with increasing rotation frequency, but these changes are negligible for the relatively low angular velocities used in the associated example in [P1]. On the other hand, an example considering a rotating blade where the centrifugal stiffening is more pronounced is presented in [P2] and excellent agreement has been found with the reference solution, based on geometrically exact beams presented in Maqueda et. al. [72].

Three-blade rotor

The effect of introducing algorithmic damping is illustrated on a three-blade rotor system. The blades are modeled as tapered pre-twisted beams connected to the end of a flexible shaft. The flexibility of the shaft is an important structural feature. In a three-bladed rotor with identical blades the vibration modes occur in sets of three. For a fully rigid connection the vibration modes for the three blades decouple and the eigenfrequencies and associated modes occur in sets of three - each corresponding to those of a single blade. On the other hand when flexibility is introduced a coupling occurs and the three rotor modes realize themselves in terms of one collective mode and two 'whirling' modes. In the collective mode all blades oscillate in phase, while the blades exhibit a mutual phase difference of $\frac{2}{3}\pi$ in the whirling modes, which may be characterized as a forward and a backward whirling mode, respectively, see e.g. Krenk et. al. [63] or Hansen [42].

The blade is considered in a state of steady rotation with an angular velocity representing a realistic operation speed. Local vibrations are initiated by the two load cases illustrated in Fig. 2.4. These are deliberately designed to excite the first collective mode and the first two whirling modes with frequencies ω_k of 7.84 rad/s and 12.6 rad/s, respectively. The development of the local mechanical energy ΔE is illustrated in Fig. 2.5(a) and 2.5(b) along with the asymptotic approximation $\Delta E \simeq \Delta E_0 e^{-2\zeta_k(\omega_k h)}$ for $h = 0.02$ and $\alpha = 0.05$. This corresponds to the modal damping ratios ζ_k of approximately 0.4% and 0.6%, respectively. It is seen that the present algorithm including numerical dissipation is capable of distinguishing between the different modes even for a non-pure mode excitation, and provide the highest amount of dissipation to the highest frequency mode.

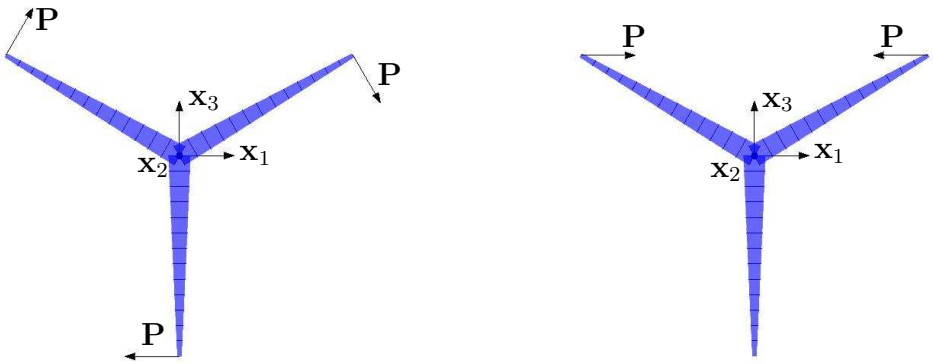

FIGURE 2.4. Rotor configuration with initial load cases.

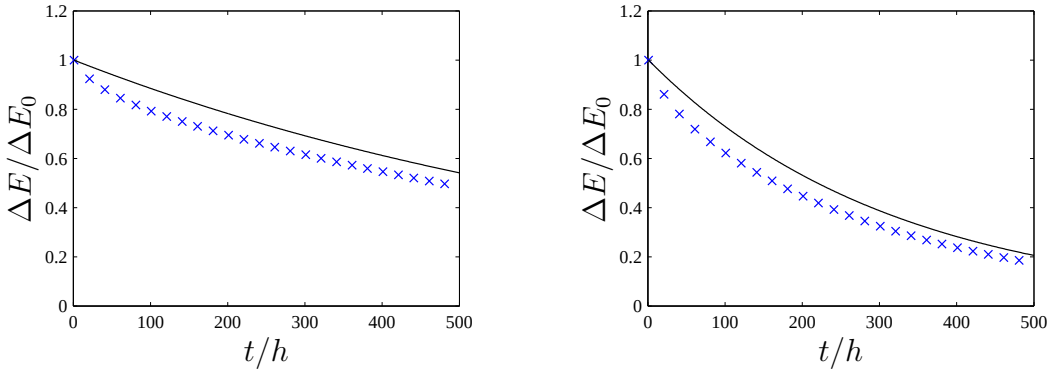

FIGURE 2.5. Three-blade rotor: (a) Energy decay for the load case at Fig. 2.4(a). (b) Energy decay for the load case at Fig. 2.4(b). $h = 0.02$, $\alpha = 0.05$ ($\times$), $e^{-2\zeta_j \omega_j t}$ (–).

3. Conservative integration of implicitly constrained rigid body motion

The basis for describing general motion in three-dimensional space and also the overall motion of the floating frame presented in the preceding chapter is closely related to the kinematics of rigid body motion. In particular the handling of finite rotations requires special features that account for their non-vectorial nature. In essence a rotation is fully described by the nine components of a proper orthogonal tensor, yet only three of them are independent.

In classic dynamics and in connection with robotics, mechanisms and aerospace it may be desirable to express a rotation by three consecutive rotations about different axis in terms of Euler angles, Bryant angles etc. This provides a straightforward geometrical interpretation and represents a minimum set of parameters. However, as pointed out by Stuelpnagel [99] any global three component representation will exhibit singularity, and thus it may be desirable rather to represent rotations by a pseudo-vector defining a rotation angle and the corresponding axis of rotation. The magnitude can be expressed in several ways leading to various representations as described in e.g. Argyris [5] or Bauchau and Trainelli [14]. A non-singular and fully algebraic representation of the rotation tensor can be obtained by using the four-component quaternion description [18,80,91,102] or by using a direct representation via the nine components of the cosine directors, Betsch and Steinmann [19]. Both cases result in a redundant formulation, and thus a number of constraint relations enforcing unit length and orthogonality have to be introduced - typically by means of Lagrange multipliers. Besides further increasing the number of unknowns, the resulting equations of motion now yield a set of algebraic differential equations (DAEs) of index three.

Numerous methods exist for handling constrained mechanical systems. In particular, a comprehensive review is given in Bauchau et. al. [13,68]. A common approach is based on direct algebraic elimination of the Lagrange multipliers from the original continuous equations either by using an instantaneous null-space matrix [71, 83] or via a Moore-Penrose generalized inverse, Udwadia and Kabala [101]. This reduces the number of unknowns along with the index of the DAEs from three to two [22], but at the expense of increased complexity. Consequently such formulations are not easily discretized within the framework of a conservative integration scheme such as the ones presented in [12, 20, 40, 70, 98].

Additionally it is common to further lower the index by introducing the constraints in differentiated form, - typically at acceleration level. However, when discretized using standard collocation-based schemes such as the implicit Newmark [81] or Runge-kutta based methods [64, 88], constraint violations - also known as drift from the constraint manifold - are commonly observed. To alleviate this drift, stabilization methods of Baumgarte type [15] or projection onto the constraint manifold [23, 100, 106] can be applied.

In contrast to the direct elimination methods the original index three DAEs are well-suited for direct development of a conservative scheme [12, 20, 40, 70]. This approach has been applied by Betsch et. al. [16, 17] combined with a subsequent elimination of the Lagrange multipliers using the discrete equivalent of the null-space matrix. The basic idea of conservative methods is to apply a discretization that exactly reproduces the correct incremental change of energy and momentum over a finite time increment. This may be accomplished by suitable combinations of mean values and increments or via the notion of discrete derivatives, Gonzalez [40]. Similarly, when considering a constrained system it is crucial for exact conservation of energy that vanishing of the work done by the constraint forces are implemented at algorithmic level [12, 70]. This is conveniently accomplished by enforcing the constraints in incremental form, whereby the associated Lagrange multipliers are represented by their mid-point value.

In the papers [P3] and [P4] conservative integration schemes for rigid body motion are presented in terms of the four-component quaternion parameterization and the nine component base vector representation, respectively. As mentioned above both representations are redundant and require introduction of additional kinematic constraints. However, a main feature of these formulations is that the constraints can be enforced implicitly as a part of the discrete equations of motion without recourse to Lagrange multipliers. Here, the basic procedure will be presented in a common notation covering both parameterizations, while the details and their individual characteristics are given in [P3] and [P4].

3.1. Kinematics and kinetic energy

The configuration of a rigid body can be described in terms of a local coordinate system centered at a point O defined by the position vector $\mathbf{r}_0$ as illustrated in Fig. 3.1. The orientation of the coordinate system is specified by a rotation matrix $\mathbf{R}$, and thus a point located inside the rigid body with coordinates $\mathbf{x}_0$ has the global components

$$\mathbf{x}(t) \;=\; \mathbf{r}_0(t) \;+\; \mathbf{R}(t)\mathbf{x}_0, \tag{3.1}$$

where $\mathbf{R}$ is a proper orthogonal rotation tensor. For simplicity of notation it is here assumed that the origins of the local and the global frames coincide, i.e. $\mathbf{r}_0 = \mathbf{0}$. However, as illustrated in [P4] and the proceedings paper [A5] the extension to also

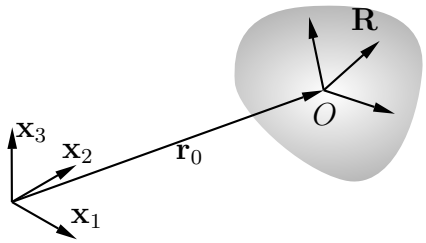

FIGURE 3.1. Rigid body described by position vector $\mathbf{r}_0$ and rotation matrix $\mathbf{R}$.

include translations is straightforward.

Though the rotation matrix $\mathbf{R}$ in principle is uniquely defined by three independent scalar parameters it is often convenient to use a larger number or parameters in order to avoid singularities and obtain a purely algebraic form. This can be obtained by using a redundant set of N generalized displacements $\mathbf{q}$ submitted to $N-3$ homogeneous algebraic constraints of the form

$$\mathbf{e}(\mathbf{q}) \;=\; \mathbf{0}\,. \tag{3.2}$$

For the four component quaternion parametrization considered in [P3] the constraint equation (3.2) reduces to a single quadratic scalar relation, while six quadratic relations are required for enforcing the redundant director format in [P4]. The constraint derivative (or constraint Jacobian) then follow by differentiation with respect to the independent coordinates and yields the $(N-3)\times N$ matrix $\mathbf{C}(\mathbf{q}) = \partial\mathbf{e}/\partial\mathbf{q}$.

The kinematic relation defining a set of $M \leq N$ associated velocity components can be expressed as a bi-linear form of the generalized displacements $\mathbf{q}$ and their derivatives, see e.g. [35]. In particular, the local or material components of the angular velocity $\boldsymbol{\Omega}$ may be expressed as

$$\boldsymbol{\Omega} \;=\; \mathbf{G}(\mathbf{q})\dot{\mathbf{q}}\,, \tag{3.3}$$

where the motion gradient $\mathbf{G}(\mathbf{q})$ is a $M\times N$ matrix. It should be noted that for the quaternion parametrization used in [P3], it is convenient to express kinematic relation (3.3) in the extended format $[0, \boldsymbol{\Omega}^T]^T$ - i.e. with the same number of components as the generalized variables. Providing that the generalized displacements $\mathbf{q}$ satisfy the constraint relations (3.2), the columns of $\mathbf{G}(\mathbf{q})$ span the null-space of the constraint gradient matrix $\mathbf{C}(\mathbf{q})$. This is an important property that can be stated as an orthogonality relation in the form

$$\mathbf{C}(\mathbf{q})\mathbf{G}(\mathbf{q})^T \;=\; \mathbf{0}\,. \tag{3.4}$$

The kinetic energy is conveniently expressed with respect to the local frame in terms of the local angular velocity $\boldsymbol{\Omega}$ and the constant $M\times M$ inertia tensor $\mathbf{J}$. Upon

substitution of the bi-linear relation (3.3), the kinetic energy assumes a bi-quadratic form in the generalized displacements and their derivatives

$$T \;=\; \tfrac{1}{2}\boldsymbol{\Omega}^T\mathbf{J}\boldsymbol{\Omega} \;=\; \tfrac{1}{2}\dot{\mathbf{q}}^T\mathbf{G}(\mathbf{q})^T\mathbf{J}\mathbf{G}(\mathbf{q})\dot{\mathbf{q}}\,. \tag{3.5}$$

When using a quaternion parametrization it is common to introduce an extended form of the inertia tensor given by $\lceil J_0, \mathbf{J} \rfloor$ where the auxiliary parameter J_0 is a scalar parameter. The kinetic energy is independent of this parameter, hence it is merely an artefact of expanding the number of independent velocity parameters. Nonetheless several proposals for specific values based on physical reasoning has been given in e.g. [18,80]. However, as demonstrated in [P3] the parameter J_0 serves the role as a multiplier on the kinematic constraint (3.2) rather than a physical parameter, and thus an optimal choice for J_0 seems to be a mainly numerical issue.

3.2. Equations of motion

The equations of motion governing the dynamics of a constrained rigid body system can be identified via the variational principles of Lagrange and Hamilton, see e.g [39]. Here, the equations of motion are conveniently derived via Hamilton's equations, which yields a set of first order evolution equations for the generalized displacements $\mathbf{q}$ and the conjugate momentum components $\mathbf{p}$.

The generalized momentum components conjugate to $\mathbf{q}$ are defined as the partial derivatives of the kinetic energy T from (3.5) with respect to $\dot{\mathbf{q}}$, whereby

$$\mathbf{p} \;=\; \frac{\partial T}{\partial \dot{\mathbf{q}}^T} \;=\; \mathbf{G}(\mathbf{q})^T\mathbf{J}\,\mathbf{G}(\mathbf{q})\,\dot{\mathbf{q}}\,. \tag{3.6}$$

A central point in the present formulation is the establishment of an orthogonality condition between the generalized displacements $\mathbf{q}$ and the conjugate momentum vector $\mathbf{p}$. This can readily be obtained by pre-multiplication of the relation (3.6) defining $\mathbf{p}$ with the constraint gradient matrix $\mathbf{C}(\mathbf{q})$. According to the orthogonality condition (3.4) the product between $\mathbf{C}(\mathbf{q})$ and $\mathbf{G}(\mathbf{q})$ vanish, whereby the displacement-momentum orthogonality condition takes the bi-linear form

$$\mathbf{C}(\mathbf{q})\,\mathbf{p} \;=\; \mathbf{0}\,. \tag{3.7}$$

It is important to realize that these relations constitute a dynamic complement to the kinematic constraints (3.2) rather than a simple reformulation. Furthermore they play a central role in obtaining the equations of motion in an implicitly constrained format.

In a Hamiltonian formulation the kinetic energy must be recast into a displacement-momentum form, hence the velocities $\dot{\mathbf{q}}$ must be eliminated from the relation (3.5). The matrix $\mathbf{G}$ in both cases satisfies a product relation of the form $\mathbf{G}\mathbf{G}^T = \beta\mathbf{I}$,

where the factor β depends on the specific parameterization, see [P3] and [P4] for explicit relations based on quaternions and directors, respectively. This enables the angular velocity relation (3.3) to be expressed in terms of $\mathbf{p}$ by pre-multiplication of (3.6) with $\beta^{-1}\mathbf{J}^{-1}\mathbf{G}(\mathbf{q})$, and thus the desired form of the kinetic energy follows by substitution into (3.5). The final result can then be expressed in either of the forms

$$T \;=\; \tfrac{1}{2}\mathbf{p}^T\mathbf{G}(\mathbf{q})^T\mathbb{J}^{-1}\mathbf{G}(\mathbf{q})\mathbf{p} \;=\; \tfrac{1}{2}\mathbf{q}^T\mathbf{G}(\mathbf{p})^T\mathbb{J}^{-1}\mathbf{G}(\mathbf{p})\mathbf{q}\,, \tag{3.8}$$

where the factor β is embedded in the modified inertia matrix $\mathbb{J} = \beta^{-2}\mathbf{J}$. The latter expression is valid, since the structure of $\mathbf{G}$ ensures that simultaneous interchange of $\mathbf{q}$ and $\mathbf{p}$ in the two factors on each side of $\mathbb{J}$ does not change the value of the product.

In the present context it is advantageous to use an extended form of the Hamiltonian in which the sum of the kinetic energy from (3.8) and the potential energy function $V(\mathbf{q})$ are augmented by the kinematic constraints given by (3.2),

$$H \;=\; T(\mathbf{q},\mathbf{p}) \;+\; V(\mathbf{q}) + \mathbf{e}(\mathbf{q})^T\boldsymbol{\lambda}\,. \tag{3.9}$$

The latter are initially enforced via $N-3$ Lagrange multipliers $\boldsymbol{\lambda}$. However as illustrated next a particular feature of the present formulation is that these can be eliminated by using the orthogonality condition (3.7), - a task that will be performed first in the continuous format via the time derivative of (3.7), and subsequently repeated for the discretized equations by using the discrete analogous incremental form. The system may be extended to account for translations [P4], or external constraints associated with linking several bodies together [A5].

The equations of motion are obtained from the augmented Hamiltonian (3.9) by differentiation. The kinetic energy is a bi-quadratic form in both $\mathbf{q}$ and $\mathbf{p}$, hence the equations of motion yields the following set of evolution equations

$$\dot{\mathbf{q}} \;=\; \frac{\partial H}{\partial \mathbf{p}^T} \;=\; \mathbf{G}(\mathbf{q})^T\mathbb{J}^{-1}\mathbf{G}(\mathbf{q})\,\mathbf{p}\,, \tag{3.10}$$

$$\dot{\mathbf{p}} \;=\; -\frac{\partial H}{\partial \mathbf{q}^T} \;=\; -\,\mathbf{G}(\mathbf{p})^T\mathbb{J}^{-1}\mathbf{G}(\mathbf{p})\,\mathbf{q} \;-\; \frac{\partial V}{\partial \mathbf{q}^T} \;-\; \mathbf{C}(\mathbf{q})^T\boldsymbol{\lambda}\,. \tag{3.11}$$

The constraint gradient $\mathbf{C}(\mathbf{q})^T$ in the last term of the second equation is the derivative of the kinematic constraints (3.2). The first equation (3.10) is the kinematic equation for the evolution of the generalized displacement vector, while the second equation (3.11) gives the development of the conjugate momentum vector. Additionally differentiation of (3.9) with respect to $\boldsymbol{\lambda}$ yields the kinematic constraint relations (3.2), which along with (3.10) and (3.11) constitute a set of differential algebraic equations. This is the starting point in e.g. [19] and [18].

The main feature of this particular formulation is that the Lagrange multipliers associated with the kinematic constraint equations (3.2) can be eliminated explicitly via the time derivative of the homogeneous orthogonality relation (3.7). The

derivative of this relation yield a sum of two bi-linear terms in $\mathbf{q}$ and $\mathbf{p}$ (and their derivatives), that can be expressed via the evolution equations (3.10) and (3.11). The first two terms, i.e. the terms associated with the homogeneous equations, cancel due to the orthogonality relation (3.7), and leaves a much simplified equation for the Lagrange multiplier vector $\boldsymbol{\lambda}$. Upon solving for $\boldsymbol{\lambda}$ and substitution into (3.11), the modified dynamic equation is obtained

$$\dot{\mathbf{p}} \;=\; -\,\mathbf{G}(\mathbf{p})^T \mathbb{J}^{-1} \mathbf{G}(\mathbf{p})\,\mathbf{q} \;-\; \Big(\mathbf{I} \;-\; \mathbf{C}(\mathbf{q})^T \big[\mathbf{C}(\mathbf{q})\,\mathbf{C}(\mathbf{q})^T\big]^{-1} \mathbf{C}(\mathbf{q})\Big) \frac{\partial V}{\partial \mathbf{q}^T}\,. \qquad (3.12)$$

It is seen that explicit elimination of the Lagrange multiplier amounts to introducing an orthogonal projection operator on the external potential gradient, which subtract the projection of the gradient via $\mathbf{C}(\mathbf{q})$ from the unconstrained gradient. In particular, in the absence of external loads the last term vanish identically, hence the corresponding homogeneous Hamilton equations can be solved directly without introducing the Lagrange multipliers in the first place. An overview of the explicit matrix expressions used in the two formulations [P3] and [P4], respectively, is given in Table 3.1.

3.3. State-space time integration

In essence, conservative integration amounts to ensuring that the discrete form of the evolution equations (3.10) and (3.11) reproduces the correct incremental changes of energy and momentum over a finite time increment. Similarly, when it comes to enforcements of constraints in conservative schemes via Lagrange multipliers, the role of the multipliers is to ensure that the work performed by the constraints over each time interval vanishes, see e.g. Lanczos [66]. Hence rather than enforcing constraints explicitly at the interval boundaries, they are expressed via their increment over the current time interval. The Lagrange multipliers therefore represent a set of generalized reaction forces needed to uphold the constraints over the current interval, and thus it seems natural to represent these as constant effective mean values over each interval. Thus, by initiating a numerical integration from a state that satisfies constraints, the correct representation of the incremental changes over each interval, will ensure continued satisfaction.

A conservative discretization can be obtained directly by equating a finite increment of the Hamiltonian (3.9) over a time step $h = t_{n+1} - t_n$ to zero. The kinetic energy is bi-quadratic in $\mathbf{q}$ and $\mathbf{p}$, and thus its incremental form can be expressed as twice the product of the increment of the first factor and the algebraic mean value of the second factor, see Krenk [61]. The external potential $V(\mathbf{q})$ can in general be represented by its finite derivative $\partial V_*/\partial \mathbf{q}^T$, [41]. However, potentials are often given in terms of powers of the generalized displacements and the finite derivatives can then be expressed in explicit form as well. The discrete form of the constraint term is similar to the kinetic energy obtained as a product of increments and mean

TABLE 3.1. Explicit relations.

Directors	**Quaternions**
Generalized displacements	
$\mathbf{q}^T = [\mathbf{q}_1^T, \mathbf{q}_2^T, \mathbf{q}_3^T]$	$\mathbf{q}^T = [\cos\frac{1}{2}\varphi, \mathbf{n}^T \sin\frac{1}{2}\varphi]$
Kinematic constraints	
$\mathbf{e}(\mathbf{q}) = \begin{bmatrix} \mathbf{q}_1^T\mathbf{q}_1 - \mathbf{I} \\ \mathbf{q}_2^T\mathbf{q}_2 - \mathbf{I} \\ \mathbf{q}_3^T\mathbf{q}_3 - \mathbf{I} \\ \mathbf{q}_2^T\mathbf{q}_3 + \mathbf{q}_3^T\mathbf{q}_2 \\ \mathbf{q}_3^T\mathbf{q}_1 + \mathbf{q}_1^T\mathbf{q}_3 \\ \mathbf{q}_1^T\mathbf{q}_2 + \mathbf{q}_2^T\mathbf{q}_1 \end{bmatrix}$	$\mathbf{e}(\mathbf{q}) = \mathbf{q}^T\mathbf{q} - 1$
Constraint gradient	
$\mathbf{C}(\mathbf{q}) = \begin{bmatrix} \mathbf{q}_1^T & \mathbf{0} & \mathbf{0} \\ \mathbf{0} & \mathbf{q}_2^T & \mathbf{0} \\ \mathbf{0} & \mathbf{0} & \mathbf{q}_3^T \\ \mathbf{0} & \mathbf{q}_3^T & \mathbf{q}_2^T \\ \mathbf{q}_3^T & \mathbf{0} & \mathbf{q}_1^T \\ \mathbf{q}_2^T & \mathbf{q}_1^T & \mathbf{0} \end{bmatrix}$	$\mathbf{C}(\mathbf{q}) = 2\mathbf{q}^T$
Motion gradient	
$\mathbf{G}(\mathbf{q}) = -\frac{1}{2}\begin{bmatrix} \mathbf{0} & -\mathbf{q}_3^T & \mathbf{q}_2^T \\ \mathbf{q}_3^T & \mathbf{0} & -\mathbf{q}_1^T \\ -\mathbf{q}_2^T & \mathbf{q}_1^T & \mathbf{0} \end{bmatrix}$	$\mathbf{G}(\mathbf{q}) = 2\begin{bmatrix} q_0 & \mathbf{q}^T \\ -\mathbf{q} & q_0\mathbf{I} - \tilde{\mathbf{q}} \end{bmatrix}$
Projection operator	
$\mathbf{I} - \mathbf{C}(\mathbf{q})^T[\mathbf{C}(\mathbf{q})\mathbf{C}(\mathbf{q})^T]^{-1}\mathbf{C}(\mathbf{q})$	$\mathbf{I} - \mathbf{q}\mathbf{q}^T/(\mathbf{q}^T\mathbf{q})$

values due to its homogeneous quadratic form, while the Lagrange multipliers are introduced as constant values representing effective reaction forces over the interval. This identifies the discrete equations of motion as

$$\Delta\mathbf{q} \;=\; \frac{\partial H_*}{\partial \mathbf{p}^T} \;=\; h\,\mathbf{G}(\overline{\mathbf{q}})^T\mathbb{J}^{-1}\overline{\mathbf{G}(\mathbf{q})\,\mathbf{p}}\,, \tag{3.13}$$

$$\Delta\mathbf{p} \;=\; -\frac{\partial H_*}{\partial \mathbf{q}^T} \;=\; -\,h\,\mathbf{G}(\overline{\mathbf{p}})^T\mathbb{J}^{-1}\overline{\mathbf{G}(\mathbf{p})\,\mathbf{q}} \;-\; h\left[\frac{\partial V_*}{\partial \mathbf{q}^T} \;+\; \mathbf{C}(\overline{\mathbf{q}})^T\boldsymbol{\lambda}\right]. \tag{3.14}$$

It is seen that these constitute a clear discrete equivalent to the continuous equations (3.10) and (3.11). These discrete equations inherently obey conservation of energy, as these are derived via the condition $\Delta H = 0$, while conservation of momentum is demonstrated in [P3] and [P4], respectively.

As in the continuous case it is convenient to eliminate the explicit dependence on the Lagrange multipliers. This is performed by repeating the steps from the continuous format, via the incremental form of the bi-linear constraint relation (3.7) given by

$$\mathbf{C}(\overline{\mathbf{p}})\,\Delta\mathbf{q} \,+\, \mathbf{C}(\overline{\mathbf{q}})\,\Delta\mathbf{p} \,=\, \mathbf{0}\,. \tag{3.15}$$

When substituting the increments from (3.13) and (3.14) a relation for the discrete Lagrange multipliers is obtained. This can then be used to eliminate the Lagrange multipliers $\boldsymbol{\lambda}$ from the discrete dynamic equation (3.14), which then takes the form

$$\Delta\mathbf{p} \,=\, -h\,\mathbf{G}(\overline{\mathbf{p}})^T\mathbb{J}^{-1}\overline{\mathbf{G}(\mathbf{p})\,\mathbf{q}} - h\left(\mathbf{I} - \mathbf{C}(\overline{\mathbf{q}})^T\left[\mathbf{C}(\overline{\mathbf{q}})\,\mathbf{C}(\overline{\mathbf{q}})^T\right]^{-1}\mathbf{C}(\overline{\mathbf{q}})\right)\frac{\partial V_*}{\partial\mathbf{q}^T}\,. \tag{3.16}$$

This constitutes the discrete equivalent to (3.12). It is important to realize that the particular format, where each factor in the projection operator is represented by its mean value $\mathbf{C}(\bar{\mathbf{q}})$, is a direct consequence of the consistent discretization, and thus it does not introduce any approximations to the conservation properties. The canceling of the homogenous contributions on the other hand may rely on the orthogonality condition (3.7), hence it may be necessary to include an additional term of order h^2 in order to realize exact conservation of discretized equations. This is the case in [P4], while the canceling follow from the very format of the matrix representing the motion gradient $\mathbf{G}$ in [P3].

3.4. Numerical examples

Several examples have been used to demonstrate the accuracy and conservation properties of the presented time integration algorithm for rigid body rotation. In [P3] and [P4] classic examples concerning free rotation of a rigid body and a spinning top in a gravitational field are considered, while the formulation is generalized to a multibody system representing a falling chain in [A5].

Free rigid body rotation

The properties of the homogeneous form of the algorithm, i.e. with $V(\mathbf{q}) = 0$, are considered by application to free rotation of a rigid body. The rigid body is represented as box with parameters given in [59], and the motion is initiated as unstable rotation around its intermediate axis of inertia with a small perturbation. The configurations of the box at specific points in time are illustrated in Fig. 3.2. The associated components of the local angular velocity are shown in Fig. 3.3(a) where the sign change in Ω_3 corresponds to the case where the box is turned upside down. Algorithmic conservation of the mechanical energy and the magnitude of the local angular momentum to well within the iteration tolerance have been demonstrated in [P3] and [A4] for the algorithms based on quaternions and directors, respectively. Furthermore numerical satisfaction of the kinematic constraints (3.2) and the orthogonality relation (3.7) have been verified. Both algorithms exhibit second order

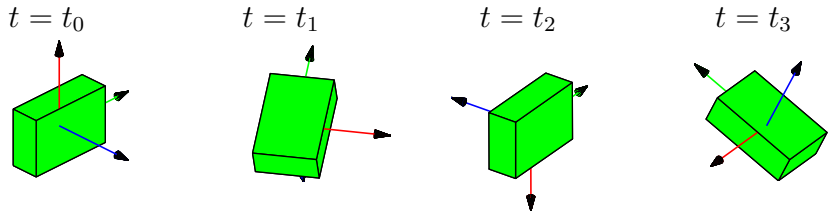

FIGURE 3.2. Motion of box at selected time steps, $h = 0.01$.

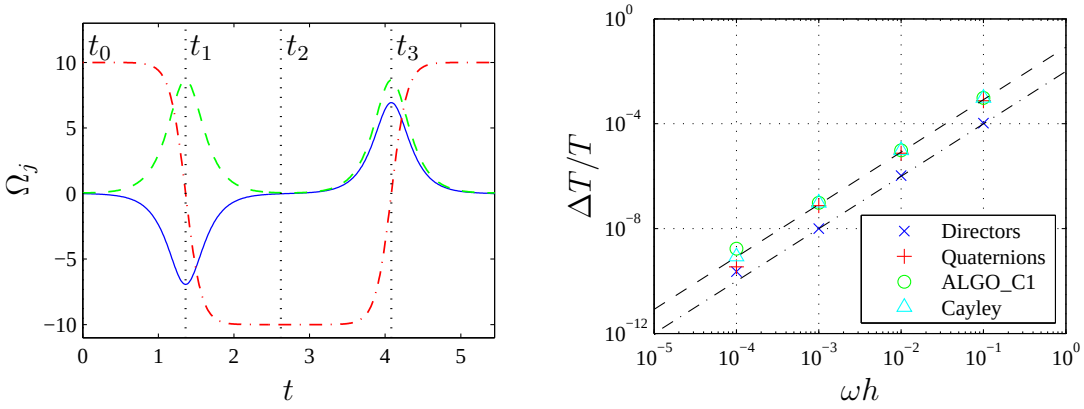

FIGURE 3.3. Free rotation of box: (a) Local angular velocity components. Ω_1 (—), Ω_2 (- -), Ω_3 (- · -). (b) Relative period error. $(\omega h)^2/12$ (- -), $(\omega h)^2/100$ (- · -).

accuracy. This is illustrated in Fig. 3.3(b) in terms of the relative period error $\Delta T/T$ for Ω_3 along with comparable results obtained by the energy-momentum scheme ALGO_C1 presented in Simo and Wong [98] and the algorithm based on the Cayley representation of the rotation tensor from Krenk [59]. It is seen that the algorithm presented in [P4] based on directors performs particularly well, while the accuracy of the others roughly correspond to the well-known asymptotic result for a single linear load component $\Delta T/T = (\omega h)^2/12$, see e.g. Krenk [61].

Constrained rigid body motion

The classic example of a heavy symmetrical top in a gravitational field constitutes a convenient means for illustrating the performance of the presented algorithms for implicitly constrained rigid body rotation including an external potential. The dimensions are equivalent to the ones used in [17, 18] and the special case of steady precession is considered, see e.g. Goldstein [39]. The motion of the top is characterized in terms of the angle of nutation θ, the angle of precession φ and the spin angle ψ as illustrated in Fig. 3.4(a). It has been demonstrated in [P3] and [P4] that the mechanical energy as well as the spatial component l_3 of angular momentum are conserved well within the iteration tolerance when projection operators of the form (3.16) are included in front of the potential gradient. The second order convergence for the period error $\Delta T/T$ is illustrated in Fig. 3.4(b) for the quaternion and the

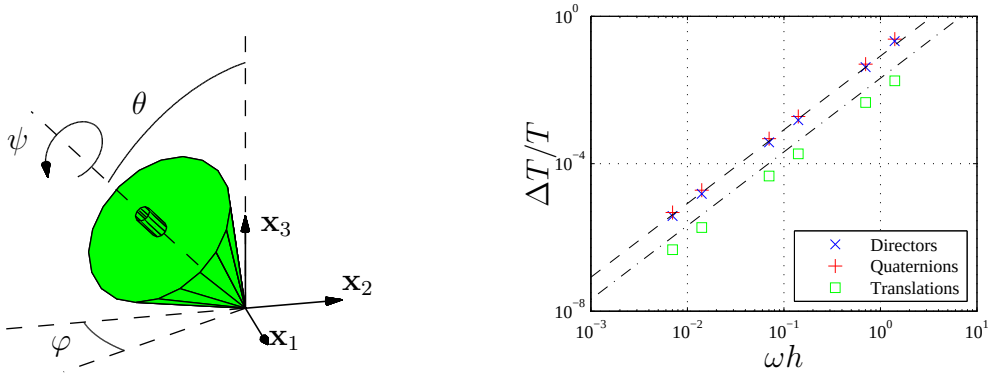

FIGURE 3.4. Spinning top: (a) Initial configuration. (b) Relative period error. $(\omega h)^2/12$ $(--)$, $(\omega h)^2/100$ $(-\cdot-)$.

director formulation for finite rotations, respectively. This has been measured as the relative period error for the periodic x_1-component of the center of mass.

Alternatively, the top motion can be represented by a combination of translations and rotations by introducing a spherical joint at the tip as shown in [P4]. By fixing the local convected coordinate system at the center of mass, the motion is mainly governed by translational components. In that context it should be noted that while the equations associated with rotational motion include a representation of the rotating moment of inertia tensor $\mathbf{J}$ via the $\mathbf{G}$-matrices, the inertia effects associated with translation of the center of mass only contain the mass of the body m as a scalar factor. Therefore a higher accuracy is obtained when translations are included as illustrated in Fig. 3.4(b).

Multibody motion

The final example illustrates the application of the director based formulation from [P4] to a simple multibody system. The details can be found in [A5]. A hanging chain represented by four rigid bodies linked together by spherical joins is considered. Each spherical joint is described via three algebraic constraints of the form

$$\mathbf{\Phi}^{(S)}(\mathbf{q}) \;=\; \mathbf{q}_0^J + x_j^{S,J}\mathbf{q}_j^J \;-\; (\mathbf{q}_0^I + x_j^{S,I}\mathbf{q}_j^I) \;=\; \mathbf{0}\,, \tag{3.17}$$

where $x_j^{S,I}$ and $x_j^{S,J}$ denote the local coordinates of the connection points S in the bodies I and J, respectively. The motion of the chain is initiated by releasing it from the position illustrated in Fig. 3.5(a) where the four bodies form a v-shape in an inclined plane with respect to vertical, thereby introducing out-of-plane motion. It is illustrated in [A5] that the mechanical energy and the vertical component of the spatial angular momentum are conserved quantities - even when multiple bodies are considered. The algorithmic conservation of the internal constraints - i.e. the kinematic constraint (3.2) and the momentum constraints (3.7) - as well as the external constraints associated with the spherical joints (3.17) are illustrated

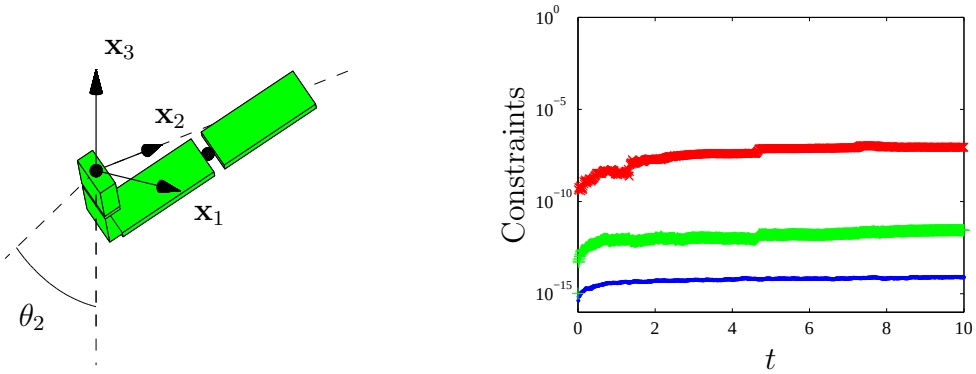

FIGURE 3.5. Multibody system: (a) Initial configuration. (b) Algorithmic conservation of constraints. (•) Kinematic constraints given by (3.7), (×) Dynamic constraints given by (3.7), (+) External constraints given by (3.17).

in Fig. 3.5(b). It is seen that the homogeneous constraints in all three cases are satisfied to within the iteration tolerance of $\varepsilon_r = 10^{-8}$.

4. Explicit elastic three-dimensional beam element

Flexible beams are slender structural members and have found applications in civil engineering, mechanical engineering and aerospace engineering. Beam elements are traditionally developed using a kinematic description of the translations and rotations of each cross-section. While the hypothesis of small to moderate displacements and rotations within a rotating frame of reference may be advantageous for some applications as described in Section 2, such approaches are not very well suited for modeling of highly flexible members. Indeed, a fully non-linear formulation would defy the purpose of introducing a rotating frame in the first place.

Instead, it might be desirable to develop a fully non-linear theory accounting for large displacements and finite rotations with respect to an inertial reference frame. Common approaches for modeling flexible beams in an inertial frame of reference are the so-called 'geometrically exact' beam formulations, which are based on Euler's elastica, and thus in principle are capable of representing arbitrary large deformations and finite rotations. A finite deformation beam theory was presented by Reissner [85, 86] and used as basis for the development of computational procedures for non-linear static and dynamic analysis by Simo and Vu-Quoc [92, 95, 97]. However, while the underlying continuous theoretical basis is well-established, the spatial discretization introduces a number of difficulties, which may be in contradiction to the exact geometric description. In particular, the direct interpolation of kinematic variables requires special measures in order to avoid the various locking phenomena such as shear or membrane locking. Furthermore, an inconsistent representation of the non-commutative rotations may lead to non-objective strain descriptions that lack in frame-invariance and even result in a path-dependent formulation [29]. These numerical issues have introduced a significant increase in complexity, which has led to the development of a wide variety of different formulations, see e.g. [21, 27, 45, 46, 87].

Here a brief description of the beam element developed in [P5] is given. The configuration of the element in a global frame is fully represented in terms of the global components of the position of two end nodes and an associated set of convected base vectors (directors) as described in [P4]. The local constitutive stiffness is derived from the complementary energy of six equilibrium modes, each characterized as a mode of constant internal force [55, 61]. These are closely related to the concept of 'natural modes' described by Argyris [6], yet they are identified from statics alone.

This approach avoids explicit interpolation of kinematic variables, which leads to a locking-free and intrinsic objective and frame-invariant formulation. The present element takes a particularly simple and explicit form that permits easy and direct implementation.

4.1. Element configuration

In the present formulation a beam element in three-dimensional space is uniquely defined by the position and orientation of the cross-sections at its end-points as illustrated in Fig. 4.1. The deformation in the plane of the cross-section is neglected, which implies that the vectors spanning the cross-section planes, here denoted $\mathbf{q}_1$ and $\mathbf{q}_2$, must remain orthonormal. A third unit vector orthogonal to the cross-section plane is then defined by $\mathbf{q}_3 = \mathbf{q}_1 \times \mathbf{q}_2$. The global positions of the beam end-points A and B with respect to the global frame of reference $\{\mathbf{x}_1, \mathbf{x}_2, \mathbf{x}_3\}$ are described by the vectors $\mathbf{q}_0^A$ and $\mathbf{q}_0^B$, respectively, while the orientations of the associated cross-sections are represented via $[\mathbf{q}_1^T, \mathbf{q}_2^T]_A^T$ and $[\mathbf{q}_1^T, \mathbf{q}_2^T]_B^T$.

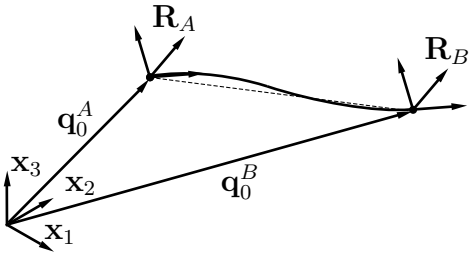

FIGURE 4.1. Configuration of a beam element in the global frame of reference.

In this representation each of the two element nodes are described by nine vector components, and thus three orthonormality constraints for the cross-section vectors $\mathbf{q}_1$ and $\mathbf{q}_2$ are introduced for each node, thereby reducing the number of free components to six. This is in principle equivalent to enforcing vanishing of all in-plane Green strain components, and thus the constraint relation can be expressed in the form,

$$\mathbf{e}(\mathbf{q}) \;=\; \frac{1}{2}\begin{bmatrix} \mathbf{q}_1^T\mathbf{q}_1 - 1 \\ \mathbf{q}_2^T\mathbf{q}_2 - 1 \\ \mathbf{q}_1^T\mathbf{q}_2 + \mathbf{q}_2^T\mathbf{q}_1 \end{bmatrix} \;=\; \mathbf{0}. \tag{4.1}$$

The 2×9 vector components representing the nodal configurations are conveniently collected in a vector $\mathbf{q}$, which then holds the full set of generalized displacements associated with a single element. Similarly the 18 conjugate force components are collected in a vector $\mathbf{g}$. These are identified as the derivative of an elastic energy potential G, as

$$\mathbf{g} \;=\; \frac{\partial G}{\partial \mathbf{q}^T}\,. \tag{4.2}$$

It is noted that the differentiation is performed with respect to the unconstrained components of $\mathbf{q}$, while constraints of the form (4.1) are imposed subsequently as a part of the global system equations.

4.2. Kinematic relations

The internal elastic energy G associated with a single beam element can be solely defined by a set of generalized strain components $\mathbf{v}$, each defining a mode of deformation. Rigid body motion does not contribute to the elastic energy, and thus the number of generalized strains is smaller than the number of generalized displacements. However, the stiffness matrix associated with the full set of generalized displacements can be readily obtained by a transformation between the generalized strains $\mathbf{v}$ and generalized displacements $\mathbf{q}$.

It is convenient to choose the deformation modes such that they each correspond to a set of end loads in equilibrium; i.e. three modes corresponding to constant internal force and three modes corresponding to constant internal moment. The original idea was presented in Krenk [55]. The constant force modes represent constant internal shear forces Q_α and constant normal force N, while the three constant moment modes represent two symmetric bending modes with constant moments M^s_α and a pure torsion mode with torsional moment M. It should be noted that the shear forces are accompanied by a linear anti-symmetric moment variation. The components of the generalized stresses and conjugate strains for the six equilibrium modes are conveniently collected in the vectors

$$\mathbf{t} = [Q_1, Q_2, N, M^s_1, M^s_2, M]^T \quad , \quad \mathbf{v} = [u_1, u_2, u, \varphi^s_1, \varphi^s_2, \varphi]^T . \tag{4.3}$$

A similar approach is used in [61] for co-rotating beam elements. However, a central point of the present formulation is that the deformation modes are expressed in terms of the global components of the generalized displacements $\mathbf{q}$, which circumvents the need for introducing intermediate coordinate systems. This has two main advantages compared to co-rotating formulations: No special features are needed for combining overall rigid body rotations with local rotations of the displacement modes, and a symmetric stiffness matrix is obtained directly due to its reference to global frame.

In the present formulation the generalized displacements $\mathbf{q}$ associated with the element nodes account for arbitrary large displacements and finite rotations in the global frame of reference. While a large displacement analysis in principle is associated with large deformations, the accumulated effect within a single element of a suitable discretized structure is often moderate. Therefore a set of non-linear kinematic relations defining the generalized strains $\mathbf{v}$ in terms of the generalized displacements $\mathbf{q}$ are sought in a homogeneous quadratic form. This is the minimum order of non-linearity that preserves the effect of geometric stiffness, and thus

such formulations are often used for stability analysis [52]. Furthermore the use of linear elastic internal element properties leads to a bi-quadratic internal energy, which particularly facilitates the development of a conservative integration scheme in global form [58].

It is illustrated in [P5] that a quadratic strain definition can be obtained by assuming that the local rotations of the cross-sections at the beam end nodes with respect to the beam reference axis $\Delta\mathbf{q}_0 = \mathbf{q}_0^B - \mathbf{q}_0^A$ are small. This enables the local nodal rotations to be computed by simple projections of the vectors $\mathbf{q}_1$ and $\mathbf{q}_2$ spanning the cross-section plane on the beam axis $\Delta\mathbf{q}$. In the present formulation the projections are performed with respect to initial element length, i.e. without accounting for local geometric changes. This may put certain restrictions on what can be represented by a single element. However, as demonstrated in the examples in [P5], non-linear geometric effects can be accurately captured by slightly increasing the number of elements, whereby the effect is accounted for via the external rotation of the element nodal forces.

The kinematic components u_α and φ_α^s associated with constant shear force Q_α and symmetric bending moments M_α^s are expressed via the difference and the mean of the rotation angles at A and B, the angle of twist φ associated with pure torsion is approximated by in-plane projections of the cross-section vectors, while the Green strain measure is introduced for the axial extension u. It is noted that the quadratic form of the local strain components $\mathbf{v}$ is obtained solely via scalar products of the global components of the generalized displacements $\mathbf{q}$, and thus they are inherently invariant to rigid body motion and satisfy the notion of objectivity described in [29].

4.3. Beam element stiffness

The constitutive stiffness properties representing the elastic deformation of the element are conveniently identified via the complementary energy of the local deformation modes. This provides a simple procedure for obtaining the stiffness matrix for fairly general beam elements [54] and circumvents the locking related phenomena often encountered in low order beam formulations due to inconsistent interpolation of displacements and rotations. For a linear elastic material model, the internal energy is a quadratic function of the generalized strain components $\mathbf{v}$, and can be expressed in the form

$$G(\mathbf{v}) = \tfrac{1}{2}\mathbf{v}^T\mathbf{A}\mathbf{v}\,, \tag{4.4}$$

where $\mathbf{A}$ represents the local stiffness associated with the deformation modes. The particular form of $\mathbf{A}$ can be obtained from complementary energy following the procedure presented in [55]. A detailed derivation is given in [P5], and illustrates a number of advantages: The stiffness matrix is obtained by a minimum set of components; no special measures are needed for including shear deformation; extension to pre-twisted and curved beams is straightforward [53, 54].

The conjugate internal forces $\mathbf{t}$ are defined as the partial derivatives of the internal energy with respect to the internal strains $\mathbf{v}$ from (4.3) as,

$$\mathbf{t} = \frac{\partial G}{\partial \mathbf{v}^T} = \mathbf{A}\mathbf{v}\,. \tag{4.5}$$

The relation between the global generalized forces $\mathbf{g}$ and the local internal stresses $\mathbf{t}$ from (4.3) is obtained by differentiation of the internal energy (4.4), as

$$\mathbf{g} = \left(\frac{\partial \mathbf{v}}{\partial \mathbf{q}}\right)^T \frac{\partial G}{\partial \mathbf{v}^T} = \left(\frac{\partial \mathbf{v}}{\partial \mathbf{q}}\right)^T \mathbf{t} = \mathbf{F}^T\mathbf{t}\,. \tag{4.6}$$

This identifies the transformation matrix as the derivatives of their conjugate kinematic counterparts via the relation,

$$\mathbf{F} = \frac{\partial \mathbf{v}}{\partial \mathbf{q}}\,. \tag{4.7}$$

The role of the transformation matrix is to expand the reduced set of internal stresses to the full number of generalized forces. This is similar to the transformation matrix used in [61] Chapter 5 in relation to a co-rotating formulation.

The tangent stiffness matrix can be derived by considering the incremental form of the generalized internal force relation (4.6). The changes in the internal force vector are related to the changes in the deformation state, and thus it can be represented by a relation of the form,

$$d\mathbf{g} = \mathbf{K}\,d\mathbf{q}\,, \tag{4.8}$$

which serves to identify the tangent stiffness matrix $\mathbf{K}$ associated with the beam element. This can be expressed in the following symmetric form

$$\mathbf{K} = \mathbf{F}^T\mathbf{A}\mathbf{F} + \frac{\partial^2 v_k}{\partial \mathbf{q}^T \partial \mathbf{q}} t_k\,, \tag{4.9}$$

in terms of the equilibrium mode stiffness matrix $\mathbf{A}$, the transformation matrix $\mathbf{F}$ from (4.7) and the second derivatives of the generalized strains v_k. It is noted that the very format is a characteristic of Lagrange type finite element formulations. The first term is the constitutive stiffness associated with changes of the internal stress state, transformed from local to global representation via the matrix $\mathbf{F}$, while the second term is the geometric stiffness $\mathbf{K}^g$ representing the effect of rotating the current internal stresses, see e.g. [61]. Explicit and compact forms for the matrices $\mathbf{A}$, $\mathbf{F}$ and $\mathbf{K}^g$ are given in [P5], which enables a straightforward implementation.

4.4. Numerical examples

The numerical performance of the present explicit beam element is illustrated by a number of representative examples in [P5]. Here, the main results are summarized based on two selected examples. In particular, the capability of representing large overall displacements and finite rotations and the accurate representation of the geometric stiffness effect via external element contributions are considered.

Large deformation of cantilever

The first example is associated with large deformation of the cantilever beam illustrated in Fig. 4.2(a). The example is particularly useful for illustrating the effect of geometric stiffness, and has been considered by a number of authors for verifying various beam formulations, see e.g. [37, 47, 61]. The cantilever is described in terms of its length L and subjected to a transverse force P, specified via the non-dimensional parameter PL^2/EI at its free end. The force is assumed to retain its direction while following the position of the tip. Results for the non-dimensional axial and transverse displacements u_1/L and u_2/L are illustrated in Fig 4.2(b) using 4 and 8 straight beam elements, respectively. Furthermore, an accurate elliptic integral solution based on in-extendable elastica theory given by Mattiasson [73] is shown. The load has been applied in 10 equal load steps using standard Newton-Raphson iterations. With a relative tolerance $\varepsilon_r = 10^{-6}$, the average number of iterations was around 6.2. An excellent agreement has been found between the reference solution and the results obtained by the present formulation, even at the final highly deformed state where the horizontal tip displacement exceeds half the initial length. It is furthermore demonstrated in [P5] that the present formulation exhibits second order convergence.

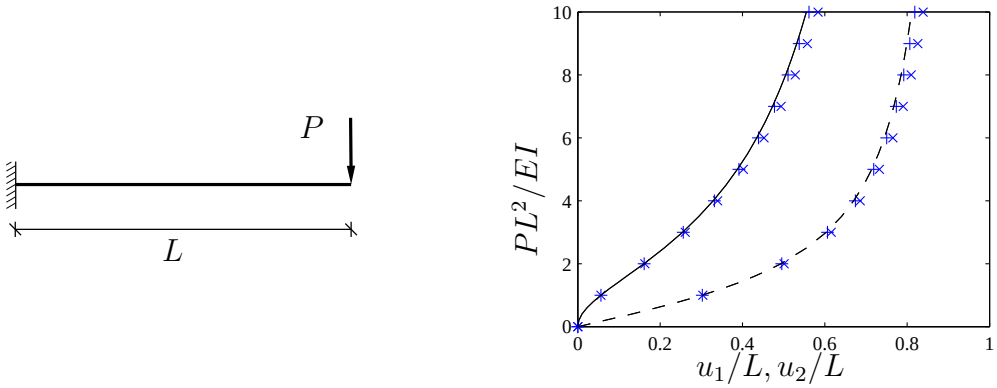

FIGURE 4.2. Cantilever with conservative end force. (×) 4 elements, (+) 8 elements.

Clamped-hinged circular arch

This example considers a non-linear pre- and post-buckling analysis of the clamped-hinged circular arch illustrated in Fig. 4.3(a). The arch has served to illustrate the performance of a number of different beam formulations presented in e.g. Simo and Vu-Qouc [95], Géradin and Cardona [35], Ibrahimbegovic [45] and Gerstmayr and Irschik [37]. Furthermore numerical results for the buckling load have been provided by da Deppo and Schmidt [30] according to in-extendable elastica theory. Parameters similar to [45] have been used. However, the shear and axial stiffness are defined as 10^2EI in order to approximate the in-extendable elastica solution. Results for the normalized horizontal displacements u_1/R and the vertical displacements u_2/R for varying normalized load PR^2/EI are shown in Fig 4.3(b) for discretizations

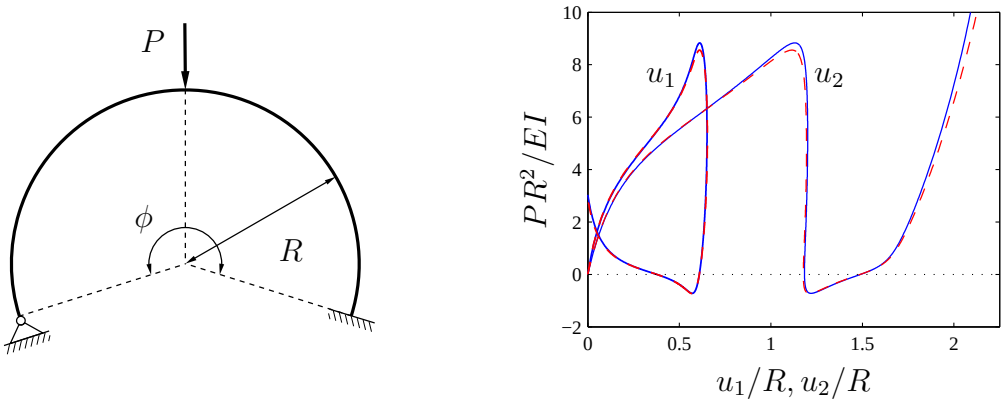

FIGURE 4.3. Buckling of clamped-hinged circular arch. (—) 40 elements, (- - -) 20 elements.

corresponding to 20 and 40 elements, respectively. The results are obtained via the arc-length solver with a hyperplane constraint for mutual control of the current load and displacement increments presented in Krenk [61]. The overall behavior as well as the buckling load predicted by the 40 element discretization agree well with the reference solution in [30] and the numerical results in [95] and [35] where 40 linearly interpolated elements have been used. The results predicted by the 20-element discretization gives a slightly lower buckling load. However, it should be noted that the performance of the present explicit beam formulation is fully competitive with significantly more complex beam formulations from the literature, when the same number of nodes is used.

5. Multi-level analysis of wind turbine blades

A typical application of the procedures presented in the preceding sections is concerned with modeling and design of wind turbine blades. Proper design of wind turbine blades is a multi-disciplinary optimization problem that requires efficient and accurate computational tools. A full design process of a wind turbine involves many different aspects such as aerodynamic performance, weight, manufacturing costs, transportability etc. within the overall aim of minimizing the cost of the produced energy.

The scope of the present section is limited to considering the structural design for a given aerodynamic shape of the airfoil. However, this is still a highly complex task involving multiple disciplines and considerations at several levels of detail. A particular challenge is the need for combining efficient computational models - typically used for analysis of the overall dynamic behavior of the full wind turbine structure subjected to a large number of transient loadings - with the need for capturing local effects such as stress concentrations and local stability behavior. The common approach is to perform the analysis in two stages: First a preliminary design optimization is conducted based on beam-like models associated with representative aerodynamic models and control laws that enables simulation of realistic operating conditions, determination of extreme loads and fatigue analysis. Next a detailed verification of local stress and strain states as well as a local buckling analysis is performed with detailed 3D static FE-models subjected to loading conditions representing the ones from the beam-like models. The process of generating the detailed 3D model as well as the dynamic interaction among the two design levels are typically performed "by hand", which besides being a very time consuming process may lead to sub-optimal design solutions, since there is no consistent way to reflect the results from the detailed analysis into modification of the original design.

For preliminary analysis a 'coarse' beam model is often sufficient as this is capable of providing fast results for primary parameters such as important natural frequencies, maximum deflections, and the overall dynamic behavior for wide range of parameters. At this stage multibody procedures, as described in the preceding sections, have been widely adopted. This may be in terms of geometrically exact beams as in [69] and in the non-linear finite element based multibody code Cp-Lambda (Code for Performance, Loads, Aero-Elasticity by Multi-Body Dynamic Analysis) [10, 26] used here, or with Timoshenko beam elements as in [67]. Modal

representations are also widely used as in the aero-elastic codes FAST [49] and FLEX5 [82]. Due to their relatively low computational cost, beam models are particularly suitable for implementation in integrated design environments for rotor blades. As examples can be mentioned ROTOROPT [2, 33], FOCUS [32] and the design tools used at NREL [48]. Recently a suite of integrated design procedures for multi-disciplinary constrained optimization of wind turbine blades CP-MAX (Code for Performance Maximization) has been developed [24]. The wind turbine is in this context represented by a high-fidelity aero-servo-elastic beam-model that accurately accounts for a wide range of important aspects such as structural and aerodynamic behavior, relevant load cases, synthesis and control laws as well as their interactions. Simulations are performed with the multibody code CP-LAMBDA [26], while the desirable design properties are enforced as constraints within an optimization problem aiming at minimizing the cost; here represented as the total mass of the blade. This provides the framework for performing an efficient preliminary design that accounts for a number design considerations including placement of rotor natural frequencies, structural sizing of the various blade components by constraining maximum tip deflection, fatigue damage and limits on span-wise ply tapering rates.

At the later stages detailed 3D finite element models are required in order to conduct a 'fine'-level verification of the design constraints accounting for the various effects that cannot be represented by the 'coarse'-level beam models. These include identification of possible stress-concentrations, analysis of the local buckling behavior as well as a detailed representation of the complex geometry including rapid span-wise variations, which provides an improved estimate of the blade mass and thereby its dynamic properties.

The generation of a detailed 3D model, execution of relevant analysis and post-processing procedures are associated with a large amount of work, especially when the model is subject to continuous changes during the design process. Several tools have been developed directly for detailed structural analysis of wind turbine blades, see e.g. NUMAD [65] and NSE-BLADE-MESHER [44]. However, these are typically developed in the form of pre- and post-processing tools for commercial FE-solvers with the aim of performing stand-alone analysis of a single blade, and thus they are not integrated in a automatic multi-level design framework that reflects the complex interaction between fine-level modifications and the impact on the full wind turbine model.

5.1. Multi-level design of wind turbine blades

The work presented in [P6] constitutes an extension of the multi-disciplinary design tool CP-MAX [24] and provides facilities for automatic generation and analysis of a detailed 3D FE structural blade model. This enables a detailed 'fine'-level verification of the stress, strain and fatigue constraints. Additionally, by incorporating the effects from the 3D model back into the coarse-level model, the present extension

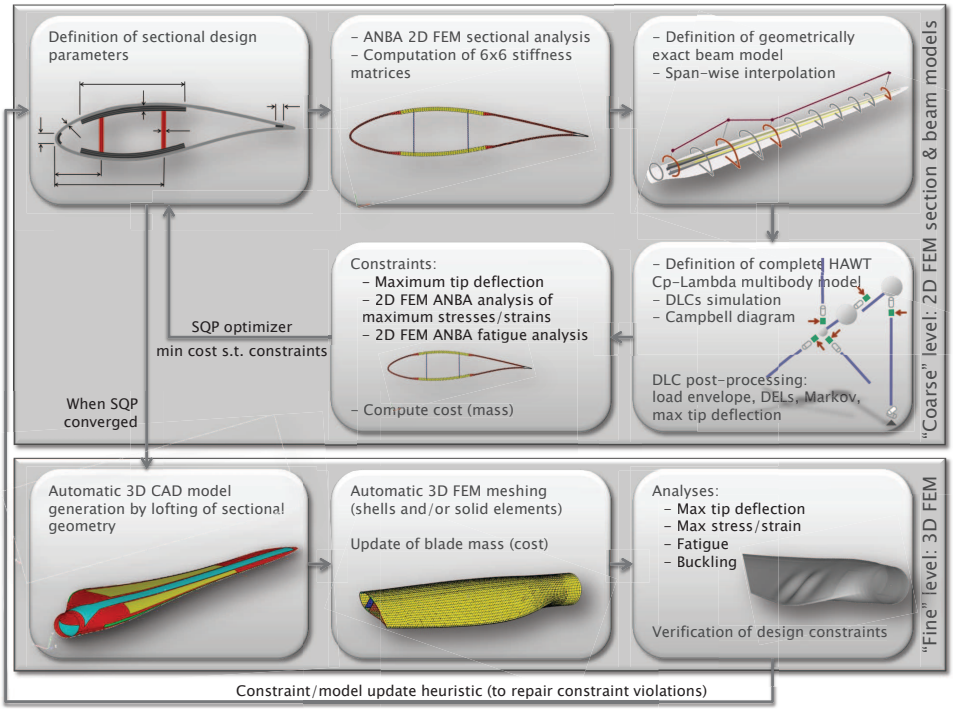

FIGURE 5.1. Multi-level structural blade optimization for given aerodynamic shape

provides the framework for a multi-level optimization procedure for determining cost-minimizing solutions that satisfy the design constraints at the finest level of detail within a reasonable computational cost.

The overall procedure is described in Fig. 5.1. The first step in the present multi-level optimization procedure is to define the initial structural configuration of the blade as well as the associated material properties. The primary design variables, such as the thicknesses of the skin, shear webs and spar caps as well as the area of the leading and trailing edge reinforcements, are then defined at selected sections along the blade span, while intermediate values are interpolated using shape functions.

Based on these and other relevant input parameters a comprehensive aero-servo-elastic model is generated by using the wind turbine simulation code CP-LAMBDA [26]. The model is defined with respect to an inertial frame and constraints associated with linking the various bodies together are enforced using Lagrange multipliers. Each blade is represented by a geometrically exact shear and torsion deformable beam model, [10] accounting for arbitrary large displacements and finite rotations. The associated cross-sectional analysis is performed using the code ANBA (ANisotropic Beam Analysis) [38] based on either 2D finite element meshes or equivalent panels. This includes evaluation of the possibly fully-populated six by six stiffness matrices accounting for all possible structural couplings according to anisotropic beam theory. In addition the code provides the recovery relations for evaluation of the local sectional stresses and strains based on internal stress resultants from the beam model.

The code supports static and transient dynamic analysis as well as computation of frequencies and mode shapes in deformed equilibrium configurations. Transient design load cases (DLC's) are simulated according to relevant design codes [1, 3] using the energy-decaying scheme [11], while automatic procedures handle the post-processing. The latter include computation of the relevant design quantities such as maximum tip deflection, stress and strain states at selected verification points along the blade span via recovery relations provided by the sectional analysis in ANBA, and the level of fatigue-induced damage evaluated at the same verification spots. These quantities are then enforced as inequality constraint conditions for the coarse constrained multi-disciplinary optimization problem which is run until convergence using the sequential quadratic programming (SQP) algorithm. The coarse-level optimization process is not a part of the present thesis, but details can be found in [24].

When a converged solution has been obtained for the coarse-level optimization problem, the corresponding computed blade geometry/airfoil data are used for automatic generation of a detailed 3D CAD model, which precisely accounts for all components of the blade as well as their laminate characteristics. First a chord-wise spline interpolation of the airfoil data points is performed. The data points are obtained from the coarse-level optimization at a number of span-wise cross-sections (typically in the order of one hundred). The extension of the internal blade components is then identified via their projection on the blade surface as illustrated in Fig. 5.2(a). From the chordwise interpolations collocation data points are determined with a sufficiently high sampling resolution to allow for an accurate NURBS-parametrization of the various blade components [84]. The NURBS-representation of the various blade components is shown in Fig. 5.2(b), while a partitioning into simple sub-surfaces as illustrated in 5.2(c) facilitates the subsequent automatic mesh generation. The information associated with the NURBS parameterization is then exported in a data format suitable for digital exchange of information with standard CAD-systems. It should be noted that this approach is fundamentally different from the procedure described in e.g. [8] based on lofting from pre-defined cross-sectional meshes, and enables a precise definition of the internal blade components including span-wise transition zones with rapidly varying thicknesses.

Automatic generation of equivalent loading conditions is performed based on the distribution of internal stresses from the multibody model. In particular, the RBE3-interpolation elements provided by the commercial FE-software NASTRAN [4] are used to distribute the sectional loads to the 3D blade model. This allows for applying the aerodynamic loads acting on the blade surface to the skin nodes only, while inertial forces are applied to all sectional nodes.

Finally the meshing procedure is conducted in a fully automatic way by using the commercial pre-processing software HYPERMESH, as this provides macro-based facilities for mesh generation and subsequent export of the model data in the form of an input file compatible with various commercial FE-solvers.

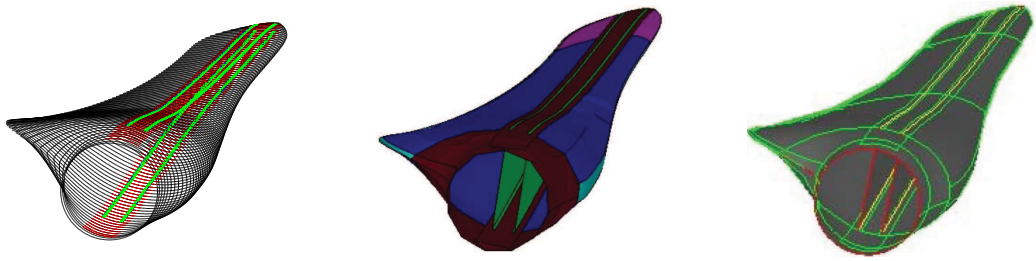

FIGURE 5.2. Selected steps in the generation of the CAD model of a wind turbine blade: (a) Airfoil discretization. (b) NURBS representation. (c) Partitioning in simple sub-surfaces.

The 3D FE-model provides the framework for performing a fine-level analysis of the blade model and subsequent verification of the constraint inequalities associated with admissible stresses, strains, deflections and fatigue damage. In particular, the enhanced geometric description may reveal effects, that are not represented by the quasi 3D beam model, at certain sections such as the beginning and end of the spar caps or at regions with rapidly changing geometry in the span-wise direction. In the cases where analysis conducted for the fine-level model reveal that some design inequalities are not satisfied, a heuristic approach is applied in which the constraints are modified proportionally to their amount of violation. Consider a case where a condition for the maximum stress $\sigma_{\max,2D}$ is satisfied at a given section $\sigma_{\max,2D} < \sigma_{\text{adm}}$ at the end of the ith coarse-level optimization, but violated when the fine-level 3D analysis are performed, i.e. $\sigma_{\max,3D} > \sigma_{\text{adm}}$. Then the admissible stress for the $(i+1)$th iteration is modified as

$$\sigma_{\text{adm}}^{(i+1)} = s_\sigma \, \sigma_{\text{adm}}^{(i)}, \tag{5.1}$$

by means of the tightening parameter $s_\sigma = \sigma_{\max,3D}/\sigma_{\max,2D}$. This leads to a more stringent constraint condition for the next coarse-level iteration, which in an automatic and consistent way accounts for the effects highlighted by the detailed 3D model.

In addition the 3D model can be used for designing the secondary structural parameters such as the thickness of the skin core via a linearized buckling analysis. Despite its secondary role seen from a structural point of view, this in turn affects the non-structural mass of the blade model, and provides an improved estimate for the cost function. This along with the heuristic tightening of constraints described above closes the loop between the fine- and coarse-level analysis in a fully automatic way. The combined multi-level optimization procedure iterating between the two levels is repeated until the design constraints are satisfied at both levels. The procedure has been demonstrated on a 2 MW horizontal wind turbine in [P6], which shows that convergence is accomplished in a few iterations.

6. Conclusions

The main topic of the present thesis is modeling of rotating structures. Both structures consisting of rigid bodies and flexible beams have been considered. A common aim in all theoretical developments in this thesis is the development of energy conserving time integration algorithms - possibly with controlled dissipation, as these provide efficient and unconditionally stable schemes for dynamic analysis of rotating structures. It has been demonstrated in [58] for translation based elements that the use of quadratic kinematics allows the conservative form of the algorithm to be expressed in a particularly attractive format, where the conservation of energy is ensured by a global term expressed via the increment of the geometric stiffness. Thus the scope of the thesis is to extend this property to models where rotations play an important role.

It was first demonstrated in [P1] and [P2] that a particularly simple formulation for motion in a rotating frame of reference is obtained when starting from a hybrid state-space in terms of local displacements and global velocities. In particular, it was shown that use of the same interpolation functions for both state-space variables permits all inertia effects associated with the rotation of the local frame to be represented via external matrix operations on the classic constant mass matrix. Neither centrifugal forces nor angular acceleration appear explicitly in the hybrid state-space format, but are contained implicitly via the use of global velocity. The hybrid state-space lends itself easily for discretization within a conservative integration scheme and enables introduction of algorithmic dissipation on the local motion without affecting the convective motion from rotation of the frame. The formulation has been developed for translation-based elements in [P1] and extended to beam elements with quadratic kinematics accommodating both translations and moderate rotations in [P2].

Irrespective of whether rotational motion is considered in a rotating frame of reference or with respect to an inertial frame the non-commutative properties of finite rotations need to be accounted for. In the papers [P3] and [P4] conservative integration schemes for general rigid body motion are developed based on a four-component quaternion representation or a nine-component convected base vector description of rotations, respectively. Discretized forms of the equations of motion, obeying conservation of energy and momentum, are identified by forming a finite increment of an augmented Hamiltonian that includes the kinematic constraints associated

with the redundant rotation representations. These are introduced in incremental form, while the associated Lagrange multipliers are represented by effective mean values over the interval, thereby providing a clear physical interpretation as effective reaction forces needed for maintaining the constraints. A key feature of both formulations is that the Lagrange multipliers can be replaced by a projection operator applied to the external load potential gradient and the gradients of possible external constraints.

Modeling of flexible structures in an inertial frame is considered in [P5], where a two-node free-floating beam element is presented. It is demonstrated that a homogeneous quadratic form can be achieved by deriving the constitutive stiffness from the complementary energy of a set of equilibrium modes expressed via the global components of the position of the beam nodes and an associated set of convected base vectors [P4]. This approach circumvents interpolation of kinematic variables and leads to an inherently locking-free and frame-independent formulation. The tangent stiffness matrix is derived in explicit form and resembles the format for a co-rotating formulation, but without the need for introducing local element coordinate systems. The quadratic form is obtained by sacrificing the geometric stiffness effects from the local equilibrium modes. However, as demonstrated by a number of static benchmark examples these effects are often sufficiently accounted for by the external rotation of the element nodal forces. If desired, local geometric effects such as shorting due to bending can be included as described in [61], but the present simple homogenous quadratic form provides a promising starting point for extension to dynamics within the global format [58].

In the final part of the thesis covered in [P6], a multi-level optimization method for wind turbine rotor blades that operates at different description levels is presented. It is demonstrated that an effective procedure ensuring satisfaction of relevant design criteria at the finest level of detail follows by coupling a coarse-level analysis of a beam-based multibody model of the full wind turbine with detailed analysis based on a three-dimensional FE-blade model using a simple heuristic approach. All necessary steps are performed in a fully automatic way, and it has been demonstrated on a 2 MW wind turbine that convergence between the two levels are obtained very rapidly. The proposed method provides an automated design tool for streamlining the design process of a complex engineering system such as a wind turbine blade.

6.1. Recommendations for future work

The following recommendations are suggested for directing future research towards extending, improving or applying the current work:

- At the current state the hybrid state-space formulation for dynamics in a rotating frame of reference has only been considered in relation to a single

structure in a local frame with prescribed angular velocity. Therefore, it could be interesting to extend the formulation to account for full multibody systems. In particular the description of connections between different reference frames via the hybrid state-space variables is of interest.

- The implicitly constrained formulations for rigid body dynamics in a global frame are formulated via a set of generalized displacements and conjugate momentum variables. However, when it comes to modeling of flexible structures - in particular within the framework of the finite element method - the use of momentum variables is not well-suited, hence it is of particular interest to recast the present format for finite rigid body motion into the classic state-space form in terms of displacements and velocities.

- The explicit free-floating beam element has only been developed for static analysis. Efficient extension to dynamics along with the development of a conservative time integration scheme may rely on the formulation of a classic state-space format for finite rotations as mentioned above. Furthermore the local beam representation could be enhanced by including pre-curvature [54], warping effects [62] or local geometric stiffness e.g. accounting for shortening due to bending [61].

- The multi-level optimization procedure for wind turbine blades has been developed for structural optimization of a single blade for a given aerodynamic shape. Possible extensions include detailed aerodynamic optimization, optimization of the tower structure and utilization of the anisotropic composite material properties for inducing load mitigating couplings between blade bending and twisting [25].

References

[1] Wind turbines – Part 1: Design requirements, Ed. 3. Technical report, International Standard IEC 61400-1, 2005.

[2] `RotorOpt` perfects rotor design. LM Glasfiber, News Letter, September, 2007.

[3] Guideline for the certification of wind turbines. Technical report, Germanischer Lloyd Industrial Services GmbH, Hamburg, Germany, 2010.

[4] `MD/MSC NASTRAN` 2011: Linear static analysis user's guide. Technical report, MSC Software, 2011.

[5] J. Argyris. An excursion into large rotations. *Computer Methods in Applied Mechanics and Engineering*, **32**:85–155, 1982.

[6] J.H. Argyris, H. Balmer, J.St. Doltsinis, P.C. Dunne, M. Haase, M. Kleiber, G.A. Malejannakis, H.P. Mlejnek, M. Müller, and D.W. Scharpf. Finite element method – the natural approach. *Computer Methods in Applied Mechanics and Engineering*, **17–18**:1–106, 1979.

[7] F. Armero and I. Romero. On the formulation of high-frequency dissipative time-stepping algorithms for nonlinear dynamics. Part II: Second-order methods. *Computer Methods in Applied Mechanics and Engineering*, **190**:6783–6824, 2001.

[8] T. Ashwill. Sweep-Twist adaptive rotor blade: Final project report. Technical Report Sandia Report SAND2009-8037, Sandia National Laboratories, Albuquerque, NM, USA, 2010.

[9] O.A. Bauchau. *Flexible Multibody Dynamics*. Springer, Dordrecht, The Netherlands, 2011.

[10] O.A. Bauchau, C.L. Bottasso, and Y.G. Nikishkov. Modeling rotorcraft dynamics with finite element multibody procedures. *Mathematical and Computer Modelling*, **33**:1113–1137, 2001.

[11] O.A. Bauchau, C.L. Bottasso, and L. Trainelli. Robust integration schemes for flexible multibody systems. *Computer Methods in Applied Mechanics and Engineering*, **192**:395–420, 2003.

[12] O.A. Bauchau, G. Damilano, and N.J. Theron. Numerical integration of non-linear elastic multi-body systems. *International Journal for Numerical Methods in Engineering*, **38**:2727–2751, 1995.

[13] O.A. Bauchau and A. Laulusa. Review of contemporary approaches for constraint enforcement in multibody systems. *Journal of Computational and Nonlinear Dynamics*, **3**:011005.1–8, 2008.

[14] O.A. Bauchau and L. Trainelli. The vectorial parametrization of rotation. *Nonlinear Dynamics*, **32**:71–92, 2003.

[15] J.W. Baumgarte. Stabilization of constraints and integrals of motion in dynamical systems. *Computer Methods in Applied Mechanics and Engineering*, **1**:1–16, 1972.

[16] P. Betsch. The discrete null space method for the energy consistent integration of constrained mechanical systems. Part I: Holonomic constraints. *Computer Methods in Applied Mechanics and Engineering*, **194**:5159–5190, 2005.

[17] P. Betsch and S. Leyendecker. The discrete null space method for the energy consistent integration of constrained mechanical systems. Part II: Multibody dynamics. *International Journal for Numerical Methods in Engineering*, **67**:499–552, 2006.

[18] P. Betsch and R. Siebert. Rigid body dynamics in terms of quaternions: Hamiltonian formulation and conserving numerical integration. *International Journal for Numerical Methods in Engineering*, **79**:444–473, 2009.

[19] P. Betsch and P. Steinmann. Constrained integration of rigid body dynamics. *Computer Methods in Applied Mechanics and Engineering*, **191**:467–488, 2001.

[20] P. Betsch and P. Steinmann. A DAE approach to flexible multibody dynamics. *Multibody System Dynamics*, **8**:365–389, 2002.

[21] P. Betsch and P. Steinmann. Frame-indifferent beam finite elements based upon the geometrically exact beam theory. *International Journal for Numerical Methods in Engineering*, **54**:1775–1788, 2002.

[22] W. Blajer. Index of differential-algebraic equations governing the dynamics of constrained mechanical systems. *Applied Mathematical Modelling*, **16**:70–77, 1992.

[23] W. Blajer. Elimination of constraint violation and accuracy aspects in numerical simulation of multibody systems. *Multibody System Dynamics*, **7**:265–284, 2002.

[24] C.L. Bottasso, F. Campagnolo, and A. Croce. Multi-disciplinary constrained optimization of wind turbines. *Multibody System Dynamics*, **27**:21–53, 2012.

[25] C.L. Bottasso, F. Campagnolo, A. Croce, and C. Tibaldi. Optimization-based study of bend-twist coupled rotor blades for passive and integrated passive/active load alleviation. *Wind Energy*, 2012.

[26] C.L. Bottasso and A. Croce. Cp-Lambda: user's manual. Technical report, Dipartimento di Ingegneria Aerospaziale, Politecnico di Milano, Milano, 2006.

[27] A. Cardona and M. Geradin. A beam finite element nonlinear theory with finite rotations. *International Journal for Numerical Methods in Engineering*, **26**:2403–2438, 1988.

[28] J. Chung and G.M. Hulbert. A time integration algorithm for structural dynamics with improved numerical dissipation: The generalized-alpha method. *Journal of Applied Mechanics*, **60**:371–375, 1993.

[29] M.A. Crisfield and G. Jelenic. Objectivity of strain measures in the geometrically exact three-dimensional beam theory and its finite-element implementation. *Proceedings: Mathematical Physical and Engineering Sciences*, **455**:1125–1147, 1999.

[30] D.A. DaDeppo and R. Schmidt. Instability of clamped-hinged circular aches subjected to a point load. *Journal of Applied Mechanics, Transactions ASME*, **42**:894–896, 1975.

[31] J.D. Downer, K.C. Park, and J.C. Chiou. Dynamics of flexible beams for multibody systems: A computational procedure. *Computer Methods in Applied Mechanics and Engineering*, **96**:373–408, 1992.

[32] N.P. Duineveld. Structure and possibilities of the FOCUS design package. Dutch Wind Workshops, TU Delft, The Netherlands, 2008.

[33] L. Fuglsang. Integrated design of turbine rotors. In *European Wind Energy Conference & Exhibition EWEC 2008*, Brussels, Belgium, March 2008.

[34] J.García de Jalón and E. Bayo. *Kinematic and Dynamic Simulation of Multibody Systems - The Real-Time Challenge*. Springer, New York, USA, 1994.

[35] M. Géradin and A. Cardona. *Flexible Multibody Dynamics: A Finite Element Approach*. Wiley, Chichester, UK, 2001.

[36] M. Géradin and D. Rixen. *Mechanical Vibrations: Theory and Application to Structural Dynamics*. Wiley, Chichester, UK, 2nd edition, 1997.

[37] J. Gerstmayr and H. Irschik. On the correct representation of bending and axial deformation in the absolute nodal coordinate formulation with an elastic line approach. *Journal of Sound and vibration*, **318**:461–487, 2008.

[38] V. Giavotto, M. Borri, P. Mantegazza, G. Ghiringhelli, V. Carmaschi, G.C. Maffioli, and F. Mussi. Anisotropic beam theory and applications. *Computers & Structures*, **16**:403–413, 1983.

[39] H. Goldstein, C. Poole, and J. Safko. *Classical Mechanics*. Addison Wesley, 3rd edition, 2001.

[40] O. Gonzalez. Mechanical systems subject to holonomic constraints: Differential-algebraic formulations and conservative integration. *Physica D*, **132**:165–174, 1999.

[41] O. Gonzalez. Exact energy and momentum conserving algorithms for general models in nonlinear elasticity. *Computer Methods in Applied Mechanics and Engineering*, **190**:1763–1783, 2000.

[42] M.H. Hansen. Aeroelastic stability analysis of wind turbines using an eigenvalue approach. *Wind Energy*, **7**:133–143, 2004.

[43] H.M. Hilber, T.J.R. Hughes, and R.L. Taylor. Improved numerical dissipation for time integration algorithms in structural dynamics. *Earthquake Engineering and Structural Dynamics*, **5**:283–292, 1977.

[44] D.M. Hoyt and D. Graesser. Rapid FEA of wind turbine blades – Summary of NSE composites' structural analysis capabilities for blade NSE–blademesher in-house software. Technical report, NSE Composites, Seattle, WA 98103, 2008.

[45] A. Ibrahimbegovic. On finite element implementation of geometrically nonlinear reissner's beam theory: Three-dimensional curved beam elements. *Computer Methods in Applied Mechanics and Engineering*, **122**:11–26, 1995.

[46] G. Jelenic and M.A. Crisfield. Geometrically exact 3D beam theory: implementation of a strain-invariant finite element for statics and dynamics. *Computer Methods in Applied Mechanics and Engineering*, **171**:141–171, 1999.

[47] J.B. Jonker and J.P. Meijaard. A geometrically non-linear formulation of a three-dimensional beam element for solving large deflection multibody system problems. *International Journal of Non-Linear Mechanics*, **53**:63–74, 2013.

[48] J. Jonkman. NREL structural and aeroelastic codes. Wind Turbine Workshop, Sandia National Laboratories, Albuquerque, NM, USA, 2008.

[49] J.M. Jonkman and M.L. Buhl Jr. FAST user's guide. Technical Report NREL/EL-500-38230, National Renewable Energy Laboratory, Colorado, USA, 2005.

[50] T.R. Kane, R.R. Ryan, and A.K. Banerjee. Dynamics of a cantilever beam attached to a moving base. *Journal of Guidance Control and Dynamics*, **10**:139–151, 1987.

[51] A. Kawamoto, S. Krenk, A. Suzuki, and M. Inagaki. Flexible body dynamics in a local frame with explicitly predicted motion. *International Journal for Numerical Methods in Engineering*, **81**:246–268, 2009.

[52] R. Kouhia. Kinematical relations of spatial framed structures. *Computers & Structures*, **40**:1185–1191, 1991.

[53] S. Krenk. The torsion-extension coupling in pretwisted elastic beams. *International Journal of Solids and Structures*, **19**:67–72, 1983.

[54] S. Krenk. A general format for curved and non-homogeneous beam elements. *Computers & Structures*, **50**:449–454, 1994.

[55] S Krenk. Element stiffness matrix for beams with general cross-section properties. Department of Mechanical Engineering, Technical University of Denmark, 2006.

[56] S. Krenk. Energy conservation in newmark based time integration algorithms. *Computer Methods in Applied Mechanics and Engineering*, **195**:6110–6124, 2006.

[57] S. Krenk. State-space time integration with energy control and fourth-order accuracy for linear dynamic systems. *International Journal for Numerical Methods in Engineering*, **65**:595–619, 2006.

[58] S. Krenk. The role of geometric stiffness in momentum and energy conserving time integration. *International Journal for Numerical Methods in Engineering*, **71**:631–651, 2007.

[59] S. Krenk. A vector format for conservative time integration of rotations. In *Multibody Dynamics 2007, ECCOMAS Thematic Conference* 1–12, Milan, Italy, 2007.

[60] S. Krenk. Extended state-space time integration with high-frequency energy dissipation. *International Journal for Numerical Methods in Engineering*, **73**:1767–1787, 2008.

[61] S. Krenk. *Non-linear Modeling and Analysis of Solids and Structures*. Cambridge University Press, Cambridge, UK, 2009.

[62] S. Krenk and O. Gunneskov. Pretwist and shear flexibility in the vibrations of turbine blades. *Journal of Applied Mechanics*, **52**:409–415, 1985.

[63] S. Krenk, M.N. Svendsen, and J. Høgsberg. Resonant vibration control of three-bladed wind turbine rotors. *AIAA Journal*, **50**:148–161, 2012.

[64] W. Kutta. Beitrag zur naherungsweisen integration von differentialgleichungen. *Zeitschrift für angewandte Mathematik und Physik*, **46**:435–453, 1901.

[65] D.L. Laird. NUMAD user's manual - numerical manufactoring and design tool. Technical report, SAND2001-2375, Wind Energy Technology, Sandia National Laboratories, 2001.

[66] C. Lanczos. *The Variational Principles of Mechanics*. Dover, New York, 4th edition, 1986.

[67] T.J. Larsen and A.M Hansen. How 2 HAWC2: The user's manual. Technical Report Risø-R-1597(ver. 3-1)(EN), Risø National Laboratory, Roskilde, Denmark, 2007.

[68] A. Laulusa and O.A. Bauchau. Review of classical approaches for constraint enforcement in multibody systems. *Journal of Computational and Nonlinear Dynamics*, **3**:011004.1–8, 2008.

[69] D. Lee, D.H. Hodges, and M.J. Patil. Multi-flexible-body dynamic analysis of horizontal axis wind turbines. *Wind Energy*, **5**:281–300, 2002.

[70] E.V. Lens, A. Cardona, and M. Géradin. Energy preserving time integration for constrained multibody systems. *Multibody System Dynamics*, **11**:41–61, 2004.

[71] C.G. Liang. A differentiable null space method for constrained dynamic analysis. *Journal of Mechanisms Transmissions and Automation in Design*, **109**:405–411, 1987.

[72] L.G. Maqueda, O.A. Bauchau, and A.A. Shabana. Effect of the centrifugal forces on the finite element eigenvalue solution of a rotating blade: a comparative study. *Multibody System Dynamics*, **19**:281–302, 2007.

[73] K. Mattiasson. Numerical results from large deflection beam and frame problems analysed by means of elliptic integrals. *International Journal for Numerical Methods in Engineering*, **17**:145–153, 1981.

[74] J. Mayo and J. Dominguez. Geometrically non-linear formulation of flexible multibody systems in terms of beam elements: Geometric stiffness. *Computers & Structures*, **59**:1039–1050, 1996.

[75] J.M. Mayo, D. Garcia-Vallejo, and J. Dominguez. Study of the geometric stiffening effect: Comparison of different formulations. *Multibody System Dynamics*, **11**:321–341, 2004.

[76] J.P. Meijaard. Validation of flexible beam elements in dynamics programs. *Nonlinear Dynamics*, **9**:21–36, 1996.

[77] L. Meirovitch. A new method of solution of the eigenvalue problem for gyroscopic systems. *AIAA Journal*, **12**:1337–1342, 1974.

[78] L. Meirovitch. A new modal method for the response of structures rotating in space. *Acta Astronautica*, **2**:563–576, 1975.

[79] L. Meirovitch. *Computational Methods in Structural Dynamics*. Sijthoff and Noordhoff, New York, 1980.

[80] H.S. Morton Jr. Hamiltonian and Lagrangian formulations of rigid-body rotational dynamics based on the Euler parameters. *Journal of the Astronautical Sciences*, **41**:569–591, 1993.

[81] N.M. Newmark. A method of computation for structural dynamics. *Journal of Engineering Mechanics division (ASCE)*, **85**:67–94, 1959.

[82] S. Øye. Flex4 simulation of wind turbine dynamics. In *28th IEA Meeting of Experts Concerning State of the Art of Aeroelastic Codes for Wind Turbine Calculations*, 1996.

[83] J.G. Papastavridis. Maggi's equations of motion and the determination of constraint reactions. *Journal of Guidance, Control, and Dynamics*, **13**:213–220, 1990.

[84] L.A. Piegl and W. Tiller. *The NURBS Book*. Springer, 2nd edition, 1996.

[85] E. Reissner. On one-dimensional finite-strain beam theory: The plane problem. *Zeitschrift für angewandte Mathematik und Physik*, **23**:795–804, 1972.

[86] E. Reissner. On finite deformations of space-curved beams. *Zeitschrift für angewandte Mathematik und Physik*, **32**:734–744, 1981.

[87] I. Romero and F. Armero. An objective finite element approximation of the kinematics of geometrically exact rods and its use in the formulation of an energy-momentum conserving scheme in dynamics. *International Journal for Numerical Methods in Engineering*, **54**:1683–1716, 2002.

[88] C. Runge. Über die numerische auflösung von differentialgleichungen. *Mathematische Annalen*, **46**:167–178, 1895.

[89] A.A. Shabana. Flexible multibody dynamics: Review of past and recent developments. *Multibody System Dynamics*, **2**:189–222, 1997.

[90] A.A. Shabana. *Dynamics of Multibody Systems*. Cambridge University Press, Cambridge, UK, 2005.

[91] R. Shivarama and E.P. Fahrenthold. Hamilton's equations with Euler parameters for rigid body dynamics modeling. *Journal of Dynamic Systems, Measurement, and Control*, **126**:124–130, 2004.

[92] J.C. Simo. A finite strain beam formulation. The three-dimensional dynamic problem. Part I. *Computer Methods in Applied Mechanics and Engineering*, **49**:55–70, 1985.

[93] J.C. Simo and N. Tarnow. The discrete energy-momentum method. conserving algorithms for nonlinear elastodynamics. *Zeitschrift für angewandte Mathematik und Physik*, **43**:757–792, 1992.

[94] J.C. Simo and L. Vu-Quoc. On the dynamics of flexible beams under large overall motions - The plane case: Part II. *Journal of Applied Mechanics*, **53**:855–863, 1986.

[95] J.C. Simo and L. Vu-Quoc. A three-dimensional finite-strain rod model. Part II: Computational aspects. *Computer Methods in Applied Mechanics and Engineering*, **58**:79–116, 1986.

[96] J.C. Simo and L. Vu-Quoc. The role of non-linear theories in transient dynamic analysis of flexible structures. *Jounal of Sound and Vibration*, **119**:487–508, 1987.

[97] J.C. Simo and L. Vu-Quoc. On the dynamics in space of rods undergoing large motions - a geometrically exact approach. *Computer Methods in Applied Mechanics and Engineering*, **66**:125–161, 1988.

[98] J.C. Simo and K.K. Wong. Unconditionally stable algorithms for rigid body dynamics that exactly preserve energy and momentum. *International Journal for Numerical Methods in Engineering*, **31**:19–52, 1991.

[99] J. Stuelpnagel. On the parametrization of the three-dimensional rotation group. *SIAM Review*, **6**:422–430, 1964.

[100] Z. Terze, D. Lefeber, and O. Muftić. Null space integration method for constrained multibody systems with no constraint violation. *Multibody System Dynamics*, **6**:229–243, 2001.

[101] F.E. Udwadia and R.E. Kalaba. A new perspective on constrained motion. *Proceedings of the Royal Society of London. Series A: Mathematical and Physical Sciences*, **439**:407–410, 1992.

[102] F.E. Udwadia and A.D. Schutte. An alternative derivation of the quaternion equations of motion for Rigid-Body rotational dynamics. *Journal of Applied Mechanics*, **77**:044505:1–4, 2010.

[103] O. Wallrapp and R. Schwertassek. Representation of geometric stiffening in multibody system simulation. *International Journal for Numerical Methods in Engineering*, **32**:1833–1850, 1991.

[104] K. Washizu. *Variational Methods in Elasticity and Plasticity*. Pergamon Press, Oxford, UK, 2 edition, 1974.

[105] W.L. Wood, M. Bossak, and O.C. Zienkiewicz. An alpha modification of newmark's method. *International Journal for Numerical Methods in Engineering*, **15**:1562–1566, 1980.

[106] S. Yoon, R.M. Howe, and D.T. Greenwood. Geometric elimination of constraint violations in numerical simulation of Lagrangian equations. *Journal of Mechanical Design*, **116**:1058–1064, 1994.

P1

Hybrid state-space time integration in a rotating frame of reference

S. Krenk & M.B. Nielsen

International Journal for Numerical Methods in Engineering,
Vol **87**:1301–1324, 2011.

INTERNATIONAL JOURNAL FOR NUMERICAL METHODS IN ENGINEERING
Int. J. Numer. Meth. Engng 2011; **87**:1301–1324
Published online 7 March 2011 in Wiley Online Library (wileyonlinelibrary.com). DOI: 10.1002/nme.3169

Hybrid state-space time integration in a rotating frame of reference

Steen Krenk*, † and Martin B. Nielsen

Department of Mechanical Engineering, Technical University of Denmark, DK-2800 Kgs. Lyngby, Denmark

SUMMARY

A time integration algorithm is developed for the equations of motion of a flexible body in a rotating frame of reference. The equations are formulated in a hybrid state-space, formed by the *local* displacement components and the *global* velocity components. In the spatial discretization the local displacements and the global velocities are represented by the same shape functions. This leads to a simple generalization of the corresponding equations of motion in a stationary frame in which all inertial effects are represented via the classic global mass matrix. The formulation introduces two gyroscopic terms, while the centrifugal forces are represented implicitly via the hybrid state-space format. An angular momentum and energy conserving algorithm is developed, in which the angular velocity of the frame is represented by its mean value. A consistent algorithmic damping scheme is identified by applying the conservative algorithm to a decaying response, which is rendered stationary by an increasing exponential factor that compensates the decay. The algorithmic damping is implemented by introducing forward weighting of the mean values appearing in the algorithm. Numerical examples illustrate the simplicity and accuracy of the algorithm.

Received 18 October 2010; Revised 20 January 2011; Accepted 20 January 2011

KEY WORDS: conservative time integration; dynamics in rotating frame; energy conservation; algorithmic energy dissipation; structural dynamics

1. INTRODUCTION

Conservative time-integration algorithms for the equations of dynamics have received an increasing interest over the last two decades. The basic idea is to develop the algorithm to reproduce the integrated equations of motion in such a way that exact conservation properties are obtained for the invariants of the problem, such as momentum and energy [1]. The discretization of time in the equations leads to lack of ability to resolve phenomena at frequencies exceeding the Nyquist frequency, and the conservative algorithms are, therefore, often extended to include algorithmic dissipation terms, aiming at attenuating the part of the response at the higher frequencies. The basic idea of energy conserving algorithms for kinematically non-linear solids and structures was introduced by Simo *et al.* [2–4]. A central idea is that a representative value over a time increment should integrate to the correct momentum or energy increment over the interval. This can be formalized in the notion of a 'finite time derivative' [5]. In particular, linear elastic models in which the energy is quadratic in the strains, which are quadratic in the displacements, lead to a simple hierarchy of mean values, where the representative internal force can be expressed in explicit form as a standard mean plus a correction in terms of the global geometric stiffness [6]. Conservative

*Correspondence to: Steen Krenk, Department of Mechanical Engineering, Technical University of Denmark, DK-2800 Kgs. Lyngby, Denmark.
†E-mail: sk@mek.dtu.dk

time integration algorithms have also been developed specifically for multi-body dynamics by weighted Galerkin procedures [7], by representative mean values [8], and with augmented variables constrained by Lagrange multipliers [9]. Recently a conservative algorithm has been developed, in which the energy is discretized in step-function format [10]. An important aspect of a time integration algorithm is the possibility of introducing an algorithmic dissipation—primarily of the high-frequency components of the response. It was demonstrated by Armero and Romero [11] that algorithmic damping can be obtained in an otherwise energy conserving algorithm by forward weighting in the mean value representing the internal forces. A simplified global approach was given in [12] and extended to high-frequency form by introducing local auxiliary variables to represent the dissipation terms [13].

The present paper extends the concept of conservative time integration to a rotating frame of reference, commonly used for rotating mechanical parts. The classic approach to dynamics in a rotating frame of reference follows the formulation of Meirovitch [14, 15]. The formulation is based on local displacements and local velocities, and the equations of motion are typically obtained by use of Lagrange's equations. In the context of numerical computations the equations of motion are expressed in state-space format, using the *local* displacements and *local* velocities. The use of local variables does not lead to a direct representation of the momentum equations, and the stiffness matrix is then introduced to obtain an equation system with suitable symmetry properties [16, 17]. In Sections 2 and 3 it is demonstrated that the use of a hybrid state-space, formed by the *local* displacements together with the local components of the *global* velocities, leads to a compact and convenient format that lends itself easily to conservative discretization. A side effect of the hybrid state-space format is that it permits the use of the same spatial shape functions for the local displacements and the global velocities. This has the important consequence that all inertial effects are expressed in terms of the classic mass matrix, and convection effects like the gyroscopic terms are obtained by external operations on the assembled mass matrix. This simplifies the formulation and the computations, and leads to a very close correspondence between the discretized equations and the original differential equations. In the classic formulation in terms of local displacements and velocities the angular velocity appears inside the integrals for the mass matrix, leading to either a need for re-assembly of the rotating mass matrix at each time step, or alternatively a reorganization into several auxiliary matrices [18]. A conservative algorithm for rotating elastic bodies defined in terms of Green strain is derived in Section 4. The context of a rotating frame and the use of hybrid state-space variables leads to a need for reconsidering the concept of algorithmic damping such that it applies to the local motion. This is accomplished in Section 5 by applying the conservative algorithm to a damped response, that is made non-dissipative by applying an increasing exponential factor. The effect of the exponential is then re-interpreted in terms of weighted averages, giving a consistent dissipation as a balanced quadratic form in velocity increments and displacement increments. The algorithm is summarized in Section 6, and numerical examples in Section 7 demonstrate the properties of the algorithm, including a simple interpretation of the algorithmic damping parameter.

2. REPRESENTATION OF MOTION

The solid bodies to be considered here are represented via N nodes $\mathbf{x}_1, \ldots, \mathbf{x}_N$ given in terms of their components $\mathbf{x}_j = [x_1, x_2, x_3]_j^{\mathrm{T}}$ in a *local* frame of reference $\{x_1, x_2, x_3\}$ illustrated in Figure 1. The position of the nodes in the local frame serves to define the elastic energy. The frame of reference $\{x_1, x_2, x_3\}$ rotates about its origin with angular velocity $\boldsymbol{\Omega} = [\Omega_1, \Omega_2, \Omega_3]^{\mathrm{T}}$, illustrated as a rotation about the local x_3-axis in the figure. The kinetic energy of the body is described in terms of the *global* velocities $\mathbf{v}_1, \ldots, \mathbf{v}_N$ of the nodes, expressed in terms of their local components $\mathbf{v}_j = [v_1, v_2, v_3]_j^{\mathrm{T}}$. This section establishes the kinematic relation between the local position $\mathbf{x}_j$ of a node and its absolute velocity $\mathbf{v}_j$, and sets up expressions for the kinetic energy and the elastic potential.

DOI: 10.1002/nme

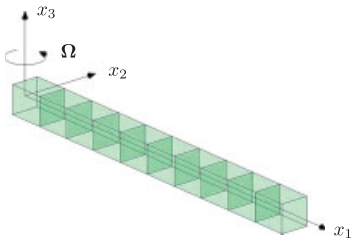

Figure 1. Solid body in frame $\{x_1, x_2, x_3\}$ rotating with angular velocity $\boldsymbol{\Omega}$.

2.1. Kinematics of a point

Let $\underline{\mathbf{x}}_j$ denote the components of the position of node j in a fixed global frame of reference with the same origin as the local rotating frame. The global components are then given in terms of the local components by the relation

$$\underline{\mathbf{x}}_j = \mathbf{R}\mathbf{x}_j, \tag{1}$$

where the matrix $\mathbf{R}$ describes the current rotation of the local frame. The global velocity of the node follows from time differentiation as

$$\underline{\mathbf{v}}_j = \mathbf{R}\dot{\mathbf{x}}_j + \dot{\mathbf{R}}\mathbf{x}_j. \tag{2}$$

As rotation matrices are orthogonal, the local components of the global velocity are obtained by pre-multiplication with $\mathbf{R}^{\mathrm{T}}$,

$$\mathbf{v}_j = \mathbf{R}^{\mathrm{T}}\underline{\mathbf{v}}_j = \dot{\mathbf{x}}_j + \mathbf{R}^{\mathrm{T}}\dot{\mathbf{R}}\mathbf{x}_j. \tag{3}$$

The matrix product in the last term is skew-symmetric and represents a cross product with the angular velocity vector $\boldsymbol{\Omega}$. This skew-symmetric matrix is denoted by

$$\tilde{\boldsymbol{\Omega}} = \boldsymbol{\Omega}\times = \mathbf{R}^{\mathrm{T}}\dot{\mathbf{R}}. \tag{4}$$

This corresponds to arranging the local components of the angular velocity $\boldsymbol{\Omega} = [\Omega_1, \Omega_2, \Omega_3]^{\mathrm{T}}$ in the matrix format

$$\tilde{\boldsymbol{\Omega}} = \boldsymbol{\Omega}\times = \begin{bmatrix} 0 & -\Omega_3 & \Omega_2 \\ \Omega_3 & 0 & -\Omega_1 \\ -\Omega_2 & \Omega_1 & 0 \end{bmatrix}. \tag{5}$$

With this definition of the angular velocity of the local frame the absolute time derivative takes the generic form

$$\mathbf{v}_j = D_t\mathbf{x}_j = (\partial_t + \tilde{\boldsymbol{\Omega}})\mathbf{x}_j, \tag{6}$$

where the convective contribution from the rotation is included in the absolute derivative D_t.

2.2. Consistent interpolation

In the following it is convenient to collect the local position vectors for the N nodes of the model in a system vector of the form

$$\mathbf{x}^{\mathrm{T}} = [\mathbf{x}_1^{\mathrm{T}}, \mathbf{x}_2^{\mathrm{T}}, \ldots, \mathbf{x}_N^{\mathrm{T}}], \tag{7}$$

and similarly for the global system velocity vector

$$\mathbf{v}^{\mathrm{T}} = [\mathbf{v}_1^{\mathrm{T}}, \mathbf{v}_2^{\mathrm{T}}, \ldots, \mathbf{v}_N^{\mathrm{T}}]. \tag{8}$$

DOI: 10.1002/nme

The definition (6) of the global velocity vector is generalized to system form as

$$\mathbf{v} = D_t \mathbf{x} = (\partial_t + \tilde{\mathbf{\Omega}}_D)\mathbf{x} \tag{9}$$

by introducing the angular velocity matrix $\tilde{\mathbf{\Omega}}_D$ of the system in the form

$$\tilde{\mathbf{\Omega}}_D = \begin{bmatrix} \tilde{\mathbf{\Omega}} & \cdots & \mathbf{0} \\ \vdots & \ddots & \vdots \\ \mathbf{0} & \cdots & \tilde{\mathbf{\Omega}} \end{bmatrix}, \tag{10}$$

where the 3×3 angular velocity matrix $\tilde{\mathbf{\Omega}}$ from (5) appears as a block diagonal.

The shape function representation of the motion of an arbitrary point $\boldsymbol{\xi}$ constitutes a crucial step in the formulation of discretized equations of motion in terms of the motion of the nodes. Let $\mathbf{x}_\xi$ denote the position of a generic point with internal coordinates $\boldsymbol{\xi}$. A representation of the position of this point $\mathbf{x}_\xi$ in terms of the position of the nodes $\mathbf{x}$ then takes the form

$$\mathbf{x}_\xi = \mathbf{N}(\boldsymbol{\xi})\mathbf{x}, \tag{11}$$

where $\mathbf{N}(\boldsymbol{\xi})$ is the $3 \times 3N$ shape function matrix. Similarly, $\mathbf{v}_\xi$ denotes the local components of the global velocity. The global velocity may be obtained in two different ways: either by using the same interpolation of the velocity as the one used for the displacements or by applying the absolute time differentiation (6) to the local point $\boldsymbol{\xi}$. The first method corresponds to independent and identical representation of position and velocity in the spirit of Hamiltonian mechanics and is the procedure adopted here. It leads to the velocity representation

$$\mathbf{v}_\xi = \mathbf{N}(\boldsymbol{\xi})\mathbf{v} = \mathbf{N}(\boldsymbol{\xi})(\partial_t + \tilde{\mathbf{\Omega}}_D)\mathbf{x}. \tag{12}$$

In the alternative method, based on direct total time differentiation, the combined time differentiation and convection via the angular velocity would appear to the left of the shape function matrix.

In the case of isotropic interpolation—i.e. equal shape functions for all components associated with a node—the shape function matrix has the form

$$\mathbf{N}(\boldsymbol{\xi}) = [N_1(\boldsymbol{\xi})\mathbf{I}, \ldots, N_N(\boldsymbol{\xi})\mathbf{I}], \tag{13}$$

where the same scalar shape function $N_j(\boldsymbol{\xi})$ applies to all three components associated with node j. In this particular case

$$(\partial_t + \tilde{\mathbf{\Omega}}_D)\mathbf{N}(\boldsymbol{\xi})\mathbf{x} = \mathbf{N}(\boldsymbol{\xi})(\partial_t + \tilde{\mathbf{\Omega}}_D)\mathbf{x}, \tag{14}$$

and the direct time integration method reproduces the equal interpolation representation. This equivalence for isoparametric elements was used in [19]. However, for non-isotropic interpolation or models including rotation degrees of freedom there will in general be a difference between the resulting equations of motion, and the direct differentiation approach will lead to additional mass matrices [18]. As demonstrated in the following the simplicity of the resulting equations of motion relies on identical spatial interpolation of local position and global velocity.

3. EQUATIONS OF MOTION IN HYBRID STATE-SPACE FORMAT

It is most convenient to obtain the equations of motion from Lagrange's equations in terms of the kinetic and potential energies. This section defines the kinetic and elastic energies in terms of global velocity $\mathbf{v}$ and local displacement $\mathbf{u}$, respectively. The equations of motion are then derived and set up in a hybrid state-space format, and the energy balance equation corresponding to this format is identified.

DOI: 10.1002/nme

3.1. Kinetic energy and elastic properties

The kinetic energy with respect to the global motion follows from integrating the local kinetic energy in terms of the global velocities (12) over the mass of the body. The result is in the classic mass matrix form

$$T = \tfrac{1}{2}\mathbf{v}^{\mathrm{T}}\mathbf{M}\mathbf{v}, \tag{15}$$

where the mass matrix $\mathbf{M}$ is constant, because the description refers to initial local geometry.

The elastic energy $G(\mathbf{u})$ is expressed in terms of the displacement $\mathbf{u}$ relative to the initial position $\mathbf{x}_0$. This corresponds to the current position of the nodes in the form

$$\mathbf{x} = \mathbf{x}_0 + \mathbf{u}. \tag{16}$$

The material is assumed to be elastic, and the corresponding energy is defined in terms of the Green strain, defined via the deformation gradient $\mathbf{F} = \partial\mathbf{x}/\partial\mathbf{x}_0$ as

$$\mathbf{E} = \tfrac{1}{2}(\mathbf{F}^{\mathrm{T}}\mathbf{F} - \mathbf{I}). \tag{17}$$

This leads to the elastic energy $G(\mathbf{u})$ of the body,

$$G(\mathbf{u}) = \int_{V_0} \varphi(\mathbf{E})\,\mathrm{d}V_0. \tag{18}$$

The generalized internal forces $\mathbf{g}(\mathbf{u})$ are defined by the displacement gradient of the elastic energy

$$\mathbf{g}(\mathbf{u}) = \frac{\mathrm{d}G(\mathbf{u})}{\mathrm{d}\mathbf{u}^{\mathrm{T}}} = \int_{V_0} \left(\frac{\partial \mathbf{E}^{\mathrm{T}}}{\partial \mathbf{u}}\right) \frac{\partial \varphi}{\partial \mathbf{E}^{\mathrm{T}}}\,\mathrm{d}V_0 = \int_{V_0} (\partial\mathbf{E}/\partial\mathbf{u})^{\mathrm{T}}\mathbf{S}\,\mathrm{d}V_0, \tag{19}$$

where the chain rule has been used to differentiate via the strain $\mathbf{E}$. The last factor $\mathbf{S} = \partial\varphi/\partial\mathbf{E}^{\mathrm{T}}$ is the Piola–Kirchhoff stresses of the second kind, conjugate to the Green strains.

In the following the work of the internal forces through a displacement $\mathrm{d}\mathbf{u}$ from the current state will be needed. According to (19) this work is

$$\mathrm{d}\mathbf{u}^{\mathrm{T}}\mathbf{g}(\mathbf{u}) = \mathrm{d}G(\mathbf{u}) = \int_{V_0} \mathrm{d}\mathbf{E}^{\mathrm{T}}\mathbf{S}\,\mathrm{d}V_0. \tag{20}$$

If the displacement $\mathbf{u}$ represents a rigid body motion the strain increment vanishes, $\mathrm{d}\mathbf{E} = \mathbf{0}$, and the work of the internal forces will be zero.

The increments of the internal force vector are defined in terms of the tangent stiffness matrix, defined via further differentiation as

$$\mathbf{K}(\mathbf{u}) = \frac{\partial \mathbf{g}(\mathbf{u})}{\partial \mathbf{u}} = \frac{\partial^2 G(\mathbf{u})}{\partial \mathbf{u}^{\mathrm{T}}\partial \mathbf{u}}. \tag{21}$$

The differentiation of $\mathbf{g}(\mathbf{u})$ consists in differentiating each of the two factors in the integrand. This gives the tangent stiffness as the sum of the geometric stiffness $\mathbf{K}^g$ and the constitutive stiffness $\mathbf{K}^c$. The specific form is

$$\mathbf{K} = \mathbf{K}^g + \mathbf{K}^c = \int_{V_0} \frac{\partial^2 \mathbf{E}^{\mathrm{T}}}{\partial \mathbf{u}^{\mathrm{T}}\partial \mathbf{u}}\mathbf{S}\,\mathrm{d}V_0 + \int_{V_0} \frac{\partial \mathbf{E}^{\mathrm{T}}}{\partial \mathbf{u}^{\mathrm{T}}}\frac{\partial \mathbf{S}}{\partial \mathbf{u}}\,\mathrm{d}V_0. \tag{22}$$

In the integrands the internal product is on $\mathbf{E}^{\mathrm{T}}\mathbf{S}$, while the components are defined via the components in the displacement vector $\mathbf{u}$. It is notable that the geometric stiffness is expressed as the product of the current stress $\mathbf{S}$ and a factor, which due to the double differentiation does not depend on the current displacement vector. This property is very convenient, when evaluating the algorithmic stiffness for finite displacement increments.

DOI: 10.1002/nme

3.2. Lagrange's equations

Lagrange's equation constitutes a convenient means for setting up the equations of motion from the derivatives of the kinetic energy T and the elastic energy G. It is expressed in terms of the variable $\mathbf{u}$ and its time derivative $\dot{\mathbf{u}}$ in the form [17]

$$\frac{\mathrm{d}}{\mathrm{d}t}\left(\frac{\partial T}{\partial \dot{\mathbf{u}}^{\mathrm{T}}}\right)-\frac{\partial T}{\partial \mathbf{u}^{\mathrm{T}}}+\frac{\partial G}{\partial \mathbf{u}^{\mathrm{T}}}=\mathbf{f}, \tag{23}$$

where $\mathbf{f}$ is the external force that is conjugate to the displacements $\mathbf{u}$. The kinetic energy T was given as a quadratic form in the global velocity $\mathbf{v}$ in (15). When using the expression (9) for the global velocity the two derivatives of the kinetic energy are found to be

$$\frac{\partial T}{\partial \dot{\mathbf{u}}^{\mathrm{T}}}=\mathbf{M}\mathbf{v} \tag{24}$$

and

$$\frac{\partial T}{\partial \mathbf{u}^{\mathrm{T}}}=\tilde{\boldsymbol{\Omega}}^{\mathrm{T}}\mathbf{M}\mathbf{v}. \tag{25}$$

The first of these relations defines the momentum

$$\mathbf{p}=\frac{\partial T}{\partial \dot{\mathbf{u}}^{\mathrm{T}}}=\mathbf{M}\mathbf{v}=\mathbf{M}D_t\mathbf{x}, \tag{26}$$

while the combination of the derivatives in Lagrange's equation (23) gives

$$\frac{\mathrm{d}}{\mathrm{d}t}\left(\frac{\partial T}{\partial \dot{\mathbf{u}}^{\mathrm{T}}}\right)-\frac{\partial T}{\partial \mathbf{u}^{\mathrm{T}}}=D_t\mathbf{p}. \tag{27}$$

It is observed that the effect of the rotation of the frame of reference is accounted for by replacing the partial time derivative ∂_t with the convected time derivative $D_t=(\partial_t+\tilde{\boldsymbol{\Omega}}_D)$. The internal forces have already been identified as the partial derivative of the elastic energy $G(\mathbf{u})$, and the equations of motion can then be written as

$$D_t(\mathbf{M}D_t\mathbf{x})+\mathbf{g}(\mathbf{u})=\mathbf{f}. \tag{28}$$

This second-order differential equation in time would be the typical starting point for a collocation-type algorithm like Newmark, Generalized alpha, or similar. These algorithms are based on asymptotic arguments in which the time increment is assumed 'small' relative to relevant vibration periods. These algorithms typically do not lead to exact conservation equations for momentum and energy due to the asymptotic nature of the approximations introduced in their derivation. In contrast, conservative time integration methods are typically based on an integrated form of two first-order state-space differential equations: the first defining the momentum in terms of the displacement variables and the second expressing the equation of motion in terms of the momentum variable. In the present case it is convenient to consider this issue in a hybrid state-space formed by the local displacement $\mathbf{u}$ and the global velocity $\mathbf{v}$.

3.3. Angular momentum

The local components of the global linear momentum $\mathbf{p}$ are arranged in a vector containing the contributions $\mathbf{p}_j$ from the individual nodes, $\mathbf{p}^{\mathrm{T}}=[\mathbf{p}_1^{\mathrm{T}},\ldots,\mathbf{p}_N^{\mathrm{T}}]$. Each of these vectors $\mathbf{p}_j$ contribute to the angular momentum $\mathbf{L}$ of the body by their moment about the origin of the frame of reference,

$$\mathbf{L}=\sum_j \mathbf{x}_j\times\mathbf{p}_j=\sum_j \tilde{\mathbf{x}}_j\mathbf{p}_j, \tag{29}$$

where the summation is over all nodes. The equation of motion (28) is now expressed in terms of the momentum vector and written in blocks corresponding to each node,

$$D_t\mathbf{p}_j+\mathbf{g}_j(\mathbf{u})=\mathbf{f}_j,\quad j=1,\ldots,N. \tag{30}$$

DOI: 10.1002/nme

This equation is multiplied by a virtual rigid body rotation represented in terms of the infinitesimal rotation vector $\boldsymbol{\alpha}$ as

$$\delta\mathbf{x}_j = \tilde{\boldsymbol{\alpha}}\mathbf{x}_j = -\tilde{\mathbf{x}}_j\boldsymbol{\alpha}, \quad j = 1, \ldots, N. \tag{31}$$

Forming the total virtual work of the equations of motion (30) through the virtual displacement field (31) gives

$$\boldsymbol{\alpha}^{\mathrm{T}} \left\{ \sum_j \tilde{\mathbf{x}}_j (D_t \mathbf{p}_j) - \sum_j \tilde{\mathbf{x}}_j \mathbf{f}_j \right\} = 0. \tag{32}$$

In this equation the internal forces $\mathbf{g}_j(\mathbf{u})$ do not contribute, because the virtual displacement field represents a rigid body motion. It can be demonstrated by using the properties of the mass matrix, that the first factor $\tilde{\mathbf{x}}_j$ of the first term can be put inside the differential operator, and thus the virtual work equation (32) corresponds to the following differential equation for the angular momentum vector $\mathbf{L}$:

$$D_t \mathbf{L} = D_t \left(\sum_j \mathbf{L}_j \right) = D_t \left(\sum_j \tilde{\mathbf{x}}_j \mathbf{p}_j \right) = \sum_j \tilde{\mathbf{x}}_j \mathbf{f}_j. \tag{33}$$

This is the well-known differential equation for the angular momentum of a body, here expressed in a local rotating frame of reference represented via the total time differentiation operator D_t. It is important to note that in order for the contribution from the internal forces to vanish all nodes representing the body must be included. Thus, the force vectors $\mathbf{f}$ also include contributions from reaction forces at supports.

3.4. Hybrid state-space equations

The equations of motion in a rotating frame can be formulated in a direct state-space format as first-order differential equations in terms of $\mathbf{u}$ and $\dot{\mathbf{u}}$ following directly from Lagrange's equations, see [15–17] for application to small vibrations of rotating structures. However, in order to obtain the symmetric/skew-symmetric structure of the equations, the kinematic equation in that case must be expressed as a stiffness relation, and angular acceleration of the rotating frame will break the symmetry properties. Thus, the hybrid state-space format using the local displacement vector $\mathbf{u}$ together with the local components of the global velocity $\mathbf{v}$ appears to be of a more general nature.

In the hybrid state-space format the kinematic relation (9) is expressed in terms of $\mathbf{u}$ and $\mathbf{v}$ by introduction of the initial position vector $\mathbf{x}_0$ from (16):

$$\mathbf{v} = (\partial_t + \tilde{\boldsymbol{\Omega}}_D)\mathbf{u} + \tilde{\boldsymbol{\Omega}}_D \mathbf{x}_0. \tag{34}$$

The dynamic equation then follows from (27) in the form:

$$(\partial_t + \tilde{\boldsymbol{\Omega}}_D)\mathbf{M}\mathbf{v} + \mathbf{g}(\mathbf{u}) = \mathbf{f}. \tag{35}$$

In the present formulation the mass matrix is assumed to be independent of time as demonstrated for iso-parametric elements, and the two equations of motion (34) and (35) can then be written in the convenient state-space format

$$\begin{bmatrix} \mathbf{0} & \mathbf{M} \\ -\mathbf{M} & \mathbf{0} \end{bmatrix} \begin{bmatrix} \dot{\mathbf{u}} \\ \dot{\mathbf{v}} \end{bmatrix} + \begin{bmatrix} \mathbf{g}(\mathbf{u}) + \tilde{\boldsymbol{\Omega}}_D \mathbf{M}\mathbf{v} \\ \mathbf{M}\tilde{\boldsymbol{\Omega}}_D^{\mathrm{T}}\mathbf{u} + \mathbf{M}\mathbf{v} \end{bmatrix} = \begin{bmatrix} \mathbf{f} \\ -\mathbf{M}\tilde{\boldsymbol{\Omega}}_D^{\mathrm{T}}\mathbf{x}_0 \end{bmatrix}. \tag{36}$$

This state-space format is of hybrid form in the sense that $\mathbf{u}$ is the local displacement in the rotating frame, whereas $\mathbf{v}$ is the global velocity in a fixed frame of reference. In this format the first block matrix is skew-symmetric, whereas the gyroscopic terms in the second block matrix are symmetric. The internal elastic force $\mathbf{g}(\mathbf{u})$ is in the form of a derivative of the elastic potential, and thus the corresponding differential form is also symmetric. It is observed that in this hybrid

DOI: 10.1002/nme

format the inertial terms arising from the rotation are represented solely via the matrix $\tilde{\boldsymbol{\Omega}}_D\mathbf{M}$ and its transpose, and thus neither the angular acceleration of the rotating frame nor the square of the angular frequency, associated with the centrifugal force, appears explicitly.

In the limit of vanishing angular velocity the state-space format typically used in a stationary frame of reference is recovered, however with the sign of the second equation changed to provide a symmetric set of equations [6, 17]. The change of sign is a trade-off, as symmetry is obtained by sacrificing the positive-definite form of the second matrix in the classic state-space format.

The energy balance equation takes a particularly simple form when expressed in terms of the hybrid state-space variables. The hybrid energy balance equation is obtained by pre-multiplication of the equation of motion (35) by the local components of the absolute velocity $\mathbf{v}^{\mathrm{T}}$, whereby

$$\mathbf{v}^{\mathrm{T}}\mathbf{M}\dot{\mathbf{v}}+(\dot{\mathbf{u}}+\tilde{\boldsymbol{\Omega}}_D\mathbf{x})^{\mathrm{T}}\mathbf{g}(\mathbf{u})+\mathbf{v}^{\mathrm{T}}\tilde{\boldsymbol{\Omega}}_D\mathbf{M}\mathbf{v}=\mathbf{v}^{\mathrm{T}}\mathbf{f}. \tag{37}$$

The first two terms in this equation are the time derivative of the mechanical energy. The factor $\tilde{\boldsymbol{\Omega}}_D\mathbf{x}$ multiplying the internal force $\mathbf{g}(\mathbf{u})$ constitutes an infinitesimal rigid body rotation, and thus the work of the internal forces through this displacement vanishes as explained in connection with the angular momentum equation (19). For isoparametric models the mass matrix consists of 3×3 blocks in the form $\mathbf{M}_{ij}=m_{ij}\mathbf{I}$, where m_{ij} is the mass coefficient and $\mathbf{I}$ is the unit matrix. When the mass matrix is in this format $\tilde{\boldsymbol{\Omega}}_D\mathbf{M}$ is formed by replacing $\mathbf{I}$ by the skew-symmetric matrix $\tilde{\boldsymbol{\Omega}}$, and thus the last term in (37) vanishes. The result is the intuitively obvious hybrid energy balance equation

$$\frac{\mathrm{d}}{\mathrm{d}t}\left\{\frac{1}{2}\mathbf{v}^{\mathrm{T}}\mathbf{M}\mathbf{v}+G(\mathbf{u})\right\}=\mathbf{v}^{\mathrm{T}}\mathbf{f}, \tag{38}$$

where the rate of change of the sum of absolute kinetic energy and locally defined internal energy is equal to the rate of work of the external forces through the global velocity. Note, that in this format centrifugal and gyroscopic effects do not appear explicitly, but only indirectly via the relation (34) between the local displacement $\mathbf{u}$ and the global velocity $\mathbf{v}$.

4. CONSERVATIVE TIME INTEGRATION

The first step in the development of the discrete conservative formulation consists in integration of the hybrid state-space equations of motion (36) over the time interval $h=t_{n+1}-t_n$, whereby

$$\begin{bmatrix}\mathbf{0} & \mathbf{M}\\ -\mathbf{M} & \mathbf{0}\end{bmatrix}\begin{bmatrix}\Delta\mathbf{u}\\ \Delta\mathbf{v}\end{bmatrix}+\int_h\begin{bmatrix}\mathbf{g}(\mathbf{u})+\tilde{\boldsymbol{\Omega}}_D\mathbf{M}\mathbf{v}\\ \mathbf{M}\tilde{\boldsymbol{\Omega}}_D^{\mathrm{T}}\mathbf{x}+\mathbf{M}\mathbf{v}\end{bmatrix}\mathrm{d}t=\int_h\begin{bmatrix}\mathbf{f}\\ \mathbf{0}\end{bmatrix}\mathrm{d}t, \tag{39}$$

where the initial position $\mathbf{x}_0$ has been absorbed into the current position $\mathbf{x}$ to facilitate the following manipulations. In order to develop the algorithm in energy conserving form an asterisk will initially be used to denote the equivalent mean value representing the integral. With this notation the equations are

$$\begin{bmatrix}\mathbf{0} & \mathbf{M}\\ -\mathbf{M} & \mathbf{0}\end{bmatrix}\begin{bmatrix}\Delta\mathbf{u}\\ \Delta\mathbf{v}\end{bmatrix}+h\begin{bmatrix}\mathbf{g}(\mathbf{u})_*+(\tilde{\boldsymbol{\Omega}}_D\mathbf{M}\mathbf{v})_*\\ (\mathbf{M}\tilde{\boldsymbol{\Omega}}_D^{\mathrm{T}}\mathbf{x})_*+(\mathbf{M}\mathbf{v})_*\end{bmatrix}=\begin{bmatrix}h\mathbf{f}_*\\ \mathbf{0}\end{bmatrix}. \tag{40}$$

The equivalent values defined by the asterisk symbol are now determined such that the discrete algorithm satisfies an energy balance equation corresponding to (38) and an angular momentum balance equation constituting a discrete equivalent of (33).

4.1. Incremental equations of motion with energy balance

A discrete energy balance hybrid format can be obtained from the discrete equations of motion (40). The procedure follows that leading to (38), and the individual steps identify the mean values

DOI: 10.1002/nme

denoted by asterisks in (40). First the dynamic equation (40a) is pre-multiplied by the mean velocity $\bar{\mathbf{v}}^{\mathrm{T}}$, whereby

$$\bar{\mathbf{v}}^{\mathrm{T}}\mathbf{M}\Delta\mathbf{v}+h\bar{\mathbf{v}}^{\mathrm{T}}\mathbf{g}(\mathbf{u})_*+h\bar{\mathbf{v}}^{\mathrm{T}}(\tilde{\boldsymbol{\Omega}}_D\mathbf{M}\mathbf{v})_*=h\bar{\mathbf{v}}^{\mathrm{T}}\mathbf{f}_*. \tag{41}$$

In the continuous formulation the last term on the left side vanishes. This property is obtained in the discrete formulation by representing the product $(\tilde{\boldsymbol{\Omega}}_D\mathbf{M}\mathbf{v})_*$ by the midpoint rule. A similar representation is made for the other gyroscopic term, and thus

$$(\tilde{\boldsymbol{\Omega}}_D\mathbf{M}\mathbf{v})_*=\bar{\tilde{\boldsymbol{\Omega}}}_D\mathbf{M}\bar{\mathbf{v}},\quad (\mathbf{M}\tilde{\boldsymbol{\Omega}}_D^{\mathrm{T}}\mathbf{x})_*=\mathbf{M}\bar{\tilde{\boldsymbol{\Omega}}}_D^{\mathrm{T}}\bar{\mathbf{x}}. \tag{42}$$

With the mid-point representation (42b) and the direct mean value representation

$$(\mathbf{M}\mathbf{v})_*=\mathbf{M}\bar{\mathbf{v}}, \tag{43}$$

the kinematic equation (40b) takes the simple form

$$h\bar{\mathbf{v}}=\Delta\mathbf{u}+h\bar{\tilde{\boldsymbol{\Omega}}}_D\bar{\mathbf{x}}. \tag{44}$$

This expression is now substituted into the second term of (41) to get

$$\Delta\mathbf{v}^{\mathrm{T}}\mathbf{M}\bar{\mathbf{v}}+\Delta\mathbf{u}^{\mathrm{T}}\mathbf{g}(\mathbf{u})_*+h(\bar{\tilde{\boldsymbol{\Omega}}}_D\bar{\mathbf{x}})^{\mathrm{T}}\mathbf{g}(\mathbf{u})_*=h\bar{\mathbf{v}}^{\mathrm{T}}\mathbf{f}_*. \tag{45}$$

The first term represents the increment of the absolute kinetic energy, given by

$$\Delta\mathbf{v}^{\mathrm{T}}\mathbf{M}\bar{\mathbf{v}}=\left[\tfrac{1}{2}\mathbf{v}^{\mathrm{T}}\mathbf{M}\mathbf{v}\right]_n^{n+1}. \tag{46}$$

The second term is the increment of the elastic energy, and thus $\mathbf{g}(\mathbf{u})_*$ is defined by the relation

$$\Delta\mathbf{u}^{\mathrm{T}}\mathbf{g}(\mathbf{u})_*=[G(\mathbf{u})]_n^{n+1}. \tag{47}$$

This is the definition of the so-called finite derivative [5]. In this case the last term on the left side in (45) represents the work of the internal forces through an infinitesimal rigid body rotation from the mid-point state $\bar{\mathbf{x}}$, and therefore vanishes. Thus, the discrete hybrid energy equation takes the form

$$\left[\tfrac{1}{2}\mathbf{v}^{\mathrm{T}}\mathbf{M}\mathbf{v}+G(\mathbf{u})\right]_n^{n+1}=h\bar{\mathbf{v}}^{\mathrm{T}}\mathbf{f}_*. \tag{48}$$

This is the discrete equivalent of the hybrid energy balance equation (38).

The derivation of the energy balance equation has identified that the gyroscopic terms must be evaluated by the mid-point rule, and that the internal force is represented by its discrete derivative interpretation. When this is introduced, the discretized equations of motion (40) take the form

$$\begin{bmatrix}\mathbf{0} & \mathbf{M}\\ -\mathbf{M} & \mathbf{0}\end{bmatrix}\begin{bmatrix}\Delta\mathbf{u}\\ \Delta\mathbf{v}\end{bmatrix}+h\begin{bmatrix}\mathbf{g}(\mathbf{u})_*+\bar{\tilde{\boldsymbol{\Omega}}}_D\mathbf{M}\bar{\mathbf{v}}\\ \mathbf{M}\bar{\tilde{\boldsymbol{\Omega}}}_D^{\mathrm{T}}\bar{\mathbf{u}}+\mathbf{M}\bar{\mathbf{v}}\end{bmatrix}=h\begin{bmatrix}\mathbf{f}_*\\ -\mathbf{M}\bar{\tilde{\boldsymbol{\Omega}}}_D^{\mathrm{T}}\mathbf{x}_0\end{bmatrix}. \tag{49}$$

This result is simple in the sense that all explicit terms involving mean values are obtained by using the mean values of the factors. It is notable that neither accelerations, angular accelerations, or the centrifugal force appear explicitly in these equations. If a potential representation of the external force $\mathbf{f}$ is known, the effective mean value $\mathbf{f}_*$ can often be expressed within the difference/mean value format.

4.2. Linear elastic properties

If the material is linear elastic in terms of the quadratic Green strain (17), the algorithmic internal force $\mathbf{g}(\mathbf{u})_*$ can be expressed in terms of a simple mean value product format. The elastic energy has the quadratic form

$$G(\mathbf{u})=\int_{V_0}\frac{1}{2}\mathbf{E}^{\mathrm{T}}\mathbf{D}\mathbf{E}\,\mathrm{d}V_0, \tag{50}$$

DOI: 10.1002/nme

where the matrix $\mathbf{D}$ contains elastic constants. The energy is a quadratic form in the Green strain $\mathbf{E}$, and the Green strain is a quadratic form in the deformation gradient $\mathbf{F}$ and thereby in the displacement $\mathbf{u}$. Thus, the increment of the elastic energy takes the form

$$[G(\mathbf{u})]_n^{n+1} = \int_{V_0} \Delta\mathbf{E}^{\mathrm{T}} \overline{\mathbf{D}\mathbf{E}}\, \mathrm{d}V_0 = \Delta\mathbf{u}^{\mathrm{T}} \int_{V_0} (\overline{\partial\mathbf{E}/\partial\mathbf{u}})^{\mathrm{T}} \bar{\mathbf{S}}\, \mathrm{d}V_0. \tag{51}$$

The algorithmic internal force for the linear elastic body now follows directly from the definition (47) as the last factor,

$$\mathbf{g}(\mathbf{u})_* = \int_{V_0} (\overline{\partial\mathbf{E}/\partial\mathbf{u}})^{\mathrm{T}} \bar{\mathbf{S}}\, \mathrm{d}V_0. \tag{52}$$

This is the mean value product format originally derived by Simo and Tarnow [3]. It is noted that the strain gradient $\partial\mathbf{E}/\partial\mathbf{u}$ is linear in $\mathbf{u}$, and thus its mean value is equal to its value at the mean displacement $\bar{\mathbf{u}}$. This makes the internal forces $\mathbf{g}(\mathbf{u})_*$ orthogonal to a rigid body displacement from the mean displacement state $\mathbf{x}$. It also enable calculation of the strain gradient from the mean state $\bar{\mathbf{x}}$.

There is a convenient alternative way of evaluating the algorithmic internal force vector directly from properties at the states at t_n and t_{n+1} [6]. The idea is to rewrite the integral (52) in terms of the product of the values at the end point plus a product of increments,

$$\mathbf{g}(\mathbf{u})_* = \int_{V_0} \left\{ \frac{1}{2}[(\partial\mathbf{E}/\partial\mathbf{u})_{n+1}^{\mathrm{T}} \mathbf{S}_{n+1} + (\partial\mathbf{E}/\partial\mathbf{u})_n^{\mathrm{T}} \mathbf{S}_n] - \frac{1}{4}\Delta(\partial\mathbf{E}/\partial\mathbf{u})^{\mathrm{T}} \Delta\mathbf{S} \right\} \mathrm{d}V_0. \tag{53}$$

The first two terms are the internal force at times t_{n+1} and t_n, respectively, and the last term can be expressed in terms of the geometric stiffness matrix. The strain gradient $\partial\mathbf{E}/\partial\mathbf{u}$ is linear in the displacement $\mathbf{u}$, and the finite increment can therefore be expressed in terms of its derivative in the form

$$\Delta(\partial\mathbf{E}/\partial\mathbf{u}) = \Delta\mathbf{u} \frac{\partial\mathbf{E}}{\partial\mathbf{u}^{\mathrm{T}} \partial\mathbf{u}}. \tag{54}$$

When this is used, the last term can be identified in terms of the increment of the geometric stiffness matrix defined in (22). As a result the algorithmic internal force takes the form

$$\mathbf{g}(\mathbf{u})_* = \overline{\mathbf{g}(\mathbf{u})} - \tfrac{1}{4}\Delta\mathbf{K}^g \Delta\mathbf{u}. \tag{55}$$

This expression of the algorithmic internal force in terms of the mean value of the internal force at the ends of the interval minus a term with the increment of the geometric stiffness is convenient for the actual calculation in a computer implementation and also plays an important role when generalizing the algorithm to include algorithmic damping in Section 5.

4.3. Angular momentum balance

In addition to the energy balance equation (48) the discrete incremental equations (49) also provide a balance equation for the angular momentum vector $\mathbf{L}$. While the energy balance equation is exact, when the effective load vector $\mathbf{f}_*$ is correctly represented, and provides energy conservation in the absence of external loads, the equation for the angular momentum vector $\mathbf{L}$ is a consistent approximation, and in general conservation only applies to the magnitude $|\mathbf{L}|$.

The first of the incremental equations (49) is a balance of forces. The terms containing the mass matrix $\mathbf{M}$ are converted to vector form by introducing the linear momentum vector $\mathbf{p} = \mathbf{M}\mathbf{v}$, whereby

$$\Delta\mathbf{p} + h\mathbf{g}(\mathbf{u})_* + h\bar{\tilde{\boldsymbol{\Omega}}}_D \bar{\mathbf{p}} = h\mathbf{f}_*. \tag{56}$$

DOI: 10.1002/nme

This equation is converted to angular momentum by forming the moment of the vector components at each node j via pre-multiplication with $\bar{\mathbf{x}}_j\times=\tilde{\bar{\mathbf{x}}}_j$. These products are conveniently expressed by use of the diagonal block matrix

$$\tilde{\mathbf{x}}_D=\begin{bmatrix}\tilde{\mathbf{x}}_1 & \cdots & \mathbf{0}\\ \vdots & \ddots & \vdots\\ \mathbf{0} & \cdots & \tilde{\mathbf{x}}_n\end{bmatrix}, \tag{57}$$

a notation already introduced for the angular velocity in (10). The contribution from the internal forces $\mathbf{g}(\mathbf{u})_*$ vanishes, because the factor corresponds to a scaled form of an infinitesimal rigid body rotation. This leaves

$$\bar{\tilde{\mathbf{x}}}_D\Delta\mathbf{p}+h\bar{\tilde{\mathbf{x}}}_D\bar{\tilde{\boldsymbol{\Omega}}}_D\bar{\mathbf{p}}=h\bar{\tilde{\mathbf{x}}}_D\mathbf{f}_*. \tag{58}$$

This equation can be expressed in terms of vector products at each node j,

$$\bar{\mathbf{x}}_j\times\Delta\mathbf{p}_j+h\bar{\mathbf{x}}_j\times(\bar{\boldsymbol{\Omega}}\times\bar{\mathbf{p}}_j)=h\bar{\mathbf{x}}_j\times\mathbf{f}_j^*. \tag{59}$$

This equation needs to be combined with the similar result from the kinematic equation in (49).

When written out in detail the kinematic equation from (49) is

$$-\mathbf{M}\Delta\mathbf{u}+h\mathbf{M}\bar{\tilde{\boldsymbol{\Omega}}}_D^{\mathrm{T}}\bar{\mathbf{x}}+h\mathbf{M}\bar{\mathbf{v}}=\mathbf{0}. \tag{60}$$

In this equation the contribution from each node j is pre-multiplied with $\bar{\mathbf{v}}_j\times=\bar{\tilde{\mathbf{v}}}_j$. When arranged in block diagonal form corresponding to (57) the equation takes the form

$$-(\bar{\tilde{\mathbf{v}}}_D\mathbf{M})\Delta\mathbf{u}-h(\bar{\tilde{\mathbf{v}}}_D\mathbf{M})\bar{\tilde{\boldsymbol{\Omega}}}_D\bar{\mathbf{x}}+\cdots=\mathbf{0}. \tag{61}$$

The contributions from the last term have the form $\bar{\tilde{\mathbf{v}}}_D\mathbf{M}\bar{\mathbf{v}}$ and cancel each other in the final result due to the isotropic block matrix structure of the isoparametric mass matrix. The parenthesis including the mass matrix is expressed by using the following property of the linear momentum vector:

$$\bar{\mathbf{p}}=\mathbf{M}\bar{\mathbf{v}}\ \Rightarrow\ \bar{\tilde{\mathbf{p}}}=\mathbf{M}\bar{\tilde{\mathbf{v}}}\ \Rightarrow\ \bar{\tilde{\mathbf{p}}}=-\bar{\tilde{\mathbf{p}}}^{\mathrm{T}}=\bar{\tilde{\mathbf{v}}}\mathbf{M}. \tag{62}$$

When using this relation to express the factors containing the mass matrix, the kinematic relation (61) takes the form

$$-\bar{\tilde{\mathbf{p}}}_D\Delta\mathbf{u}-h\bar{\tilde{\mathbf{p}}}_D(\bar{\tilde{\boldsymbol{\Omega}}}_D\bar{\mathbf{x}})+\cdots=\mathbf{0}. \tag{63}$$

This equation is written in terms of vector products of the individual nodal contributions, and the order of the factors in the second term is rearranged to give

$$\Delta\mathbf{u}_j\times\bar{\mathbf{p}}_j-h(\bar{\mathbf{x}}_j\times\bar{\boldsymbol{\Omega}})\times\bar{\mathbf{p}}_j+\cdots=\mathbf{0}. \tag{64}$$

This is the kinematic equivalent to the dynamic equation (59).

When the two equations (59) and (64) are added, the result takes the form

$$[\bar{\mathbf{x}}_j\times\Delta\mathbf{p}_j+\Delta\mathbf{u}_j\times\bar{\mathbf{p}}_j]+h[\bar{\mathbf{x}}_j\times(\bar{\boldsymbol{\Omega}}\times\bar{\mathbf{p}}_j)-(\bar{\mathbf{x}}_j\times\bar{\boldsymbol{\Omega}})\times\bar{\mathbf{p}}_j]+\cdots=h\bar{\mathbf{x}}_j\times\mathbf{f}_j^*. \tag{65}$$

The first term is recognized as the finite increment of the product $\mathbf{x}_j\times\mathbf{p}_j$. The two triple vector products in the second term combine into a single triple vector product. Finally, summation over all nodes cancels the third term, which is indicated by dots. The final angular momentum balance is

$$\Delta\left(\sum_j\mathbf{x}_j\times\mathbf{p}_j\right)+h\bar{\boldsymbol{\Omega}}\times\left(\sum_j\bar{\mathbf{x}}_j\times\bar{\mathbf{p}}_j\right)=h\left(\sum_j\bar{\mathbf{x}}_j\times\mathbf{f}_j^*\right). \tag{66}$$

This is the discrete analogue to the continuous angular momentum balance equation (33). It is seen that the discretized convection term is formed as a triple vector product in which each

DOI: 10.1002/nme

factor is represented by its mean value. For a body rotating freely around a fixed axis the motion in any transverse plane will conserve the angular momentum, because the convection term vanishes.

5. ALGORITHMIC DAMPING

A linear viscous damping can be represented by including the corresponding damping matrix $\mathbf{C}$ in the upper left position of the first block matrix [6, 12]. However, a frequency analysis of the linearized problem demonstrates that the time discretization of a mode with natural angular frequency ω_n leads to increasing damping up to $\omega_n h = 2$, while decreasing again for larger frequencies [20]. Thus, direct representation of viscous damping will lead to decreasing damping for components with frequencies above the aliasing limit, $\omega_n h = \pi$. These components are undesirable as they will appear as aliased extra contributions to the low-frequency components of the response, and furthermore may lead to iteration problems in non-linear problems. Thus, it is often desirable to introduce an algorithmic damping that increases monotonically with the frequency of the response.

5.1. Damped equations of motion

A suitable form of the algorithmic damping is identified by a simple qualitative argument, and the actual damping properties are subsequently demonstrated rigorously via an exact energy balance for the modified algorithm. Algorithmic damping via weighted mean values was introduced in non-rotating systems in [11, 12] via somewhat different procedures that do not immediately generalize to the present problem.

A damped oscillation will typically attenuate exponentially like $\exp(-\beta t)$, thereby introducing a bias between the response at t_n and t_{n+1}. This effect can be countered by applying the undamped equations to a hypothetical amplified solution of the form $\exp(\beta t_n)\mathbf{u}_n$. A first-order approximation to this problem consists in introducing the response via biased mean values in the second matrix of the discretized equations (49). The α-weighted mean value of the velocity $\mathbf{v}$ is introduced as

$$\bar{\mathbf{v}}_\alpha = \tfrac{1}{2}(1+\alpha)\mathbf{v}_{n+1} + \tfrac{1}{2}(1-\alpha)\mathbf{v}_n = \tfrac{1}{2}\alpha\Delta\mathbf{v} + \bar{\mathbf{v}}. \tag{67}$$

The similar formula for the position $\mathbf{x} = \mathbf{x}_0 + \mathbf{u}$ is

$$\bar{\mathbf{x}}_\alpha = \tfrac{1}{2}(1+\alpha)\mathbf{x}_{n+1} + \tfrac{1}{2}(1-\alpha)\mathbf{x}_n = \tfrac{1}{2}\alpha\Delta\mathbf{u} + \bar{\mathbf{x}}. \tag{68}$$

It is seen that in accordance with the underlying assumption the α-modification only concerns the displacement $\mathbf{u}$, and not the initial position $\mathbf{x}_0$.

It is important to introduce an appropriate definition of the α-modified form $\mathbf{g}(\mathbf{u})^*_\alpha$ of the internal force to be used in the algorithm. There are two conditions that must be met: the modification must introduce energy dissipation also in the small-displacement limit and the modified internal force must satisfy orthogonality to a rigid body rotation. These two conditions imply that both the mean values in the original definition (51) of the algorithmic internal force must be represented via α-weighted mean values. Thus, the internal force in the damped algorithm is defined as

$$\mathbf{g}(\mathbf{u})^*_\alpha = \int_{V_0} (\overline{\partial\mathbf{E}/\partial\mathbf{u}})^{\mathrm{T}}_\alpha \bar{\mathbf{S}}_\alpha \, \mathrm{d}V_0. \tag{69}$$

The α-weighting of the second factor represents the amplification of the stress $\mathbf{S}$ which is part of the response. The first factor represents the effect of finite deformation on the strain. As in the case of the position $\mathbf{x}$ the α-weighting of this factor only concerns the displacement part, which will be small for moderate displacements. Thus, the α-weighting of this factor is introduced for consistency and has only modest damping effect.

DOI: 10.1002/nme

When the α-weighted mean values (67) and (68) together with the α-modified form (69) of the internal force are introduced into the discrete equations (49) the following set of equations is obtained:

$$\begin{bmatrix} \mathbf{0} & \mathbf{M} \\ -\mathbf{M} & \mathbf{0} \end{bmatrix} \begin{bmatrix} \Delta\mathbf{u} \\ \Delta\mathbf{v} \end{bmatrix} + h \begin{bmatrix} \mathbf{g}(\mathbf{u})^*_\alpha + \bar{\tilde{\mathbf{\Omega}}}_D \mathbf{M} \bar{\mathbf{v}}_\alpha \\ \mathbf{M} \bar{\tilde{\mathbf{\Omega}}}^{\mathrm{T}}_D \bar{\mathbf{x}}_\alpha + \mathbf{M} \bar{\mathbf{v}}_\alpha \end{bmatrix} = h \begin{bmatrix} \mathbf{f}_* \\ \mathbf{0} \end{bmatrix}. \tag{70}$$

In the following the algorithmic internal force $\mathbf{g}(\mathbf{u})^*_\alpha$ is rewritten in a form that simplifies computation and identifies the contribution to damping. The energy balance with dissipation is presented in the next subsection, and a full algorithm for both damped and undamped dynamics is presented in Section 6.

The expression (69) for the α-modified form of the internal force must be reformulated in order to identify its contribution to energy dissipation. The first step is to rewrite the factors in the integrand in terms of increments and classic mean values

$$\mathbf{g}(\mathbf{u})^*_\alpha = \int_{V_0} \left[(\overline{\partial \mathbf{E}/\partial \mathbf{u}}) + \tfrac{1}{2}\alpha \Delta(\partial \mathbf{E}/\partial \mathbf{u}) \right]^{\mathrm{T}} \left[\bar{\mathbf{S}} + \tfrac{1}{2}\alpha \Delta \mathbf{S} \right] \mathrm{d}V_0. \tag{71}$$

When forming the product, the integral takes the form

$$\mathbf{g}(\mathbf{u})^*_\alpha = \int_{V_0} \left\{ (\overline{\partial \mathbf{E}/\partial \mathbf{u}})^{\mathrm{T}} \bar{\mathbf{S}} + \frac{\alpha}{2} \left[\Delta(\partial \mathbf{E}/\partial \mathbf{u})^{\mathrm{T}} \bar{\mathbf{S}} + (\overline{\partial \mathbf{E}/\partial \mathbf{u}})^{\mathrm{T}} \Delta \mathbf{S} \right] + \left(\frac{\alpha}{2}\right)^2 \Delta(\partial \mathbf{E}/\partial \mathbf{u})^{\mathrm{T}} \Delta \mathbf{S} \right\} \mathrm{d}V_0. \tag{72}$$

The first term gives the undamped algorithmic internal force $\mathbf{g}(\mathbf{u})_*$ defined in (52). In the second term the square brackets define the increment $\Delta[(\partial \mathbf{E}/\partial \mathbf{u})^{\mathrm{T}} \mathbf{S}]$, and thereby the increment of the internal force $\Delta \mathbf{g}(\mathbf{u})$. Finally, the last term can be expressed via the increment of the geometric stiffness by use of (54). Altogether this implies that the algorithmic internal force, defined by a product of α-weighted mean values in (69), can be expressed in the following form:

$$\mathbf{g}(\mathbf{u})^*_\alpha = \mathbf{g}(\mathbf{u})_* + \frac{\alpha}{2} \Delta \mathbf{g}(\mathbf{u}) + \left(\frac{\alpha}{2}\right)^2 \Delta \mathbf{K}^g \Delta \mathbf{u}. \tag{73}$$

The final step in the expression of the damped algorithmic internal force is to introduce the expression (55) for the undamped algorithmic internal force $\mathbf{g}(\mathbf{u})_*$ in terms of the mean value and the geometric stiffness. The final result is then obtained as

$$\mathbf{g}(\mathbf{u})^*_\alpha = \overline{\mathbf{g}(\mathbf{u})}_\alpha - \tfrac{1}{4}(1-\alpha^2) \Delta \mathbf{K}^g \Delta \mathbf{u}. \tag{74}$$

It is seen that the α-weighted product format (69) used to define the damped internal algorithmic force results in α-weighting of the internal force at the interval end points, plus a small modification of order α^2 of the geometric stiffness term.

5.2. Energy balance with dissipation

It remains to demonstrate that the equations developed above actually lead to damping, and to estimate the magnitude of the damping associated with a particular value of the parameter α. The procedure follows that used for the undamped case in Section 4.1. The first step is to express the velocity in terms of the displacements by the kinematic equation (70b),

$$h \bar{\mathbf{v}}_\alpha = \Delta \mathbf{u} + h \bar{\tilde{\mathbf{\Omega}}}_D \bar{\mathbf{x}}_\alpha. \tag{75}$$

This equation is combined with the dynamic equation (70a),

$$\mathbf{M} \Delta \mathbf{v} + h \bar{\tilde{\mathbf{\Omega}}}_D \mathbf{M} \bar{\mathbf{v}}_\alpha + h \mathbf{g}(\mathbf{u})^*_\alpha = h \mathbf{f}_*. \tag{76}$$

Pre-multiplication of the terms of this equation with either the left- or right-hand side of (75) leads to

$$\bar{\mathbf{v}}^{\mathrm{T}}_\alpha \mathbf{M} \Delta \mathbf{v} + (\Delta \mathbf{u} + h \bar{\tilde{\mathbf{\Omega}}}_D \bar{\mathbf{x}}_\alpha)^{\mathrm{T}} \mathbf{g}(\mathbf{u})^*_\alpha + \bar{\mathbf{v}}^{\mathrm{T}}_\alpha \bar{\tilde{\mathbf{\Omega}}}_D \mathbf{M} \bar{\mathbf{v}}_\alpha = h \bar{\mathbf{v}}^{\mathrm{T}}_\alpha \mathbf{f}_*. \tag{77}$$

DOI: 10.1002/nme

The last term on the left side vanishes due to antisymmetry. The term $\bar{\tilde{\mathbf{\Omega}}}_D\bar{\mathbf{x}}_\alpha$ in the parenthesis represents a rigid body motion from the state $\bar{\mathbf{x}}_\alpha$. The first factor in the α-weighted definition (69) of the internal force $\mathbf{g}(\mathbf{u})^*_\alpha$ ensures orthogonality to this motion, and thus this product vanishes. When the α-weighted velocity in the first term is expressed via (67) the energy balance then takes the form

$$\left[\tfrac{1}{2}\mathbf{v}^{\mathrm{T}}\mathbf{M}\mathbf{v}\right]_n^{n+1}+\Delta\mathbf{u}^{\mathrm{T}}\mathbf{g}(\mathbf{u})^*_\alpha=h\bar{\mathbf{v}}_\alpha^{\mathrm{T}}\mathbf{f}_*-\tfrac{1}{2}\alpha\Delta\mathbf{v}^{\mathrm{T}}\mathbf{M}\Delta\mathbf{v}. \tag{78}$$

In this equation the α-weighted algorithmic internal force $\mathbf{g}(\mathbf{u})^*_\alpha$ is substituted from (73). By its definition (47) the algorithmic internal force $\mathbf{g}(\mathbf{u})^*$ represents the finite increment of the internal energy, and the energy balance is

$$\left[\tfrac{1}{2}\mathbf{v}^{\mathrm{T}}\mathbf{M}\mathbf{v}+G(\mathbf{u})\right]_n^{n+1}=h\bar{\mathbf{v}}_\alpha^{\mathrm{T}}\mathbf{f}_*-\tfrac{1}{2}\alpha\left\{\Delta\mathbf{v}^{\mathrm{T}}\mathbf{M}\Delta\mathbf{v}+\Delta\mathbf{u}^{\mathrm{T}}(\Delta\mathbf{g}+\tfrac{1}{2}\alpha\Delta\mathbf{K}^g\Delta\mathbf{u})\right\}. \tag{79}$$

When the internal force increment is represented by a secant stiffness in the form $\Delta\mathbf{g}=\mathbf{K}^s\Delta\mathbf{u}$ the dissipative energy balance takes the final form

$$\left[\tfrac{1}{2}\mathbf{v}^{\mathrm{T}}\mathbf{M}\mathbf{v}+G(\mathbf{u})\right]_n^{n+1}=h\bar{\mathbf{v}}_\alpha^{\mathrm{T}}\mathbf{f}_*-\tfrac{1}{2}\alpha\left\{\Delta\mathbf{v}^{\mathrm{T}}\mathbf{M}\Delta\mathbf{v}+\Delta\mathbf{u}^{\mathrm{T}}(\mathbf{K}^s+\tfrac{1}{2}\alpha\Delta\mathbf{K}^g)\Delta\mathbf{u}\right\}. \tag{80}$$

For bodies with positive stiffness this gives a dissipation that is locally quadratic in the velocity and displacement increments and proportional with the damping parameter α. The formula is a rigorous generalization to rotating bodies of the similar but somewhat more loosely established result for stationary bodies given in [12]. It should be noted that the dissipative energy balance illustrates the dissipation mechanism but is not used directly in the computational algorithm, and thus computation of the secant stiffness $\mathbf{K}^s$ is not needed.

A general analysis of the effect of algorithmic damping in the case of non-linear deformation is difficult, but as demonstrated in the following the main features of algorithmic damping and a direct interpretation of the non-dimensional damping parameter α can be obtained from a linearized analysis. A detailed frequency analysis of the similar algorithm for a linear non-rotating system has been given in [13]. This analysis demonstrates that the damping increases monotonically with vibration frequency over the full frequency range. The low-frequency regime can be represented by the non-dimensional frequency interval $\omega_k h\lesssim 1$, where ω_k is the natural frequency of the considered mode. This corresponds to time integration with at least six points per period. In this interval the damping ratio is well represented by the asymptotic relation

$$\zeta_k\simeq\tfrac{1}{2}\alpha(\omega_k h), \tag{81}$$

which follows directly from the asymptotic form of the energy balance (79). Thus, the effect of the parameter α depends on the the number of integration points, determined by the non-dimensional parameter $\omega_k h$, increasing for higher modes.

As seen from the energy balance equation (79) the relevant energy is a combination of the global kinetic energy and the local elastic potential

$$E=\tfrac{1}{2}\mathbf{v}^{\mathrm{T}}\mathbf{M}\mathbf{v}+G(\mathbf{u}). \tag{82}$$

Consider free damped vibrations of a system with constant angular velocity $\mathbf{\Omega}$. In the absence of external loads and angular acceleration the local motion will gradually approach a stationary equilibrium state $\mathbf{x}_\infty=\mathbf{x}_0+\mathbf{u}_\infty$, determined from (70) as the deformation under the centrifugal force

$$\mathbf{g}(\mathbf{u}_\infty)=\tilde{\mathbf{\Omega}}_D^{\mathrm{T}}\mathbf{M}\tilde{\mathbf{\Omega}}_D(\mathbf{x}_0+\mathbf{u}_\infty). \tag{83}$$

The corresponding limiting energy follows from (82) as

$$E_\infty=\tfrac{1}{2}\mathbf{x}_\infty^{\mathrm{T}}\tilde{\mathbf{\Omega}}_D^{\mathrm{T}}\mathbf{M}\tilde{\mathbf{\Omega}}_D\mathbf{x}_\infty+G(\mathbf{u}_\infty). \tag{84}$$

In a linearized analysis the excess energy of a particular mode with angular frequency ω_k attenuates exponentially,

$$\Delta E=E-E_\infty=\Delta E_0\ \mathrm{e}^{-2\zeta_k\omega_k t}. \tag{85}$$

DOI: 10.1002/nme

It is demonstrated in the following examples that this result from a linearized analysis applies with good accuracy also to vibrations in a rotating frame where the final energy E_∞ may constitute a substantial part of the initial energy.

5.3. Angular momentum balance with algorithmic damping

The angular momentum balance corresponding to the damped equations of motion (70) can be derived by the same procedure as for the undamped system in Section 4.3. The only difference is the introduction of the α-weighted mean values defined by (67) and (68). The internal force is represented by $\mathbf{g}(\mathbf{u})^*_\alpha$ and the definition by (69) implies orthogonality to a rotation from the state $\bar{\mathbf{x}}_\alpha$. The derivation is, therefore, unchanged up to (65), when mean values are replaced by their α-weighted equivalents. Thus the algorithmic damping leads to the slightly modified result

$$\Delta\left(\sum_j \mathbf{x}_j\times\mathbf{p}_j\right)+\alpha\left(\sum_j \Delta\mathbf{u}_j\times\Delta\mathbf{p}_j\right)+h\bar{\boldsymbol{\Omega}}\times\left(\sum_j \bar{\mathbf{x}}_{j,\alpha}\times\bar{\mathbf{p}}_{j,\alpha}\right)=h\left(\sum_j \bar{\mathbf{x}}_{j,\alpha}\times\mathbf{f}^*_j\right). \tag{86}$$

It is seen that the algorithmic damping introduces a new term containing products of the displacement and momentum increments, $\Delta\mathbf{u}_j\times\Delta\mathbf{p}_j$. The first term contains similar contributions, but with the position instead of the displacement increment, $\bar{\mathbf{x}}_j\times\Delta\mathbf{p}_j$, and thus the effect of the new term is expected to be small as confirmed in the examples in Section 7.

6. TIME INTEGRATION ALGORITHM

The time integration algorithm is simply a computationally convenient rearrangement of the equations of motion in the general form (70). In the formulation of the time integration algorithm it is convenient to formulate the problem in terms of known current values and unknown increments. The α-weighted mean values of the velocity and the position then take the form

$$\bar{\mathbf{v}}_\alpha=\tfrac{1}{2}(1+\alpha)\mathbf{v}_{n+1}+\tfrac{1}{2}(1-\alpha)\mathbf{v}_n=\tfrac{1}{2}\kappa\Delta\mathbf{v}+\mathbf{v}_n \tag{87}$$

and

$$\bar{\mathbf{x}}_\alpha=\tfrac{1}{2}(1+\alpha)\mathbf{x}_{n+1}+\tfrac{1}{2}(1-\alpha)\mathbf{x}_n=\tfrac{1}{2}\kappa\Delta\mathbf{u}+\mathbf{x}_n, \tag{88}$$

where the parameter κ is defined as

$$\kappa=1+\alpha\geqslant 1. \tag{89}$$

It is seen that where the previous split in increment and mean value generated the factor α on the increment, the present split in increment and previous value leads to similar formulas, but with α replaced by the parameter κ. The undamped form corresponds to $\kappa=1$. When using these relations the velocity increment $\Delta\mathbf{v}$ follows from the kinematic equation (75) as

$$\Delta\mathbf{v}=\left(\frac{2}{\kappa h}+\bar{\bar{\boldsymbol{\Omega}}}_D\right)\Delta\mathbf{u}-\frac{2}{\kappa}\left(\mathbf{v}_n-\bar{\bar{\boldsymbol{\Omega}}}_D\mathbf{x}_n\right). \tag{90}$$

In this and the following equations the factor $(2/\kappa h)\mathbf{I}+\bar{\bar{\boldsymbol{\Omega}}}_D$ appears repeatedly. It represents the usual normalization of increments over a time increment h, but here modified by the angular velocity of the frame of reference. This factor always appears as part of a product, and the unit matrix $\mathbf{I}$ is, therefore, not included explicitly.

The kinematic equation must be combined with the dynamic equation (76),

$$\mathbf{M}\Delta\mathbf{v}+h\bar{\bar{\boldsymbol{\Omega}}}_D\mathbf{M}\bar{\mathbf{v}}_\alpha+h\mathbf{g}(\mathbf{u})^*_\alpha=h\mathbf{f}_*. \tag{91}$$

DOI: 10.1002/nme

In this equation the dependence on the current velocity is eliminated by use of (87) and (90). After rearranging the terms the dynamic equation takes the form

$$2\mathbf{g}(\mathbf{u})^*_\alpha+\kappa\left(\frac{2}{\kappa h}+\bar{\tilde{\mathbf{\Omega}}}_D\right)\mathbf{M}\left(\frac{2}{\kappa h}+\bar{\tilde{\mathbf{\Omega}}}_D\right)\Delta\mathbf{u}=\mathbf{f}_*+\frac{4}{\kappa h}\mathbf{M}(\mathbf{v}_n-\bar{\tilde{\mathbf{\Omega}}}_D\mathbf{x}_n)+2\bar{\tilde{\mathbf{\Omega}}}^{\mathrm{T}}_D\mathbf{M}\bar{\tilde{\mathbf{\Omega}}}_D\mathbf{x}_n. \tag{92}$$

The terms in this equation are easily interpreted. The first term is the internal force, here represented via the α-weighted form defined by (69). When carrying out the products in the second term it is seen to consist of the classic inertial effect in a stationary frame, the Coriolis force that is linear in $\mathbf{\Omega}$, and a quadratic term in $\mathbf{\Omega}$ that combines with the last term of the equation to form an α-weighted mean value of the centrifugal force.

The solution within a time step starts with a predicted displacement increment. The displacement increment is obtained from a modified form of the discretized kinematic equation (90) in which the global velocity increment $\Delta\mathbf{v}$ is omitted and the last term representing the local velocity is given by its current value at t_n. Thus, the displacement increment is predicted from the relation

$$\left(\frac{2}{\kappa h}+\bar{\tilde{\mathbf{\Omega}}}_D\right)\Delta\mathbf{u}=\frac{2}{\kappa}\left(\mathbf{v}-\tilde{\mathbf{\Omega}}_D\mathbf{x}\right)_n. \tag{93}$$

The matrix on the left side consists of the 3×3 matrix $((2/\kappa h)+\bar{\tilde{\mathbf{\Omega}}})$ repeated N times along the diagonal of the larger system matrix. This simple structure implies that the inverse is also a diagonal block matrix formed by repetition of the 3×3 matrix $((2/\kappa h)+\bar{\tilde{\mathbf{\Omega}}})^{-1}$ along the diagonal. Thus, the inverse system matrix is defined in terms of the 3×3 inverse

$$\left(\frac{2}{\kappa h}+\bar{\tilde{\mathbf{\Omega}}}\right)^{-1}=\frac{1}{(2/\kappa h)^2+\mathbf{\Omega}^{\mathrm{T}}\mathbf{\Omega}}\left[\frac{2}{\kappa h}+\bar{\tilde{\mathbf{\Omega}}}^{\mathrm{T}}+\frac{\kappa h}{2}\bar{\tilde{\mathbf{\Omega}}}\bar{\tilde{\mathbf{\Omega}}}^{\mathrm{T}}\right]. \tag{94}$$

This result is easily verified and can be established by determining the scalar coefficients in a linear combination of the three terms, forming a basis. With this explicit inversion repeated along the diagonal of the inverse system matrix the initial displacement predictor (93) is available in explicit form. From this initial estimate the non-linear dynamic equation (92) is solved by iteration. When the increment $\Delta\mathbf{u}$ has been determined, the velocity increment $\Delta\mathbf{v}$ is determined from the explicit expression (90).

The iterative solution of the non-linear dynamic equation (92) requires determination of the incremental stiffness, based on the current state. The specific form follows from the variation of the α-weighted algorithmic internal force (69),

$$\delta[2\mathbf{g}(\mathbf{u})^*_\alpha]=\kappa\int_{V_0}\delta(\partial\mathbf{E}/\partial\mathbf{u})^{\mathrm{T}}\bar{\mathbf{S}}_\alpha\,\mathrm{d}V_0+\kappa\int_{V_0}(\overline{\partial\mathbf{E}/\partial\mathbf{u}})^{\mathrm{T}}_\alpha\delta\mathbf{S}\,\mathrm{d}V_0. \tag{95}$$

The factor κ is generated by the α-weighting of the current value in the strain gradient and the stress, respectively. The first integral represents the algorithmic form of the geometric stiffness matrix,

$$\mathbf{K}^g_*=\int_{V_0}\frac{\partial^2\mathbf{E}^{\mathrm{T}}}{\partial\mathbf{u}^{\mathrm{T}}\partial\mathbf{u}}\bar{\mathbf{S}}_\alpha\,\mathrm{d}V_0=\bar{\mathbf{K}}^g_\alpha. \tag{96}$$

Thus, the first integral is the α-weighted mean value of the geometric stiffness matrix at t_n and t_{n+1}. The result follows from the fact that the double gradient of the strain is independent of the current state of displacement. The algorithmic form of the constitutive stiffness matrix is defined by the second integral,

$$\mathbf{K}^c_*=\int_{V_0}\left(\overline{\frac{\partial\mathbf{E}}{\partial\mathbf{u}}}\right)^{\mathrm{T}}_\alpha\frac{\partial\mathbf{S}}{\partial\mathbf{u}}\,\mathrm{d}V_0=\int_{V_0}\left(\overline{\frac{\partial\mathbf{E}}{\partial\mathbf{u}}}\right)^{\mathrm{T}}_\alpha\mathbf{D}\left(\frac{\partial\mathbf{E}}{\partial\mathbf{u}}\right)\mathrm{d}V_0. \tag{97}$$

DOI: 10.1002/nme

Table I. Conservative algorithm with algorithmic damping.

(1)	Initial conditions: $\mathbf{u}_0,\ \mathbf{v}_0$
(2)	Prediction step: $\Delta\mathbf{u}=(2/\kappa)(2/\kappa h+\bar{\tilde{\mathbf{\Omega}}}_D)^{-1}(\mathbf{v}-\tilde{\mathbf{\Omega}}_D\mathbf{x})_n$
(3)	Residual calculation: $\mathbf{u}=\mathbf{u}_n+\Delta\mathbf{u}$ $\mathbf{r}=2\mathbf{f}_*-2\mathbf{g}^*_\alpha-\kappa(2/\kappa h+\bar{\tilde{\mathbf{\Omega}}}_D)\mathbf{M}(2/\kappa h+\bar{\tilde{\mathbf{\Omega}}}_D)\Delta\mathbf{u}$ $+(4/\kappa h)\mathbf{M}(\mathbf{v}_n-\bar{\tilde{\mathbf{\Omega}}}_D\mathbf{x}_n)+2\bar{\tilde{\mathbf{\Omega}}}^{\mathrm{T}}_D\mathbf{M}\bar{\tilde{\mathbf{\Omega}}}_D\mathbf{x}_n$
(4)	Displacement sub-increment: $\mathbf{K}_*=\kappa(\mathbf{K}^g_*+\mathbf{K}^c_*)+\kappa(2/\kappa h+\bar{\tilde{\mathbf{\Omega}}}_D)\mathbf{M}(2/\kappa h+\bar{\tilde{\mathbf{\Omega}}}_D)$ $\delta\mathbf{u}=\mathbf{K}_*^{-1}\mathbf{r}$ $\Delta\mathbf{u}=\Delta\mathbf{u}+\delta\mathbf{u}$ If $\mathbf{r}>\varepsilon_{\mathbf{r}}$ or $\delta\mathbf{u}>\varepsilon_{\mathbf{u}}$ repeat from (3).
(5)	State vector update: $\Delta\mathbf{v}=(2/\kappa h+\bar{\tilde{\mathbf{\Omega}}}_D)\Delta\mathbf{u}-(2/\kappa)(\mathbf{v}_n-\bar{\tilde{\mathbf{\Omega}}}_D\mathbf{x}_n)$ $\mathbf{u}_{n+1}=\mathbf{u}_n+\Delta\mathbf{u}$ $\mathbf{v}_{n+1}=\mathbf{v}_n+\Delta\mathbf{v}$
(6)	Return to (2) for new time step, or stop.

In this formula the last factor refers to the current state, and thus the algorithmic equivalent of the constitutive stiffness matrix is

$$\mathbf{K}^c_*=\int_{V_0}\left\{\frac{1+\alpha}{2}\left(\frac{\partial\mathbf{E}}{\partial\mathbf{u}}\right)^{\mathrm{T}}_{n+1}\mathbf{D}\left(\frac{\partial\mathbf{E}}{\partial\mathbf{u}}\right)_{n+1}+\frac{1-\alpha}{2}\left(\frac{\partial\mathbf{E}}{\partial\mathbf{u}}\right)^{\mathrm{T}}_{n}\mathbf{D}\left(\frac{\partial\mathbf{E}}{\partial\mathbf{u}}\right)_{n+1}\right\}\mathrm{d}V_0. \tag{98}$$

In the last term the two factors refer to the states at t_n and t_{n+1}, respectively. A formulation in which both the last factors refer to the state at t_n would correspond to a direct α-mean of the constitutive stiffness matrix,

$$\mathbf{K}^c_*\simeq\bar{\mathbf{K}}^c_\alpha. \tag{99}$$

This approximation for the algorithmic constitutive stiffness matrix corresponds in form to the exact result (96) for the geometric stiffness matrix. The approximation of the algorithmic constitutive stiffness has the advantage of avoiding any calculations with reference to combined or intermediate states, and numerical calculations, e.g. in [6], indicate the near optimal convergence when using this approximation.

The algorithm is summarized in pseudo-code format in Table I. In the examples presented in the following section both of the algorithmic stiffness matrices $\mathbf{K}^g_*$ and $\mathbf{K}^c_*$ have been represented as α-mean values as indicated in (96) and (99).

7. EXAMPLES

The following three examples illustrate the properties and accuracy of the hybrid state-space time integration algorithm. The first two examples illustrate accelerated rotation and damping properties using the rotating beam, originally introduced by Kane *et al.* [21] and later used in numerous studies, typically in the form defined by Simo and Vu-Quoc [22, 23]. The third example deals with vibrations and damping of a rotating U-shaped frame with multiple closely spaced vibration modes.

DOI: 10.1002/nme

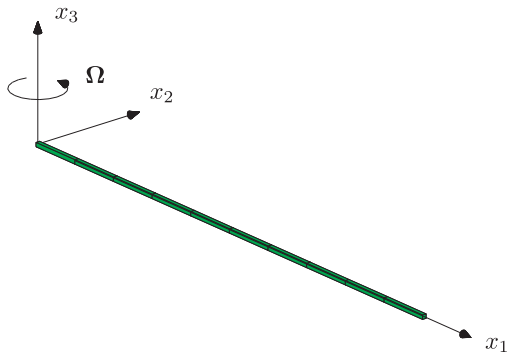

Figure 2. Kane's driver.

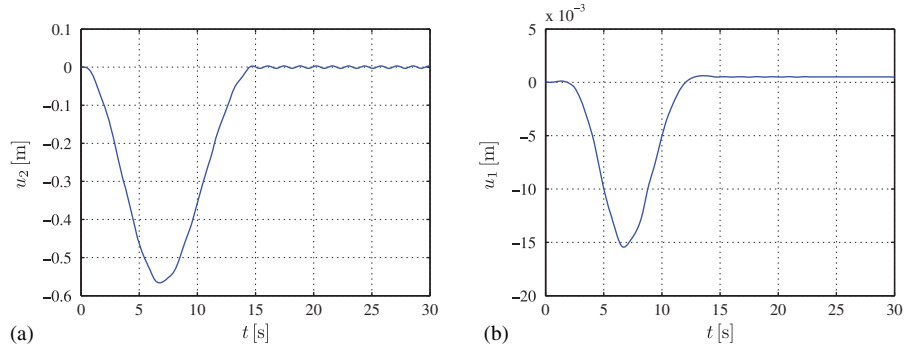

Figure 3. Kane's driver: (a) transverse displacement u_2 and (b) axial displacement u_1.

7.1. Transient acceleration of Kane's driver

The beam problem originally introduced by Kane *et al.* [21] is illustrated in Figure 2. It consists of a slender beam of square cross section with beam axis x_1, rotating around the x_3-axis with angular velocity Ω_3. The beam properties in common use were defined by Simo and Vu-Quoc [22, 23] in terms of beam section parameters. They are equivalent to a beam of length $L=10\,\mathrm{m}$, with a square cross section with side length $b=0.0775\,\mathrm{m}$. The beam material is homogeneous and isotropic elastic with $E=4.67\,\mathrm{GPa}$ and $G=2.00\,\mathrm{GPa}$, and the mass density is $\rho=200\,\mathrm{kg/m^3}$. It is noted that this is a very slender beam.

The beam is rigidly fixed at the axis and is analyzed for a spin-up in which the angular velocity increases over a period of $T_s=15\,\mathrm{s}$ to its final stationary value $\Omega_s=6\,\mathrm{rad/s}$ according to

$$\Omega_3(t)=\begin{cases}\dfrac{\Omega_s}{T_s}\left[t-\left(\dfrac{T_s}{2\pi}\right)\sin\dfrac{2\pi t}{T_s}\right], & 0\leqslant t\leqslant T_s,\\ \Omega_s, & t>T_s.\end{cases} \tag{100}$$

The beam is modeled using 10 3D 20-node iso-parametric elements with quadratic shape functions. The time step is $h=0.05\,\mathrm{s}$, and the iteration convergence criteria are $\varepsilon_{\mathbf{r}}=10^{-3}$ and $\varepsilon_{\mathbf{u}}=10^{-12}$.

Results are illustrated in Figure 3 showing the transverse displacement u_2 and the axial displacement u_1 as functions of time. The transverse components shows the backward bending of the beam in the angular acceleration phase, and the axial displacement shows an apparent shortening from bending in the acceleration phase, changing into a small elongation due to the centrifugal force in the final near-stationary phase. The results correspond closely to those of Simo and Vu-Quoc [22, 23], although the present time step is 10 times larger. Actually the critical aspect when selecting the time step in the present problem is the period error that accumulates in the vibrations generating the small ripples in the response after reaching stationary rotation speed Ω_s

DOI: 10.1002/nme

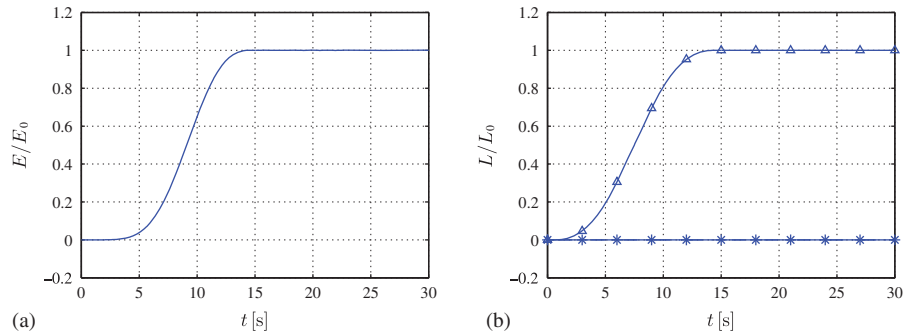

Figure 4. Kane's driver: (a) normalized energy and (b) normalized angular momentum components L_1 (+), L_2 (×), L_3 (△).

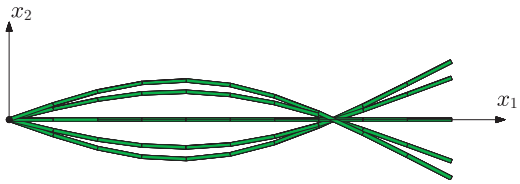

Figure 5. Local vibration shapes (×50).

at T_s. The present algorithm, like most time integration algorithms with quadratic convergence, has the same quadratic vibration period error as the Newmark algorithm, as discussed in [12]. Thus, the period offset grows linearly with time, and care must be exercised to limit the accumulated effect by selecting a sufficiently small time step.

The development of the mechanical energy and the components of the angular momentum are shown in Figures 4(a) and (b), respectively. The curves are normalized with respect to E_0 and L_0 corresponding to stationary rotation at the final angular velocity. The energy E and the axial component of the angular momentum L_3 follow the development of angular velocity with a slight delay, and the near-stationary final phase exhibits small oscillations, due to the moment arising from the fixed connection at the axis. This moment is calculated from the algorithm, and the present problem is therefore not well suited for a precise illustration of the conservation and damping properties of the algorithm. These aspects are illustrated in the following examples in connection with free vibration problems.

7.2. Vibrations of hinged rotating beam

In this example the beam from the previous example is hinged at the axis, whereby the energy is either conserved or dissipated by algorithmic damping. The frame rotates with the angular velocity $\Omega_3 = 0.1\,\text{rad/s}$, and the beam performs local vibrations within the rotating frame. The vibrations are initiated from a state in which the beam is extended by the centrifugal force and given an initial transverse velocity component

$$\dot{u}_2(x_1) = (x_1/L)[4(x_1/L) - 3]\dot{u}_{\max}$$

that does not contribute to the angular momentum (see Figure 5). Axial initial velocity components $\dot{u}_1$ are determined corresponding to the cross sections remaining orthogonal to the beam axis. The amplitude of the vibrations is determined by setting the ratio between local kinetic energy and the global kinetic energy before imposing the local velocity,

$$\tfrac{1}{2}\dot{\mathbf{u}}_0^{\mathrm{T}}\mathbf{M}\dot{\mathbf{u}}_0 = 0.15\ \tfrac{1}{2}\mathbf{v}_0^{\mathrm{T}}\mathbf{M}\mathbf{v}_0.$$

This balance leads to the local tip velocity $\dot{u}_{\max} = 0.5\,\text{m/s}$, corresponding to half of the global tip velocity contribution from the rotation of the frame, $\Omega_3 L = 1.0\,\text{m/s}$.

DOI: 10.1002/nme

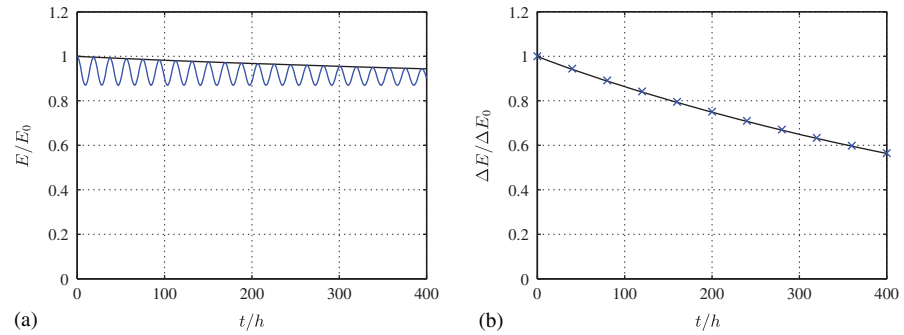

Figure 6. Hinged beam: $\Omega_3 = 0.1\,\text{rad/s}$: (a) mechanical energy E (−) and kinetic energy T (−) and (b) energy decay ΔE (−), $e^{-2\zeta_3\omega_3 t}$ (×).

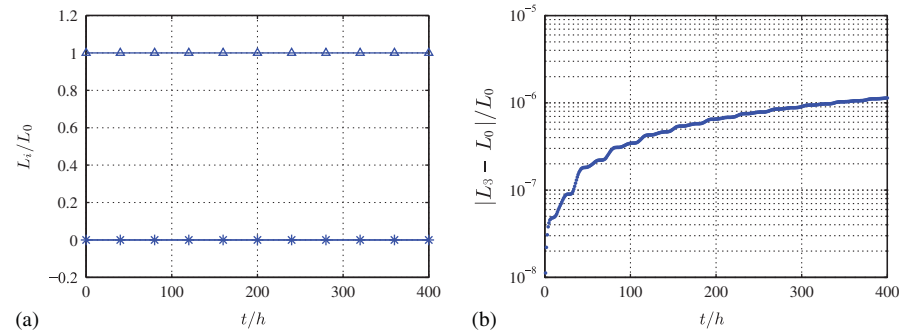

Figure 7. Hinged beam: $\Omega_3 = 0.1$ rad/s: (a) angular momentum components L_1 (+), L_2 (×), L_3 (△) and (b) relative change of angular momentum component L_3.

The beam is modeled with 10 3D 20-node iso-parametric elements as in the previous example, but using the time step $h = 0.01\,\text{s}$. With an angular vibration frequency of $\omega_3 = 16.82\,\text{rad/s}$, corresponding to $\omega_3 h = 0.17$, this gives 37 time steps per vibration period. The convergence criteria are $\varepsilon_{\mathbf{r}} = 10^{-3}$ and $\varepsilon_{\mathbf{u}} = 10^{-12}$. With these parameters and $\alpha = 0$ the energy and the angular momentum are conserved to within a relative accuracy of 10^{-12}.

Algorithmic damping is now introduced via the parameter $\alpha = 0.05$, corresponding to a damping ratio of $\zeta_3 \simeq \frac{1}{2}\alpha(\omega_3 h) = 0.0043$. The development of the mechanical energy is illustrated in Figure 6. Figure 6(a) shows the total energy as the slowly decreasing curve and the kinetic energy by the oscillating curve below. It is seen that the minima of the kinetic energy corresponds closely to the value $1/1.15 = 0.87$, which is the fraction of the kinetic energy associated with the global rotation. The attenuation of the local vibration energy is illustrated in Figure 6(b). It is seen to be well represented by the exponential decay (85) predicted by the linearized theory.

The components L_i of the angular momentum vector are shown in Figure 7(a). In the undamped case these components were conserved to within an accuracy of $10^{-12} L_0$. In the present case with algorithmic damping there is a small but systematic change in the component L_3 along the rotation axis, illustrated in Figure 7. The relative change of the L_3-component is due to the higher order additional second term in the damped momentum balance equation (86). In the present case, where a fairly fine time discretization is used, the relative decrease in L_3 grows to around 10^{-6}.

7.3. Rotating U-frame

This last example deals with a rotating frame with interior length $L = 2.0\,\text{m}$, interior height $H = 0.5\,\text{m}$, and quadratic cross section $b = 0.1$ m. The material is linear elastic in Green strains with $E = 100\,\text{MPa}$, $\nu = 0.3$, and $\rho = 10^3\,\text{kg/m}^2$. The frame is modeled by 14 20-node iso-parametric elements with quadratic shape functions. The time step is $h = 0.01\,\text{s}$, and the convergence criteria

DOI: 10.1002/nme

are $\varepsilon_{\mathbf{r}} = 10^{-3}$ and $\varepsilon_{\mathbf{u}} = 10^{-12}$. The example illustrates the effect of damping on structures with closely spaced modes and the influence of rotation speed.

The natural vibration modes and the corresponding eigenfrequencies of the undamped frame are determined from the eigenvalue problem

$$\left(\begin{bmatrix} \mathbf{K}_c + \mathbf{K}_g & \tilde{\mathbf{\Omega}}_D \mathbf{M} \\ \mathbf{M}\tilde{\mathbf{\Omega}}_D^{\mathrm{T}} & \mathbf{M} \end{bmatrix} + i\omega_j \begin{bmatrix} \mathbf{0} & \mathbf{M} \\ -\mathbf{M} & \mathbf{0} \end{bmatrix} \right) \begin{bmatrix} \mathbf{u} \\ \mathbf{v} \end{bmatrix}_j = \begin{bmatrix} \mathbf{0} \\ \mathbf{0} \end{bmatrix} \tag{101}$$

following directly from the hybrid format (36) of the equations of motion, when the internal force is linearized. These equations are somewhat simpler than the traditional format proposed in [14, 15, 17]. The first six natural vibration modes of the U-frame in a stationary frame of reference are shown in Figure 8. Mode shapes and frequencies change slightly with increasing rotation frequency, but these changes are negligible up to $\Omega_3 \simeq 1$rad/s used in the present illustrations.

In this example the vibrations are excited by combining an initial displacement field corresponding to rotation at constant angular velocity Ω_3 with an in-plane initial velocity, targeting the in-plane modes 3 and 4. The displacement field for rotation at constant angular velocity is shown in Figure 9(a). The initial velocity field is proportional to the displacement field, Figure 9(c), generated by the force couple shown in Figure 9(b), with the maximum initial velocity component $\dot{u}_{\max} = 0.5\,\mathrm{m/s}$. The initial velocity field primarily excites modes 3 and 4, and leads to interference of these modes.

Figure 10 shows the development in the mechanical energy for a rotation with angular velocity $\Omega_3 = 0.2\,\mathrm{rad/s}$. Algorithmic damping is included with $\alpha = 0.05$, corresponding to a damping ratio of $\zeta_i = \frac{1}{2}\alpha(\omega_i h) \simeq 0.004$. It is seen that the local part of the energy amounts to about 70 pct. of the total initial energy, and that the dissipation of this part of the energy is dissipated as predicted by the exponential relation (85). Figure 11 shows the similar results when the angular velocity is increased to $\Omega_3 = 1.0\,\mathrm{rad/s}$. In this case the local part of the energy initially constitutes only 10 pct. of the total energy. However, the dissipation of the local energy follows the same exponential curve, when expressed in terms of relative energy.

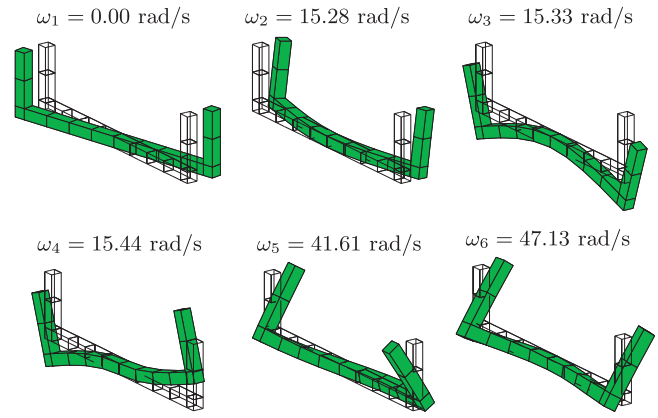

Figure 8. Solid U-frame: natural modes.

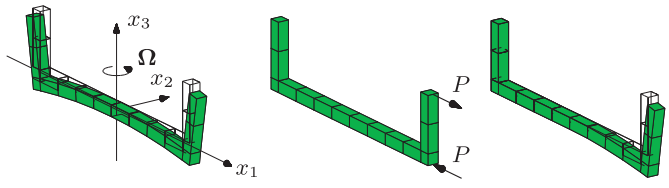

Figure 9. Solid U-frame: (a) stationary displacement field ($\times 2000$); (b) static load case; and (c) initial velocity field ($\dot{u}_{\max} = 0.5\,\mathrm{m/s}$).

DOI: 10.1002/nme

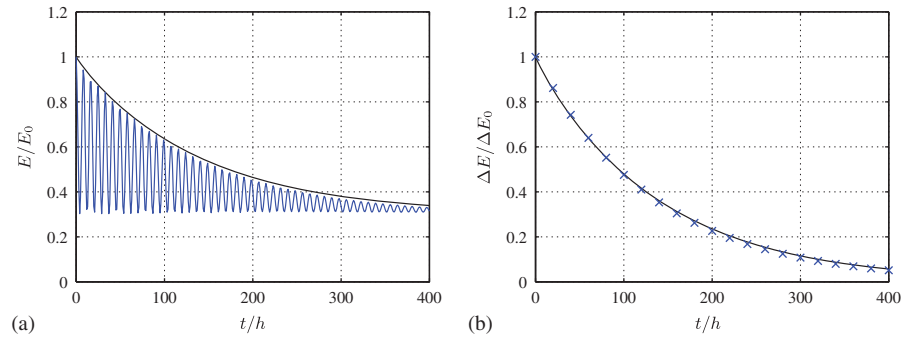

Figure 10. Solid U-frame, $\Omega_3 = 0.2\,\text{rad/s}$: (a) mechanical energy E (−) and kinetic energy T (−) and (b) energy decay ΔE (−), $e^{-2\zeta_3\omega_3 t}$ (×).

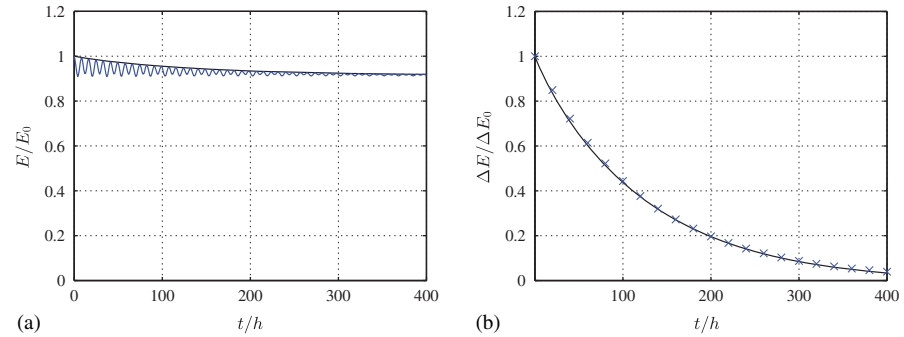

Figure 11. Solid U-frame, $\Omega_3 = 1.0\text{rad/s}$: (a) mechanical energy E (−) and kinetic energy T (−) and (b) energy decay ΔE (−), $e^{-2\zeta_3\omega_3 t}$ (×).

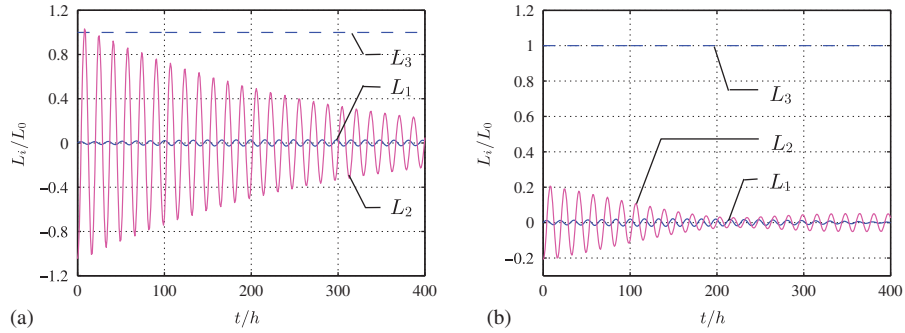

Figure 12. Solid U-frame, angular momentum components L_1 (—), L_2 (—), L_3 (- -): (a) $\Omega_3 = 0.2\,\text{rad/s}$ and (b) $\Omega_3 = 1.0\,\text{rad/s}$.

Finally, the components L_i of the angular momentum vector are shown in Figure 12. At the angular velocity $\Omega_3 = 0.2\,\text{rad/s}$, shown in Figure 12(a) the initial value of the component L_2, generated by the in-plane vibration, is comparable to L_3 from the global rotation of the frame. However, while the largely global L_3 is constant without attenuation, the L_2 component oscillates and is attenuated as part of the local vibration. At the higher rotation speed $\Omega_3 = 1.0\,\text{rad/s}$, illustrated in Figure 12(b), the relative magnitude of the local L_2 component is reduced to 20 pct. and 'beats' start to become visible because the frequency difference $\omega_4 - \omega_3$ has increased from 0.13 rad/s in the previous case to 0.31 rad/s in the present case, leading to a reduction of the beat period by a factor of 0.42.

DOI: 10.1002/nme

8. DISCUSSION

A hybrid state-space consisting of local displacements and global velocities has been developed for dynamic analysis of structures in a rotating frame of reference. An important feature is that the local displacement and the global velocity are represented in terms of the same family of shape functions. As a consequence of this discretization, all inertial effects are expressed directly in terms of the classic mass matrix. In the hybrid state-space the equations of motion correspond to the dynamic equation of motion and a momentum equation defining the absolute velocity in terms of local components. This formulation gives a very simple structure of the equations of motion, consisting of time derivatives with a skew-symmetric coefficient matrix, and current values of local displacement and global velocity combined via a symmetric coefficient matrix. It is remarkable that neither the centrifugal force nor the angular acceleration appears directly in the hybrid state-space equations of motion, but is represented indirectly via use of the global velocity.

An energy conserving time discretization is obtained by using the mean value of the angular velocity together with internal forces expressed in terms of the finite derivative of the elastic potential. Algorithmic damping is introduced via an argument by which a damped response is restored to undamped form by an increasing exponential factor. This argument can be represented in algorithmic form via forward weighting of mean values of the hybrid state-space variables. For linear elastic materials represented in terms of Green strain the effect of forward weighting of the displacements on the internal forces is expressed in explicit form in terms of forward weighting of the internal forces plus an additional term formed by the increment of the geometric stiffness. Thus, no intermediate state is needed within the time step. The effect of algorithmic damping corresponds closely to exponential decay of the local response, and the damping parameter is simply related to an algorithmic damping ratio.

REFERENCES

1. Hairer E, Lubich C, Wanner G. *Geometric Numerical Integration* (2nd edn). Springer: Berlin, 2006.
2. Simo JC, Wong KK. Unconditionally stable algorithms for rigid body dynamics that exactly preserve energy and momentum. *International Journal for Numerical Methods in Engineering* 1991; **31**:19–52.
3. Simo JC, Tarnow N. The discrete energy-momentum method. Conserving algorithms for nonlinear elastodynamics. *Zeitschrift für angewandte Mathematik und Physik* 1992; **43**:757–792.
4. Simo JC, Tarnow N, Wong KK. Exact energy-momentum conserving algorithms and symplectic schemes for nonlinear dynamics. *Computer Methods in Applied Mechanics and Engineering* 1992; **100**:63–116.
5. Gonzalez O. Exact energy and momentum conserving algorithms for general models in non-linear elasticity. *Computer Methods in Applied Mechanics and Engineering* 2000; **190**:1763–1783.
6. Krenk S. The role of geometric stiffness in momentum and energy conserving time integration. *International Journal for Numerical Methods in Engineering* 2007; **71**:631–651.
7. Bauchau OA, Bottasso CL. On the design of energy preserving and decaying schemes for flexible, nonlinear multi-body systems. *Computer Methods in Applied Mechanics and Engineering* 2000; **169**:61–79.
8. Lens EV, Cardona A, Geradin M. Energy preserving time integration for constrained multibody systems. *Multibody System Dynamics* 2004; **11**:41–61.
9. Betsch P, Uhlar S. Energy-momentum conserving integration of multibody dynamics. *Multibody System Dynamics* 2007; **17**:243–289.
10. Gonzalez M, Schmidt B, Ortiz M. Energy-stepping integrators in Lagrangian mechanics. *International Journal for Numerical Methods in Engineering* 2010; **82**:205–241.
11. Armero F, Romero I. On the formulation of high-frequency dissipative time-stepping algorithms for nonlinear dynamics. Part II: Second order methods. *Computer Methods in Applied Mechanics and Engineering* 2001; **190**:6783–6824.
12. Krenk S. *Non-Linear Modeling and Analysis of Solids and Structures*. Cambridge University Press: Cambridge, 2009.
13. Krenk S. Extended state-space time integration with high-frequency energy dissipation. *Inernational Journal for Numerical Methods in Engineering* 2008; **73**:1767–1787.
14. Meirovitch L. A new method of solution of the eigenvalue problem for gyroscopic systems. *AIAA Journal* 1974; **12**:1337–1342.
15. Meirovitch L. A new modal method for the response of structures rotating in space. *Acta Astronautica* 1975; **2**:563–576.
16. Meirovitch L. *Computational Methods in Structural Dynamics*. Sijthoff and Noordhoff: New York, 1980.
17. Geradin M, Rixen D. *Mechanical Vibrations*, *Theory and Applications to Structural Dynamics* (2nd edn). Wiley: Chichester, U.K., 1997.

DOI: 10.1002/nme

18. Shabana AA. *Dynamics of Multibody Systems*. Cambridge University Press: Cambridge, 2005.
19. Kawamoto A, Krenk S, Suzuki A, Inagaki M. Flexible body dynamics in a local frame of reference with explicitly predicted motion. *International Journal for Numerical Methods in Engineering* 2010; **81**:246–268.
20. Hughes TJR. Analysis of transient algorithms with particular reference to stability behavior. In *Computational Methods for Transient Analysis*, Belytschko T, Hughes TJR (eds). North-Holland: Amsterdam, 1983; 67–155.
21. Kane TR, Ryan RR, Banerjee AK. Dynamics of a cantilever beam attached to a moving base. *Journal of Guidance Control and Dynamics* 1987; **10**:139–151.
22. Simo JC, Vu-Quoc L. The role of non-linear theories in transient dynamic analysis of flexible structures. *Journal of Sound and Vibration* 1987; **119**:487–508.
23. Simo JC, Vu-Quoc L. On the dynamics in space of rods undergoing large motions—A geometrically exact approach. *Computer Methods in Applied Mechanics and Engineering* 1988; **66**:125–161.

DOI: 10.1002/nme

P2

Hybrid state-space time integration of rotating beams

S. Krenk & M.B. Nielsen

Computer Methods in Applied Mechanics and Engineering,
Vol **213-216**:243–254, 2012.

Comput. Methods Appl. Mech. Engrg. 213–216 (2012) 243–254

Contents lists available at SciVerse ScienceDirect

Comput. Methods Appl. Mech. Engrg.

journal homepage: www.elsevier.com/locate/cma

Hybrid state-space time integration of rotating beams

Steen Krenk *, Martin B. Nielsen

Department of Mechanical Engineering, Technical University of Denmark, DK-2800 Lyngby, Denmark

ARTICLE INFO

Article history:
Received 18 March 2011
Received in revised form 11 November 2011
Accepted 14 November 2011
Available online 25 November 2011

Keywords:
Dynamics in rotating frame
Conservative time integration
Beam elements
Algorithmic dissipation
Structural dynamics

ABSTRACT

An efficient time integration algorithm for the dynamic equations of flexible beams in a rotating frame of reference is presented. The equations of motion are formulated in a hybrid state-space format in terms of local displacements and local components of the absolute velocity. With inspiration from Hamiltonian mechanics, where displacement and momentum have similar roles, both sets of state-space variables are interpolated between nodes by the same shape functions, leading to a general format where all inertia effects are represented via the classic constant mass matrix, while effects of the system rotation enter via global operations with the angular velocity vector. The algorithm is based on an integrated form of the equations of motion with energy and momentum conserving properties, if a kinematically consistent non-linear formulation is used. A consistent monotonic scheme for algorithmic energy dissipation in terms of local displacements and velocities, typical of structural vibrations, is developed and implemented in the form of forward weighting of appropriate mean value terms in the algorithm. The algorithm is implemented for a beam theory with consistent quadratic non-linear kinematics, valid for moderate finite rotations. The equations of this non-linear beam theory are generated in explicit form by extension of the constitutive stiffness and the geometric stiffness of a linear beam theory at the element level. The performance of the algorithm is illustrated by numerical examples.

1. Introduction

The use of beam models to represent rotating structures such as wind turbine rotors or propellers has attracted considerable interest for several decades. The various formulations may be divided into two fundamentally different approaches where either one or several intermediate reference frames are introduced for the body or its substructures, allowing deformations to be considered relative to the reference frames, or geometrically fully non-linear formulations in a global frame accounting for large displacements and finite rotations. Floating frame formulations are widely used and computationally attractive, as the large overall motion can be described by the motion of the local frame, while the local deformations in many applications may be assumed small or moderate [1–3]. In spite of this kinematic simplification an accurate representation of the geometric stiffness is needed to correctly balance the effect of centrifugal forces, see e.g. [3]. The geometric stiffness may be included either with reference to a reference stress with respect to the initial configuration [4], or using the current geometry [5]. The moving frame of reference introduces additional inertia terms associated with Coriolis and centrifugal effects. In the traditional formulations the local velocities are obtained from time differentiation of the local displacements inside the element. This leads to terms representing the convected velocities, in which the angular velocity appears inside the defining integrals over the element volume. In the case of iso-parametric elements, where the coordinate components are represented by use of identical interpolation functions, the dependence of the angular velocity can be moved outside the volume integrals, but for typical beam elements the different components are represented by different interpolation functions, leaving the angular velocity inside the integrals on the element level. Therefore, such formulations require recalculation and reassembly of the global matrices accounting for the inertia effects for each time step, or alternatively, reorganization in terms of several auxiliary mass matrices [1].

For large-deformation problems the co-rotating formulation, originally proposed by Belytschko and co-workers [6,7], is often applied. This introduces a reference system that closely follows the rigid body motion of each finite element as opposed to the floating reference frame formulation, where a single reference frame is used for all or a group of elements in the structure. This allows for incremental procedures using non-isoparametric elements in terms of small rotations, while the non-linearities are accounted for by rotation of the local frames. However, this requires that changes in elastic forces due to finite rotations are represented correctly, which in the three-dimensional case is a

* Corresponding author. Address: Department of Mechanical Engineering, Technical University of Denmark, Nils Koppels Allé, Building 403, DK-2800 Kgs. Lyngby, Denmark.
E-mail addresses: sk@mek.dtu.dk (S. Krenk), mbni@mek.dtu.dk (M.B. Nielsen).

0045-7825/$ - see front matter © 2011 Elsevier B.V. All rights reserved.
doi:10.1016/j.cma.2011.11.014

non-trivial task. Consistent tangential stiffness formulations can be found in [8,9]. In [6] a convected coordinate approach is proposed for dynamic analysis under the assumption that the nodal forces are self-equilibrating. However, this condition leads to a very sensitive iteration scheme, which for small out-of-balance forces may lead to instabilities. The work has been further developed in [10], where the Cauchy stress tensor is introduced for evaluating the internal work in connection with an energy conserving integration scheme, and in [11] where a linear beam theory in the local frame is used under a small-strain assumption. Common for these approaches is that the kinetic energy is evaluated in the initial frame, while the elastic energy is derived, first in the local frame, and then transformed into the global frame using the kinematic relationship. This leads to an uncoupled form of the inertia terms and the non-linearities only appear in the transformation of the displacement components between local and global frame.

In a global frame non-linear kinematics must be used and the inertia terms appear directly [12]. These methods are well-established for iso-parametric elements, where they lead to a constant mass matrix. However, formulations involving finite rotations become considerably more complicated due to the intrinsic nonlinear nature of the parametrization of rotations. This problem is circumvented by the absolute nodal coordinate formulation [1,13,14]. The crucial step is the use of slopes as nodal coordinates instead of rotation parameters, leading to Hermitean element interpolation for beams and plates with properties similar to iso-parametric elements. The absolute nodal coordinate formulation therefore leads to a constant mass matrix, while the elastic forces are nonlinear functions of the element coordinates.

An important aspect is the integration of the dynamic equations, for which conservative methods based on an integrated form of the equations of motion have been the subject of extensive research over the last two decades. The original form was presented for rigid body dynamics by Simo and Wong [15] and extended to non-linear elastodynamics by Simo and co-workers in terms of a midpoint state of internal forces [16,17]. The basic principle has been generalized to non-linear elasticity via the concept of a finite derivative by Gonzalez [18]. An attractive formulation has been developed for linear elastic models in terms of Green strains in which the integral of the internal forces over a time step is represented by the mean value of end-point states plus an extra term involving the increment of the geometric stiffness [19]. In these methods algorithmic damping may be incorporated by forward weighting of the mean value terms as demonstrated in [20] and extended to high-frequency damping in [21].

In the present paper the conservative time integration algorithm for translation-based solid elements in a rotating frame of reference presented in [22] is extended to beam elements including finite rotations of moderate magnitude. The equations of motion are formulated in a hybrid state-space format in terms of local displacements and absolute velocities. This leads to a simple and direct form of the state-space equations of motion. The classic rotating frame formulation of dynamics in terms of local displacements and local velocities leads to a vibration eigenvalue problem with a somewhat artificial stiffness format of the momentum equation [24–26]. Furthermore, the classic approach, in which the local velocity is obtained by time differentiation of the local displacement at a generic point, leads to representation of Coriolis and centrifugal terms in which the angular velocity of the frame appears within the defining element integrals. In contrast, the present formulation makes an appeal to Hamiltonian mechanics in which momentum and displacement are treated identically. Therefore the displacement and the velocity defined at the nodes are represented by use of identical interpolation functions. Hereby, all inertial effects are described by the classic mass matrix, and operations using the angular velocity of the frame are applied to the assembled mass matrix.

In Section 2 the kinematic relations between the local displacements and the local components of the absolute velocities are established. The equations are collected in a compact block matrix/vector format, combining the translation and the rotation degrees of freedom. Furthermore, the independent interpolation of local displacements and absolute velocities is introduced. In Section 3 the equations of motion are derived from Lagrange's equations and combined with the kinematic equation into the hybrid state-space format. This constitutes the basis for the development of the integration algorithm, that is developed in Section 4. A simple consistent algorithmic dissipation is introduced via the local energy balance equation. The integration algorithm takes a particularly simple form for elements with quadratic kinematics, and this form is summarized in Section 5. Section 6 gives a brief presentation of a method for constructing structural elements with consistent quadratic kinematics from the corresponding linearized elements with geometric stiffness based on the initial stress formulation. Finally, numerical examples illustrating the accuracy and the conservation and damping properties of the algorithm are presented in Section 7.

2. Hybrid state-space

The equations of motion can be established using a configuration as illustrated in Fig. 1. The $\{\underline{x}_1,\underline{x}_2,\underline{x}_3\}$-coordinate system represents a fixed global frame of reference, while the $\{x_1,x_2,x_3\}$-coordinate system represents a rotating frame of reference in which the structure is described.

Let a discretized beam model be described via N nodes with coordinates $\underline{\mathbf{x}}_1,\ldots,\underline{\mathbf{x}}_N$ in the fixed global frame of reference and coordinates $\mathbf{x}_1,\ldots,\mathbf{x}_N$ in the local rotating frame of reference. For simplicity of notation the origin of the rotating frame coincides with the origin of the fixed frame of reference. Hereby the transformation between the position $\mathbf{x}_j$ and the absolute position $\underline{\mathbf{x}}_j$ can be expressed by a rotation in the form

$$\underline{\mathbf{x}}_j = \mathbf{R}\mathbf{x}_j, \tag{1}$$

where $\mathbf{R}$ defines a proper orthonormal tensor $\mathbf{R}^T\mathbf{R} = \mathbf{I}$, whose columns contain the global components of the rotating frame axis unit vectors $\mathbf{R} = [\hat{\mathbf{x}}_1, \hat{\mathbf{x}}_2, \hat{\mathbf{x}}_3]$. The absolute velocity components are determined from time differentiation as

$$\underline{\mathbf{v}}_j = \mathbf{R}\dot{\mathbf{x}}_j + \dot{\mathbf{R}}\mathbf{x}_j \tag{2}$$

and the corresponding local frame components follow by pre-multiplication with $\mathbf{R}^T$,

$$\mathbf{v}_j = \mathbf{R}^T\underline{\mathbf{v}}_j = \dot{\mathbf{x}}_j + \mathbf{R}^T\dot{\mathbf{R}}\mathbf{x}_j. \tag{3}$$

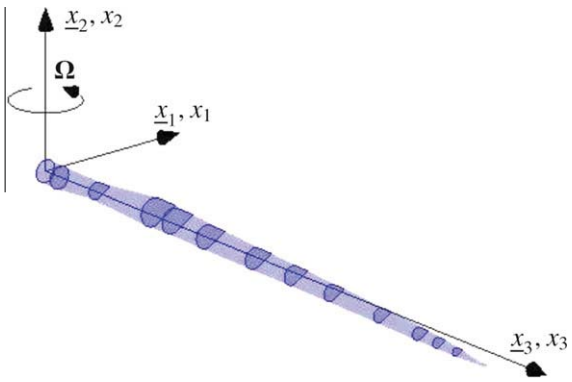

Fig. 1. Beam structure in local frame x_1, x_2, x_3 rotating with angular velocity $\boldsymbol{\Omega}$.

The product of the rotation matrices in the last term defines the local components of the angular velocity vector $\boldsymbol{\Omega}$ trough the relation,

$$\boldsymbol{\Omega}\times = \widetilde{\boldsymbol{\Omega}} = \mathbf{R}^T\dot{\mathbf{R}}, \tag{4}$$

where $\widetilde{\boldsymbol{\Omega}}$ denotes the skew-symmetric matrix representing the cross-product with the angular velocity vector $\boldsymbol{\Omega} = [\Omega_1\ \Omega_2\ \Omega_3]^T$,

$$\widetilde{\boldsymbol{\Omega}} = \begin{bmatrix} 0 & -\Omega_3 & \Omega_2 \\ \Omega_3 & 0 & -\Omega_1 \\ -\Omega_2 & \Omega_1 & 0 \end{bmatrix}. \tag{5}$$

When this is inserted into (3), the velocity relation takes the generic form

$$\mathbf{v}_j = D_t\mathbf{x}_j = (\partial_t + \widetilde{\boldsymbol{\Omega}})\mathbf{x}_j, \tag{6}$$

where ∂_t is the partial time derivative, and the convective contribution due to the angular velocity of the local frame is included in the absolute derivative D_t. This provides the basis for interpolation of translation based elements, in which the displacements are described entirely in terms of nodal translations [22]. However, for elements such as beam elements that include rotational degrees of freedom a modification is required.

For three-dimensional elements with finite rotations of moderate magnitude the configuration can be described by three translational and three rotation degrees of freedom the local configuration of node j is described by the six component format,

$$\boldsymbol{x}_j^T = [\mathbf{x}^T, \boldsymbol{\varphi}^T]_j = [x_1, x_2, x_3, \varphi_1, \varphi_2, \varphi_3]_j. \tag{7}$$

The rotations are parameterized in terms of the three-component pseudo-vector format

$$\boldsymbol{\varphi} = \varphi\mathbf{n}, \tag{8}$$

where φ denotes the angle of rotation around the direction unit vector $\mathbf{n}$, see e.g. [9]. In the following derivations it is convenient to represent the nodal position vector in terms of the initial position $\mathbf{x}_j^0$ and the local displacements $\mathbf{u}_j$,

$$\mathbf{x}_j = \mathbf{x}_j^0 + \mathbf{u}_j. \tag{9}$$

The translational velocity contribution due to the rotation of the local frame follows from (6), while the angular velocity of the local frame constitutes an additive contribution to the local angular velocity, which for moderate local rotations is represented as $\dot{\boldsymbol{\varphi}}_j$. Thus the global six-component velocity vector is expressed as

$$\boldsymbol{v}_j = \begin{bmatrix} \dot{\mathbf{u}}_j + \widetilde{\boldsymbol{\Omega}}\mathbf{x}_j \\ \dot{\boldsymbol{\varphi}}_j + \boldsymbol{\Omega} \end{bmatrix}, \tag{10}$$

where the effect of the rotation on the global velocity appears via extra terms containing the angular velocity of the frame in the form $\widetilde{\boldsymbol{\Omega}}$ and $\boldsymbol{\Omega}$, respectively.

2.1. Interpolation

The generalized local position vectors for the N nodes in the structure are conveniently organized as

$$\boldsymbol{x}^T = [\boldsymbol{x}_1^T, \boldsymbol{x}_2^T, \ldots, \boldsymbol{x}_N^T], \tag{11}$$

where $\boldsymbol{x}_j^T = \left[\mathbf{x}_j^T, \boldsymbol{\varphi}_j^T\right]$ contain the spatial position and orientation, respectively, for node j. The system format for the absolute velocity vector is organized in the similar form

$$\boldsymbol{v}^T = [\boldsymbol{v}_1^T, \boldsymbol{v}_2^T, \ldots, \boldsymbol{v}_N^T], \tag{12}$$

where the N nodal velocity vectors $\boldsymbol{v}_j$ are determined from (10). The system format for the absolute velocity can then be expressed in terms of the generalized nodal position vector $\boldsymbol{x}$, its time derivative $\dot{\boldsymbol{x}}$ and an additive contribution to the rotational degrees of freedom

$$\boldsymbol{v} = D_t\boldsymbol{x} + \boldsymbol{\Omega}_C = \dot{\boldsymbol{x}} + \widetilde{\boldsymbol{\Omega}}_D\boldsymbol{x} + \boldsymbol{\Omega}_C. \tag{13}$$

The block matrices $\widetilde{\boldsymbol{\Omega}}_D$ and $\boldsymbol{\Omega}_C$ are introduced as

$$\widetilde{\boldsymbol{\Omega}}_D = \begin{bmatrix} \widetilde{\boldsymbol{\Omega}} & & \\ & \mathbf{0} & \\ & & \ddots \end{bmatrix}, \quad \boldsymbol{\Omega}_C = \begin{bmatrix} \mathbf{0} \\ \boldsymbol{\Omega} \\ \vdots \end{bmatrix} \tag{14}$$

where the block matrices $\lceil\widetilde{\boldsymbol{\Omega}}\ \mathbf{0}\rfloor$ and $[\mathbf{0}^T\ \boldsymbol{\Omega}^T]^T$ are repeated for each node of the structure. The subscript D indicates an N-time repeated block diagonal form and the subscript C indicates a N-time stacked column format, respectively. In this way the inertia effects associated with translations are accounted for by the matrix $\widetilde{\boldsymbol{\Omega}}_D$, while the matrix $\boldsymbol{\Omega}_C$ accounts for the rotational part.

A crucial step in the finite element formulation is the shape function interpolation of the motion of an arbitrary internal point with material coordinate ξ. The interpolation of the nodal positions is expressed as

$$\mathbf{x}_\xi = \mathbf{N}(\xi)\boldsymbol{x}, \tag{15}$$

where $\mathbf{N}(\xi)$ denotes a suitable interpolation in terms of the internal coordinate ξ. Traditionally, the global velocities have been obtained from the interpolated displacement at each point of the structure. This leads to a form, in which the convective term is represented via the product $\widetilde{\boldsymbol{\Omega}}\mathbf{N}(\xi)$. When forming the mass matrix this term leaves the system rotation matrix $\widetilde{\boldsymbol{\Omega}}$ inside the integration of the element mass matrices. In case of variable angular rotation velocity $\boldsymbol{\Omega}$ the global inertial matrices will then have to be reassembled. Alternatively, the mass matrix can be reorganized into several separate matrices as explained e.g. in [1]. In the special case of isoparametric elements with translation degrees of freedom the order of the factors can be interchanged to give the interpolation of the convection velocity in the form $\mathbf{N}(\xi)\widetilde{\boldsymbol{\Omega}}_D$, see e.g. [22]. A general solution to this problem follows from the basic structure of Hamiltonian mechanics, where displacement and velocity – in the form of momentum – have the same status. In the present context this amounts to representation of local displacements and global velocities by their nodal values, with internal element values obtained by use of identical interpolation schemes. According to this principle the internal local velocity is represented as

$$\mathbf{v}_\xi = \mathbf{N}(\xi)\boldsymbol{v} = \mathbf{N}(\xi)[(\partial_t + \widetilde{\boldsymbol{\Omega}}_D)\boldsymbol{x} + \boldsymbol{\Omega}_C]. \tag{16}$$

This format, with identical interpolation of local generalized displacements and local components of the absolute velocity, constitutes a consistent generalization of the special case of isoparametric elements, where it follow by direct matrix manipulations [22]. In addition to its close link to the basic principle of Hamiltonian mechanics this format also leads to considerable simplifications in the computational procedures by placing the angular velocity of the frame of reference outside the global system matrices.

3. Equations of motion

The equations of motion are conveniently derived from Lagrange's equations. In standard notation $d\dot{\boldsymbol{u}}$ is in column format, and it then follows from the scalar nature of the increment of the kinetic energy $dT = (\partial T/\partial\dot{\boldsymbol{u}})d\dot{\boldsymbol{u}}$ that the partial derivative $\partial T/\partial\dot{\boldsymbol{u}}$ is in row format. Thus, the equations of motion are obtained from Lagrange's equations in the form

$$\frac{d}{dt}\left(\frac{\partial T}{\partial\dot{\boldsymbol{u}}^T}\right) - \frac{\partial T}{\partial\boldsymbol{u}^T} + \frac{\partial G}{\partial\boldsymbol{u}^T} = \boldsymbol{f} \tag{17}$$

in terms of the kinetic energy $T(\boldsymbol{v})$ and an elastic potential $G(\boldsymbol{u})$, where $\boldsymbol{f}$ contains the external generalized forces. The kinetic energy is determined by integration of the specific kinetic energy in terms of absolute velocities (16) over the volume of the body. As the interpolation refers to initial geometry, this leads to the form

$$T = \frac{1}{2}\boldsymbol{v}^T\mathbf{M}\boldsymbol{v} \tag{18}$$

in terms of the classic mass matrix $\mathbf{M}$, which is constant in the present application. The effect of rotation of the local frame of reference is implicitly accounted for via the representation of the absolute velocity vector $\mathbf{v}$. The first term in Lagrange's equations is determined from the time derivative of the term

$$\frac{\partial T}{\partial \dot{\boldsymbol{u}}} = \boldsymbol{v}^T\mathbf{M}\frac{\partial \boldsymbol{v}}{\partial \dot{\boldsymbol{u}}} = \boldsymbol{v}^T\mathbf{M}. \tag{19}$$

For a constant mass matrix $\mathbf{M}$ the column format of the time derivative is

$$\frac{d}{dt}\left(\frac{\partial T}{\partial \dot{\boldsymbol{u}}^T}\right) = \mathbf{M}\dot{\boldsymbol{v}}. \tag{20}$$

The second term of Lagrange's equation follows from

$$\frac{\partial T}{\partial \boldsymbol{u}} = \boldsymbol{v}^T\mathbf{M}\frac{\partial \boldsymbol{v}}{\partial \boldsymbol{u}} = \boldsymbol{v}^T\mathbf{M}\widetilde{\boldsymbol{\Omega}}_D, \tag{21}$$

where the partial derivatives $\partial\boldsymbol{v}/\partial\boldsymbol{u}$ are obtained from (13).

Finally, the third term is identified as the generalized internal forces. Assuming elastic material properties, the generalized internal forces $\boldsymbol{g}(\boldsymbol{u})$ follow as the displacement derivative of the elastic potential $G(\boldsymbol{u})$,

$$\boldsymbol{g}(\boldsymbol{u}) = \frac{dG(\boldsymbol{u})}{d\boldsymbol{u}^T}. \tag{22}$$

This gives the dynamic equations of motion in the form

$$(\partial_t + \widetilde{\boldsymbol{\Omega}}_D)\mathbf{M}\boldsymbol{v} + \boldsymbol{g}(\boldsymbol{u}) = \boldsymbol{f}, \tag{23}$$

where the overall rotation of the rotating frame is accounted for by the convective time differentiation $D_t = \partial_t + \widetilde{\boldsymbol{\Omega}}_D$ and the absolute velocity (13). Traditionally this non-linear second order differential equation is solved by collocation-based integration algorithms such as Newmark or generalized α-methods, in which approximate expressions are used to express local displacement and velocity increments in combination of matching the equations of motion at discrete points in time. This formulation leads to undesirable approximations in the representation of gyroscopic and centrifugal forces, and also has some inconsistencies in the representation of material and algorithmic damping, see e.g. [23]. In the following the hybrid state space formulation introduced in [22] for translation-based iso-parametric elements is extended to elements with rotation degrees of freedom, and an improved basis for algorithmic damping presented.

3.1. Hybrid state-space format

The hybrid state-space variables consist of the *local* node displacements $\boldsymbol{u}$ and the *absolute* node velocities $\boldsymbol{v}$. These state-space variables are governed by a kinematic equation defining the velocity and a dynamic equation determining the motion. The kinematic equation is conveniently expressed in terms of the generalized displacement $\boldsymbol{u}$ and the generalized initial position vector $\boldsymbol{x}_0$ from (9),

$$\boldsymbol{v} = (\partial_t + \widetilde{\boldsymbol{\Omega}}_D)\boldsymbol{u} + \widetilde{\boldsymbol{\Omega}}_D\boldsymbol{x}_0 + \boldsymbol{\Omega}_C. \tag{24}$$

This equation has considerable similarity with the dynamic equation of motion (23), and the two equations are conveniently combined in the following block-matrix format

$$\begin{bmatrix} \mathbf{0} & \mathbf{M} \\ -\mathbf{M} & \mathbf{0} \end{bmatrix}\begin{bmatrix} \dot{\boldsymbol{u}} \\ \dot{\boldsymbol{v}} \end{bmatrix} + \begin{bmatrix} \boldsymbol{g}(\boldsymbol{u}) + \widetilde{\boldsymbol{\Omega}}_D\mathbf{M}\boldsymbol{v} \\ \mathbf{M}\widetilde{\boldsymbol{\Omega}}_D^T\boldsymbol{u} + \mathbf{M}\boldsymbol{v} \end{bmatrix} = \begin{bmatrix} \boldsymbol{f} \\ -\mathbf{M}\left(\widetilde{\boldsymbol{\Omega}}_D^T\boldsymbol{x}_0 - \boldsymbol{\Omega}_C\right) \end{bmatrix}, \tag{25}$$

where the external load and the part of the convective terms associated with the initial position are collected at the right hand side of the equations. On the left hand side the block matrix associated with the time derivatives is anti-symmetric, while the inertial contributions in the second block matrix exhibit symmetry. It is noted that all inertia effects related to the motion of the local frame are accounted for via the gyroscopic term $\widetilde{\boldsymbol{\Omega}}_D\mathbf{M}$ and its transpose. Therefore the angular acceleration as well as quadratic terms in angular velocity, associated with centrifugal forces, are accounted for implicitly. In the classic formulation in terms of the generalized local displacement $\boldsymbol{u}$ and its time derivative $\dot{\boldsymbol{u}}$ [25,26], a similar structure in terms of anti-symmetric and symmetric block matrices is obtained by expressing the second equation in a stiffness format and neglecting the angular acceleration. The present system provides a more general format and preserves the interpretation of the second equation as a kinematic relation in terms of the momentum of the system.

The energy balance is conveniently derived directly from the hybrid state-space format (25) by pre-multiplication with $[\dot{\boldsymbol{u}}^T, \dot{\boldsymbol{v}}^T]$. This leads to the scalar equation

$$\dot{\boldsymbol{u}}^T\boldsymbol{g}(\boldsymbol{u}) + \dot{\boldsymbol{v}}^T\mathbf{M}\boldsymbol{v} + \dot{\boldsymbol{x}}^T\widetilde{\boldsymbol{\Omega}}_D\mathbf{M}\boldsymbol{v} - \dot{\boldsymbol{v}}^T\mathbf{M}(\widetilde{\boldsymbol{\Omega}}_D\boldsymbol{x} + \boldsymbol{\Omega}_C) = \dot{\boldsymbol{u}}^T\boldsymbol{f}. \tag{26}$$

The first two terms are recognized as the time derivative of the elastic potential $G(\boldsymbol{u})$ and the kinetic energy of the absolute motion. When the time-derivative of the angular velocity terms are accounted for, the latter two terms can similarly be integrated as

$$\frac{d}{dt}\left\{\frac{1}{2}\boldsymbol{v}^T\mathbf{M}\boldsymbol{v} - \boldsymbol{v}^T\mathbf{M}(\widetilde{\boldsymbol{\Omega}}_D\boldsymbol{x} + \boldsymbol{\Omega}_C) + G(\boldsymbol{u})\right\} + \boldsymbol{v}^T\mathbf{M}(\dot{\widetilde{\boldsymbol{\Omega}}}_D\boldsymbol{x} + \dot{\boldsymbol{\Omega}}_C) = \dot{\boldsymbol{u}}^T\boldsymbol{f}. \tag{27}$$

When $\boldsymbol{v}$ is substituted from the kinematic equation (24), the linear terms in $\widetilde{\boldsymbol{\Omega}}_D$ and $\boldsymbol{\Omega}_C$ are canceled by the second term and the energy equation takes the form

$$\frac{d}{dt}\left\{\frac{1}{2}\dot{\boldsymbol{u}}^T\mathbf{M}\dot{\boldsymbol{u}} - \frac{1}{2}(\widetilde{\boldsymbol{\Omega}}_D\boldsymbol{x} + \boldsymbol{\Omega}_C)^T\mathbf{M}(\widetilde{\boldsymbol{\Omega}}_D\boldsymbol{x} + \boldsymbol{\Omega}_C) + G(\boldsymbol{u})\right\} + \boldsymbol{v}^T\mathbf{M}(\dot{\widetilde{\boldsymbol{\Omega}}}_D\boldsymbol{x} + \dot{\boldsymbol{\Omega}}_C) = \dot{\boldsymbol{u}}^T\boldsymbol{f}. \tag{28}$$

This constitutes the local form of the energy balance equation. The rotation of the local frame is accounted for by a potential due to the centrifugal forces which is included inside the braces, and a term containing the angular acceleration of the local frame. It is noted that even for a stationary rotating system, the work performed by the centrifugal forces, leads to a modification of the local energy potential.

4. Integration algorithm

The hybrid state-space format (25) is particularly suitable for the development of an accurate and efficient algorithm for integration of the equations of motion in a rotating frame of reference. First the increments of the hybrid state-space variables $[\Delta\mathbf{u}^T, \Delta\mathbf{v}^T]$ are determined by integration over a time interval $h = t_{n+1} - t_n$.

$$\begin{bmatrix} \mathbf{0} & \mathbf{M} \\ -\mathbf{M} & \mathbf{0} \end{bmatrix}\begin{bmatrix} \Delta\boldsymbol{u} \\ \Delta\boldsymbol{v} \end{bmatrix} + \int_h \begin{bmatrix} \boldsymbol{g}(\boldsymbol{u}) + \widetilde{\boldsymbol{\Omega}}_D\mathbf{M}\boldsymbol{v} \\ \mathbf{M}(\widetilde{\boldsymbol{\Omega}}_D^T\boldsymbol{x} - \boldsymbol{\Omega}_C) + \mathbf{M}\boldsymbol{v} \end{bmatrix} dt = \int_h \begin{bmatrix} \boldsymbol{f} \\ \mathbf{0} \end{bmatrix} dt. \tag{29}$$

It is noted that the right hand side accounting for the initial position $\boldsymbol{x}_0$ has been absorbed in the term for the current $\boldsymbol{x}$. The involved integral terms are initially expressed in terms of 'suitable mean

values' representing the integral, which has been denoted by the asterisk.

$$\begin{bmatrix} \mathbf{0} & \mathbf{M} \\ -\mathbf{M} & \mathbf{0} \end{bmatrix} \begin{bmatrix} \Delta\boldsymbol{u} \\ \Delta\boldsymbol{v} \end{bmatrix} + h \begin{bmatrix} \boldsymbol{g}(\boldsymbol{u})_* + (\widetilde{\boldsymbol{\Omega}}_D \mathbf{M}\boldsymbol{v})_* \\ \Big(\mathbf{M}(\widetilde{\boldsymbol{\Omega}}_D^T\boldsymbol{x} - \boldsymbol{\Omega}_C)\Big)_* + (\mathbf{M}\boldsymbol{v})_* \end{bmatrix} = h \begin{bmatrix} \boldsymbol{f}_* \\ \mathbf{0} \end{bmatrix}. \tag{30}$$

The 'suitable mean values' are then determined such that the discrete version of energy balance represents the corresponding continuous balance.

The absolute velocity integral is represented by its mean value $h\bar{\boldsymbol{v}}$. Representative values for the gyroscopic terms are determined from the finite energy balance to be represented by the mid-point rule in both factors, whereby

$$(\widetilde{\boldsymbol{\Omega}}_D \mathbf{M}\boldsymbol{v})_* = \overline{\widetilde{\boldsymbol{\Omega}}}_D \mathbf{M}\bar{\boldsymbol{v}}, \quad \Big(\mathbf{M}\Big(\widetilde{\boldsymbol{\Omega}}_D^T\boldsymbol{x} - \boldsymbol{\Omega}_C\Big)\Big)_* = \mathbf{M}(\overline{\widetilde{\boldsymbol{\Omega}}}_D^T\bar{\boldsymbol{x}} - \overline{\boldsymbol{\Omega}}_C). \tag{31}$$

In the absence of an external load potential the external force $\boldsymbol{f}_*$ is approximated by its arithmetic mean value $\bar{\boldsymbol{f}}$. If a potential is available, a finite derivative can be used, [18]. When this is introduced into the discretized hybrid state-space equation (30), they take the form

$$\begin{bmatrix} \mathbf{0} & \mathbf{M} \\ -\mathbf{M} & \mathbf{0} \end{bmatrix} \begin{bmatrix} \Delta\boldsymbol{u} \\ \Delta\boldsymbol{v} \end{bmatrix} + h \begin{bmatrix} \boldsymbol{g}(\boldsymbol{u})_* + \overline{\widetilde{\boldsymbol{\Omega}}}_D \mathbf{M}\bar{\boldsymbol{v}} \\ \mathbf{M}\overline{\widetilde{\boldsymbol{\Omega}}}_D^T\bar{\boldsymbol{u}} + \mathbf{M}\bar{\boldsymbol{v}} \end{bmatrix} = h \begin{bmatrix} \bar{\boldsymbol{f}} \\ -\mathbf{M}\Big(\overline{\widetilde{\boldsymbol{\Omega}}}_D^T\boldsymbol{x}_0 - \overline{\boldsymbol{\Omega}}_C\Big) \end{bmatrix}. \tag{32}$$

For elastic material behavior the internal force term $\boldsymbol{g}(\boldsymbol{u})_*$ is the finite derivative of the elastic potential $G(\boldsymbol{u})$ [18],

$$\Delta G(\boldsymbol{u}) = \Delta\boldsymbol{u}^T \boldsymbol{g}(\boldsymbol{u})_*. \tag{33}$$

For linear elasticity with non-linear Green strain the finite derivative corresponds to using stresses and strains corresponding to a mean state [16]. When using a quadratic format for the generalized strains in the present problem, as explained in Section 6, the internal force term can be recast into the mean value of the internal forces at t_n and t_{n+1} plus an extra term,

$$\boldsymbol{g}(\boldsymbol{u})_* = \frac{1}{2}[\boldsymbol{g}_{n+1} + \boldsymbol{g}_n] - \frac{1}{4}\Delta\mathbf{K}_g\Delta\boldsymbol{u}, \tag{34}$$

where $\Delta\mathbf{K}_g$ is the increment of the geometric stiffness matrix [19]. The advantage of this formulation is that it is in global form and avoids the introduction of a mean state at the element level.

4.1. Discrete energy balance

The energy balance equation for the discretized algorithm reproduces its continuous counterpart (28). It is obtained by pre-multiplication of the hybrid state-space format (32) with $[\Delta\boldsymbol{u}^T, \Delta\boldsymbol{v}^T]$. The contributions from the first matrix vanish due the skew-symmetric format, leaving the discrete energy balance equation in the form

$$\left[\frac{1}{2}\boldsymbol{v}^T\mathbf{M}\boldsymbol{v} + G(\boldsymbol{u})\right]_n^{n+1} + \Delta\boldsymbol{u}^T\overline{\widetilde{\boldsymbol{\Omega}}}_D\mathbf{M}\bar{\boldsymbol{v}} - \Delta\boldsymbol{v}^T\mathbf{M}(\overline{\widetilde{\boldsymbol{\Omega}}}_D\bar{\boldsymbol{x}} + \overline{\boldsymbol{\Omega}}_C) = \Delta\boldsymbol{u}^T\bar{\boldsymbol{f}}, \tag{35}$$

where the contributions from the diagonal terms have been identified as the increments of the absolute kinetic energy and the local elastic energy ΔG. The angular velocity is represented by its mean value and the last two terms can then be represented in incremental form

$$\left[\frac{1}{2}\boldsymbol{v}^T\mathbf{M}\boldsymbol{v} - \boldsymbol{v}^T\mathbf{M}(\overline{\widetilde{\boldsymbol{\Omega}}}_D\boldsymbol{x} + \overline{\boldsymbol{\Omega}}_C) + G(\boldsymbol{u})\right]_n^{n+1} = \Delta\boldsymbol{u}^T\bar{\boldsymbol{f}}. \tag{36}$$

When introducing the increment of the angular velocity $\Delta\boldsymbol{\Omega}$ the mean value of the angular velocity can be expressed by its value in the upper and lower limit. Hereby the energy balance equation becomes

$$\left[\frac{1}{2}\boldsymbol{v}^T\mathbf{M}\boldsymbol{v} - \boldsymbol{v}^T\mathbf{M}(\widetilde{\boldsymbol{\Omega}}_D\boldsymbol{x} + \boldsymbol{\Omega}_C) + G(\boldsymbol{u})\right]_n^{n+1} + \overline{\boldsymbol{v}^T\mathbf{M}(\Delta\widetilde{\boldsymbol{\Omega}}_D\boldsymbol{x} + \Delta\boldsymbol{\Omega}_C)} = \Delta\boldsymbol{u}^T\bar{\boldsymbol{f}}. \tag{37}$$

This equation is an integrated form of the energy balance equation (27), in which the angular acceleration is represented via its increment, $\dot{\boldsymbol{\Omega}}h = \Delta\boldsymbol{\Omega}$.

The local form of the energy balance can now be obtained by expressing the absolute velocity $\boldsymbol{v}$ in terms of the local velocity $\dot{\boldsymbol{u}}$ from (24). Hereby the discrete energy balance equation follows as

$$\left[\frac{1}{2}\dot{\boldsymbol{u}}^T\mathbf{M}\dot{\boldsymbol{u}} - \frac{1}{2}(\widetilde{\boldsymbol{\Omega}}_D\boldsymbol{x} + \boldsymbol{\Omega}_C)^T\mathbf{M}(\widetilde{\boldsymbol{\Omega}}_D\boldsymbol{x} + \boldsymbol{\Omega}_C) + G(\boldsymbol{u})\right]_n^{n+1} + \overline{\boldsymbol{v}^T\mathbf{M}(\Delta\widetilde{\boldsymbol{\Omega}}_D\boldsymbol{x} + \Delta\boldsymbol{\Omega}_C)} = \Delta\boldsymbol{u}^T\bar{\boldsymbol{f}} \tag{38}$$

after the linear terms in the angular velocity are canceled by the second term in the brackets. This closely corresponds to the continuous energy balance (28), including the term due to accelerated rotation.

4.2. Algorithmic damping

High-frequency components in any discretized signal suffer from aliasing, whereby they are displaced from their original frequency to a frequency within the range represented in the discretization. This is an undesirable side-effect of using discrete time integration, and the effect is often reduced by introducing so-called algorithmic damping into the time integration algorithm. Ideally, the goal is to remove frequency components above the Nyquist frequency. However, in practice this ideal goal is reduced to introducing a dissipation mechanism that leaves the low-frequency regime virtually unaffected, while increasing the rate of dissipation monotonically with increasing frequency. In the present context the challenge is to introduce a form of the algorithmic damping that meets these two requirements and only affects the local motion in the local frame of reference.

A suitable format for algorithmic damping can be introduced by considering the equilibrium at the stationary state, which follows from (23) by omitting the time dependent terms. This can be expressed in terms of the stationary displacement $\boldsymbol{u}_s$ in the form

$$\boldsymbol{g}(\boldsymbol{u}_s) - \widetilde{\boldsymbol{\Omega}}_D^T\mathbf{M}\widetilde{\boldsymbol{\Omega}}_D\boldsymbol{u}_s = \boldsymbol{f} + \widetilde{\boldsymbol{\Omega}}_D^T\mathbf{M}(\widetilde{\boldsymbol{\Omega}}_D\boldsymbol{x}_0 + \boldsymbol{\Omega}_C). \tag{39}$$

This equation clearly identifies the stiffness contribution from the direct action of the centrifugal forces, leading to a modification of the local energy potential, as discussed in Section 3.1. The dissipation is now introduced as a suitable fraction α of an equivalent local energy formed on the basis of local velocity and local displacement increments, assuming that the angular velocity can be represented by its mean value,

$$D = \frac{1}{2}\alpha\Big\{\Delta\dot{\boldsymbol{u}}^T\mathbf{M}\Delta\dot{\boldsymbol{u}} + \Delta\boldsymbol{u}^T\Big(\mathbf{K} - \overline{\widetilde{\boldsymbol{\Omega}}}_D^T\mathbf{M}\overline{\widetilde{\boldsymbol{\Omega}}}_D\Big)\Delta\boldsymbol{u}\Big\}. \tag{40}$$

The important points are the use of local velocity and displacement increments, and the inclusion of the centrifugal potential in the local stiffness $\mathbf{K}$. The dissipation function (40) is now expressed in terms of increments of the hybrid state-space variables,

$$D = \frac{1}{2}\alpha\Big\{(\Delta\boldsymbol{v} - \overline{\widetilde{\boldsymbol{\Omega}}}_D\Delta\boldsymbol{u})^T\mathbf{M}(\Delta\boldsymbol{v} - \overline{\widetilde{\boldsymbol{\Omega}}}_D\Delta\boldsymbol{u}) + \Delta\boldsymbol{u}^T\Big(\mathbf{K} - \overline{\widetilde{\boldsymbol{\Omega}}}_D^T\mathbf{M}\tilde{\overline{\boldsymbol{\Omega}}}_D\Big)\Delta\boldsymbol{u}\Big\}. \tag{41}$$

The quadratic terms in the angular velocity cancel, leaving the local dissipation in the form

$$D=\frac{1}{2}\alpha\Big\{\Delta\boldsymbol{v}^T\mathbf{M}\Delta\boldsymbol{v}-\Delta\boldsymbol{v}^T\mathbf{M}\overline{\widetilde{\Omega}}_D\Delta\boldsymbol{u}-\Delta\boldsymbol{u}^T\overline{\widetilde{\Omega}}_D^T\mathbf{M}\Delta\boldsymbol{v}+\Delta\boldsymbol{u}^T\mathbf{K}\Delta\boldsymbol{u}\Big\}. \tag{42}$$

This formula can be expressed in matrix format in terms of the hybrid state-space variable increment as

$$D=\frac{1}{2}\alpha[\Delta\boldsymbol{u}^T,\Delta\boldsymbol{v}^T]\begin{bmatrix}\mathbf{K} & -\overline{\widetilde{\Omega}}_D^T\mathbf{M}\\ -\mathbf{M}\overline{\widetilde{\Omega}}_D & \mathbf{M}\end{bmatrix}\begin{bmatrix}\Delta\boldsymbol{u}\\ \Delta\boldsymbol{v}\end{bmatrix}. \tag{43}$$

For a non-rotating structure this format reduces to that used in [20,21].

When the dissipation term is included in the equations of motion (32), they take the form

$$\begin{bmatrix}\frac{1}{2}\alpha h\mathbf{K} & \Big(\mathbf{I}+\frac{1}{2}\alpha h\overline{\widetilde{\Omega}}_D\Big)\mathbf{M}\\ \mathbf{M}\Big(-\mathbf{I}+\frac{1}{2}\alpha h\overline{\widetilde{\Omega}}_D^T\Big) & \frac{1}{2}\alpha h\mathbf{M}\end{bmatrix}\begin{bmatrix}\Delta\boldsymbol{u}\\ \Delta\boldsymbol{v}\end{bmatrix}+h\begin{bmatrix}\boldsymbol{g}(\boldsymbol{u})_*+\overline{\widetilde{\Omega}}_D\mathbf{M}\bar{\boldsymbol{v}}\\ \mathbf{M}\overline{\widetilde{\Omega}}_D^T\bar{\boldsymbol{u}}+\mathbf{M}\bar{\boldsymbol{v}}\end{bmatrix}=h\begin{bmatrix}\bar{\boldsymbol{f}}\\ -\mathbf{M}\Big(\overline{\widetilde{\Omega}}_D^T\boldsymbol{x}_0-\overline{\Omega}_C\Big)\end{bmatrix}. \tag{44}$$

This constitutes an energy dissipative modification of the hybrid state-space format (32), which is recovered for $\alpha=0$. It is seen that the algorithmic dissipation is introduced via symmetric terms with the common factor $\frac{1}{2}\alpha h$ in the first block matrix. These terms may be absorbed into the second matrix by replacing the equal weighting of the mean values with a forward weighting, determined by the algorithmic damping parameter α.

The present α-damping scheme can be generalized to high-frequency dissipation by use of auxiliary variables that are updated via vector relations, and therefore nearly without additional computational cost [21]. Higher order accuracy can be obtained by introducing off-diagonal block matrices $\pm\frac{1}{12}h^2\mathbf{K}$ in the first matrix in (44) in combination with additional off-diagonal damping block matrices $\mp\frac{1}{2}\alpha h\mathbf{K}$ in the second term [27]. However, this extension requires solution of the full state-space equation system of size $2n\times 2n$. The combination of improved phase accuracy and adjustable damping can also be obtained via discontinuous interpolation, using an extended format with the discontinuities represented as internal variables [28,29].

5. Hybrid state-space integration algorithm

From an algorithmic point of view it is expedient to solve the equations of motion (44) by first eliminating the velocity $\boldsymbol{v}_{n+1}$ at t_{n+1} from the first equation by use of the second, and then solving the resulting equation for the displacement increment $\Delta\boldsymbol{u}$. It is observed that the mass matrix $\mathbf{M}$ appears as a factor of all the terms of the second equation. After removing this factor this equation takes the form

$$h\Big(\bar{\boldsymbol{v}}+\frac{1}{2}\alpha\Delta\boldsymbol{v}\Big)=\Delta\boldsymbol{u}+h\overline{\widetilde{\Omega}}_D\Big(\bar{\boldsymbol{u}}+\frac{1}{2}\alpha\Delta\boldsymbol{u}\Big)+h\Big(\overline{\widetilde{\Omega}}_D\boldsymbol{x}_0+\overline{\Omega}_C\Big). \tag{45}$$

Following [9] the algorithmic dissipation is expressed in terms of the parameter

$$\kappa=1+\alpha. \tag{46}$$

The displacement and velocity mean values occurring in (45) are then expressed in terms of previous value and increment via the relations

$$\bar{\boldsymbol{u}}+\frac{1}{2}\alpha\Delta\boldsymbol{u}=\frac{1}{2}\kappa\Delta\boldsymbol{u}+\boldsymbol{u}_n,\quad \bar{\boldsymbol{v}}+\frac{1}{2}\alpha\Delta\boldsymbol{v}=\frac{1}{2}\kappa\Delta\boldsymbol{v}+\boldsymbol{v}_n \tag{47}$$

When these expressions are substituted into (45) and $\boldsymbol{u}$ is absorbed into the generalized position $\boldsymbol{x}_n$ at t_n the following compact expression for the displacement increment is obtained

$$\Delta\boldsymbol{v}=\Big(\frac{2}{\kappa h}+\overline{\widetilde{\Omega}}_D\Big)\Delta\boldsymbol{u}-\frac{2}{\kappa}\Big[\boldsymbol{v}_n-(\overline{\widetilde{\Omega}}_D\boldsymbol{x}_n+\overline{\Omega}_C)\Big] \tag{48}$$

Here the term $2/\kappa h$ has been used without the unit matrix in accordance with standard notation in the mathematics literature. When this is inserted as replacement for the velocity increment in the first equation of (44), the discretized equation for the displacement increment $\Delta\boldsymbol{u}$ takes the form

$$2\boldsymbol{g}(\boldsymbol{u})_*+\Big[\kappa\Big(\frac{2}{\kappa h}+\overline{\widetilde{\Omega}}_D\Big)\mathbf{M}\Big(\frac{2}{\kappa h}+\overline{\widetilde{\Omega}}_D\Big)+\alpha\mathbf{K}\Big]\Delta\boldsymbol{u}=(\boldsymbol{f}_{n+1}+\boldsymbol{f}_n)+2\Big(\frac{2}{\kappa h}+\overline{\widetilde{\Omega}}_D\Big)\mathbf{M}\Big[\boldsymbol{v}_n-(\overline{\widetilde{\Omega}}_D\boldsymbol{x}_n+\overline{\Omega}_C)\Big]-2\overline{\widetilde{\Omega}}_D\mathbf{M}\boldsymbol{v}_n. \tag{49}$$

A typical time step requires iterative solution of (49) for the generalized displacement increment $\Delta\boldsymbol{u}$, followed by evaluation of the generalized velocity increment $\Delta\boldsymbol{v}$ from (48).

The time integration algorithm is shown in pseudo-code format in Table 1. At the beginning of a time step a predictor for the generalized displacement increment $\Delta\boldsymbol{u}$ is formed by using the kinematic relation (48) with the assumption that the generalized velocity increment vanishes, whereby

$$\Delta\boldsymbol{u}=h\Big(\mathbf{I}+\frac{1}{2}\kappa h\overline{\widetilde{\Omega}}_D\Big)^{-1}\Big[\mathbf{v}-(\widetilde{\Omega}_D\mathbf{x}+\boldsymbol{\Omega}_C)\Big]_n. \tag{50}$$

For time steps during which the angle of rotation of the frame of reference is modest the first parenthesis can be omitted without causing essential reduction of the convergence rate. In the following step the current value of the residual of the generalized force balance is calculated. This residual is associated with an algorithmic stiffness matrix $\mathbf{K}_*$ determined from the first variation of the current displacement,

$$\delta(2\boldsymbol{g}_*+\alpha\mathbf{K}\Delta\boldsymbol{u})=\delta\Big(\boldsymbol{g}_{n+1}+\boldsymbol{g}_n-\frac{1}{2}\Delta\mathbf{K}_g\Delta\boldsymbol{u}+\alpha\mathbf{K}\Delta\boldsymbol{u}\Big)\simeq\Big(\mathbf{K}_c^{n+1}+\mathbf{K}_g^{n+1}-\frac{1}{2}\Delta\mathbf{K}_g+\alpha\mathbf{K}\Big)\delta\boldsymbol{u}, \tag{51}$$

where the first equality follows from (34) for elements with quadratic nonlinearity. When the representative stiffness matrix $\mathbf{K}$, introduced in the definition (40) of the algorithmic dissipation, is identified as the average stiffness matrix, $\mathbf{K}=\overline{\mathbf{K}}$, the algorithmic stiffness matrix follows from (51) in the form

$$\mathbf{K}_*=\mathbf{K}_c^{n+1}+\overline{\mathbf{K}}_g+\alpha\overline{\mathbf{K}}=\kappa\overline{\mathbf{K}}+\frac{1}{2}\Delta\mathbf{K}_c. \tag{52}$$

This stiffness matrix and the residual are used to solve for the sub-increment $\delta\boldsymbol{u}$, and the generalized velocity increment $\Delta\boldsymbol{v}$ then follows from the kinematic equation (48).

Table 1
Hybrid state-space algorithm for rotating structure.

(1)	Initial conditions: $\boldsymbol{u}_0$, $\boldsymbol{v}_0$
(2)	Prediction step ($n:=n+1$):
	$\Delta\boldsymbol{u}=h\Big(\mathbf{I}+\frac{1}{2}\kappa h\overline{\widetilde{\Omega}}_D\Big)^{-1}[\mathbf{v}-(\widetilde{\Omega}_D\boldsymbol{x}+\boldsymbol{\Omega}_C)]_n$
(3)	Residual calculation: $\boldsymbol{u}=\boldsymbol{u}_n+\Delta\boldsymbol{u}$
	$\mathbf{r}=2\boldsymbol{f}_*-2\boldsymbol{g}_*-\alpha\overline{\mathbf{K}}\Delta\boldsymbol{u}-\kappa(2/\kappa h+\overline{\widetilde{\Omega}}_D)\mathbf{M}(2/\kappa h+\overline{\widetilde{\Omega}}_D)\Delta\boldsymbol{u}$
	$+(4/\kappa h)\mathbf{M}\boldsymbol{v}_n-2(2/\kappa h+\overline{\widetilde{\Omega}}_D)\mathbf{M}(\overline{\widetilde{\Omega}}_D\boldsymbol{x}_n+\overline{\Omega}_C)$
(4)	Displacement sub-increment:
	$\mathbf{K}_*=\kappa\overline{\mathbf{K}}+\frac{1}{2}\Delta\mathbf{K}_c+\kappa(2/\kappa h+\overline{\widetilde{\Omega}}_D)\mathbf{M}(2/\kappa h+\bar{\widetilde{\Omega}}_D)$
	$\delta\boldsymbol{u}=\mathbf{K}_*^{-1}\mathbf{r},\quad \Delta\boldsymbol{u}=\Delta\boldsymbol{u}+\delta\boldsymbol{u}$
	If $\lvert\mathbf{r}\rvert>\varepsilon_{\mathbf{r}}$ or $\lvert\delta\boldsymbol{u}\rvert>\varepsilon_{\boldsymbol{u}}$ repeat from (3)
(5)	State vector update:
	$\Delta\boldsymbol{v}=(2/\kappa h+\overline{\widetilde{\Omega}}_D)\Delta\boldsymbol{u}-(2/\kappa)[\boldsymbol{v}_n-(\overline{\widetilde{\Omega}}_D\boldsymbol{x}_n+\overline{\Omega}_C)]$
	$\boldsymbol{u}_{n+1}=\boldsymbol{u}_n+\Delta\boldsymbol{u},\quad \boldsymbol{v}_{n+1}=\boldsymbol{v}_n+\Delta\boldsymbol{v}$
(6)	Return to (2) for new time step, or stop

For rotating beams the main effect of the rotation is often associated with the additional stiffness from the centrifugal force. If the local generalized displacements of the beam are small this enables the use of a simple two-step procedure. In the first step a generalized displacement state is determined corresponding to stationary rotation with the current angular velocity,

$$\boldsymbol{g}(\boldsymbol{u}_s) = \boldsymbol{f} - \widetilde{\boldsymbol{\Omega}}_D^T \mathbf{M}(\widetilde{\boldsymbol{\Omega}}_D \boldsymbol{x}_s + \boldsymbol{\Omega}_C). \tag{53}$$

For small displacements the stationary generalized displacements $\boldsymbol{u}_s$ can be calculated by using the constitutive matrix $\mathbf{K}_c$ with centrifugal forces based on the initial position $\boldsymbol{x}_0$,

$$\mathbf{K}_c \boldsymbol{u}_s = \boldsymbol{f} - \widetilde{\boldsymbol{\Omega}}_D^T \mathbf{M}(\widetilde{\boldsymbol{\Omega}}_D \boldsymbol{x}_0 + \boldsymbol{\Omega}_C). \tag{54}$$

The displacement field $\boldsymbol{u}_s$ is then used to determine the internal forces and the corresponding geometric stiffness matrix. In the second step the generalized displacement increment $\Delta\boldsymbol{u}$ is found from the linearized form of (49) using the a stiffness matrix formed by combining the linearized constitutive and estimated geometric stiffness. The accuracy of this approximation is illustrated in Example 7.2.

6. Beam elements with quadratic kinematics

The present formulation assumes the structure to have an elastic potential function $G(\mathbf{u})$, where $\mathbf{u}$ contains the components of the generalized displacements. For rotations of unlimited magnitude special measures must be taken to account for their non-Euclidean nature. If using a three-parameter pseudo-vector representation of rotations an extra term appears in the second variation to account for the curvature of the underlying parameter space, see e.g. [30,9]. Alternatively, a higher-dimensional parameter representation can be used in connection with constraints, e.g. the four parameter quaternion parameter representation [31], or a nine parameter representation of the components of the rotation matrix [32]. In the present context the structure is fixed in the rotating frame of reference, whereby typical local displacements are moderate. In this case considerable simplifications can be obtained by using a kinematically quadratic theory in the local frame. Kinematically quadratic beam theories have been used successfully in connection with finite rotations e.g. for post-buckling analysis by Kouhia [33] and for rotating beams by Meijaard [34]. A key point is the consistency of the structural model within its range of application. It has recently been demonstrated that the classic linearized theories for structural elements supplemented by a geometric stiffness matrix based on an initial stress formulation, typically used for stability analysis, can be extended to consistent quadratic kinematics directly at the assembled element level by using the constitutive and geometric stiffness matrices. A brief outline of the structure of this formulation is given here, while the full details are given in [35].

A structural element with generalized displacements $\boldsymbol{u}$ contains a number of rigid body modes, and the elastic energy can therefore be expressed in terms of a number of deformation modes $\boldsymbol{\gamma}$ with fewer components than the number of generalized displacements, see e.g. Sections 5.1 and 5.2 in [9]. The elastic energy of the element is of the form $G(\boldsymbol{\gamma})$, and the corresponding generalized internal forces are defined by

$$\boldsymbol{\tau} = \frac{\partial G(\boldsymbol{\gamma})}{\partial \boldsymbol{\gamma}^T}. \tag{55}$$

The generalized forces are obtained from the elastic energy by differentiation 'through' the generalized strains $\boldsymbol{\gamma}$ as

$$\boldsymbol{g} = \left(\frac{\partial \boldsymbol{\gamma}}{\partial \boldsymbol{u}}\right)^T \frac{\partial G}{\partial \boldsymbol{\gamma}^T} = \mathbf{F}^T \boldsymbol{\tau}, \tag{56}$$

where the strain gradient matrix $\mathbf{F}(\boldsymbol{u})$ is defined by

$$\mathbf{F} = \frac{\partial \boldsymbol{\gamma}}{\partial \boldsymbol{u}}. \tag{57}$$

The incremental force–displacement relation is of the form

$$d\boldsymbol{g} = \mathbf{K} d\boldsymbol{u}, \tag{58}$$

where the tangent stiffness matrix $\mathbf{K}$ follows from differentiation of (56) as

$$\mathbf{K} = \mathbf{F}^T \frac{\partial^2 G(\boldsymbol{\gamma})}{\partial \boldsymbol{\gamma}^T \partial \boldsymbol{\gamma}} \mathbf{F} + \tau_k \frac{\partial^2 \gamma_k}{\partial \boldsymbol{u}^T \partial \boldsymbol{u}}. \tag{59}$$

This relation has the well known form

$$\mathbf{K} = \mathbf{K}_c + \mathbf{K}_g, \tag{60}$$

where $\mathbf{K}_c$ represents the constitutive stiffness matrix, while $\mathbf{K}_g$ is the geometric stiffness matrix, represented as a summation of contributions from each of the equilibrium states with generalized internal force τ_k.

The theory outlined above is closed in a consistent way by assuming that the generalized strain components γ_k are quadratic functions of the generalized displacement components u_j. The strain gradient matrix $\mathbf{F}$ is then linear in the displacement components, and the matrices formed by the second derivatives of γ_k, defining the geometric stiffness, have constant components. For a linearly elastic beam element the second strain derivatives of the elastic energy are defined by a symmetric constant matrix. Thus, the beam theory with quadratic kinematics is defined completely by the elastic stiffness of the deformation modes, $\partial_{\boldsymbol{\gamma}}^T \partial_{\boldsymbol{\gamma}} G$, and the coefficient matrices $\partial_{\boldsymbol{u}}^T \partial_{\boldsymbol{u}} \gamma_k$. These matrices constitute the basis of classic linear initial stress analysis, used e.g. for stability analysis [36,37]. In the linearized initial stress formulation the stress state τ_k in the geometric stiffness is assumed in the form of initial stresses, and the strain gradient matrix $\mathbf{F}(\boldsymbol{0})$ is evaluated corresponding to the undeformed state. Thus, the defining matrices can be extracted directly from existing linearized theory. The extension to kinematically quadratic form consists in using the current state strain gradient $\mathbf{F}(\boldsymbol{u})$ and the current value of the internal stress components τ_k [35].

The present beam theory with quadratic kinematics is based on an initially straight element and an asymptotic approximation of the rotations. The range of validity of the approximation can be estimated by comparing the numerical solution of selected examples with exact analytical results in terms of elliptic integrals for an elastica, given e.g. by Mattiasson [38,39]. These results include finite displacement of a cantilever elastica loaded by a transverse force of constant direction at the tip. As an indication of the error a load corresponding to the tip inclination 0.15 gives a transverse tip displacement of $u_1 = 0.066\,L$ with an error of 0.8 pct.

7. Examples

This section presents four numerical examples. The first example illustrates the accuracy of the present procedure in relation to the eigenvalue solution of a stationary rotating blade. The second example considers an accelerated rotation of a cantilevered beam, originally introduced by Kane et al. [3]. This example illustrates the transient performance of the algorithm, and presents comparisons with fully non-linear solutions as well as the linearized formulation. The last two examples illustrate conservation properties of the algorithm and the controlled dissipation effects related to algorithmic damping in relation to a wind turbine blade and a three-bladed wind turbine rotor, respectively.

7.1. Effect of centrifugal forces on rotating blade

The accuracy of the present beam formulation and its associated geometric stiffness is illustrated considering a frequency analysis of a rotating blade for different angular velocities. The analysis is based on the numerical example presented by Maqueda et al. [40], and illustrates the capability of the present formulation to account for the effect of the centrifugal stiffening, induced by the local frame rotation, on the eigenvalue solution. The blade is modeled as a beam of length L with solid rectangular section of height h and width w, rotating with constant angular velocity Ω_0 around an axis that is orthogonal to the axis and the long side of the cross-section. The dimensions and material properties are summarized in Table 2.

The blade is modeled as a cantilever beam represented by 10 beam elements with a total of 66 degrees of freedom. A vibration analysis is carried out based on the constitutive stiffness $\mathbf{K}_c^0$ in the initial configuration plus a geometric stiffness established from the corresponding stationary rotation state $\mathbf{K}_g^0$. The eigenfrequencies for the two first flap modes and the first lag mode are shown in Table 3 for the angular velocities; $0.1\,\Omega_0, 0.2\,\Omega_0, \ldots, \Omega_0$.

For each of the three natural frequencies the table gives the results of the present analysis plus two sets of results from the benchmark study of Maqueda et al. [40]. The results marked MBS are from a non-linear theory based on the Green strains associated with large rotations of undeformed cross-sections. In [40] this formulation is considered as 'geometrically exact' and is used as reference. Of the several other beam element formulations investigated in [40] the Absolute Nodal Coordinate Formulation using an elastic line approach, here denoted ANCF, is the alternative theory that reproduces the results of the 'geometrically exact' theory most closely. It is seen that the present formulation in terms of simple explicit matrices agrees with the reference results within an accuracy of 0.1% over the full range of rotation frequencies and performs better than the various fully kinematically non-linear formulations in terms of absolute nodal coordinates, also considered in [40].

7.2. Kane's driver

This example illustrates the properties and accuracy of the hybrid state-space algorithm, and the relation between non-linear and linearized beam theory in relation to transient analysis is considered. A spin-up sequence of a prismatic beam rotating about a fixed axis is considered. The beam was originally introduced by Kane et al. [3], and has been widely adopted as a benchmark problem when modeling rotating structures, see e.g. [12,10,34], where the latter provides numerical values suitable for comparison. For the present analysis parameters corresponding to [12] have been used. These are equivalent to a beam of length $L = 10$ m with a square cross-section with side length $b = 0.0775$ m. The beam is homogeneous and isotropic elastic with parameters $E = 6.67$ GPa and $G = 2.00$ GPa, and has mass density $\rho = 200$ kg/m^3. The angular velocity is increased over a period $T_s = 15$ s to its final value $\Omega_s = 6$ rad/s according to

$$\Omega_2(t) = \begin{cases} \dfrac{\Omega_s}{T_s}\left[t - \dfrac{T_s}{2\pi}\sin\dfrac{2\pi t}{T_s}\right], & 0 \leqslant t \leqslant T_s, \\ \Omega_s, & t > T_s. \end{cases} \tag{61}$$

In the present analysis 10 elements are used with a time step $h = 0.05$ s, which is ten times larger than in [12]. The primary influence of the magnitude of the time increment is its influence on the phase error, which increases proportionally with the time for second order algorithms like the present and those used in the references.

The results for the transverse and axial tip displacement are shown in Fig. 2(a) and (b), respectively. The response is characterized by the maximum magnitude of the displacement components, occurring after about 7 s, and the behavior in the stationary state occurring after the end of the transient at $T_s = 15$ s. Numerical values for these magnitudes are collected in Table 4 for the present quadratic theory, the linearized beam theory, a fully non-linear isoparametric element with quadratic interpolation [22], and results published by Simo and Vu-Quoc [12], Downer et al. [10] and Meijaard [34]. The final axial displacement $u_3^{\text{fin}} = 5.14 \times 10^{-4}$ corresponds to the elongation in steady rotation without vibrations and is given in analytic form in [12]. This value is reproduced by the three numerical methods to within less than 0.5 pct. In the linearized initial stress results the axial displacement has been obtained by post-processing of the transverse translations and rotations at the beam element ends. The results for the axial displacement $u_3^{\min}$ at the point of maximum bending agree well between the beam formulations, while the quadratically interpolated isoparametric element shows a somewhat smaller value. The main characteristic in the problem is the transverse tip displacement, shown in the two last columns. The results for largest value $u_1^{\min}$ occurring near the middle of the transient differ by less than 0.5 pct. According to [34] the value of $u_1^{\min}$ in [12] is about 1 pct. lower, and that in [10] about 2 pct. higher. The amplitude for the transverse vibrations are slightly higher in both these references.

The evolution of the mechanical energy is illustrated in Fig. 3(a). The results agree well with the corresponding energy development obtained by a fully non-linear solid model [22]. In the algorithm the energy increment is directly related to the external work, rep-

Table 2
Parameters of rotating blade.

ρ	2699.23	kg/m^3
E	727777×10^5	N/m^2
ν	0.3	–
L	8.178698	m
w	0.33528	m
h	0.033528	m
Ω_0	27.02	rad/s

Table 3
Natural frequencies for rotating blade with varying angular velocity.

Method	Ω/Ω_0	0.0	0.1	0.2	0.3	0.4	0.5	0.6	0.7	0.8	0.9	1.0
Present	ω_1	2.64	3.95	6.37	9.00	11.67	14.36	17.05	19.74	22.44	25.14	27.84
MBS		2.64	3.95	6.37	9.00	11.67	14.35	17.04	19.74	22.44	25.13	27.83
ANCF		2.64	3.95	6.38	9.02	11.71	14.41	17.12	19.85	22.57	25.30	28.03
Present	ω_2	16.55	17.93	21.52	26.43	32.02	37.98	44.14	50.42	56.79	63.20	69.66
MBS		16.55	17.92	21.52	26.42	32.01	37.96	44.12	50.40	56.76	63.17	69.62
ANCF		16.76	18.13	21.71	26.62	32.22	38.21	44.41	50.74	57.16	63.64	70.17
Present	ω_3	26.39	26.42	26.49	26.62	26.80	27.02	27.29	27.60	27.94	28.31	28.71
MBS		26.34	26.41	26.49	26.61	26.79	27.02	27.29	27.60	27.94	28.32	28.72
ANCF		25.34	25.38	25.45	25.57	25.74	25.95	26.20	26.48	26.80	27.14	27.52

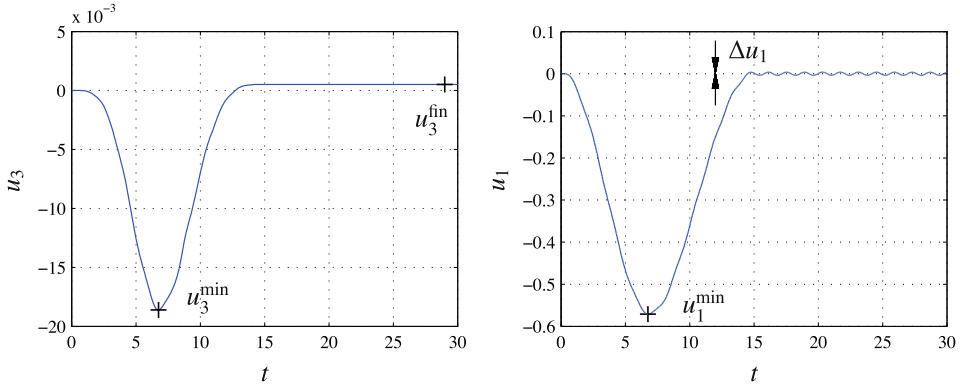

Fig. 2. (a) Axial tip displacement u_3. (b) Transverse tip displacement u_1.

Table 4
Calculated tip displacements in Kane's driver.

	N	$u_3^{\min}$	$u_3^{\text{fin}} \times 10^4$	$u_1^{\min}$	Δu_1
Quadratic	4	−0.0185	5.156	−0.5693	0.0035
	8	−0.0186	5.133	−0.5710	0.0038
Initial stress	4	−0.0187	5.159	−0.5721	0.0036
	8	−0.0188	5.147	−0.5740	0.0039
Isoparametic	8	−0.0153	5.130	−0.5639	0.0027
	16	−0.0156	5.134	−0.5701	0.0036
Refs. [12], [34]	4	–	5.14[(a)]	−0.5739[(b)]	0.0037[(b)]

(a) refers to Ref [12].
(b) refers to Ref [34].

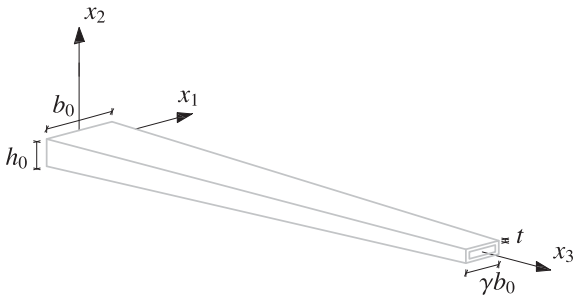

Fig. 4. Configuration of blade with linearly varying box cross-section.

resented by $\Delta \boldsymbol{u}^T \boldsymbol{f}$, where $\mathbf{f}$ is the load vector appearing on the right side of the discretized state-space equation (32). Thus, the first six components of the vector $\mathbf{f}$ represent the reactions needed to produce the imposed motion of the support. The support moment, extracted from the left side of the state-space equation (32), is shown in Fig. 3(b). The curve has a maximum around $t = 7$ s at the peak of the imposed angular acceleration and exhibits oscillations after the transient in order to maintain constant angular velocity of the support.

7.3. Rotating wind turbine blade

The basic properties of the algorithmic damping are illustrated with reference to a structure representing a simplified wind turbine blade. The blade is modeled as a tapered cantilever beam with a closed box section as illustrated in Fig. 4. The blade model is chosen in a simple parametric form to enable its use as reference.

The blade geometry is described by a parametric set of data in terms of the length L and the width $b_0 = L/15$ at the root. A constant width to height ratio $b/h = 4$ applies to all cross-sections as well as the constant wall thickness $t = b_0/50$. The width of the cross-section varies linearly along the length as described by the expression

$$b(\xi) = b_0[1 - (1-\gamma)\xi], \quad \xi = x_3/L. \tag{62}$$

The cross-section parameters are summarized in Table 5. For the present analysis the length has been chosen to $L = 50$ m and $\gamma = 0.2$. The elastic parameters are $E = 100$ GPa and $G = 20$ GPa, and the mass density is $\rho = 2000$ kg/m^3. The blade is discretized using 10 beam elements with shear flexibility determined by the flanges parallel to the load direction.

Table 5
Cross-section properties.

A	$2ht + 2bt$
I_1	$\frac{1}{2}bth^2 + \frac{1}{6}th^3$
I_2	$\frac{1}{2}htb^2 + \frac{1}{6}tb^3$
J	$(2b^2h^2t)/(b+h)$

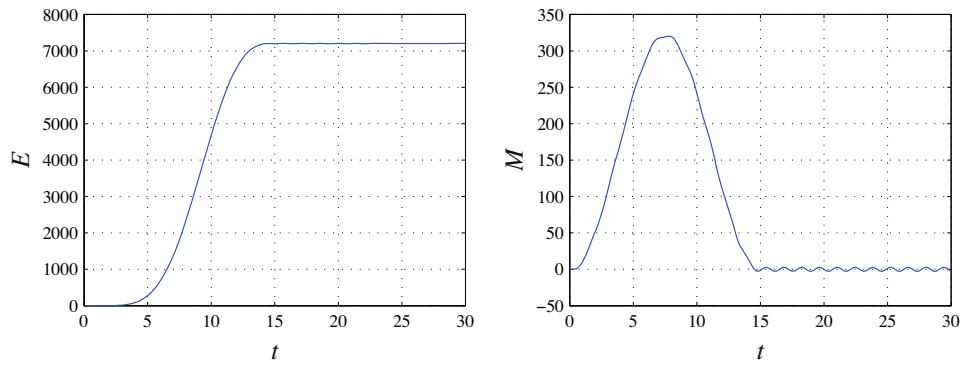

Fig. 3. (a) Mechanical energy. (b) Moment at support.

A steady state situation where the blade rotates with constant angular velocity $\Omega_2 = 2$ rad/s is considered. Local vibrations are initiated by an initial displacement field corresponding to first edge-wise mode in the steady rotating state with tip displacement $u_1^{\max} = L/10$. A time step $h = 0.02$ s is used and with an angular frequency $\omega_2 = 13.65$ rad/s this corresponds to 23 steps per vibration period.

Fig. 5 illustrates the influence of the algorithmic damping on the development of the local energy $\Delta E = E - E_s$, obtained by subtracting the energy

$$E_s = G(\boldsymbol{u}_s) - \frac{1}{2}(\widetilde{\boldsymbol{\Omega}}_D \boldsymbol{x}_s + \boldsymbol{\Omega}_C)^T \mathbf{M}(\widetilde{\boldsymbol{\Omega}}_D \boldsymbol{x}_s + \boldsymbol{\Omega}_C), \tag{63}$$

corresponding to a stationary rotation from the total mechanical energy E. The time scale is normalized with respect to the vibration period T_2 of the first edge-wise mode. Fig. 5(a) shows the undamped case corresponding to $\alpha = 0$, and it is observed that the local mechanical energy is constant to within a relative accuracy of 10^{-12}. Fig. 5(b) shows the similar damped case for $\alpha = 0.05$, indicating what appears to be exponential decay of the local mechanical energy. The algorithmic damping was introduced in a form depending only on the local motion in order not to influence the general rotation of the structure. This is illustrated in Fig. 6(a), showing the angular momentum component L_2 along the axis of rotation for the two cases described above. It is seen that the algorithmic damping leads to a decrease in the oscillations in the angular momentum, while leaving the mean value unaffected.

In the frequency interval below the aliasing limit, $\omega_k h < 1$, the damping parameter α can be linked to the modal damping ratio of the local vibration mode by the asymptotic relation $\zeta_k = \frac{1}{2}\alpha(\omega_k h)$ [21], whereby

$$\Delta E \simeq \Delta E_0 e^{-2\zeta_k \omega_k t}. \tag{64}$$

In the present example this corresponds to a damping ratio of the first edge-wise mode of $\zeta_2 = 0.0068$. The attenuation of the local vibration energy ΔE is illustrated in Fig. 6(b), clearly demonstrating the accuracy of this representation with respect to the local mechanical energy.

7.4. Three-blade rotor system

This example illustrates the effect of multiple modes on the damping of a system representing a three blade rotor. The rotor consists of three blades modeled as tapered beams as described in the previous example. The three blades are connected to the end of a flexible shaft as illustrated in Fig. 7. In order to approximate the structural behavior of a typical wind turbine rotor, the blades have been twisted corresponding to a linearly varying pitch angle with a maximum angle of $\psi_0 = 15°$. Each blade is modeled by 10 beam elements as in the previous example, while the shaft is modeled by a single beam element providing support flexibility.

The flexibility of the shaft is an important structural feature. In a three-bladed rotor with identical blades the vibration modes occur in sets of three. If the shaft is modeled as a fully rigid connection, the vibration modes for the three blades decouple and the eigenfrequencies associated with each set of modes correspond to those of a single blade. Reduction of the shaft stiffness leads to coupling of the blade modes and as a consequence the modes occur in sets of one collective mode and two 'whirling' modes. In the collective modes all blades have identical motion, while the 'whirling' modes correspond to a phase difference of $\frac{2}{3}\pi$ in the vibration of each of the three blades, corresponding to a forward and a backward whirling mode, see e.g. [41,42]. For the present analysis the shaft is represented by a solid steel cylinder of length $L_s = 1$ m and diameter $d_s = 0.5$ m with elastic parameters $E = 210$ GPa and $\nu = 0.3$ and

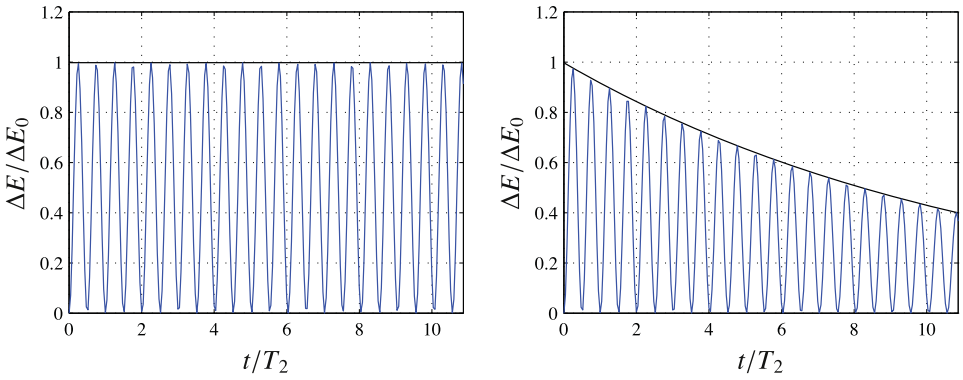

Fig. 5. Local mechanical energy: (a) $\alpha = 0$, (b) $\alpha = 0.05$. Mechanical energy (−), local kinetic energy (—).

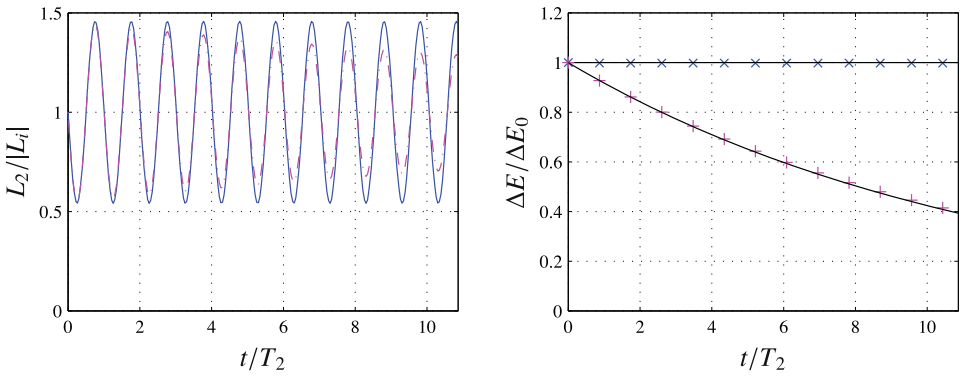

Fig. 6. (a) Angular momentum for $\alpha = 0$ (—) and $\alpha = 0.05$ (—). (b) Energy decay for $\alpha = 0$ (×) and $\alpha = 0.05$ (+), $e^{-2\zeta_2\omega_2 t}$ (−).

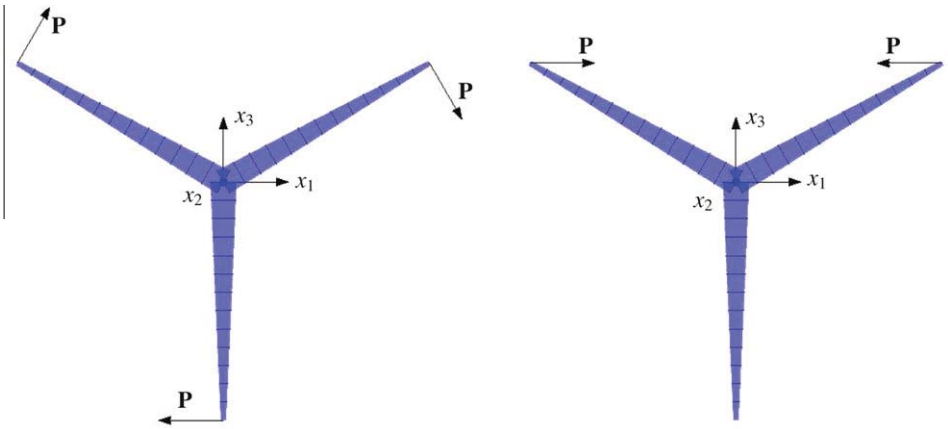

Fig. 7. Rotor configuration with initial load cases.

mass density 7850 kg/m^2. However, the torsional stiffness is increased by a factor ten in order to represent a realistic ratio between eigenfrequencies for the first edge-wise collective mode and corresponding pair of whirling modes.

A situation where the blades rotate at a realistic operating speed $\Omega_2 = 1.65$ rad/s is considered. The effect of simultaneous excitation of several modes on the damping properties is illustrated by two load cases with an initial displacement field: in Fig. 7(a) three forces $P = 10$kN are applied at the tip in the direction of the overall rotation, and in Fig. 7(b) a pair of equal but opposite forces $P = 10$ kN are applied at the tip of two blades. The first displacement field mainly excites the collective vibration mode with the lowest angular frequency of $\omega_4 = 7.84$ rad/s, with all blades performing simultaneous edge-wise displacement leading to an overall torsional motion around the shaft. The second load case is designed to excite the corresponding forward and backward whirling modes, with a slightly higher angular frequency around $\omega_{5-6} = 12.6$ rad/s. A time step of $h = 0.02$ is used, corresponding to 40 and 25 time steps per vibration period of the collective and whirling modes, respectively.

The development of the local mechanical energy ΔE in each of the two load cases is illustrated in Fig. 8(a) and (b) with $\alpha = 0.05$. This corresponds to the modal damping ratios $\zeta_4 = 0.0039$ and $\zeta_{5-6} = 0.0063$. It is seen that the present algorithmic damping is capable of distinguishing between the different modes in a more complex structure and provide the highest damping to the highest frequency mode. The contributions from higher frequency modes lead to a faster initial decay as predicted by the modal energy decay formula (64).

8. Conclusions

A time integration algorithm for flexible beams with moderate finite rotations in a rotating frame of reference has been developed in terms of hybrid state-space variables consisting of local displacements and global velocities. The formulation is an extension of [22] in which the displacement field was represented entirely in terms of nodal translations. An important feature of the present element discretization involving nodal translations and rotations is the use of identical interpolation functions for the local displacements and the global velocities. This is different from the traditional approach in which velocities are obtained via time differentiation at a generic material point. The identical interpolation is justified by the equal status of displacement and momentum in Hamiltonian mechanics, and it leads to representation of all inertial effects in terms of the classic mass matrix, with Coriolis and centrifugal effects represented via global operations on the assembled mass matrix using the angular velocity of the rotating frame.

In the hybrid state-space format a conservative time discretization is obtained by use of the mean value of the angular velocity. A simple algorithmic dissipation scheme is developed in terms of the local motion, thereby avoiding algorithmic resistance to the convective motion from rotation of the frame. The algorithmic damping scheme takes the form of simple forward weighting of the representative mean values, and degenerates to known schemes for a non-rotating structure.

The performance of the algorithm has been illustrated using a beam theory with quadratically non-linear rotations. The accuracy

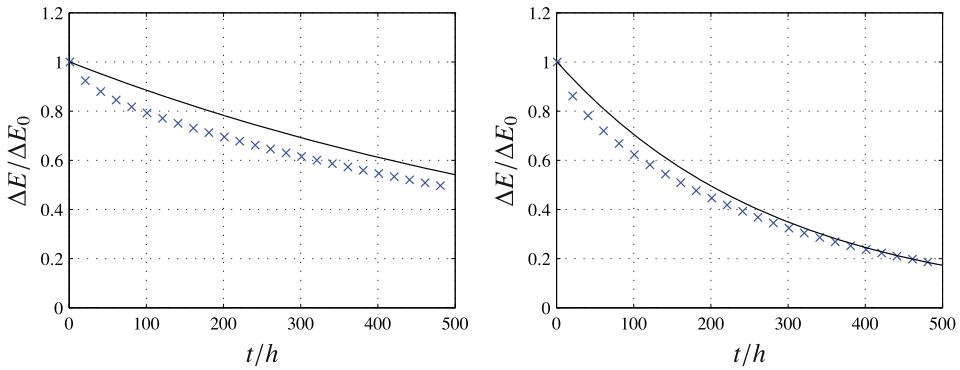

Fig. 8. (a) Energy decay for load case (a). (b) Energy decay for load case (b). $\alpha = 0.05$ (×), $e^{-2\zeta_j\omega_j t}$ (−).

of the algorithm and the conservative properties are demonstrated by examples, illustrating that the algorithmic dissipation can be approximated by an exponential decay of the local mode of vibration. The examples demonstrate that for vibrations of rotors typical of wind turbine operations the non-linearity is dominated by the geometric stiffness.

References

[1] A.A. Shabana, Dynamics of Multibody Systems, Cambridge University Press, Cambridge, 2005.
[2] J. Song, E.J. Haug, Dynamic analysis of planar flexible mechanisms, Comput. Methods Appl. Mech. Engrg. 24 (1980) 359–381.
[3] T.R. Kane, R.R. Ryan, A.K. Banerjee, Dynamics of a cantilever beam attached to a moving base, J. Guidance Control Dyn. 10 (1987) 139–151.
[4] O. Wallrapp, R. Schwertassek, Representation of geometric stiffening in multibody system simulation, Int. J. Numer. Methods Engrg. 32 (1991) 1833–1850.
[5] J. Mayo, J. Dominguez, Geometrically non-linear formulation of flexible multibody systems in terms of beam elements: geometric stiffness, Comput. Struct. 59 (1996) 1039–1050.
[6] T. Belytschko, B.J. Hsieh, M.J. Klein, Non-linear transient finite element analysis with convected co-ordinates, Int. J. Numer. Methods Engrg. 7 (1973) 255–271.
[7] T. Belytschko, L. Schwer, M.J. Klein, Large displacement, transient analysis of space frames, Int. J. Numer. Methods Engrg. 11 (1977) 65–84.
[8] M.A. Crisfield, A consistent co-rotational formulation for non-linear, three-dimensional, beam-elements, Comput. Methods Appl. Mech. Engrg. 81 (1990) 131–150.
[9] S. Krenk, Non-linear Modeling and Analysis of Solids and Structures, Cambridge University Press, Cambridge, 2009.
[10] J.D. Downer, K.C. Park, J.C. Chiou, Dynamics of flexible beams for multibody systems: a computational procedure, Comput. Methods Appl. Mech. Engrg. 96 (1992) 373–408.
[11] M. Iura, S.N. Atluri, Dynamics analysis of planar flexible beams with finite rotations by using inertial and rotating frames, Comput. Struct. 55 (1995) 453–462.
[12] J.C. Simo, L. Vu-Quoc, On the dynamics of flexible beams under large overall motions-The plane case: part I & II, J. Appl. Mech. 53 (1986) 849–863.
[13] A.A. Shabana, H. Hussien, J. Escalona, Application of the absolute nodal coordinate formulation to large rotation and large deformation problems, ASME J. Mech. Design 120 (1998) 188–195.
[14] A.A. Shabana, Computer implementation of the absolute nodal coordinate formulation for flexible multibody dynamics, Nonlinear Dyn. 16 (1998) 293–306.
[15] J.C. Simo, K.K. Wong, Unconditionally stable algorithms for rigid body dynamics that exactly preserve energy and momentum, Int. J. Numer. Methods Engrg. 31 (1991) 19–52.
[16] J.C. Simo, N. Tarnow, The discrete energy-momentum method. Conserving algorithms for nonlinear elastodynamics, Zeitschrift für Angewandte Mathematik und Physik 43 (1992) 757–792.
[17] J.C. Simo, N. Tarnow, K.K. Wong, Exact energy-momentum conserving algorithms and symplectic schemes for nonlinear dynamics, Comput. Methods Appl. Mech. Engrg. 100 (1992) 63–116.
[18] O. Gonzalez, Exact energy and momentum conserving algorithms for general models in nonlinear elasticity, Comput. Methods Appl. Mech. Engrg. 190 (2000) 1763–1783.
[19] S. Krenk, The role of geometric stiffness in momentum and energy conserving time integration, Int. J. Numer. Methods Engrg. 71 (2007) 631–651.
[20] F. Armero, I. Romero, On the formulation of high-frequency dissipative time-stepping algorithms for nonlinear dynamics, Part II, Comput. Methods Appl. Mech. Engrg. 190 (2001) 6783–6824.
[21] S. Krenk, Extended state-space time integration with high-frequency energy dissipation, Int. J. Numer. Methods Engrg. 73 (2008) 1767–1787.
[22] S. Krenk, M.B. Nielsen, Hybrid state-space time integration in a rotating frame of reference, Int. J. Numer. Methods Engrg. 87 (2011) 1301–1324.
[23] S. Krenk, Energy conservation in Newmark based time integration algorithms, Comput. Methods Appl. Mech. Engrg. 195 (2006) 6110–6124.
[24] L. Meirovitch, Computational Methods in Structural Dynamics, Sijthoff & Noordhoff, Alphen aan den Rijn, The Netherlands, 1980.
[25] L. Meirovitch, A new method of solution of the eigenvalue problem for gyroscopic systems, AIAA J. 12 (1974) 1337–1342.
[26] M. Géradin, D. Rixen, Mechanical Vibrations, Theory and Applications to Structural Dynamics, second ed., Wiley, Chichhester, 1997.
[27] S. Krenk, State-space time integration with energy control and fourth-order accuracy for linear dynamic systems, Int. J. Numer. Methods Engrg. 65 (2006) 595–619.
[28] M. Borri, C.L. Bottasso, L. Trainelli, An invariant-preserving approach to robust finite-element multi-body simulation, Zeitschrift für angewandte Mathematik und Mechanik 83 (2003) 663–676.
[29] C.L. Bottasso, L. Trainelli, An attempt at the classification of energy decaying schemes for structural and multibody dynamics, Multibody Syst. Dyn. 12 (2004) 173–185.
[30] A. Ibrahimbegović, On finite element implementation of geometrically non-linear Reissner's beam theory: three-dimensional curved beam elements, Comput. Methods Appl. Mech. Engrg. 122 (1995) 11–26.
[31] E. Zupan, M. Saje, D. Zupan, The quaternion-based three-dimensional beam theory, Comput. Methods Appl. Mech. Engrg. 198 (2009) 3944–3956.
[32] P. Betsch, P. Steinmann, Frame-indifferent beam finite elements based upon the geometrically exact beam theory, Int. J. Numer. Methods Engrg. 54 (2002) 1775–1788.
[33] R. Kouhia, On kinematical relations of spatial framed structures, Comput. Struct. 40 (1991) 1185–1191.
[34] J.F. Meijaard, Validation of flexible beam elements in dynamics programs, Non-linear Dyn. 9 (1996) 21–36.
[35] S. Krenk, Consistent quadratic kinematics for linearized structural elements with geometric stiffness, Department of Mechanical Engineering, Technical University of Denmark, submitted for Publication.
[36] K. Washizu, Variational Methods in Elasticity and Plasticity, second ed., Pergamon Press, Oxford, 1974.
[37] Z.P. Bažant, L. Cedolin, Stability of Structures, Oxford University Press, Oxford, 1991.
[38] K. Mattiasson, Numerical results from elliptic integral solutions of some elastica problems of beams and frames, Report 79:10, Department of Structural Mechanics, Chalmers University of Technology, Sweden, 1979.
[39] K. Mattiasson, Numerical results from large deflection beam and frame problems analysed by means of elliptic integrals, Int. J. Numer. Methods Engrg. 17 (1981) 145–153.
[40] L.G. Maqueda, O.A. Bauchau, A.A. Shabana, Effect of the centrifugal forces on the finite element eigenvalue solution of a rotating blade: a comparative study, Multibody Syst. Dyn. 19 (2008) 281–302.
[41] M.H. Hansen, Improved modal dynamics of wind turbines to avoid stall-induced vibrations, Wind Energy 6 (2003) 179–195.
[42] M.H. Hansen, Aeroelastic stability analysis of wind turbines using an eigenvalue approach, Wind Energy 7 (2004) 133–143.

P3

Conservative integration of rigid body motion by quaternion parameters with implicit constraints

M.B. Nielsen & S. Krenk

International Journal for Numerical Methods in Engineering,
Vol **92**:734–752, 2012.

INTERNATIONAL JOURNAL FOR NUMERICAL METHODS IN ENGINEERING
Int. J. Numer. Meth. Engng 2012; **92**:734–752
Published online 11 July 2012 in Wiley Online Library (wileyonlinelibrary.com). DOI: 10.1002/nme.4363

Conservative integration of rigid body motion by quaternion parameters with implicit constraints

M. B. Nielsen and S. Krenk*,†

Department of Mechanical Engineering, Technical University of Denmark, DK-2800 Kgs. Lyngby, Denmark

SUMMARY

An angular momentum and energy-conserving time integration algorithm for rigid body rotation is formulated in terms of the quaternion parameters and the corresponding four-component conjugate momentum vector via Hamilton's equations. The introduction of an extended mass matrix leads to a symmetric set of eight state-space equations of motion. The extra inertial parameter serves as a multiplier on the kinematic constraint, and it is demonstrated that convergence characteristics are improved by selecting this parameter somewhat larger than the inertial moments. External loads enter these equations via the set of momentum equations. Initially, the normalization of the quaternion array is introduced via a Lagrange multiplier. However, this Lagrange multiplier can be expressed explicitly in terms of the gradient of the external load potential, and elimination of the Lagrange multiplier from the final format leaves only an explicit projection applied to the external load potential gradient. An algorithm is developed by forming a finite increment of the Hamiltonian. This procedure identifies the proper selection of increments and mean values, and leads to an algorithm with conservation of momentum and energy. Implementation, conservation properties, and accuracy of the algorithm are illustrated by examples with a flying box and a spinning top. Copyright © 2012 John Wiley & Sons, Ltd.

Received 18 March 2012; Revised 3 May 2012; Accepted 5 May 2012

KEY WORDS: rigid body dynamics; quaternion parameters; conservative integration; energy conservation; time integration

1. INTRODUCTION

The motion of rigid bodies is encountered frequently in engineering, physics, and chemistry. Although the description and integration of the translation part of the motion has found a fairly conclusive form, rigid body rotation is still actively investigated. In contrast to translations, where the motion is formed by addition of incremental displacements, rotations combine in the form of products of the incremental rotation matrices. Thus, efficient and accurate integration of rotations requires that the special features associated with accumulating finite rotations are accounted for. The components of the rotation tensor constitute an orthogonal matrix and thus has only three independent components. In connection with robotics and mechanisms, it may be desirable to use the Euler angles, forming a sequence of three rotations about particular selected axes; but for general motion involving rotations, it is often preferable to describe the rotation in terms of a pseudo-vector, describing the magnitude of the rotation and direction of its axis. In particular, the magnitude may be represented in different ways, leading to various forms of the pseudo-vector representation as described, for example, in [1] and [2].

The classic methods of numerical time integration, such as the Newmark method, are based on matching of the equation of motion at specific points in time, supplemented by approximate relations

*Correspondence to: Steen Krenk, Department of Mechanical Engineering, Building 403, Nils Koppel's Alle, DK-2800 Kgs. Lyngby, Denmark.
†E-mail: sk@mek.dtu.dk

between generalized displacement, velocity, and acceleration. This line of approach is based on a full parameter representation of the motion and does not in itself account for the fact that the differential equations of rigid body rotation typically are related to a tangent space. In relation to Newmark type methods, this may be accounted for by introducing a suitable tangent space projection [3], or more directly by including the nonlinear convected form of the equations as in the algorithm of Krysl and Endres [4], in which the current rotation matrix is predicted from the last established angular velocity and acceleration, whereas the new angular velocity and acceleration are determined via the equation of motion and a kinematic difference equation. A general formulation of the Newmark scheme for rotations including the alpha-modification for high-frequency dissipation has been presented by Brüls *et al.* [5,6]. Algorithms, in which a complete time step is formed by parts using different integration rules have been developed, for example, by Krysl [7] and Nukala and Shelton [8]. A particular role is taken by algorithms based on midpoint integration, whereby the structure of the original differential equations is conserved, see for example, [9,10]. A different approach is based on an integrated form of the equations of motion, in which the equation of motion is then replaced by the increment of the angular momentum, see for example, Simo *et al.* [11,12]. By suitable integration of external loads and convection terms, these algorithms conserve momentum and energy. A particular simple form was obtained in [13] by use of the Cayley representation of the rotation, whereas conservative integration of a more general class of equations was considered by Lens *et al.* [14].

Common to the algorithms previously mentioned is the occurrence of trigonometric functions to accomplish the finite update of the rotation and the use of a local formulation to express angular velocity and in some of the cases the angular acceleration. In contrast, a fully algebraic formulation can be obtained by using a representation of the rotation tensor in terms of the four-component quaternion parameters [15–18], or by using a representation of the rotation tensor as a set of three vectors with six length and orthogonality constraints introduced via Lagrange multipliers, [19,20].

The present paper presents a compact and direct development of the Hamilton equations of motion of a rigid body based on quaternion parameters and a corresponding implicit conservative integration algorithm. The paper starts with a brief summary of kinematics in terms of quaternion parameters and then proceeds to the dynamics of a rigid body in Hamiltonian form. An essential feature of this formulation is that the extension from six Hamiltonian equations to eight because of the four-component quaternion format is accompanied by two constraint equations: a normalization condition on the quaternion parameters, and an orthogonality relation between the quaternion parameters and the corresponding momentum parameters. These conditions form an integral part of the four-component format and do not require independent representation. However, in the presence of a load potential, the corresponding derivatives in terms of the quaternion parameters must be constrained in view of the quaternion normalization condition. It is demonstrated for both the original momentum differential equations and the discretized algorithmic form that this constraint may be introduced directly into the dynamic equation of motion in the form of a projection operator on the gradient of the potential. Hereby, the algorithm takes a simple form in which the quaternion and momentum parameter increments are given by suitably formed explicit mean values securing both momentum and energy conservation. The quaternion parameter formulation has been considered recently by Betsch and Siebert [21] but in a different form, in which the Lagrange multiplier is retained in the algorithm. The discretized algorithm is derived directly from a finite increment of the Hamiltonian and takes a simple form because of elimination of the constraint Lagrange multiplier that leaves only a projection operator on the load potential gradient. The formulation makes use of an extended inertia matrix, and it is demonstrated that the auxiliary parameter in this matrix is mainly related to the quaternion constraint and should be given sufficient magnitude relative to the moments of inertia to implement this constraint with full accuracy.

2. KINEMATICS

Let the position of a point in a rigid body have the material coordinates $\boldsymbol{X}$, corresponding to the spatial coordinates $\boldsymbol{x}$. If the body is rotated about the common origin of these coordinate systems,

DOI: 10.1002/nme

the spatial coordinates are given by the relation

$$\boldsymbol{x} = \boldsymbol{R}\boldsymbol{X}, \tag{1}$$

where $\boldsymbol{R}$ is the component matrix of the rotation tensor. The rotation may be specified in terms of the rotation vector $\boldsymbol{\varphi} = \varphi\boldsymbol{n}$ with length φ representing the rotation angle and direction given by the unit vector $\boldsymbol{n}$. The rotation tensor is expressed in terms of the angle φ and the direction vector $\boldsymbol{n}$ as [22, 23],

$$\boldsymbol{R} = \cos\varphi\, \boldsymbol{I} + \sin\varphi\, \hat{\boldsymbol{n}} + (1 - \cos\varphi)\boldsymbol{n}\boldsymbol{n}^T, \tag{2}$$

where $\hat{\boldsymbol{n}}$ denotes the skew-symmetric tensor corresponding to the vector product $\boldsymbol{n}\times$. The vector has the same length in the local and in the spatial coordinate system, and thus the rotation tensor $\boldsymbol{R}$ satisfies the identity $\boldsymbol{R}^T\boldsymbol{R} = \boldsymbol{I}$, whereby $\boldsymbol{R}$ is a proper orthogonal tensor with inverse $\boldsymbol{R}^{-1} = \boldsymbol{R}^T$.

The time derivative of the rotation relation (1) gives

$$\dot{\boldsymbol{x}} = \dot{\boldsymbol{R}}\boldsymbol{X} = \dot{\boldsymbol{R}}\boldsymbol{R}^T\boldsymbol{x} = \hat{\boldsymbol{\omega}}\boldsymbol{x}, \tag{3}$$

where $\hat{\boldsymbol{\omega}}$ denotes to the skew-symmetric angular velocity matrix associated with the spatial angular velocity $\boldsymbol{\omega}$,

$$\hat{\boldsymbol{\omega}} = \boldsymbol{\omega}\times = \dot{\boldsymbol{R}}\boldsymbol{R}^T. \tag{4}$$

The local components of the skew-symmetric angular velocity tensor are obtained by a transformation involving the rotation tensor $\boldsymbol{R}$,

$$\hat{\boldsymbol{\Omega}} = \boldsymbol{R}^T\hat{\boldsymbol{\omega}}\boldsymbol{R} = \boldsymbol{R}^T\dot{\boldsymbol{R}}. \tag{5}$$

It is seen that the local components of the rotation tensor are obtained by interchanging the order of the factors in the matrix product in (4).

2.1. Quaternion parametrization of rotations

The rotation tensor $\boldsymbol{R}$ given by (1) can be expressed in homogeneous algebraic form by introducing the following four-component representation in terms of the half-angle $\frac{1}{2}\varphi$,

$$\mathbf{q}^T = \left[q_0, \boldsymbol{q}^T\right] \tag{6}$$

with the components

$$q_0 = \cos\left(\tfrac{1}{2}\varphi\right), \qquad \boldsymbol{q} = \sin\left(\tfrac{1}{2}\varphi\right)\boldsymbol{n}. \tag{7}$$

The four components $[q_0, q_1, q_2, q_3]$ are known either as the Euler parameters or the quaternion parameters. The latter is used here to be more specific. It is an important property of these parameters that they satisfy the identity

$$\mathbf{q}^T\mathbf{q} = q_0^2 + q_1^2 + q_2^2 + q_3^2 = 1. \tag{8}$$

When using the set of four-quaternion parameters, this equation appears in the form of a constraint equation. Here and in the following, three-component vectors and the corresponding 3×3 matrices are denoted by boldface italics, whereas the corresponding four-component quaternion quantities are denoted by boldface roman type.

DOI: 10.1002/nme

An important feature of the quaternion representation is that the rotation tensor $\boldsymbol{R}$ in (1) takes the following homogeneous quadratic form

$$\boldsymbol{R}(\mathbf{q}) = \begin{bmatrix} q_0^2+q_1^2-q_2^2-q_3^2 & 2(q_1q_2-q_0q_3) & 2(q_1q_3+q_0q_2) \\ 2(q_2q_1+q_0q_3) & q_0^2-q_1^2+q_2^2-q_3^2 & 2(q_2q_3-q_0q_1) \\ 2(q_3q_1-q_0q_2) & 2(q_3q_2+q_0q_1) & q_0^2-q_1^2-q_2^2+q_3^2 \end{bmatrix}. \tag{9}$$

The formula follows directly from (2) by expressing the trigonometric functions in terms of the half-angle $\frac{1}{2}\varphi$. An important property of the homogeneous quadratic quaternion parameter representation of the rotation tensor is that it can be split into the product of two matrix transformations in the form [22],

$$\boldsymbol{R}(\mathbf{q}) = \boldsymbol{H}(\mathbf{q})\boldsymbol{G}(\mathbf{q})^T, \tag{10}$$

where both the 3×4 matrices $\boldsymbol{G}(\mathbf{q})$ and $\boldsymbol{H}(\mathbf{q})$ are linear in the quaternion parameters and given by

$$\boldsymbol{G}(\mathbf{q}) = \begin{bmatrix} -\boldsymbol{q} & q_0\boldsymbol{I}-\hat{\boldsymbol{q}} \end{bmatrix}, \qquad \boldsymbol{H}(\mathbf{q}) = \begin{bmatrix} -\boldsymbol{q} & q_0\boldsymbol{I}+\hat{\boldsymbol{q}} \end{bmatrix}. \tag{11}$$

These matrices are easily shown to satisfy the quaternion parameter relations

$$\boldsymbol{G}(\mathbf{q})\,\mathbf{q} = \boldsymbol{H}(\mathbf{q})\,\mathbf{q} = \mathbf{0}, \tag{12}$$

implying orthogonality between the four-component quaternion parameter vector $\mathbf{q}$ with each row in the matrices $\boldsymbol{G}(\mathbf{q})$ and $\boldsymbol{H}(\mathbf{q})$. The orthogonality relations between the four-component quaternion parameter vector $\mathbf{q}$, and each of the rows imply that the original 4×3 matrices $\boldsymbol{G}(\mathbf{q})^T$, and $\boldsymbol{H}(\mathbf{q})^T$ can be extended to a nonsingular 4×4 format by including $\mathbf{q}$ as an extra column, defining the regular matrices

$$\mathbf{Q}(\mathbf{q}) = \begin{bmatrix} \mathbf{q} & \boldsymbol{G}(\mathbf{q})^T \end{bmatrix} = \begin{bmatrix} q_0 & -\boldsymbol{q}^T \\ \boldsymbol{q} & q_0\boldsymbol{I}+\tilde{\boldsymbol{q}} \end{bmatrix} \tag{13}$$

and

$$\mathbf{P}(\mathbf{q}) = \begin{bmatrix} \mathbf{q} & \boldsymbol{H}(\mathbf{q})^T \end{bmatrix} = \begin{bmatrix} q_0 & -\boldsymbol{q}^T \\ \boldsymbol{q} & q_0\boldsymbol{I}-\tilde{\boldsymbol{q}} \end{bmatrix}. \tag{14}$$

It is easily verified that these matrices are orthogonal, satisfying the relations

$$\mathbf{Q}(\mathbf{q})\mathbf{Q}(\mathbf{q})^T = \mathbf{P}(\mathbf{q})\mathbf{P}(\mathbf{q})^T = \mathbf{I}. \tag{15}$$

These matrices play a central role in the four-component formulation of rigid body dynamics because they constitute regular linear factors in a product representation of the extended 4×4 rotation matrix,

$$\mathbf{R}(\mathbf{q}) = \mathbf{Q}(\mathbf{q})\mathbf{P}(\mathbf{q})^T = \begin{bmatrix} 1 & \mathbf{0}^T \\ \mathbf{0} & \boldsymbol{R}(\mathbf{q}) \end{bmatrix}. \tag{16}$$

This product decomposition of the extended rotation matrix in terms of regular 4×4 matrices generalizes the product decomposition of the classic 3×3 rotation matrix (10). The formula is easily verified by use of the defining relations (13) and (14). It is observed that the format of the extended rotation matrix corresponds to the transformation of four-component quaternion arrays, where the first scalar component remains unchanged, whereas the vector part is rotated by the classic rotation tensor $\boldsymbol{R}$.

The angular velocity can be obtained via its skew-symmetric matrix representation $\hat{\boldsymbol{\omega}}$ from (4). The vector format must then be extracted by suitable matrix operations. The four by four format of this procedure has been described, for example in [24]. A more direct approach, described in

DOI: 10.1002/nme

detail in [23] Sections 3.5.2–3.5.3, consists in considering the relation between a state of rotation given by the quaternion parameter representation $\mathbf{q}$ and a subsequent state $\mathbf{q} + \dot{\mathbf{q}}dt$ obtained by an extra infinitesimal rotation $\boldsymbol{\omega}dt$. The incremental rotation is represented by the linearized quaternion $[1, \frac{1}{2}\boldsymbol{\omega}dt]$, and the quaternion representation of the final state is obtained by the addition formula for quaternion parameters. This relation is then inverted to yield the incremental angle $\frac{1}{2}\boldsymbol{\omega}dt$ in terms of the original quaternion vector $\mathbf{q}$ and its increment $\dot{\mathbf{q}}dt$. After division by dt, the result of these operations is

$$\frac{1}{2}\boldsymbol{\omega} = -\dot{q}_0\boldsymbol{q} + q_0\dot{\boldsymbol{q}} + \hat{\boldsymbol{q}}\,\dot{\boldsymbol{q}}. \tag{17}$$

This result is given in a three-component vector format. In the present context, it is convenient to expand this format to the full 4×4 matrix form

$$\boldsymbol{\omega} = \begin{bmatrix} 0 \\ \boldsymbol{\omega} \end{bmatrix} = 2\,\mathbf{P}(\mathbf{q})^T\dot{\mathbf{q}}. \tag{18}$$

The angular velocity is a three-component vector, and therefore, the scalar quaternion component vanishes. The corresponding components in the local frame are obtained by pre-multiplication with the 4×4 rotation matrix $\mathbf{R}(\mathbf{q})^T$ given by (16), whereby

$$\boldsymbol{\Omega} = \begin{bmatrix} 0 \\ \boldsymbol{\Omega} \end{bmatrix} = 2\,\mathbf{Q}(\mathbf{q})^T\dot{\mathbf{q}}. \tag{19}$$

A particular feature of the quaternion representation of angular velocity is its bilinear form in the quaternion $\mathbf{q}$ and its time derivative $\dot{\mathbf{q}}$.

The inverse relations providing the time derivative $\dot{\mathbf{q}}$ in terms of the global or local components of the angular velocity follow from the orthogonality relations (15) in the form

$$\dot{\mathbf{q}} = \frac{1}{2}\mathbf{P}(\mathbf{q})\boldsymbol{\omega}, \qquad \dot{\mathbf{q}} = \frac{1}{2}\mathbf{Q}(\mathbf{q})\boldsymbol{\Omega}. \tag{20}$$

These relations are used to express nonhomogeneous initial angular velocity conditions.

3. DYNAMICS

The motion of a rigid body is governed by its kinetic and potential energy via the variational principles of Lagrange or Hamilton, see for example [25]. The present paper concentrates on the motion due to rotation, which is here referred to the origin of the frame(s) of reference.

3.1. Kinetic energy and momentum

In the present context, the kinetic energy is conveniently expressed with respect to the local frame as

$$\mathcal{T} = \frac{1}{2}\boldsymbol{\Omega}^T\boldsymbol{J}\,\boldsymbol{\Omega}, \tag{21}$$

where $\boldsymbol{\Omega}$ is the local component angular velocity, and $\boldsymbol{J}$ is the local inertia tensor defined by the volume integral

$$\boldsymbol{J} = \int_V \left[\left(\boldsymbol{X}^T\boldsymbol{X}\right)\boldsymbol{I} - \boldsymbol{X}\,\boldsymbol{X}^T\right]\rho\,dV, \tag{22}$$

where ρ is the mass density.

DOI: 10.1002/nme

When introducing the quaternion representation (19) of the local or material angular velocity, the expression for the rotational kinetic energy assumes a biquadratic form in the quaternion $\mathbf{q}$ and its time derivative

$$\mathcal{T} = \frac{1}{2}\left[0, \boldsymbol{\Omega}^T\right]\begin{bmatrix} J_0 & \mathbf{0}^T \\ \mathbf{0} & \boldsymbol{J} \end{bmatrix}\begin{bmatrix} 0 \\ \boldsymbol{\Omega} \end{bmatrix} = 2\,\dot{\mathbf{q}}^T\mathbf{Q}(\mathbf{q})\,\mathbf{J}\,\mathbf{Q}(\mathbf{q})^T\dot{\mathbf{q}}, \tag{23}$$

where the augmented 4×4 inertia matrix is introduced as $\mathbf{J} = \mathrm{diag}[J_0, \boldsymbol{J}]$. The kinetic energy is independent of the value of the parameter J_0, which is an artifact of expanding the number of independent velocity parameters from the original three to four. Specific proposals for the value of J_0 have been given in [15] and [21] based on the assumption that it serves a role similar to the components of the inertial tensor $\boldsymbol{J}$. However, as demonstrated in the following, the role of J_0 is not directly related to the physics of the equations of motion but rather to the non-dimensional constraint (8) on the quaternion parameters and thus an 'optimal' choice of J_0 appears to be mainly a numerical issue.

The quaternion form of the momentum $\mathbf{p}$, conjugate to the quaternion parameters representation $\mathbf{q}$ of the generalized displacements, is defined as the partial derivative of the kinetic energy $\mathcal{T}$ from (23) with respect to $\dot{\mathbf{q}}$, whereby

$$\mathbf{p} = \frac{\partial \mathcal{T}}{\partial \dot{\mathbf{q}}^T} = 4\,\mathbf{Q}(\mathbf{q})\,\mathbf{J}\,\mathbf{Q}(\mathbf{q})^T\dot{\mathbf{q}}. \tag{24}$$

On the basis of this expression, it is easily shown by using (12) that the quaternion form of the generalized displacements $\mathbf{q}$ and their conjugate momentum variables $\mathbf{p}$ satisfy the following orthogonality relation

$$\mathbf{q}^T\mathbf{p} = 0. \tag{25}$$

This relation constitutes the dynamic constraint complementing the kinematic constraint (8) expressing normalization of the quaternion parameters $\mathbf{q}$.

The four-component format for the angular momentum in local form is expressed via the local angular velocity relation (19) as

$$\mathbf{L} = \begin{bmatrix} 0 \\ \boldsymbol{L} \end{bmatrix} = \begin{bmatrix} J_0 & \mathbf{0}^T \\ \mathbf{0} & \boldsymbol{J} \end{bmatrix}\begin{bmatrix} 0 \\ \boldsymbol{\Omega} \end{bmatrix} = \mathbf{J}\,\boldsymbol{\Omega} = 2\mathbf{J}\,\mathbf{Q}(\mathbf{q})^T\dot{\mathbf{q}} = \frac{1}{2}\mathbf{Q}(\mathbf{q})^T\mathbf{p}, \tag{26}$$

where the last equality follows from (24). According to (15a), $\mathbf{Q}(\mathbf{q})$ is an orthogonal matrix, and the magnitude of the angular momentum therefore follows from (26) in the form

$$\|\boldsymbol{L}\|^2 = \boldsymbol{L}^T\boldsymbol{L} = \frac{1}{4}\mathbf{p}^T\mathbf{p} = \frac{1}{4}\|\mathbf{p}\|^2. \tag{27}$$

Conservation properties for this length are established in the following sections.

In the Hamiltonian formulation, the kinetic energy is expressed as a function of the generalized displacement variables and the corresponding conjugate momentum variables. This requires the inverse of the quaternion momentum relation (24), obtained by use of the orthogonality relation (15a) for $\mathbf{Q}(\mathbf{q})$,

$$\dot{\mathbf{q}} = \frac{1}{4}\,\mathbf{Q}(\mathbf{q})\,\mathbf{J}^{-1}\,\mathbf{Q}(\mathbf{q})^T\mathbf{p}. \tag{28}$$

Substitution of this expression into the kinetic energy (23) gives

$$\mathcal{T} = \frac{1}{8}\,\mathbf{p}^T\mathbf{Q}(\mathbf{q})\,\mathbf{J}^{-1}\,\mathbf{Q}(\mathbf{q})^T\mathbf{p}, \tag{29}$$

where the kinetic energy is expressed solely in terms of the generalized displacement $\mathbf{q}$ and the conjugate momentum $\mathbf{p}$. In this expression, the roles of $\mathbf{q}$ and $\mathbf{p}$ can be interchanged without changing the value of the total product. This property is most easily established via the following result for

DOI: 10.1002/nme

the product of the first two factors. By use of the specific form of the component matrix $\mathbf{Q}(\mathbf{q})$ given in (13), it follows that

$$\mathbf{p}^T\mathbf{Q}(\mathbf{q}) = \mathbf{p}^T\begin{bmatrix}\mathbf{q} & \boldsymbol{G}(\mathbf{q})^T\end{bmatrix} = \begin{bmatrix}\mathbf{q}^T\mathbf{p} & -\mathbf{q}^T\boldsymbol{G}(\mathbf{p})^T\end{bmatrix} = \mathbf{q}^T\begin{bmatrix}\mathbf{p} & -\boldsymbol{G}(\mathbf{p})^T\end{bmatrix}. \tag{30}$$

Thus, the interchange of the arguments $\mathbf{q}$ and $\mathbf{p}$ leads to a change of sign on the last three components, that is, the vector part of the four-component array. The inverse inertia matrix $\mathbf{J}^{-1}$ does not couple the scalar and the vector parts of the four-vectors in the product, and thus simultaneous interchange of the arguments in the first two factors and in the last two factors leaves the total product unaffected. A particular consequence of this result is that the kinetic energy can be expressed in the alternative form

$$\mathcal{T} = \frac{1}{8}\,\mathbf{q}^T\mathbf{Q}(\mathbf{p})\,\mathbf{J}^{-1}\,\mathbf{Q}(\mathbf{p})^T\mathbf{q}. \tag{31}$$

The more general form of the argument interchange result is used in connection with the discrete algorithm in Section 4.

3.2. Hamilton equations

Hamilton's equations constitute a convenient means of deriving the equations of motion for rigid body rotation in terms of quaternions. While a Lagrangian formulation relies on a set of generalized displacements and their time derivatives, Hamiltonian mechanics considers the generalized displacements and their conjugate momentum components as independent variables. The governing equations then follow as two sets of first-order differential equations in the form

$$\dot{\mathbf{q}} = \frac{\partial\mathcal{H}}{\partial\mathbf{p}^T}, \qquad \dot{\mathbf{p}} = -\frac{\partial\mathcal{H}}{\partial\mathbf{q}^T}. \tag{32}$$

These are commonly known as Hamilton's canonical equations. In the present context, it is advantageous to use an extended form of the Hamiltonian that includes the quaternion normalization condition (8) via a Lagrange multiplier λ,

$$\mathcal{H} = \mathcal{T}(\mathbf{q},\mathbf{p}) + \mathcal{V}(\mathbf{q}) + \lambda\left(\mathbf{q}^T\mathbf{q} - 1\right), \tag{33}$$

where the external forces are generated by the potential $\mathcal{V}(\mathbf{q})$. The kinetic energy is biquadratic in the quaternion parameters $\mathbf{q}$ and the conjugate momentum variables $\mathbf{p}$, and the kinematic equation of motion is obtained from (29) as

$$\dot{\mathbf{q}} = \frac{1}{4}\mathbf{Q}(\mathbf{q})\,\mathbf{J}^{-1}\,\mathbf{Q}(\mathbf{q})^T\mathbf{p}, \tag{34}$$

while the dynamic equation follows from (31) as

$$\dot{\mathbf{p}} = -\frac{1}{4}\mathbf{Q}(\mathbf{p})\,\mathbf{J}^{-1}\,\mathbf{Q}(\mathbf{p})^T\mathbf{q} \;-\; \partial\mathcal{V}/\partial\mathbf{q}^T \;-\; 2\lambda\mathbf{q}. \tag{35}$$

In addition to these equations, differentiation with respect to λ gives the quaternion constraint (8). This is the starting point of the solution of the problem as a system of differential algebraic equations in [21].

The explicit elimination of the Lagrange multiplier λ constitutes a crucial step in the present formulation. Differentiation of the orthogonality constraint (25) gives the condition

$$\mathbf{q}^T\dot{\mathbf{p}} + \mathbf{p}^T\dot{\mathbf{q}} = 0. \tag{36}$$

DOI: 10.1002/nme

The two products in this condition can be expressed by pre-multiplication of (35) with $\mathbf{q}^T$ and (34) with $\mathbf{p}^T$. When adding the resulting two equations, their first terms on the right side are equal to $\pm 2\mathcal{T}$ by (29) and (31) and therefore cancel. This leaves the simplified equation

$$\mathbf{q}^T \dot{\mathbf{p}} + \mathbf{p}^T \dot{\mathbf{q}} = -\mathbf{q}^T \left(\partial \mathcal{V} / \partial \mathbf{q}^T + 2\lambda \mathbf{q} \right). \tag{37}$$

In order to satisfy the constraint derivative equation (36), the Lagrange multiplier must be determined as

$$2\lambda = -\frac{\mathbf{q}^T}{\mathbf{q}^T \mathbf{q}} \frac{\partial \mathcal{V}}{\partial \mathbf{q}^T}. \tag{38}$$

When this expression is used to eliminate λ, the second equation of motion (35) takes the form

$$\dot{\mathbf{p}} = -\frac{1}{4} \mathbf{Q}(\mathbf{p}) \, \mathbf{J}^{-1} \, \mathbf{Q}(\mathbf{p})^T \mathbf{q} - \left(\mathbf{I} - \frac{\mathbf{q}\,\mathbf{q}^T}{\mathbf{q}^T \mathbf{q}} \right) \frac{\partial \mathcal{V}}{\partial \mathbf{q}^T}. \tag{39}$$

It is seen that the effect of eliminating the Lagrange multiplier λ is to introduce a projection operator in front of the potential gradient. Hereby, any component in the potential gradient proportional to $\mathbf{q}$ will be eliminated, and the orthogonality constraint derivative (36) is satisfied identically, irrespective of the properties of the potential $\mathcal{V}(\mathbf{q})$.

The quaternion normalization equation (8) is contained in the kinematic equation (34), where pre-multiplication with $\mathbf{q}^T$ yields

$$\mathbf{q}^T \dot{\mathbf{q}} = \frac{1}{4} \mathbf{q}^T \mathbf{Q}(\mathbf{q}) \, \mathbf{J}^{-1} \, \mathbf{Q}(\mathbf{q})^T \mathbf{p} = 0. \tag{40}$$

The last equality follows from the orthogonality between $\mathbf{q}$ and $\mathbf{p}$, which has just been established. Similarly, a balance equation of the magnitude of the angular momentum follows from pre-multiplication of the dynamic equation (39) with $\mathbf{p}^T$, whereby

$$\mathbf{p}^T \dot{\mathbf{p}} = -\frac{1}{4} \mathbf{p}^T \mathbf{Q}(\mathbf{p}) \, \mathbf{J}^{-1} \, \mathbf{Q}(\mathbf{p})^T \mathbf{q} - \mathbf{p}^T \frac{\partial \mathcal{V}}{\partial \mathbf{q}^T} = -\mathbf{p}^T \frac{\partial \mathcal{V}}{\partial \mathbf{q}^T}. \tag{41}$$

The first term vanishes because the product $\mathbf{p}^T \mathbf{Q}(\mathbf{p})$ only has a scalar component, while the scalar component vanishes in the product $\mathbf{Q}(\mathbf{p})^T \mathbf{q}$ because of the orthogonality relation (25). It follows from this scalar balance equation that the length of the angular momentum vector $\|\boldsymbol{L}\| = \frac{1}{2}\|\mathbf{p}\|$ is conserved in the absence of external loads.

In summary, after elimination of the Lagrange multiplier λ, the two sets of equations of motion (34) and (39) contain the six equations of dynamics plus the time derivatives of the normalization constraint (8) and the orthogonality constraint (25). Thus, to the extent the equations are integrated with due respect for exact conservation of the constraints they can be used directly as demonstrated by the discretized form derived in the following section.

4. STATE-SPACE INTEGRATION ALGORITHM

The first step in the development of a conservative time integration algorithm is to express the evolution equations (34) and (39) in a discrete format. Conservative time integration algorithms do not rely on collocation of the equations of motion at selected points in time but rather on an integrated form such that the basic physical quantities like momentum and energy are conserved over a finite time step from t_n to t_{n+1} or such that the energy is dissipated in a controlled manner—see for example [11, 12, 14, 26]. A similar approach can be used for constraint conditions. Rather than enforcing the constraints at selected points in time, they are introduced via their increments over

DOI: 10.1002/nme

the integration interval. Thus, if the constraints are satisfied initially, they will also be satisfied at any later time step, if the constraint increments are represented without approximation error. In the present context, the quadratic constraint conditions (8) and (25) are represented via their increments as a byproduct of using the extended Hamilton functional (33).

4.1. Conservation of energy

The discretized form of the equations of motion are derived by considering a finite increment over the time interval $\Delta t = [t_n, t_{n+1}]$ of the extended Hamiltonian defined from (33) in the form

$$\mathcal{H} = \mathcal{T}(\mathbf{q}, \mathbf{p}) + \mathcal{V}(\mathbf{q}) + \bar{\lambda}\left(\mathbf{q}^T\mathbf{q} - 1\right). \tag{42}$$

The Lagrange multiplier λ in the continuous form represents a generalized reaction force needed to uphold the kinematic constraint. In the discretized form, the Lagrange multiplier is replaced by a constant $\bar{\lambda}$ representing the effective mean value over the interval. It is noted that Lagrange multipliers often represent an action over a time interval, and thus the value of the multiplier is associated with the time interval rather than specific values at interval end points t_n and t_{n+1}, see for example the discussion of the role of Lagrange multipliers in [27].

The kinetic energy has a symmetric quadratic format, given by either of the forms (29) or (31). The increment can therefore be expressed as twice the product of the increment of one factor and the mean value of the other factor. Using the expression (29), this corresponds to

$$\Delta\mathcal{T} = \frac{1}{4}\Delta\left[\mathbf{q}^T\mathbf{Q}(\mathbf{p})\right]\mathbf{J}^{-1}\left[\overline{\mathbf{Q}(\mathbf{p})^T\mathbf{q}}\right], \tag{43}$$

where the overbar denotes the arithmetic mean, $[\bar{\ }] = \frac{1}{2}[(\ )_n + (\ )_{n+1}]$. The increment in the first factor is evaluated similarly as products of increments and mean values, whereby

$$\Delta\mathcal{T} = \frac{1}{4}\left[\Delta\mathbf{q}^T\mathbf{Q}(\bar{\mathbf{p}}) + \bar{\mathbf{q}}^T\mathbf{Q}(\Delta\mathbf{p})\right]\mathbf{J}^{-1}\left[\overline{\mathbf{Q}(\mathbf{p})^T\mathbf{q}}\right]. \tag{44}$$

Finally, when the expression is separated into two additive terms, it can be verified by use of (30) that the positions of the arguments in the last term can be interchanged, giving the kinetic energy increment in the form

$$\Delta\mathcal{T} = \frac{1}{4}\left\{\Delta\mathbf{q}^T\left[\mathbf{Q}(\bar{\mathbf{p}})\,\mathbf{J}^{-1}\,\overline{\mathbf{Q}(\mathbf{p})^T\mathbf{q}}\right] + \Delta\mathbf{p}^T\left[\mathbf{Q}(\bar{\mathbf{q}})\,\mathbf{J}^{-1}\,\overline{\mathbf{Q}(\mathbf{q})^T\mathbf{p}}\right]\right\}. \tag{45}$$

This relation represents a discretized equivalent of the rule of partial differentiation with the factors to $\Delta\mathbf{q}$ and $\Delta\mathbf{p}$ defining appropriate finite partial derivatives, see for example [26] for a similar approach to finite Green strain. It is important to note the special combination of mean values in the finite derivatives that are needed to provide energy conservation and correct representation of the constraints in the discretized equations.

In a similar way, the gradient of the potential $\mathcal{V}(\mathbf{q})$ must be introduced via its finite derivative $\partial\mathcal{V}_*/\partial\mathbf{q}$, defined by [28],

$$\Delta\mathcal{V}(\mathbf{q}) = \Delta\mathbf{q}^T\partial\mathcal{V}_*/\partial\mathbf{q}^T. \tag{46}$$

Potentials in connection with rigid body motion are often given in terms of powers of the quaternion parameters, and the finite derivative can then typically be extracted directly from the definition (46). When using this definition of the finite derivative of the potential, the increment of the Hamiltonian (42) takes the form

$$\Delta\mathcal{H} = \Delta\mathcal{T} + \Delta\mathbf{q}^T\left(\partial\mathcal{V}_*/\partial\mathbf{q}^T + 2\bar{\lambda}\bar{\mathbf{q}}\right), \tag{47}$$

DOI: 10.1002/nme

with ΔT already determined by (45). In order for the discretized equations to satisfy the incremental form of the orthogonality equation (36), the load provided by the parenthesis in (47) must be orthogonal to the mean value of the quaternion vector $\bar{\mathbf{q}}$,

$$\bar{\mathbf{q}}^T \left(\partial \mathcal{V}_*/\partial \mathbf{q}^T + 2\bar{\lambda}\bar{\mathbf{q}}\right) = 0. \tag{48}$$

This equation determines the Lagrange multiplier $\bar{\lambda}$, and elimination of the multiplier then gives the final form of the increment of the Hamiltonian in the form

$$\Delta \mathcal{H} = \Delta \mathcal{T} + \Delta \mathbf{q}^T \left(\mathbf{I} - \frac{\bar{\mathbf{q}}\,\bar{\mathbf{q}}^T}{\bar{\mathbf{q}}^T\bar{\mathbf{q}}}\right) \frac{\partial \mathcal{V}_*}{\partial \mathbf{q}^T}. \tag{49}$$

Upon substitution of $\Delta \mathcal{T}$ from (45), this equation takes the form

$$\Delta \mathcal{H} = \Delta \mathbf{p}^T \frac{\partial \mathcal{T}_*}{\partial \mathbf{p}^T} + \Delta \mathbf{q}^T \left[\frac{\partial \mathcal{T}_*}{\partial \mathbf{q}^T} + \left(\mathbf{I} - \frac{\bar{\mathbf{q}}\,\bar{\mathbf{q}}^T}{\bar{\mathbf{q}}^T\bar{\mathbf{q}}}\right) \frac{\partial \mathcal{V}_*}{\partial \mathbf{q}^T}\right], \tag{50}$$

where the finite derivatives of the kinetic energy $\mathcal{T}$ are defined by the square brackets in (45).

The discretized equations of motion follow directly from equating the increment of the Hamiltonian (50) to zero, whereby

$$\Delta \mathbf{q} = \frac{1}{4}\,\Delta t\,\mathbf{Q}(\bar{\mathbf{q}})\,\mathbf{J}^{-1}\,\overline{\mathbf{Q}(\mathbf{q})^T\mathbf{p}}, \tag{51}$$

$$\Delta \mathbf{p} = -\frac{1}{4}\,\Delta t\,\mathbf{Q}(\bar{\mathbf{p}})\,\mathbf{J}^{-1}\,\overline{\mathbf{Q}(\mathbf{p})^T\mathbf{q}} - \Delta t\,\left(\mathbf{I} - \frac{\bar{\mathbf{q}}\,\bar{\mathbf{q}}^T}{\bar{\mathbf{q}}^T\bar{\mathbf{q}}}\right) \frac{\partial \mathcal{V}_*}{\partial \mathbf{q}^T}. \tag{52}$$

These equations form a clear discretized analog to the kinematic equation (34) and the extended dynamic equation (39). The solution to these equations satisfies the energy conservation condition, expressed in incremental form as $\Delta \mathcal{H} = 0$, by the construction of the equations using finite derivatives and the introduction of the discretized form of the projection operator on the finite derivative of the potential.

4.2. Constraints and angular momentum

The remaining scalar identities consist of the quaternion-momentum orthogonality condition (25), the quaternion normalization condition (8), and the conservation of the magnitude of the angular momentum in the absence of external loads as expressed in (41). The discrete form of the quaternion-momentum orthogonality condition is obtained from (51)–(52) by pre-multiplication with $\bar{\mathbf{p}}$ and $\bar{\mathbf{q}}$, respectively. The external load term vanishes because of the projection operator, leaving

$$\Delta\left(\mathbf{q}^T\mathbf{p}\right) = \bar{\mathbf{q}}^T\Delta\mathbf{p} + \bar{\mathbf{p}}^T\Delta\mathbf{q} = \frac{1}{4}\,\Delta t\,\bar{\mathbf{q}}^T\mathbf{Q}(\bar{\mathbf{p}})\,\mathbf{J}^{-1}\overline{\mathbf{Q}(\mathbf{p})^T\mathbf{q}} - \frac{1}{4}\,\Delta t\,\bar{\mathbf{p}}^T\mathbf{Q}(\bar{\mathbf{q}})\,\mathbf{J}^{-1}\overline{\mathbf{Q}(\mathbf{q})^T\mathbf{p}} = 0. \tag{53}$$

The last quality follows from use of the result (30) about simultaneous interchange of the arguments in the two first factors and in the two last factors in for example the second term. The quaternion normalization condition is formulated in incremental form as

$$\frac{1}{2}\Delta\left(\mathbf{q}^T\mathbf{q} - 1\right) = \bar{\mathbf{q}}^T\Delta\mathbf{q} = \frac{1}{4}\,\Delta t\,\bar{\mathbf{q}}^T\mathbf{Q}(\bar{\mathbf{q}})\,\mathbf{J}^{-1}\overline{\mathbf{Q}(\mathbf{q})^T\mathbf{p}} = \frac{1}{4}\,\Delta t\,\bar{\mathbf{q}}^T\bar{\mathbf{q}}\,J_0^{-1}\overline{\mathbf{q}^T\mathbf{p}} = 0, \tag{54}$$

where the last equality follows from the orthogonality relation (53). Finally, the increment of the angular momentum follows from pre-multiplication of (52) with $\bar{\mathbf{p}}$, giving

$$2\Delta\|\boldsymbol{L}\|^2 = \frac{1}{2}\Delta\left(\mathbf{p}^T\mathbf{p}\right) = \bar{\mathbf{p}}^T\Delta\mathbf{p} = -\Delta t\,\bar{\mathbf{p}}^T\left(\mathbf{I} - \frac{\bar{\mathbf{q}}\,\bar{\mathbf{q}}^T}{\bar{\mathbf{q}}^T\bar{\mathbf{q}}}\right) \frac{\partial \mathcal{V}_*}{\partial \mathbf{q}^T}. \tag{55}$$

DOI: 10.1002/nme

Here, the contribution from the first term in (52) vanishes because of the orthogonality condition $\mathbf{q}^T\mathbf{p} = 0$ as in the corresponding differential relation (41). Clearly, this relation leads to conservation of the magnitude of the angular momentum in the absence of external load, whereas the projection operator leads to a higher-order modification of the discretized contribution from the external load when present.

4.3. Discrete integration algorithm

The time integration algorithm is a simultaneous Newton–Raphson solution of the discrete dynamic equation of motion (52) and the kinematic equation (51). The residual vector $\mathbf{r}^T = [\mathbf{r_q}, \mathbf{r_p}]$ is the difference between the right and the left-hand sides,

$$\mathbf{r_q} = \Delta\mathbf{q} - \frac{1}{4}\Delta t\,\mathbf{Q}(\bar{\mathbf{q}})\,\mathbf{J}^{-1}\,\overline{\mathbf{Q}(\mathbf{q})^T\mathbf{p}}\,, \tag{56}$$

$$\mathbf{r_p} = \Delta\mathbf{p} + \frac{1}{4}\Delta t\,\mathbf{Q}(\bar{\mathbf{p}})\,\mathbf{J}^{-1}\,\overline{\mathbf{Q}(\mathbf{p})^T\mathbf{q}} \;+\; \Delta t\left(\mathbf{I} - \frac{\bar{\mathbf{q}}\,\bar{\mathbf{q}}^T}{\bar{\mathbf{q}}^T\bar{\mathbf{q}}}\right)\frac{\partial \mathcal{V}_*}{\partial \mathbf{q}^T}. \tag{57}$$

In the Newton–Raphson procedure, the iterative step amounts to equating the linearized residual equation to zero. The equation is formulated in terms of the current residual $\mathbf{r}$ and the linearized increment $\delta\mathbf{r}$ as

$$\mathbf{r} + \delta\mathbf{r} = \mathbf{r} + \left(\frac{\partial \mathbf{r}}{\partial \mathbf{q}}\delta\mathbf{q} + \frac{\partial \mathbf{r}}{\partial \mathbf{p}}\delta\mathbf{p} + \ldots\right) = \mathbf{0} \tag{58}$$

where the dots denote contributions from higher-order derivatives. When using the condensed notation $\mathbf{g}^T = [\mathbf{q}^T, \mathbf{p}^T]$, the equation take the form

$$\mathbf{K}\,\delta\mathbf{g} = -\mathbf{r}, \tag{59}$$

where the tangent stiffness matrix

$$\mathbf{K} = \begin{bmatrix} \mathbf{K_{qq}} & \mathbf{K_{qp}} \\ \mathbf{K_{pq}} & \mathbf{K_{pp}} \end{bmatrix} \tag{60}$$

follows from differentiation of (56) and (57).

The iteration process is implemented with convergence criteria on the equations of motion with a prescribed tolerance, represented as a fraction ε_r of the initial length of the considered vector

$$\left\|\mathbf{r_q}\right\| \leqslant \varepsilon_r \quad , \quad \left\|\mathbf{r_p}\right\| \leqslant \varepsilon_r \left\|\mathbf{p}_0\right\|. \tag{61}$$

The kinematic constraint $\|\mathbf{q}\| = 1$ and the dynamic constraint $\mathbf{p}^T\mathbf{q} = 0$ must be satisfied by the initial conditions. Ideally, they are satisfied at later times via their increments as demonstrated in (53) and (54). The orthogonality constraint (53) follows from symmetry properties, whereas the rounding error in the normalization condition (54) on the quaternion parameters depends directly on the parameter J_0. In the algorithm, the orthogonality condition is enforced via the tolerance condition

$$|\mathbf{p}^T\mathbf{q}| \leqslant \varepsilon_c \left\|\mathbf{p}\right\|, \tag{62}$$

whereas the dependence of the convergence on the parameter J_0 is largely eliminated by renormalizing the quaternion parameters $\mathbf{q}$ at the end of each time increment. The conservative time integration algorithm for rigid body rotations is summarized in pseudo-code format in Table I.

5. NUMERICAL EXAMPLES

In this section two numerical examples are used to illustrate the accuracy and conservation properties of the presented time integration algorithm for rigid body rotation. Furthermore, the role

DOI: 10.1002/nme

Table I. Conservative time integration algorithm.

1)	Initial conditions: $\mathbf{q}_0, \mathbf{p}_0$.
2)	Prediction step: $\mathbf{q} = \mathbf{q}_n$, $\mathbf{p} = \mathbf{p}_n$.
3)	Residual calculation: $\mathbf{r}_\mathbf{q} = \Delta\mathbf{q} - \frac{1}{4}\Delta t \mathbf{Q}(\bar{\mathbf{q}})\,\mathbf{J}^{-1}\,\overline{\mathbf{Q}(\mathbf{q})^T\mathbf{p}}$, $\mathbf{r}_\mathbf{p} = \Delta\mathbf{p} + \frac{1}{4}\Delta t \mathbf{Q}(\bar{\mathbf{p}})\,\mathbf{J}^{-1}\,\overline{\mathbf{Q}(\mathbf{p})^T\mathbf{q}}$ $+\ \Delta t\big[\mathbf{I} - (\bar{\mathbf{q}}\,\bar{\mathbf{q}}^T)/(\bar{\mathbf{q}}^T\bar{\mathbf{q}})\big]\partial\mathcal{V}_*/\partial\mathbf{q}^T$.
4)	Update incremental rotation parameters: $\delta\mathbf{g} = -\mathbf{K}^{-1}\,\mathbf{r}$, $\mathbf{g} = \mathbf{g} + \delta\mathbf{g}$, If $\|\mathbf{r}\| > \varepsilon_r$ and $\|\mathbf{p}^T\mathbf{q}\| > \varepsilon_c\|\mathbf{p}\|$ repeat from 3).
5)	Renormalize quaternion parameter: $\mathbf{q} = \mathbf{q}/\|\mathbf{q}\|$.
6)	Return to 2) for new time step, or stop.

of the auxiliary parameter J_0 as a weighting factor for the normalization constraint rather than a physical property is highlighted. In the first example the free motion of a rigid box is considered, while the second example deals with a spinning top in a gravitational field.

5.1. Spinning box

This example considers the box introduced in [13] with side lengths $[1, 3, 2]$ and mass 12. The principal moment of inertia tensor with respect to the center of mass is then given by $\boldsymbol{J} = \text{diag}\,[12, 5, 10]$. It is noted that the maximum principal moment of inertia is smaller than the sum of the two smallest, that is, $J_i \leqslant J_j + J_k$, a condition sometimes violated by examples used to illustrate rigid body motion in the literature. The auxiliary parameter J_0 is initially chosen as $J_0 = \text{tr}(\boldsymbol{J})$, that is, a value in the same order of magnitude as the remaining coefficients in the moment of inertia tensor as suggested in [15] and [21].

The box is illustrated in its initial position in Figure 1(a) at $t = t_0$. The motion is started with an initial angular velocity of $\boldsymbol{\Omega}_0 = [0.0, 0.05, 10.0]^T$, that is, the box spinning around its intermediate axis of inertia with a small perturbation. It is well-known that free rigid body rotations are stable only about the axis of maximum or minimum moment of inertia, whereas spinning motion around the intermediate axis is unstable in the sense that a small perturbation leads to reversal of the body at regular intervals, see for example [25] Section 5.6. This property makes the present choice of initial conditions particularly suitable for testing numerical algorithms for rigid body motion, [11, 13].

The iteration tolerances are chosen as $\varepsilon_r = \varepsilon_c = 10^{-6}$. In the present case the active conditions are on the unbalances in the equations of motion (61), while the constraint conditions (62)

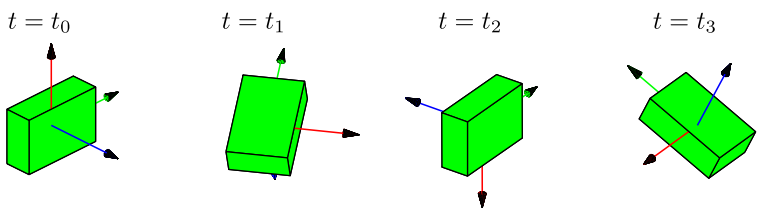

Figure 1. Motion of box at selected time steps, $\Delta t = 0.01$.

DOI: 10.1002/nme

are satisfied automatically within a relative error of 10^{-13}, when the tolerance on the residual is satisfied. It was demonstrated in Sections 4.1 and 4.2 that in the absence of approximation error, the algorithm conserves the energy and the magnitude of the angular momentum. For the present tolerances, the kinetic energy $\mathcal{T} = 500$ as well as the magnitude of the angular momentum $\|\boldsymbol{L}\|$ are conserved to an accuracy around 10^{-12}. The global components of the angular momentum vector $\boldsymbol{l} = [0, 0.25, 100]^T$ are conserved to a similar accuracy.

The local components of the angular velocity are illustrated in Figure 2. Initially, the box spins around the global x_3-axis as shown in Figure 1(a). At $t = t_1$, the local angular velocity component Ω_3 approaches zero, when the box tips over as illustrated in Figure 1(b). At $t = t_2$ the sign of Ω_3 is reversed corresponding to the situation where the box is turned upside down, see Figure 1(c). Finally, the box tips over again at $t = t_3$ and approaches the initial configuration. This pattern repeats itself in a periodical manner with period $T = 5.446$ (evaluated for $\Delta t = 10^{-6}$). The results presented in Figures 2(a) and 2(b) are determined for time steps $\Delta t = 0.1$ and $\Delta t = 0.01$, respectively. These are identical apart from a small change in time scale. For the present simulation, the time difference between two turns is 2.50 for $\Delta t = 0.1$ and 2.72 for $\Delta t = 0.01$ corresponding to a shortening of time scale of approximately 8% when using $\Delta t = 0.1$.

The second-order accuracy of the present algorithm is illustrated in Figure 3, showing the period error for different time steps Δt. The period is evaluated from the angular velocity and compared with the reference period T evaluated for a fine discretization of $\Delta t = 10^{-6}$. The figure also shows

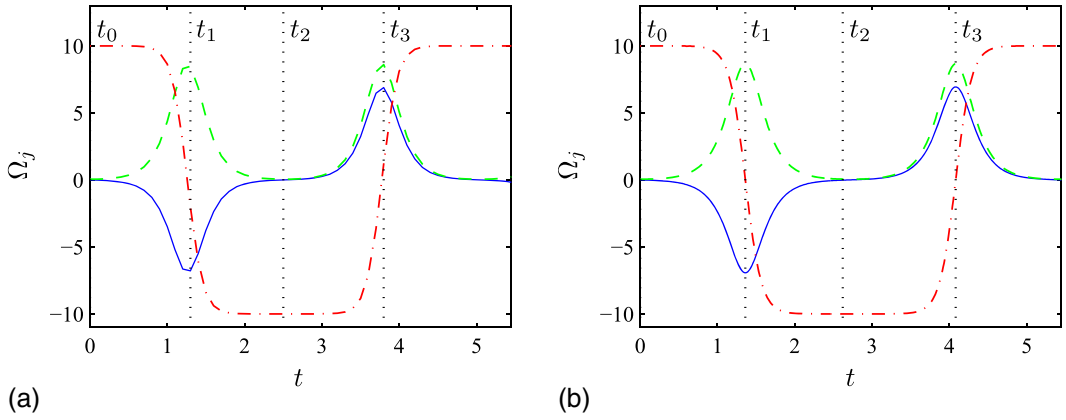

Figure 2. Local angular velocity components Ω_1 (—), Ω_2 (- -), Ω_3 (-·-). (a) $\Delta t = 0.1$, (b) $\Delta t = 0.01$.

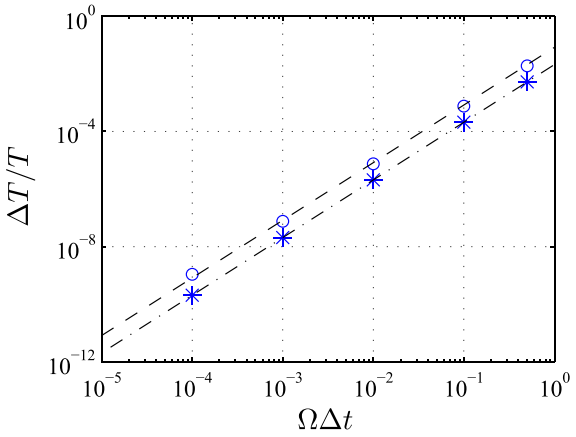

Figure 3. Relative period error. $\Omega_0 = [10, 0, 0]^T$ (+), $\Omega_0 = [0, 0, 10]^T$ (×), $\Omega_0 = [0, 0.05, 10]^T$ (∘), $(\Omega\Delta t)^2/12$ (– –), $(\Omega\Delta t)^2/48$ (– · –).

DOI: 10.1002/nme

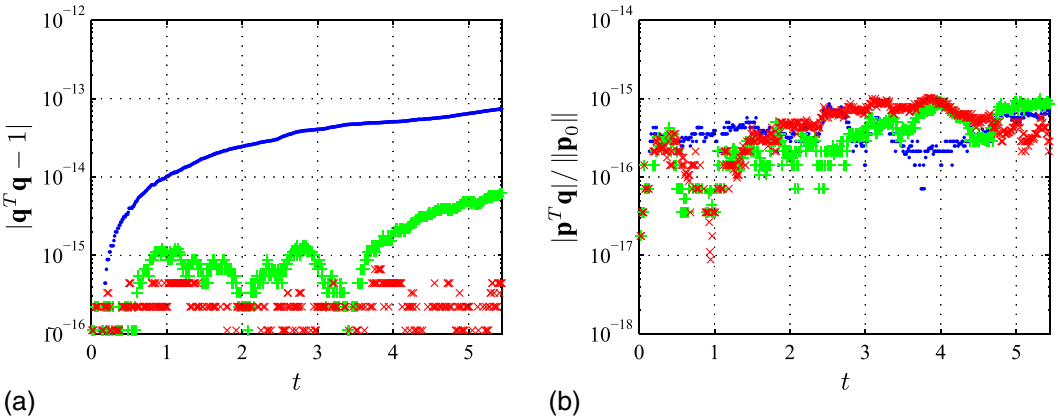

Figure 4. Error on homogeneous constrains: (a) normalization constraint and (b) orthogonality constraint. $J_0 = J_{ii}/10$ (•), $J_0 = J_{ii}$ (+), $J_0 = 10J_{ii}$ (×).

the well-known asymptotic result for integration of a single component, see for example [23],

$$\frac{\Delta T}{T} \simeq \frac{1}{12}(\Omega \Delta t)^2.$$

In addition to the combined motion resulting from the initial conditions with a small perturbation, the figure also shows results for the trivial cases where the box rotates with constant angular velocity about the axis of maximum moment of inertia (x_1-axis) and the intermediate axis (x_3-axis), respectively. In these two special cases, the representation of the motion through the half-angle leads to a reduction of the convergence constant by a factor of 4, and the line with coefficient $1/48$ shows an excellent fit to these special cases.

As discussed in Section 3.1, the auxiliary parameter J_0 is associated with the normalization constraint (8) rather than a physical property. This is illustrated in Figure 4, showing results for an algorithm without renormalization of the quaternion parameters. The development of the error in the quaternion parameter constraint is illustrated in Figure 4(a) for $J_0/J_{ii} = 0.1, 1, 10$, respectively. It is seen that the relative error on the normalization constraint decreases roughly in proportion to the increase in J_0/J_{ii}, indicating that J_0 acts as a weighting factor on this constraint. In contrast, the orthogonality constraint is satisfied to high accuracy irrespective of the value of J_0. When repeating the calculation with the algorithm including renormalization as shown in Table I, the normalization error drops to the numerical accuracy of the MATLAB (The MathWorks, Natick, Mass.) implementation around $2 \cdot 10^{-16}$, whereas the error on the orthogonality condition remains virtually unaffected.

5.2. *Spinning top in gravitational field*

This example considers the motion of a conical top with one point fixed as illustrated in Fig. 5. The top motion is expressed in terms of the angle of nutation θ, the angle of precession φ, and the spin angle ψ.

The top has the same dimensions as in [21] with height $h = 0.1$ and radius $r = h/2$. The mass is $m = \rho\pi^2 h/3$ with mass density $\rho = 2700$. The center of gravity is located at a distance $l = 3h/4$ from the origin, described by the vector with local components $\boldsymbol{X} = [0,\ 0,\ l]^T$. The local components of the inertia tensor are

$$J_1 = J_2 = \frac{3}{5}m\left(\frac{r^2}{4} + h^2\right) \quad , \quad J_3 = \frac{3}{10}mr^2.$$

DOI: 10.1002/nme

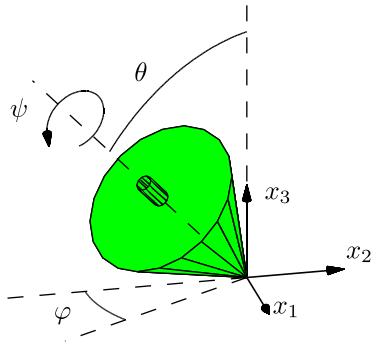

Figure 5. Configuration of rotating top.

These are supplemented by the auxiliary inertia parameter $J_0 = 10J_{ii}$. The top is in a uniform gravitational field with acceleration $g = 9.81$ in the negative x_3-direction. This corresponds to the potential energy

$$\mathcal{V}(\mathbf{q}) = mgl\cos(\theta) = mgl\,\left(q_0^2 - q_1^2 - q_2^2 + q_3^2\right).$$

The last expression is obtained by noticing that the projection of the gravitational acceleration vector on the global center of gravity vector $\boldsymbol{R}(\mathbf{q})\boldsymbol{X}$ extracts the diagonal component R_{33} of the quaternion rotation tensor defined in (9).

5.2.1. Fast top. First, a fast top is considered, i.e. a top where the initial kinetic energy $\mathcal{T}$ due to rotation about the local X_3-axis is large compared to the maximum variation in potential energy $\mathcal{V}$. The following initial conditions have been used corresponding to a ratio $2\mathcal{V}/\mathcal{T} < 0.05$

$$\theta_0 = \frac{\pi}{3} \quad , \quad \boldsymbol{\Omega}_0 = [0,\, 0,\, 300]^T.$$

According to [25] Section 5.7 approximate values for the angular precession and nutation frequencies can be expressed as

$$\dot{\theta} \simeq \frac{J_3}{J_1}\Omega_3 = 35.3 \quad , \quad \dot{\varphi} \simeq \frac{mgl}{J_3\Omega_3} = 3.27$$

corresponding to the periods $T_\theta \simeq 0.18$ and $T_\varphi \simeq 1.9$.

The motion of the center of gravity for the fast top is illustrated in Figure 6. It is seen that the top displays a combined motion composed of precession about the global x_3-axis and nutation between two bounding angles as described in [25]. The precession is illustrated via the x_1-component of the center of mass in Figure 6(a). The precession period corresponds roughly to the estimate T_φ with small perturbations because of nutation. The nutation is illustrated in Figure 6(b) by the x_3-component, oscillating with a period close to the estimated T_θ. The equations of motion have been solved for the three time steps $\Delta t = (40, 20, 2)\cdot 10^{-4}$, corresponding to approximately 5, 10 and 100 time steps per full revolution of the top around its local axis in terms of the initial angular velocity $\Omega_0 = \|\boldsymbol{\Omega}_0\|$. Furthermore, a reference solution determined for a very fine time step $\Delta t = 10^{-6}$ is also presented. The convergence limits are set to $\varepsilon_r = \varepsilon_c = 10^{-6}$.

The vertical component of the external moment vanishes, and thus both the total mechanical energy and the l_3-component of the spatial angular momentum vector are conserved, if the processes were carried to complete convergence. The relative error on the total mechanical energy and the l_3-component of the spatial angular momentum vector are presented in Figure 7(a) and 7(b) for the relatively crude discretization $\Delta t = 0.004$. It is seen that E and l_3 are conserved within a relative error of 10^{-8}.

DOI: 10.1002/nme

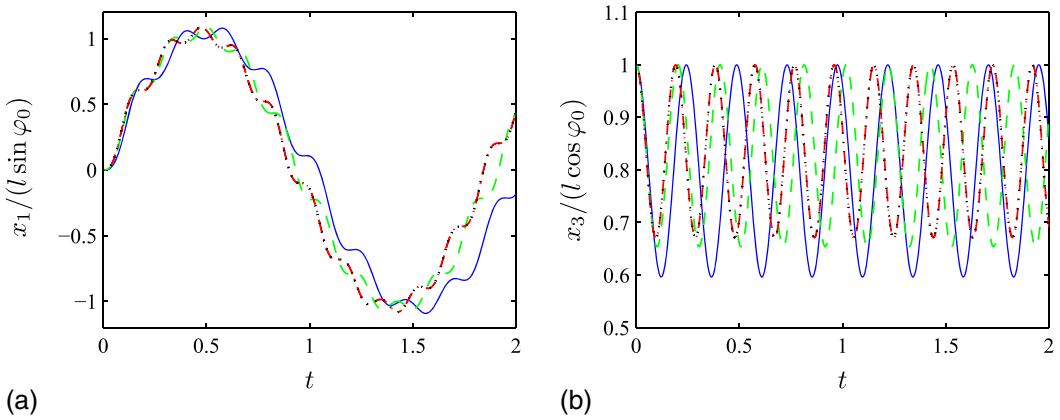

Figure 6. Motion of center of mass for fast top: (a) $x_1(t)$, (b) $x_3(t)$. $\Delta t = 0.004$ (—), $\Delta t = 0.002$ (- -), $\Delta t = 2 \cdot 10^{-4}$ (-·-), reference solution (· · ·).

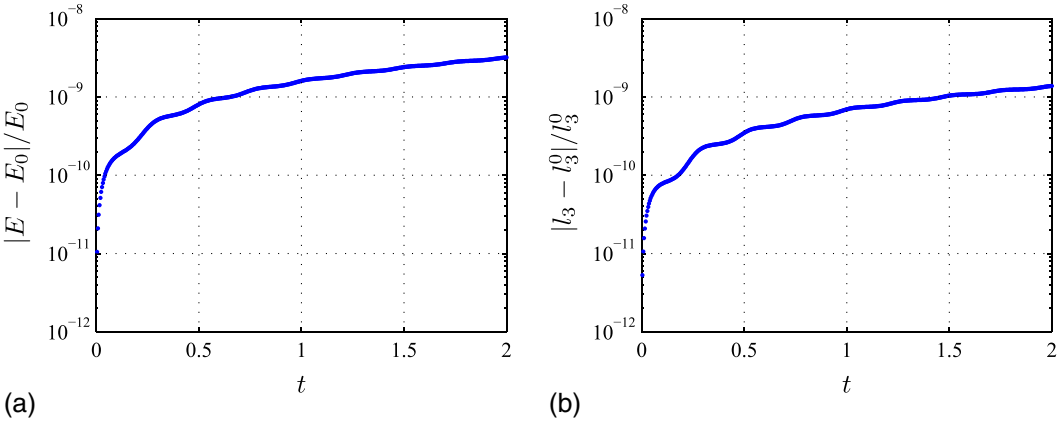

Figure 7. Conserved quantities: (a) energy and (b) spatial component of angular momentum l_3. $\Delta t = 0.004$.

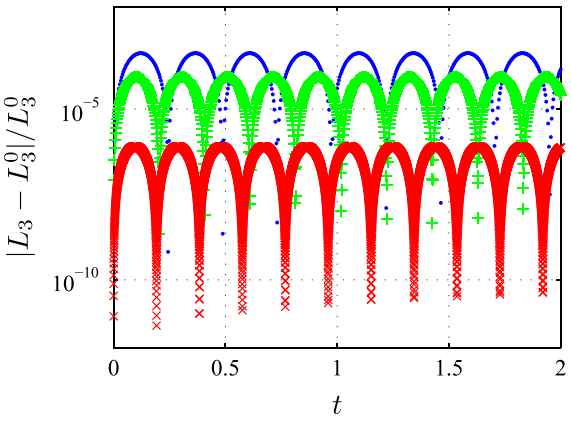

Figure 8. Local component of angular velocity L_3. $\Delta t = 0.004$ (•), $\Delta t = 0.002$ (+), $\Delta t = 2 \cdot 10^{-4}$ (×).

It can be shown, see for example [25] p. 211, that also the local angular momentum component L_3 is a conserved quantity. The error on L_3 is illustrated in Figure 8. The error exhibits a regular variation matching the period of the nutation shown in Figure 6. In contrast to the energy E and the vertical momentum component l_3, conservation of the momentum component L_3 along the axis of the top relies on exact representation of the time integral of the external moment. As this contribution is only evaluated to within the accuracy of the present second-order approximation of the equations

DOI: 10.1002/nme

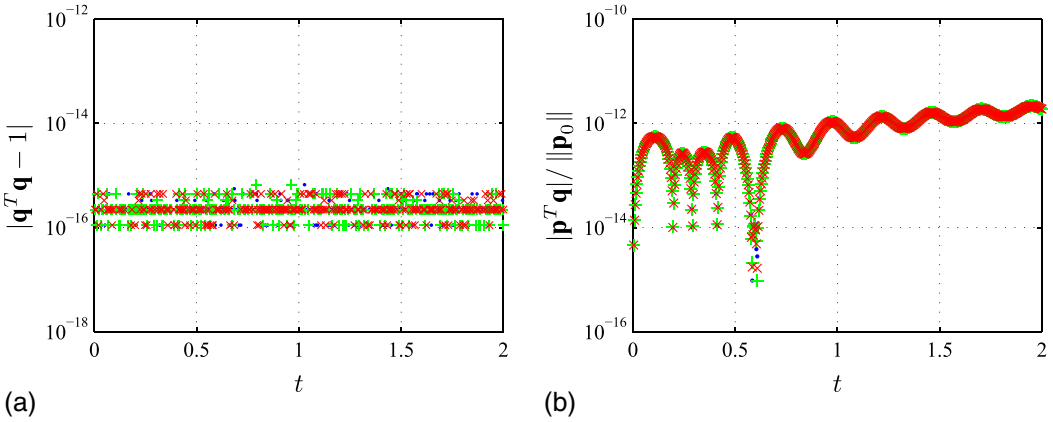

Figure 9. Conservation of constraints: (a) normalization constraint, (b) orthogonality constraint. $J_0 = J_{ii}$ ($\bullet$), $J_0 = 10J_{ii}$ ($+$), $J_0 = 10^2\ J_{ii}$ ($\times$). $\Delta t = 0.004$.

of motion, a second-order error is introduced into the conservation of L_3. The error is introduced because the moment is only represented via the energy conserving finite differential $\partial\mathcal{V}_*/\partial\mathbf{q}$ and a projection operator based on the mean value $\bar{\mathbf{q}}$ of the quaternion parameters. The inherent second-order accuracy leads to a relative period error for the primary variables $\mathbf{q}$, which is proportional to $(\|\boldsymbol{\Omega}_0\|\,\Delta t)^2$, and thus the error on the external potential is expected to be proportional to this error squared. For the large time step of $\Delta t = 0.004$ and current nutational frequency of approximately 35.3, this yields a relative error of $4 \cdot 10^{-4}$, which corresponds closely to the error on L_3 illustrated in Figure 8. It is seen that the error is reduced when a smaller time step is applied.

The accuracy with which the constraint equations are satisfied is illustrated in Figure 9 with Figure 9(a) showing the effect of renormalization of the quaternion parameters and Figure 9(b) showing that the error on the orthogonality condition is well below the tolerance of $\varepsilon_c = 10^{-6}$. The figure also illustrates that with the normalized algorithm, the error on the constraints is unaffected by the specific value of the parameter J_0.

5.2.2. Precessing top. Finally, the special case of a top in uniform precession without nutation is considered. The initial conditions are taken corresponding to those considered in [21] with precession rate $\dot{\varphi} = 10$ and

$$\theta_0 = \frac{\pi}{3}, \qquad \boldsymbol{\Omega}_0 = [0,\ \dot{\varphi}\sin(\theta_0),\ \dot{\psi} + \dot{\varphi}\cos(\theta_0)]^T.$$

In order to obtain the case of regular precession for a given initial inclination angle θ_0, the angular velocities $\dot{\psi}$ and $\dot{\varphi}$ must be determined such that they satisfy the following relation, see for example [25] Section 5.7,

$$\dot{\psi} = \frac{mgl}{J_3\,\dot{\varphi}} + \frac{J_1 - J_3}{J_3}\,\dot{\varphi}\,\cos(\theta_0). \tag{63}$$

The x_1-component and x_3-component of the motion of the center of mass are illustrated in Figure 10 for $\Delta t = 0.01, 0.005, 0.002$ together with the exact analytical solution. The chosen time discretizations correspond to approximately 5, 9 and 22 time steps per revolution time $T = 2\pi/\|\boldsymbol{\Omega}_0\|$. It is seen from the numerical simulations that the top exhibits nutation. This is a consequence of the period error predicted by the algorithm which essentially corresponds to underestimating the angular frequencies for rotational motion, thereby violating the condition for steady precession (63). As expected, this deviation from the ideal behavior is reduced for smaller time steps. The apparent coincidence between the precession and the nutation period is a consequence of the particular choice of parameters rather than a general physical property. As in the case of a fast top, the total mechanical energy and the spatial angular momentum component l_3 are conserved within a relative error of 10^{-6} for convergence parameters $\varepsilon_r = \varepsilon_c = 10^{-6}$. For this value of the

DOI: 10.1002/nme

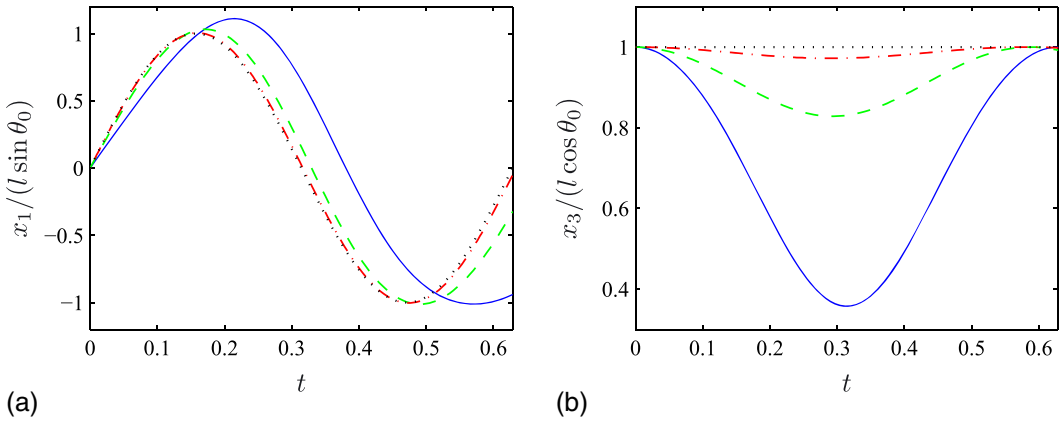

Figure 10. Motion of center of mass for precessing top: (a) $x_1(t)$, (b) $x_3(t)$. $\Delta t = 0.01$ (—), $\Delta t = 0.005$ (- -), $\Delta t = 0.002$ (-·-), analytical solution (· · ·).

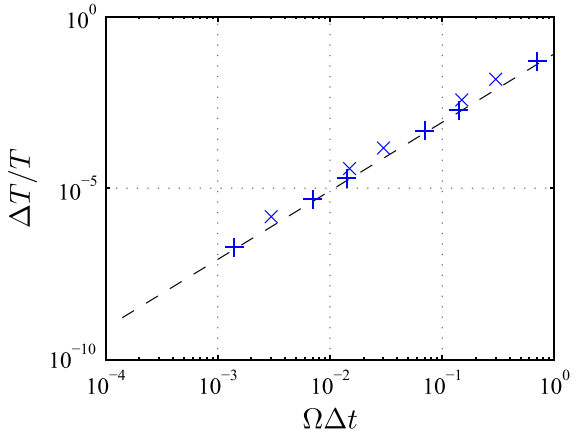

Figure 11. Relative period error. Precessing top (+), fast top (×), $(\Omega\Delta t)^2/12$ (– –).

tolerances, convergence was obtained using $i_{mean} = i_{max} = 5$ for the time increment $\Delta t = 0.01$ and by using $i_{mean} = i_{max} = 4$ for the smaller time increments $\Delta t = 0.005, 0.002$.

The second-order convergence of the algorithm is illustrated in Figure 11, showing the relative period error $\Delta T/T$ for the nutation of the fast top in Figure 6(b) and the rotation of the precessing top in Figure 10(a). The time increment is made non-dimensional via the parameter $\Omega\Delta t$, where Ω is formed as the algebraic mean of $\|\boldsymbol{\Omega}\|$ over the individual time steps. The analytical solution is used as reference for the precessing top, whereas a numerical solution obtained with a fine time discretization of $\Delta t = 10^{-6}$ is used as reference solution for the fast top. In both problems, the development of the period error fits well with the asymptotic formula.

6. CONCLUSIONS

A direct momentum and energy conserving integration procedure has been developed for rigid body motion. The formulation makes use of the four quaternion parameters and the corresponding four generalized momentum variables, connected via an augmented inertia matrix that contains an auxiliary inertia parameter. The equations of motion are obtained by considering a finite increment of the corresponding Hamiltonian and representing external loads via a finite gradient of the load potential in terms of the quaternion parameters. The gradient of the load potential must be constrained, but it is a key feature of the present formulation that this constraint—originally introduced via a Lagrange multiplier—is reformulated by elimination of the Lagrange multiplier, leaving only a simple projection operator applied to the four-component load gradient. The present formulation

DOI: 10.1002/nme

results in an explicit discretized form of the Hamilton equations for the quaternion and momentum increments, where the conservation properties are generated by the use of appropriately defined mean values in the finite derivatives of the Hamiltonian function. The two extra conditions of the quaternion formulation—the quaternion parameter constraint and the orthogonality condition of the quaternion and momentum vectors—are imbedded in the generalized equations of motion and do not require special attention, apart from the projection operator on the load potential gradient. The role of the auxiliary inertia parameter is to act as a weight on the quaternion normalization constraint, as illustrated in the numerical examples, suggesting a value somewhat larger than the physical moments of inertia.

REFERENCES

1. Argyris J. An excursion into large rotations. *Computer Methods in Applied Mechanics and Engineering* 1982; **32**:85–155.
2. Bauchau OA, Trainelli L. The vectorial parametrization of rotation. *Nonlinear Dynamics* 2003; **32**:71–92.
3. Mäkinen J. Critical study of Newmark-scheme on manifold of finite rotations. *Computer Methods in Applied Mechanics and Engineering* 2001; **191**:817–828.
4. Krysl P, Endres L. Explicit Newmark/Verlet algorithm for time integration of the rotational dynamics of rigid bodies. *International Journal for Numerical Methods in Engineering* 2005; **62**:2154–2177.
5. Brüls O, Cardona A. On the use of Lie group time integrators in multibody dynamics. *ASME Journal of Computational and Nonlinear Dynamics* 2010; **5**(3):031002:1–13.
6. Brüls O, Cardona A, Arnold M. Lie group generalized-α time integration of constrained flexible multibody systems. *Mechanism and Machine Theory* 2012; **48**:121–137.
7. Krysl P. Explicit momentum-conserving integrator for dynamics of rigid bodies approximating the midpoint Lie algorithm. *International Journal for Numerical Methods in Engineering* 2005; **63**:2171–2193.
8. Nukala PKVV, Shelton W. Semi-implicit reversible algorithms for rigid body rotational dynamics. *International Journal for Numerical Methods in Engineering* 2007; **69**:2636–2662.
9. Austin MA, Krishnaprasad PS, Wang LS. Almost Poisson integration of rigid body systems. *Journal of Computational Physics* 1993; **107**:105–117.
10. Hairer E, Lubich C, Wanner G. *Geometric Numerical Integration*, 2nd ed. Springer: Berlin, 2006.
11. Simo JC, Wong KK. Unconditionally stable algorithms for rigid body dynamics that exactly preserve energy and momentum. *International Journal for Numerical Methods in Engineering* 1991; **31**:19–52.
12. Simo JC, Tarnow N, Wong KK. Exact energy-momentum conserving algorithms and symplectic schemes for nonlinear dynamics. *Computer Methods in Applied Mechanics and Engineering* 1992; **100**:63–116.
13. Krenk S. A vector format for conservative time integration of rotations. *Multibody Dynamics 2007, ECCOMAS Thematic Conference*, Milan, Italy, 2007; 1–12.
14. Lens EV, Cardona A, Géradin M. Energy preserving time integration for constrained multibody systems. *Multibody System Dynamics* 2004; **11**:41–61.
15. Morton Jr. HS. Hamiltonian and Lagrangian formulations of rigid-body rotational dynamics based on the Euler parameters. *Journal of the Astronautical Sciences* 1993; **41**:569–591.
16. Shivarama R, Fahrenthold EP. Hamilton's equations with Euler parameters for rigid body dynamics modeling. *Journal of Dynamic Systems, Measurement, and Control* 2004; **126**:124–130.
17. Udwadia FE, Schutte AD. An alternative derivation of the quaternion equations of motion for rigid-body rotational dynamics. *Journal of Applied Mechanics* 2010; **77**:044505:1–4.
18. Möller M, Glocker C. Rigid body dynamics with a scalable body, quaternions and perfect constraints. *Multibody System Dynamics* 2012; **27**:437–454.
19. Betsch P, Steinmann P. Constrained integration of rigid body dynamics. *Computer Methods in Applied Mechanics and Engineering* 2001; **191**:467–488.
20. Betsch P, Leyendecker S. The discrete null space method for the energy consistent integration of constrained mechanical systems. Part II: multibody dynamics. *International Journal for Numerical Methods in Engineering* 2006; **67**:499–552.
21. Betsch P, Siebert R. Rigid body dynamics in terms of quaternions: Hamiltonian formulation and conserving numerical integration. *International Journal for Numerical Methods in Engineering* 2009; **79**:444–473.
22. Géradin M, Cardona A. *Flexible Multibody Dynamics: A Finite Element Approach*. Wiley: Chichester, UK, 2001.
23. Krenk S. *Non-linear Modeling and Analysis of Solids and Structures*. Cambridge University Press: Cambridge, UK, 2009.
24. Bauchau OA. *Flexible Multibody Dynamics*. Springer: Dordrecht, The Netherlands, 2010.
25. Goldstein H, Poole C, Safko J. *Classical Mechanics*, 3rd ed. Addison Wesley: San Francisco, 2001.
26. Krenk S. The role of geometric stiffness in momentum and energy conserving time integration. *International Journal for Numerical Methods in Engineering* 2007; **71**:631–651.
27. Lanczos C. *The Variational Principles of Mechanics*, 4th ed. Dover: New York, 1986.
28. Gonzalez O. Exact energy and momentum conserving algorithms for general models in nonlinear elasticity. *Computer Methods in Applied Mechanics and Engineering* 2000; **190**:1763–1783.

DOI: 10.1002/nme

P4

Conservative rigid body dynamics by convected base vectors with implicit constraints

S. Krenk & M.B. Nielsen

Computer Methods in Applied Mechanics and Engineering,
Vol **269**:437–453, 2014.

Comput. Methods Appl. Mech. Engrg. 269 (2014) 437–453

Contents lists available at ScienceDirect

Comput. Methods Appl. Mech. Engrg.

journal homepage: www.elsevier.com/locate/cma

Conservative rigid body dynamics by convected base vectors with implicit constraints

Steen Krenk *, Martin B. Nielsen

Department of Mechanical Engineering, Technical University of Denmark, DK-2800 Lyngby, Denmark

ARTICLE INFO

Article history:
Received 18 May 2013
Received in revised form 23 October 2013
Accepted 24 October 2013
Available online 7 November 2013

Keywords:
Rigid body dynamics
Conservative time integration
Implicit constraints
Hamiltonian dynamics

ABSTRACT

A conservative time integration formulation is developed for rigid bodies based on a convected set of orthonormal base vectors. The base vectors are represented in terms of their absolute coordinates, and thus the formulation makes use of three translation components, plus nine components of the base vectors. Orthogonality and unit length of the base vectors are imposed by constraining the equivalent Green strain components, and the kinetic energy is represented corresponding to rigid body motion. The equations of motion are obtained via Hamilton's equations including the zero-strain conditions as well as external constraints via Lagrange multipliers. Subsequently, the Lagrange multipliers associated with the internal zero-strain constraints are eliminated by use of a set of orthogonality conditions between the generalized displacements and the momentum vector, leaving a set of differential equations without additional algebraic constraints on the base vectors. A discretized form of the equations of motion is obtained by starting from a finite time increment of the Hamiltonian, and retracing the steps of the continuous formulation in discrete form in terms of increments and mean values over each integration time increment. In this discrete form the Lagrange multipliers are given in terms of a representative value within the integration time interval, and the equations of motion are recast into a conservative mean-value and finite difference format. The Lagrange multipliers are eliminated explicitly within each integration interval leaving a projection operator expressed in terms of displacement component mean values. Hereby the number of variables is reduced by six for each rigid body in the problem, and the difference equations lead to conservation of the orthonormality conditions for the local base vectors. Examples demonstrate the efficiency and accuracy of the procedure.

1. Introduction

Numerous computational methods for analyzing constrained mechanical systems have been developed over the last two decades. The governing equations of motion for a mechanical system with holonomic constraints typically yields a set of differential algebraic equations (DAEs) of index three, when constraint equations are included via Lagrange multipliers. Several methods exist for direct algebraic elimination of the Lagrange multipliers, which in addition to reducing the size the underlying equations leads to an index-reduction from three to two. The most widely used methods within constrained mechanical systems are Maggi's formulation, see e.g. [1], and the null space formulation, [2], where the Lagrange multipliers are eliminated by construction of an instantaneous null space matrix. Alternatively a Moore–Penrose generalized inverse can be used as described by Udwadia and Kabala [3]. The index can be further lowered by introducing the constraints in

* Corresponding author. Tel.: +45 40 60 17 02.
E-mail address: sk@mek.dtu.dk (S. Krenk).

0045-7825/$ - see front matter © 2013 Elsevier B.V. All rights reserved.
http://dx.doi.org/10.1016/j.cma.2013.10.028

differentiated form – typically at the acceleration level. However, common for these approaches is that the elimination process is performed prior to the discretization process. When recast into a discrete form the matrices used for elimination of the Lagrange multipliers depend on time, and therefore require evaluation at each time step. Furthermore, when constraints are enforced in differentiated form, use of classical time discretization schemes based on asymptotic properties typically lead to violation of the original constraints, also known as drift from the invariant constraint manifold. In these cases the numerical behavior can be improved by stabilizing the constraint equations by using e.g. Baumgarte stabilization [4] or penalty-based stabilization techniques based on an augmented Lagrangian formulation, [5]. Alternatively, constraint violations may be eliminated by geometric projection onto the constraints manifold, [6,7,8], where the latter is in the framework of the null space formulation. Comprehensive reviews of procedures for constraint enforcement have been given by Bauchau and Laulusa [9,10] and Bauchau [11].

The efficient and accurate handling of the constraints in the form of stable numerical schemes for time integration has been the subject of substantial research in recent years. A particular role has been taken by the energy and momentum conserving schemes, in which the underlying equations of motion are recast into incremental form by suitable integration of internal and external work as well as convection terms, thereby leading to the correct change in energy and momentum over a finite time step. These methods were originally developed for rigid body dynamics [12], and later extended to non-linear elastodynamics [13]. Gonzalez [14] presented energy and momentum conserving schemes for general models in non-linear elasticity via the introduction of a discrete derivative. A similar approach can be used for enforcing constraints in multibody dynamics. Rather than enforcing the constraints at discrete points in time, constraints can be enforced in incremental form along with the associated Lagrange multipliers represented by their mid-point value, see e.g. [15]. This is equivalent to imposing a condition of zero work done by the constraint forces. A fairly general mid-point based scheme with conservation properties for constrained multibody dynamics has been proposed by Lens et al. [16]. In the constraint elimination methods discussed above the constraint elimination is performed prior to the discretization in time, and these methods are therefore not well-suited for development of discrete conservative time integration schemes. A different path is followed in the discrete null space method [17]. The original equations are first discretized into an energy/momentum preserving form, and subsequently the Lagrange multipliers are eliminated via the discrete null space matrix, which constitutes the orthogonal complement to the gradient matrix of the constraints. In particular, the discrete null space matrix can be obtained in explicit form for are wide number of kinematic constraints as is illustrated in [18].

In the present paper a conservative time integration algorithm is presented, based on a direct discretization of Hamilton's equations for rigid body motion and the constraints in terms of finite increments in time. The formulation uses three translational components and nine convected base vector components as kinematic variables plus six Lagrange multipliers for enforcing orthonormality of the base vectors. The use of the local base vector components is similar to the approach in [19]. However, while in [19] the inertia of the body is represented via the constant Euler tensor, the present approach represents the kinematics of the rigid body rotation via the instantaneous angular velocity corresponding to rigid body rotation. Hereby the kinetic rotation energy is expressed directly in terms of the moment of inertia tensor of the rigid body. In this format the kinematic constraints of the base vectors are incorporated into the kinematic equations of motion, facilitating direct elimination of the Lagrange multipliers initially introduced to enforce the rigid-body constraints. The elimination is based on a set of orthogonality relations between the generalized displacements and their conjugate momentum variables, leaving only a projection operator applied to the gradients of the external potential and possible kinematic constraints.

2. Kinematics

The motion of a solid body is illustrated in Fig. 1. A local coordinate system with base vectors $\boldsymbol{q}_1, \boldsymbol{q}_2, \boldsymbol{q}_3$ is centered at a point O defined by the position vector $\boldsymbol{q}_0$. A point located inside the solid body with coordinates $\boldsymbol{x}_0 = [x_1^0, x_2^0, x_3^0]^T$ has the global components

$$\boldsymbol{x}(t) = \boldsymbol{q}_0(t) + \boldsymbol{Q}(t)\boldsymbol{x}_0, \tag{1}$$

where $\boldsymbol{Q}$ is the deformation gradient tensor, defined by

$$\boldsymbol{Q} = [\boldsymbol{q}_1, \boldsymbol{q}_2, \boldsymbol{q}_3] = \frac{\partial \boldsymbol{x}}{\partial \boldsymbol{x}_0}. \tag{2}$$

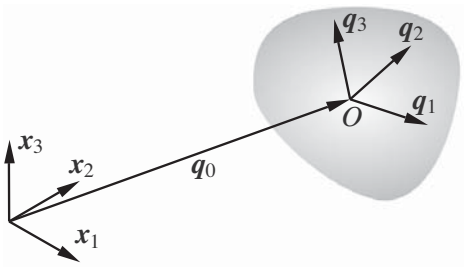

Fig. 1. Rigid body described by position vector $\boldsymbol{q}_0$ and base vectors $\boldsymbol{q}_1, \boldsymbol{q}_2, \boldsymbol{q}_3$.

In the case of a rigid body rotation the base vectors remain an orthonormal triple, as expressed by the matrix condition

$$\mathbf{Q}^T\mathbf{Q} = \mathbf{I}, \tag{3}$$

where $\mathbf{I}$ is the 3×3 unit matrix. In the following the global components of the position vector $\boldsymbol{q}_0$ and the base vectors $\boldsymbol{q}_1, \boldsymbol{q}_2, \boldsymbol{q}_3$ are used as independent variables, and the six independent equations contained in the rigid body condition (3) appear as constraints.

The kinetic energy of a body with volume V_0 can be expressed by the integral

$$T = \frac{1}{2}\int_{V_0} \dot{\boldsymbol{x}}^T\dot{\boldsymbol{x}}\rho dV_0, \tag{4}$$

where ρ denotes the mass density, and where the global velocity $\dot{\boldsymbol{x}}$ follows by differentiation of (1), as

$$\dot{\boldsymbol{x}} = \dot{\boldsymbol{q}}_0(t) + \dot{\mathbf{Q}}(t)\boldsymbol{x}_0. \tag{5}$$

When the reference point O is selected as the center of mass, the kinetic energy takes a particularly simple form where the translational kinetic energy of the center of mass T_t decouples from the rotational kinetic energy of the body T_r as

$$T = T_\mathrm{t} + T_\mathrm{r}. \tag{6}$$

First, the kinetic energy associated with translational motion is expressed in terms of the global velocity of the center of mass $\boldsymbol{v}$ as

$$T_\mathrm{t} = \frac{1}{2}\int_{V_0} \boldsymbol{v}^T\boldsymbol{v}\rho dV_0 = \frac{1}{2}m\dot{\boldsymbol{q}}_0^T\dot{\boldsymbol{q}}_0, \tag{7}$$

where m denotes the mass of the body, and $\dot{\boldsymbol{q}}_0$ is the velocity of the center of mass, corresponding to $\boldsymbol{x}_0 = \mathbf{0}$ in (5). Similarly, the rotational part of the kinetic energy can be expressed in terms of the velocity $\boldsymbol{v}_\mathrm{r}$ due to rotation in the form

$$T_\mathrm{r} = \frac{1}{2}\int_{V_0} \boldsymbol{v}_\mathrm{r}^T\boldsymbol{v}_\mathrm{r}\rho dV_0. \tag{8}$$

It is noted that $\boldsymbol{v}_\mathrm{r}$ is represented by its local components, while the translational velocity $\dot{\boldsymbol{q}}_0$ is in global components.

2.1. Rigid body motion

In the present formulation the kinetic energy is based on a rigid body rotating with angular velocity $\boldsymbol{\Omega}$. The rotation velocity can therefore be expressed in terms of the angular velocity $\boldsymbol{\Omega}$ as

$$\boldsymbol{v}_\mathrm{r} = \boldsymbol{\Omega} \times \boldsymbol{x}_0 = \hat{\boldsymbol{\Omega}}\boldsymbol{x}_0 = -\hat{\boldsymbol{x}}_0\boldsymbol{\Omega}, \tag{9}$$

where the symbol $\hat{(\,)}$ denotes the vector product via the skew-symmetric local component matrix

$$\hat{\boldsymbol{\Omega}} = \boldsymbol{\Omega}\times = \begin{bmatrix} 0 & -\Omega_3 & \Omega_2 \\ \Omega_3 & 0 & -\Omega_1 \\ -\Omega_2 & \Omega_1 & 0 \end{bmatrix}. \tag{10}$$

The rotation velocity $\boldsymbol{v}_\mathrm{r}$ is expressed in local components by the last expression in (9) and substituted into (8), whereby

$$T_\mathrm{r} = \frac{1}{2}\boldsymbol{\Omega}^T\left(\int_{V_0} \hat{\boldsymbol{x}}_0^T\hat{\boldsymbol{x}}_0\rho dV_0\right)\boldsymbol{\Omega} = \frac{1}{2}\boldsymbol{\Omega}^T\boldsymbol{J}\boldsymbol{\Omega}. \tag{11}$$

The inertia tensor is defined by the volume integral

$$\boldsymbol{J} = \int_{V_0} \hat{\boldsymbol{x}}_0^T\hat{\boldsymbol{x}}_0\rho dV_0 = \int_{V_0} (\boldsymbol{x}_0^T\boldsymbol{x}_0\mathbf{I} - \boldsymbol{x}_0\boldsymbol{x}_0^T)\rho dV_0, \tag{12}$$

conveniently expressed in local components, whereby $\boldsymbol{J}$ is constant.

When assuming that the base vectors remain orthonormal, the local components of the angular velocity can be expressed by projection of the base vector derivatives $\dot{\boldsymbol{q}}_i$ on the base vectors $\boldsymbol{q}_j$ via the relations

$$\begin{aligned} \Omega_1 &= \dot{\boldsymbol{q}}_2^T\boldsymbol{q}_3 = -\dot{\boldsymbol{q}}_3^T\boldsymbol{q}_2, \\ \Omega_2 &= \dot{\boldsymbol{q}}_3^T\boldsymbol{q}_1 = -\dot{\boldsymbol{q}}_1^T\boldsymbol{q}_3, \\ \Omega_3 &= \dot{\boldsymbol{q}}_1^T\boldsymbol{q}_2 = -\dot{\boldsymbol{q}}_2^T\boldsymbol{q}_1. \end{aligned} \tag{13}$$

These relations are conveniently given in matrix format by arranging the global components of the base vectors in column format as

$$\boldsymbol{q} = [\boldsymbol{q}_1^T, \boldsymbol{q}_2^T, \boldsymbol{q}_3^T]^T. \tag{14}$$

The angular velocity is then given as

$$\boldsymbol{\Omega} = -\frac{1}{2}\boldsymbol{G}(\boldsymbol{q})\dot{\boldsymbol{q}} = \frac{1}{2}\boldsymbol{G}(\dot{\boldsymbol{q}})\boldsymbol{q}, \tag{15}$$

in terms of the matrix

$$\boldsymbol{G}(\boldsymbol{q}) = \begin{bmatrix} \boldsymbol{0} & -\boldsymbol{q}_3^T & \boldsymbol{q}_2^T \\ \boldsymbol{q}_3^T & \boldsymbol{0} & -\boldsymbol{q}_1^T \\ -\boldsymbol{q}_2^T & \boldsymbol{q}_1^T & \boldsymbol{0} \end{bmatrix}. \tag{16}$$

The matrix $\boldsymbol{G}(\boldsymbol{q})$ has the same structure in terms of the three vectors $\boldsymbol{q}_1, \boldsymbol{q}_3, \boldsymbol{q}_3$, as the skew-symmetric 3×3 matrix for the vector product defined by the symbol $(\hat{\ })$ in (10). The structure of the $\boldsymbol{G}$-matrix implies the identity

$$\underset{3\times 9}{\boldsymbol{G}(\boldsymbol{q})\boldsymbol{q}} = \underset{3\times 1}{\boldsymbol{0}}. \tag{17}$$

It is convenient to combine the expressions for the global translation velocity $\boldsymbol{v}$ and local components of the angular velocity $\boldsymbol{\Omega}$ in terms of the vector of independent coordinates $\mathbf{q}^T = [\boldsymbol{q}_0^T, \boldsymbol{q}_1^T, \boldsymbol{q}_2^T, \boldsymbol{q}_3^T]$ in the compact matrix format

$$\begin{bmatrix} \boldsymbol{v} \\ \boldsymbol{\Omega} \end{bmatrix} = \begin{bmatrix} \mathbf{I} & \mathbf{0} \\ \mathbf{0} & -\frac{1}{2}\boldsymbol{G}(\boldsymbol{q}) \end{bmatrix} \begin{bmatrix} \dot{\boldsymbol{q}}_0 \\ \dot{\boldsymbol{q}} \end{bmatrix} = \mathbf{G}(\mathbf{q})\dot{\mathbf{q}}, \tag{18}$$

where the 6×12 matrix $\mathbf{G}(\mathbf{q})$ is a block diagonal form of the $\boldsymbol{G}$-matrix from (16) and a 3×3 unit matrix $\mathbf{I}$. In the particular case, where the base vectors $\boldsymbol{q}_j$ are orthonormal, the matrix $\mathbf{G}(\mathbf{q})$ satisfies the orthogonality relation

$$\underset{6\times 12}{\mathbf{G}(\mathbf{q})}\ \underset{12\times 6}{\mathbf{G}(\mathbf{q})}^T = \begin{bmatrix} \mathbf{I} & \mathbf{0} \\ \mathbf{0} & \frac{1}{2}\mathbf{I} \end{bmatrix}. \tag{19}$$

In essence this relation defines a generalized inverse of the matrix $\mathbf{G}(\mathbf{q})^T$.

The kinetic energy associated with rigid body motion can now be expressed in terms of the current value of $\mathbf{q}$ and the time derivative $\dot{\mathbf{q}}$ by substitution of the translation velocity and angular velocity from (18) into the expressions (7) and (11), whereby

$$T = \frac{1}{2}\begin{bmatrix} \boldsymbol{v}^T & \boldsymbol{\Omega}^T \end{bmatrix} \begin{bmatrix} m\mathbf{I} & \\ & \boldsymbol{J} \end{bmatrix} \begin{bmatrix} \boldsymbol{v} \\ \boldsymbol{\Omega} \end{bmatrix} = \frac{1}{2}\dot{\mathbf{q}}^T\mathbf{G}(\mathbf{q})^T\mathbf{J}\mathbf{G}(\mathbf{q})\dot{\mathbf{q}}. \tag{20}$$

The extended inertia tensor $\mathbf{J}$ is introduced as a block diagonal form of the mass m and the inertia tensor $\boldsymbol{J}$. This expression for the kinetic energy is based on the assumption of rigid body motion, as expressed by the constraint equations (3).

2.2. Rigid body constraints

The rigid body constraints (3) on the deformation gradient matrix $\mathbf{Q}$ correspond to vanishing of all Green strain components, as expressed by the matrix relation

$$\boldsymbol{E} = \frac{1}{2}\left(\mathbf{Q}^T\mathbf{Q} - \mathbf{I}\right) = \mathbf{0}. \tag{21}$$

When expressed in terms of the columns $\boldsymbol{q}_j$ of the deformation gradient tensor $\mathbf{Q}$ the six independent strain components are

$$\mathbf{e}(\mathbf{q}) = \frac{1}{2}\begin{bmatrix} \boldsymbol{q}_1^T\boldsymbol{q}_1 - 1 \\ \boldsymbol{q}_2^T\boldsymbol{q}_2 - 1 \\ \boldsymbol{q}_3^T\boldsymbol{q}_3 - 1 \\ \boldsymbol{q}_2^T\boldsymbol{q}_3 + \boldsymbol{q}_3^T\boldsymbol{q}_2 \\ \boldsymbol{q}_3^T\boldsymbol{q}_1 + \boldsymbol{q}_1^T\boldsymbol{q}_3 \\ \boldsymbol{q}_1^T\boldsymbol{q}_2 + \boldsymbol{q}_2^T\boldsymbol{q}_1 \end{bmatrix}. \tag{22}$$

The kinematic constraints appear in the present formulation through their time derivative, conveniently written in the form

$$\dot{\mathbf{e}} = \mathbf{C}(\mathbf{q})\dot{\mathbf{q}} = \mathbf{C}(\dot{\mathbf{q}})\mathbf{q} = \mathbf{0}, \tag{23}$$

with the rearranged 6×12 deformation gradient matrix

$$\mathbf{C}(\mathbf{q}) = \frac{\partial \mathbf{e}}{\partial \mathbf{q}} = \begin{bmatrix} \mathbf{0} & \boldsymbol{q}_1^T & \mathbf{0} & \mathbf{0} \\ \mathbf{0} & \mathbf{0} & \boldsymbol{q}_2^T & \mathbf{0} \\ \mathbf{0} & \mathbf{0} & \mathbf{0} & \boldsymbol{q}_3^T \\ \mathbf{0} & \mathbf{0} & \boldsymbol{q}_3^T & \boldsymbol{q}_2^T \\ \mathbf{0} & \boldsymbol{q}_3^T & \mathbf{0} & \boldsymbol{q}_1^T \\ \mathbf{0} & \boldsymbol{q}_2^T & \boldsymbol{q}_1^T & \mathbf{0} \end{bmatrix}. \tag{24}$$

In the present formulation $\mathbf{C}(\mathbf{q})$ acts as constraint matrix. It satisfies the orthogonality relation

$$\underset{6\times 12}{\mathbf{C}(\mathbf{q})}\ \underset{12\times 6}{\mathbf{C}(\mathbf{q})}^{\,T} = \begin{bmatrix} \mathbf{I} & \mathbf{0} \\ \mathbf{0} & 2\mathbf{I} \end{bmatrix}, \tag{25}$$

provided the base vectors $\boldsymbol{q}_j$ are orthonormal. The factor 2 on the lower diagonal block is due to the representation of shear strains in terms of angular strain.

It is an important property of the present formulation that for orthonormal base vectors $\boldsymbol{q}_j$ the constraint matrix $\mathbf{C}(\mathbf{q})$ is orthogonal to the rotation matrix $\mathbf{G}(\mathbf{q})$ in the sense

$$\underset{6\times 12}{\mathbf{C}(\mathbf{q})}\ \underset{12\times 6}{\mathbf{G}(\mathbf{q})}^{\,T} = \underset{6\times 6}{\mathbf{0}} \tag{26}$$

This relation follows directly by substitution of the matrix definitions (24) and (16).

3. Dynamics

The equations governing the motion for a constrained rigid body can be obtained via the variational principles of Lagrange and Hamilton, see e.g. [20]. Here, the equations of motion for translational and rotational motion are derived simultaneously based on the kinetic energy (20) with extended inertia tensor.

3.1. Kinetic energy and momentum

The momentum components $\mathbf{p} = [\boldsymbol{p}_0^T, \boldsymbol{p}_1^T, \boldsymbol{p}_2^T, \boldsymbol{p}_3^T]^T$ associated with the motion described by the kinematic components $\mathbf{q} = [\boldsymbol{q}_0^T, \boldsymbol{q}_1^T, \boldsymbol{q}_2^T, \boldsymbol{q}_3^T]^T$ follow from differentiation of the kinetic energy (20) as

$$\mathbf{p} = \frac{\partial T}{\partial \dot{\mathbf{q}}^T} = \mathbf{G}(\mathbf{q})^T \mathbb{J} \mathbf{G}(\mathbf{q}) \dot{\mathbf{q}}. \tag{27}$$

This relation gives the momentum $\mathbf{p}$ in terms of the generalized velocity $\dot{\mathbf{q}}$. In order to obtain the Hamiltonian as a function of the generalized displacements $\mathbf{q}$ and the corresponding momentum $\mathbf{p}$ the relation (27) must be inverted. For a rigid body the base vectors $\boldsymbol{q}_j$ are orthonormal, and it then follows from pre-multiplication with $\mathbf{G}(\mathbf{q})$ that

$$\mathbf{G}(\mathbf{q})\mathbf{p} = \mathbf{G}(\mathbf{q})\mathbf{G}(\mathbf{q})^T \mathbb{J} \mathbf{G}(\mathbf{q}) \dot{\mathbf{q}} = \begin{bmatrix} \mathbf{I} & \mathbf{0} \\ \mathbf{0} & \frac{1}{2}\mathbf{I} \end{bmatrix} \mathbb{J} \mathbf{G}(\mathbf{q}) \dot{\mathbf{q}}, \tag{28}$$

where the orthogonality relation (19) has been used. This relation is now used to eliminate $\dot{\mathbf{q}}$ from the kinetic energy (20), whereby the following expressions in terms of the momentum vector $\mathbf{p}$ are obtained,

$$T(\mathbf{q}, \mathbf{p}) = \frac{1}{2} \mathbf{p}^T \mathbf{G}(\mathbf{q})^T \begin{bmatrix} m^{-1}\mathbf{I} & \mathbf{0} \\ \mathbf{0} & 4\boldsymbol{J}^{-1} \end{bmatrix} \mathbf{G}(\mathbf{q})\mathbf{p} = \frac{1}{2} \mathbf{p}^T \mathbf{G}(\mathbf{q})^T \mathbb{J}^{-1} \mathbf{G}(\mathbf{q}) \mathbf{p}. \tag{29}$$

The factor 4 appears in the lower block of the inertia matrix because the rotation matrix $\boldsymbol{G}$ constituting the lower block of $\mathbf{G}$ is not normalized, but satisfies the product relation $\boldsymbol{G}\boldsymbol{G}^T = 2\mathbf{I}$. This is accounted for by including a factor 4 on the inverse inertia tensor $\boldsymbol{J}^{-1}$ associated with rotational motion in the matrix $\mathbb{J}^{-1}$. This relation serves as the basis of a Hamilton formulation of the dynamic equations of motion for rigid body rotation.

The choice of the local reference point O as the center of mass gives the matrices in the kinetic energy a block-diagonal structure, whereby generalized momentum $\boldsymbol{p}_0$ is the momentum associated with the translation $\boldsymbol{q}_0$ of O. The local angular momentum with respect to the origin of the local frame O is obtained by representing the angular velocity in terms of $\boldsymbol{q}$ and $\dot{\boldsymbol{q}}$ via (15),

$$\boldsymbol{L} = \boldsymbol{J}\boldsymbol{\Omega} = -\frac{1}{2}\boldsymbol{J}\boldsymbol{G}(\boldsymbol{q})\dot{\boldsymbol{q}}. \tag{30}$$

The momentum vector $\boldsymbol{p}$ associated with the rotation of the base vectors can be expressed in terms of the angular momentum $\boldsymbol{L}$ by pre-multiplication of (30) with the rotation matrix $-\frac{1}{2}\boldsymbol{G}(\boldsymbol{q})^T$, introduced in (15) to represent the angular velocity,

$$-\frac{1}{2}\boldsymbol{G}(\boldsymbol{q})^T\boldsymbol{L}=\frac{1}{4}\boldsymbol{G}(\boldsymbol{q})^T\boldsymbol{J}\boldsymbol{G}(\boldsymbol{q})\dot{\boldsymbol{q}}=\boldsymbol{p}, \tag{31}$$

where the last equality follows from the momentum definition (27), when recalling the factor $\frac{1}{2}$ in the relation (18) between the matrices $\boldsymbol{G}(\boldsymbol{q})$ and $\mathbf{G}(\mathbf{q})$. For a rigid body the matrix $\boldsymbol{G}(\boldsymbol{q})$ satisfies the orthogonality relation (19), and thus the magnitude of the angular momentum vector takes the form

$$\|\boldsymbol{p}\|^2=\boldsymbol{p}^T\boldsymbol{p}=\frac{1}{4}\boldsymbol{L}^T\boldsymbol{G}(\boldsymbol{q})\boldsymbol{G}(\boldsymbol{q})^T\boldsymbol{L}=\frac{1}{2}\|\boldsymbol{L}\|^2. \tag{32}$$

In case of free rigid body rotation this length represents an invariant and the conservation of this property is considered in the following sections. It is seen that while the vector relation (31) between $\boldsymbol{L}$ and $\boldsymbol{p}$ contains a transformation matrix the lengths of the two vectors are related by a constant factor. Conservation properties for the generalized momentum vector $\mathbf{p}$ are considered in Section 3.4.

3.2. Hamilton's equations

The present formulation is based on an extended form of Hamilton's energy functional in which the sum of the rotational kinetic energy $T(\mathbf{q},\mathbf{p})$ and the potential energy function $V(\mathbf{q})$ is augmented by a set of zero Green strain constraints specified via (22). Furthermore external constraints e.g. associated with the presence of joints may be included, whereby the augmented Hamiltonian can takes the form

$$H(\mathbf{q},\mathbf{p})=T(\mathbf{q},\mathbf{p})+V(\mathbf{q})+\boldsymbol{\Phi}(\mathbf{q})^T\boldsymbol{\lambda}-\mathbf{e}(\mathbf{q})^T\boldsymbol{\gamma}. \tag{33}$$

Here $\mathbf{e}(\mathbf{q})$ is the six-component strain vector (22) associated with deformation of the basis $\boldsymbol{q}_j$, and $\boldsymbol{\gamma}$ is the corresponding six-component vector of Lagrange multipliers, while $\boldsymbol{\Phi}(\mathbf{q})$ and the corresponding vector of Lagrange multipliers $\boldsymbol{\lambda}$ account for the external constraints.The equations of motion follow from the extended Hamiltonian (33) by differentiation, using the expression (29) for the kinetic energy,

$$\dot{\mathbf{q}}=\frac{\partial H}{\partial\mathbf{p}^T}=\mathbf{G}(\mathbf{q})^T\mathbb{J}^{-1}\mathbf{G}(\mathbf{q})\mathbf{p}, \tag{34}$$

$$\dot{\mathbf{p}}=\frac{\partial H}{\partial\mathbf{q}^T}=-\mathbf{G}(\mathbf{p})^T\mathbb{J}_0^{-1}\mathbf{G}(\mathbf{p})\mathbf{q}-\frac{\partial V}{\partial\mathbf{q}^T}-\left(\frac{\partial\boldsymbol{\Phi}}{\partial\mathbf{q}}\right)^T\boldsymbol{\lambda}+\mathbf{C}(\mathbf{q})^T\boldsymbol{\gamma}. \tag{35}$$

The constraint matrix $\mathbf{C}(\mathbf{q})^T$ in the last term of the second equation is the derivative of the strain vector, as shown in (23). The kinetic energy is independent of the translation $\boldsymbol{q}_0$, and thus the upper left diagonal block in the extended inertia tensor in the second equation vanishes. This is denoted by a subscript as $\mathbb{J}_0^{-1}=\mathrm{diag}[\mathbf{0},4\boldsymbol{J}^{-1}]$. The first equation (34) is the kinematic equation for the development of the generalized displacement vector, while the dynamic equation (35) gives the development of the conjugate momentum vector.In the case of an augmented Hamiltonian, the equations associated with the external constraints may be obtained from stationarity with respect to $\boldsymbol{\lambda}$. This gives the external constraint equation,

$$\frac{\partial H}{\partial\boldsymbol{\lambda}^T}=\boldsymbol{\Phi}(\mathbf{q})=\mathbf{0}. \tag{36}$$

A particular feature of the present formulation is that the Lagrange multipliers $\boldsymbol{\gamma}$ associated with internal constraints (23) can be eliminated, whereby these constraints do not appear directly in the final equations.

3.3. Momentum constraint equation

The representation of the kinetic energy via the three-component angular velocity of a rigid body leads to the key property of the present formulation, that the time derivative of the six constraints are then included in the kinematic equation (34). Substitution of $\dot{\mathbf{q}}$ from the kinematic evolution equation (34) into the strain rate expression (23) gives

$$\dot{\mathbf{e}}=\mathbf{C}(\mathbf{q})\mathbf{G}(\mathbf{q})^T\mathbf{J}^{-1}\mathbf{G}(\mathbf{q})\mathbf{p}=\mathbf{0}, \tag{37}$$

where the last equality follows from the matrix product relation (26), which is valid when the vectors $\boldsymbol{q}_j$ constitute an orthonormal basis. Thus, when starting with an orthonormal basis $\boldsymbol{q}_j$, this property will be propagated via the kinematic Hamilton equation (34).

A central point in the present formulation is the elimination of the Lagrange multipliers $\boldsymbol{\gamma}$ associated with the orthonormality constraints on the base vectors. This is accomplished by establishing a set of orthogonality relations between the convected base vectors $\boldsymbol{q}_j$ and the corresponding momentum vectors $\boldsymbol{p}_k$. The defining relation (27) of the momentum vector is pre-multiplied by the constraint matrix $\mathbf{C}(\mathbf{q})$,

$$\mathbf{C}(\mathbf{q})\mathbf{p}=\mathbf{C}(\mathbf{q})\mathbf{G}(\mathbf{q})^T\mathbf{J}\mathbf{G}(\mathbf{q})\dot{\mathbf{q}}. \tag{38}$$

According to (26) the product of the constraint matrix $\mathbf{C}(\mathbf{q})$ and the rotation matrix $\mathbf{G}(\mathbf{q})^T$ vanishes, leaving the six orthogonality relations

$$\mathbf{C}(\mathbf{q})\mathbf{p} = \mathbf{0}. \tag{39}$$

These relations constitute a complement to the kinematic constraints (23), and correspond to replacing $\dot{\mathbf{q}}$ by $\mathbf{p}$. They play central roles both in connection with momentum conservation and elimination of the Lagrange multipliers associated with orthonormality of the base vectors $\mathbf{q}_j$, as discussed in the following two sections.

3.4. Conservation of momentum

It was shown in (37) that the time-derivatives of the zero-strain constraints are contained in the kinematic equation of motion. A conservation equation for the magnitude of the local angular momentum $\|\boldsymbol{L}\|$ is obtained by pre-multiplication of the rotational part $\dot{\boldsymbol{p}}$ in the dynamic equation of motion (35) with the corresponding momentum vector $\boldsymbol{p}$. The first term vanishes due to the skew-symmetric structure of $\boldsymbol{G}(\boldsymbol{p})$. Furthermore, the last term vanishes due to the displacement-momentum orthogonality relation (39). This leaves the result

$$\frac{1}{4}\frac{d(\|\boldsymbol{L}\|^2)}{dt} = \boldsymbol{p}^T\dot{\boldsymbol{p}} = -\boldsymbol{p}^T\left[\frac{\partial V}{\partial \boldsymbol{q}^T} + \left(\frac{\partial \boldsymbol{\Phi}}{\partial \boldsymbol{q}}\right)^T\boldsymbol{\lambda}\right] \tag{40}$$

showing conservation of the length of the local angular momentum vector $\boldsymbol{L}$ in the absence of external loads and constraints.

Component relations for the linear and angular momentum are obtained as follows. As already observed the linear momentum is equal to $\boldsymbol{p}_0$. The angular momentum is obtained by pre-multiplication of the relation (31) with $\boldsymbol{G}(\boldsymbol{q})$, whereby

$$\boldsymbol{G}(\boldsymbol{q})\boldsymbol{p} = -\frac{1}{2}\boldsymbol{G}(\boldsymbol{q})\boldsymbol{G}(\boldsymbol{q})^T\boldsymbol{L} = -\boldsymbol{L}, \tag{41}$$

where the last equality follows from the lower part of the orthogonality relation (19). This gives the following relation between the linear and the angular momentum $\boldsymbol{p}_0$ and $\boldsymbol{L}$, and the 12-component generalized momentum vector $\mathbf{p}$,

$$\begin{bmatrix}\boldsymbol{p}_0 \\ \frac{1}{2}\boldsymbol{L}\end{bmatrix} = \mathbf{G}(\mathbf{q})\mathbf{p}. \tag{42}$$

The three first components in this relation are the global components of the linear momentum, while the three last components are the local components of the angular momentum.

Conservation properties are associated with the absolute derivative, and the angular momentum $\boldsymbol{L}$ must therefore be transformed into global components, differentiated and the derivative then transformed back into local components, as expressed by

$$\frac{D\boldsymbol{L}}{Dt} = -\boldsymbol{Q}^T\frac{d}{dt}[\boldsymbol{Q}\boldsymbol{G}(\boldsymbol{q})\boldsymbol{p}] = -\frac{d}{dt}[\boldsymbol{G}(\boldsymbol{q})\boldsymbol{p}] - \boldsymbol{Q}^T\dot{\boldsymbol{Q}}[\boldsymbol{G}(\boldsymbol{q})\boldsymbol{p}], \tag{43}$$

where the factors on the last term represents the rotation of the base vectors. When the vectors $\boldsymbol{q}_j$ constitute an orthonormal basis this rotation factor can be expressed as

$$-\boldsymbol{Q}^T\dot{\boldsymbol{Q}} = \dot{\boldsymbol{Q}}^T\boldsymbol{Q} = \boldsymbol{G}(\dot{\boldsymbol{q}})\boldsymbol{G}(\boldsymbol{q})^T. \tag{44}$$

When using this result the last term in the absolute derivative (43) can be expressed as

$$-\boldsymbol{Q}^T\dot{\boldsymbol{Q}}[\boldsymbol{G}(\boldsymbol{q})\boldsymbol{p}] = \boldsymbol{G}(\dot{\boldsymbol{q}})\Big[\boldsymbol{G}(\boldsymbol{q})^T\boldsymbol{G}(\boldsymbol{q})\Big]\boldsymbol{p} = 2\boldsymbol{G}(\dot{\boldsymbol{q}})\boldsymbol{p}. \tag{45}$$

The last equality is obtained by using the momentum constraint equations (39) to rearrange terms in the matrix within the square brackets. When substituting this expression into (43), the absolute time derivative of the angular momentum is obtained in the form

$$\frac{D\boldsymbol{L}}{Dt} = \boldsymbol{G}(\dot{\boldsymbol{q}})\boldsymbol{p} - \boldsymbol{G}(\boldsymbol{q})\dot{\boldsymbol{p}} = -\boldsymbol{G}(\boldsymbol{p})\dot{\boldsymbol{q}} - \boldsymbol{G}(\boldsymbol{q})\dot{\boldsymbol{p}}. \tag{46}$$

It is seen that the effect of the rotation of the basis is to change the sign of the first term.In order to establish the momentum conservation properties it is convenient to combine the linear and angular momentum derivatives in the form

$$\frac{D}{Dt}[\mathbf{G}(\mathbf{q})\mathbf{p}] = \mathbf{G}_0(\mathbf{p})\dot{\mathbf{q}} + \mathbf{G}(\mathbf{q})\dot{\mathbf{p}}. \tag{47}$$

where the matrix $\mathbf{G}_0$ is obtained from $\mathbf{G}$ by omitting the unit matrix in the upper left diagonal position. The time derivatives $\dot{\mathbf{q}}$ and $\dot{\mathbf{p}}$ are now substituted from the Hamilton Equations (34) and (35), whereby

$$\frac{D}{Dt}[\mathbf{G}(\mathbf{q})\mathbf{p}] = \mathbf{G}_0(\mathbf{p})\mathbf{G}(\mathbf{q})^T\mathbb{J}^{-1}\mathbf{G}(\mathbf{q})\mathbf{p} - \mathbf{G}(\mathbf{q})\mathbf{G}(\mathbf{p})^T\mathbb{J}_0^{-1}\mathbf{G}(\mathbf{p})\mathbf{q} - \mathbf{G}(\mathbf{q})\left[\frac{\partial V}{\partial \mathbf{q}^T} + \left(\frac{\partial \boldsymbol{\Phi}}{\partial \mathbf{q}}\right)^T\boldsymbol{\lambda} - \mathbf{C}(\mathbf{q})^T\boldsymbol{\gamma}\right]. \tag{48}$$

The result from the last term in the square brackets vanishes due to the orthogonality relation (26) between the matrix $\mathbf{G}(\mathbf{q})$ and the constraint matrix $\mathbf{C}(\mathbf{q})$. The first two terms are reduced by observing that due to the diagonal block matrix format of the matrices $\mathbf{G}$ and $\mathbb{J}^{-1}$ the presence of a factor with vanishing upper left block will eliminate the corresponding block in a product of these matrices. Thus, only the lower right diagonal blocks contribute to the first two terms. The structure of the matrix $\boldsymbol{G}$ implies that $\mathbf{G}_0(\mathbf{p})\mathbf{q} = -\mathbf{G}_0(\mathbf{q})\mathbf{p}$, and thus the equation reduces to

$$\frac{D}{Dt}[\mathbf{G}(\mathbf{q})\mathbf{p}] = \left[\mathbf{G}_0(\mathbf{p})\mathbf{G}_0(\mathbf{q})^T + \mathbf{G}_0(\mathbf{q})\mathbf{G}_0(\mathbf{p})^T\right]\mathbb{J}_0^{-1}\mathbf{G}_0(\mathbf{q})\mathbf{p} - \mathbf{G}(\mathbf{q})\left[\frac{\partial V}{\partial \mathbf{q}^T} + \left(\frac{\partial \boldsymbol{\Phi}}{\partial \mathbf{q}}\right)^T \boldsymbol{\lambda}\right]. \tag{49}$$

Finally, when carrying out the matrix products in the first set of brackets the resulting diagonal terms vanish due to the first three momentum constraint conditions in (39), while the off-diagonal terms vanish due to the last three conditions. This leaves the momentum balance equation in the form

$$\frac{D}{Dt}[\mathbf{G}(\mathbf{q})\mathbf{p}] = -\mathbf{G}(\mathbf{q})\left[\frac{\partial V}{\partial \mathbf{q}^T} + \left(\frac{\partial \boldsymbol{\Phi}}{\partial \mathbf{q}}\right)^T \boldsymbol{\lambda}\right]. \tag{50}$$

These equations demonstrate conservation of linear and angular momentum components without external or constraint force components. Furthermore, mutual constraints linking two bodies lead to constraint forces that cancel when considering the total momentum of the combined system. As demonstrated in the examples in Section 5, this conservation property is retained in the discretized time integration algorithm.

3.5. Elimination of internal constraints

The Lagrange multipliers $\boldsymbol{\gamma}$ associated with the internal constraints that maintain orthonormality of the local basis are eliminated by use of the momentum constraint equations (39). Time differentiation of the displacement-momentum constraint relation gives the equation

$$\mathbf{C}(\mathbf{p})\dot{\mathbf{q}} + \mathbf{C}(\mathbf{q})\dot{\mathbf{p}} = \mathbf{0}, \tag{51}$$

where the positions of the factors $\dot{\mathbf{q}}$ and $\mathbf{p}$ have been interchanged in the first term. It may be noted that the form of this incremental constraint relation is similar to the absolute derivative of the momentum vector (47), when replacing the rotation matrix with the constraint matrix. Substitution of the time derivatives $\dot{\mathbf{q}}$ and $\dot{\mathbf{p}}$ from (34) and (35) gives

$$\mathbf{C}(\mathbf{p})\mathbf{G}(\mathbf{q})^T\mathbb{J}^{-1}\mathbf{G}(\mathbf{q})\mathbf{p} - \mathbf{C}(\mathbf{q})\mathbf{G}(\mathbf{p})^T\mathbb{J}_0^{-1}\mathbf{G}(\mathbf{p})\mathbf{q} - \mathbf{C}(\mathbf{q})\left[\frac{\partial V}{\partial \mathbf{q}^T} + \left(\frac{\partial \boldsymbol{\Phi}}{\partial \mathbf{q}}\right)^T \boldsymbol{\lambda} - \mathbf{C}(\mathbf{q})^T\boldsymbol{\gamma}\right] = \mathbf{0}. \tag{52}$$

The structure of the matrix $\mathbf{C}(\mathbf{q})$ eliminates contributions from translational components. Furthermore, it can be demonstrated by direct computation and use of the displacement-momentum orthogonality relation (39) that the matrix products constituting the first part of the two first terms satisfy the identity

$$\mathbf{C}(\mathbf{p})\mathbf{G}(\mathbf{q})^T + \mathbf{C}(\mathbf{q})\mathbf{G}(\mathbf{p})^T = \mathbf{0}, \tag{53}$$

When interchanging the roles of $\mathbf{q}$ and $\mathbf{p}$ in the last two factors of the second term in (52) the sign changes, and the identity (53) then leads to cancellation of the first two terms. This leaves the much simplified equation

$$\mathbf{C}(\mathbf{q})\left[\frac{\partial V}{\partial \mathbf{q}^T} + \left(\frac{\partial \boldsymbol{\Phi}}{\partial \mathbf{q}}\right)^T \boldsymbol{\lambda} - \mathbf{C}(\mathbf{q})^T\boldsymbol{\gamma}\right] = \mathbf{0}, \tag{54}$$

which determines the Lagrange multiplier vector as

$$\boldsymbol{\gamma} = \left[\mathbf{C}(\mathbf{q})\mathbf{C}(\mathbf{q})^T\right]^{-1}\mathbf{C}(\mathbf{q})\left[\frac{\partial V}{\partial \mathbf{q}^T} + \left(\frac{\partial \boldsymbol{\Phi}}{\partial \mathbf{q}}\right)^T \boldsymbol{\lambda}\right]. \tag{55}$$

It is notable that the internal Lagrange multiplier vector $\boldsymbol{\gamma}$ vanishes in the absence of external loads and external constraints. In fact, the corresponding homogeneous Hamilton equations can be solved directly without imposing the internal constraints explicitly.

Substitution of the internal Lagrange multiplier from (55) gives the dynamic Hamilton equation (35) in the form

$$\dot{\mathbf{p}} = -\mathbf{G}(\mathbf{p})^T\mathbb{J}_0^{-1}\mathbf{G}(\mathbf{p})\mathbf{q} - \left(\mathbf{I} - \mathbf{C}(\mathbf{q})^T\left[\mathbf{C}(\mathbf{q})\mathbf{C}(\mathbf{q})^T\right]^{-1}\mathbf{C}(\mathbf{q})\right)\left[\frac{\partial V}{\partial \mathbf{q}^T} + \left(\frac{\partial \boldsymbol{\Phi}}{\partial \mathbf{q}}\right)^T \boldsymbol{\lambda}\right]. \tag{56}$$

It follows from (25) that when $\mathbf{q}_j$ is an orthogonal basis, the inverse matrix has the simple diagonal form

$$\left[\mathbf{C}(\mathbf{q})\mathbf{C}(\mathbf{q})^T\right]^{-1} = \begin{bmatrix} \mathbf{I} & \mathbf{0} \\ \mathbf{0} & \frac{1}{2}\mathbf{I} \end{bmatrix}. \tag{57}$$

When the modified dynamic Hamilton equation (56) is solved together with the kinematic Hamilton equation (34), the constraints are maintained via their time derivatives, and the contribution from the external force potential and the external constraint gradients act via a projection operator without reference to a Lagrange multiplier. A similar feature was found in [21] regarding elimination of the Lagrange multiplier associated with the scalar constraint for quaternion parameters.

The extended dynamic Hamilton equation (56) can be given a simplified form in which the constraint matrix $\mathbf{C}(\mathbf{q})$ does not appear. In the projection operator appearing in front of the potential gradient and the external constraint gradient in (56) the projection of the gradients on the deformation modes via the constraint matrix $\mathbf{C}(\mathbf{q})$ is subtracted from the unconstrained gradients. The remaining part corresponds to the components in terms of rotation modes. In fact, this part can be obtained directly by projection on the rotation modes by use of the matrix $\mathbf{G}(\mathbf{q})$. Direct substitution of the vector expressions of the matrices gives the following identity, when $\mathbf{q}$ represents an orthonormal basis,

$$\mathbf{I} - \mathbf{C}(\mathbf{q})^T\left[\mathbf{C}(\mathbf{q})\mathbf{C}(\mathbf{q})^T\right]^{-1}\mathbf{C}(\mathbf{q}) = \mathbf{G}(\mathbf{q})^T[\mathbf{G}(\mathbf{q})\mathbf{G}(\mathbf{q})^T]^{-1}\mathbf{G}(\mathbf{q}). \tag{58}$$

This leads to the more compact form of the dynamic Hamilton equation

$$\dot{\mathbf{p}} = -\frac{\partial H}{\partial \mathbf{q}^T} = -\mathbf{G}(\mathbf{p})^T\mathbf{J}^{-1}\mathbf{G}(\mathbf{p})\mathbf{q} - \mathbf{G}(\mathbf{q})^T[\mathbf{G}(\mathbf{q})\mathbf{G}(\mathbf{q})^T]^{-1}\mathbf{G}(\mathbf{q})\left[\frac{\partial V}{\partial \mathbf{q}^T} + \left(\frac{\partial \boldsymbol{\Phi}}{\partial \mathbf{q}}\right)^T\boldsymbol{\lambda}\right], \tag{59}$$

where the constraint matrix $\mathbf{C}(\mathbf{q})$ does not appear. In particular, when the vectors $\boldsymbol{q}_j$ constitute an orthonormal basis, the normalizing matrix expressed by the inverse matrix product from (19) can be replaced by the diagonal matrix $\mathrm{diag}[\mathbf{I}, 2\mathbf{I}]$. It is noted that in the discretized form developed in Section 4 the equations of motion are used in connection with mean values of two sets of base vectors $\overline{\boldsymbol{q}}_j$. These mean vectors are not orthonormal, and a suitable mean value form of the original dynamic equation (56) must be used.

4. State-space time integration

The key point in developing a conservative time integration algorithm is to discretize the evolution equations based on an integrated form, such that the correct incremental change of the energy and momentum is obtained over a finite time step from t_n to t_{n+1}. This approach is different from the collocation-based methods, in which the equations are matched at discrete points in time. Similarly, constraints are included via exact representation over the finite time integration increment. In this context it is important to realize that the role of the associated Lagrange multipliers is to ensure the satisfaction of the constraints at the end of the current interval of integration, see e.g. [22] for a discussion of the role of Lagrange multipliers in mechanics. The Lagrange multipliers are therefore associated with the integration interval, and not the selected points in time. Hence, if simulations are initiated with proper initial conditions satisfying the constraints, exact integration of the constraint increments will ensure continued satisfaction at any later time step.

4.1. Energy conservation for rigid body rotations

The discretized conservative form of the equations of motion (34) and (56) is obtained by considering a finite increment of the augmented Hamiltonian defined in (33) over the time interval $[t_n, t_{n+1}]$. This increment is expressed as

$$\Delta H = \Delta T(\mathbf{q}, \mathbf{p}) + \Delta V(\mathbf{q}) + \Delta\boldsymbol{\Phi}(\mathbf{q})^T\boldsymbol{\lambda} - \Delta\mathbf{e}(\mathbf{q})^T\boldsymbol{\gamma}. \tag{60}$$

The role of the Lagrange multipliers $\boldsymbol{\lambda}$ and $\boldsymbol{\gamma}$ is to impose the constraints at the end of the time interval, when they are satisfied at the beginning. The Lagrange multipliers are therefore introduced in the form of a representative value that is associated with their role over the interval, i.e. an effective mean value. There has been some uncertainty about this point in the literature, and Lagrange multipliers have sometimes been interpolated between the integration time points, typically leading to oscillatory behavior.

The kinetic energy is a symmetric bi-quadratic form given by either of the expressions in (29). It is easily shown that the time increment of a quadratic form is obtained by replacing in turn one factor with its increment, while the other is represented by its mean value, see e.g. [23,24]. For the present symmetric form this gives

$$\Delta T = \Delta\left[\mathbf{p}^T\mathbf{G}(\mathbf{q})^T\right]\mathbb{J}^{-1}\left[\overline{\mathbf{G}(\mathbf{q})\mathbf{p}}\right]. \tag{61}$$

By the same argument the first factor can further be factored into products of increments and mean values, whereby

$$\Delta T = \left[\Delta\mathbf{p}^T\mathbf{G}(\overline{\mathbf{q}})^T + \overline{\mathbf{p}}^T\mathbf{G}(\Delta\mathbf{q})^T\right]\mathbb{J}^{-1}\left[\overline{\mathbf{G}(\mathbf{q})\mathbf{p}}\right]. \tag{62}$$

By interchanging the roles of $\mathbf{q}$ and $\mathbf{p}$ in all factors associated with the second term the following structure of the increment of the kinetic energy ΔT is identified

$$\Delta T = \Delta\mathbf{q}^T\frac{\partial T_*}{\partial \mathbf{q}^T} + \Delta\mathbf{p}^T\frac{\partial T_*}{\partial \mathbf{p}^T}, \tag{63}$$

defining the finite derivatives of T as

$$\frac{\partial T_*}{\partial \mathbf{q}^T} = \mathbf{G}(\overline{\mathbf{p}})^T \mathbb{J}_0^{-1} \overline{\mathbf{G}(\mathbf{p})\mathbf{q}}, \quad \frac{\partial T_*}{\partial \mathbf{p}^T} = \mathbf{G}(\overline{\mathbf{q}})^T \mathbb{J}^{-1} \overline{\mathbf{G}(\mathbf{q})\mathbf{p}}. \tag{64}$$

Similarly as in the continuous dynamic equation (35), the matrix $\mathbb{J}_0^{-1}$ is introduced since T does not depend on $\boldsymbol{q}_0$. It is seen that (63) represents a discrete equivalence to partial differentiation where the finite increments $\Delta\mathbf{q}$ and $\Delta\mathbf{p}$ serve to identify the finite derivatives that reproduce the exact energy increment, see e.g. [14]. In particular, the conservative properties of the algorithm rely on the special combination of increments and mean values in (64). The increment of the potential $V(\mathbf{q})$ is represented similarly in terms of its finite derivative $\partial V_*/\partial \mathbf{q}$,

$$\Delta V = \Delta \mathbf{q}^T \frac{\partial V_*}{\partial \mathbf{q}^T}. \tag{65}$$

The particular form of the finite derivative can often be extracted in explicit form via a finite difference.

The internal constraints (23) are homogeneous quadratic forms of the generalized displacements $\mathbf{q}$, and thus the increment of the strain constraints can be expressed as a combination of increments and mean values as

$$\Delta \mathbf{e} = \mathbf{C}(\overline{\mathbf{q}})\Delta \mathbf{q} = \mathbf{0}. \tag{66}$$

It is seen that this equation constitutes the discrete form equivalent to (23). Finally, the increment of the external constraints is expressed in terms of its finite derivatives as

$$\Delta \boldsymbol{\Phi} = \Delta \mathbf{q}^T \frac{\partial \boldsymbol{\Phi}_*}{\partial \mathbf{q}^T} = \mathbf{0}. \tag{67}$$

External constraints often describe a distance or an angle, and this would lead to an explicit expression of the finite derivative with respect to the generalized displacements $\mathbf{q}$.

The specific form of the discretized equations of motion with the finite time increment h follow from (60) by introducing the increments in terms of the finite derivatives by (63) and (65)–(67),

$$\Delta \mathbf{q} = \frac{\partial H_*}{\partial \mathbf{p}^T} = \quad h\mathbf{G}(\overline{\mathbf{q}})^T \mathbb{J}^{-1} \overline{\mathbf{G}(\mathbf{q})\mathbf{p}}, \tag{68}$$

$$\Delta \mathbf{p} = \frac{\partial H_*}{\partial \mathbf{q}^T} = -h\mathbf{G}(\overline{\mathbf{p}})^T \mathbb{J}_0^{-1} \overline{\mathbf{G}(\mathbf{p})\mathbf{q}} - h\left[\frac{\partial V_*}{\partial \mathbf{q}^T} + \left(\frac{\partial \boldsymbol{\Phi}_*}{\partial \mathbf{q}}\right)^T \boldsymbol{\lambda} - \mathbf{C}(\overline{\mathbf{q}})^T \boldsymbol{\gamma}\right]. \tag{69}$$

These equations are constructed such that a finite increment of the Hamiltonian $\Delta H = 0$, which is an expression of conservation of energy. Furthermore, it is seen that the discrete equations of motion constitute a clear equivalent to the kinematic equation (34) and the dynamic equation (35), when the respective gradients are represented by their finite derivatives. It is also clear from the form of these equations that the Lagrange multipliers $\boldsymbol{\gamma}$ and $\boldsymbol{\lambda}$ are associated with the time interval $[t_n, t_{n+1}]$, rather than any particular point in time.

4.2. Elimination of internal constraints

As in the continuous case it is convenient to eliminate the explicit dependence on the Lagrange multipliers $\boldsymbol{\gamma}$ associated with the internal constraints. The elimination is based on the incremental form of the displacement-momentum relation (51), given by

$$\mathbf{C}(\overline{\mathbf{p}})\Delta \mathbf{q} + \mathbf{C}(\overline{\mathbf{q}})\Delta \mathbf{p} = \mathbf{0}. \tag{70}$$

When substituting the increments from (68) and (69) the following relation for $\boldsymbol{\gamma}$ is obtained

$$\mathbf{C}(\overline{\mathbf{p}})\mathbf{G}(\overline{\mathbf{q}})^T \mathbb{J}^{-1} \overline{\mathbf{G}(\mathbf{q})\mathbf{p}} - \mathbf{C}(\overline{\mathbf{q}})\mathbf{G}(\overline{\mathbf{p}})^T \mathbb{J}_0^{-1} \overline{\mathbf{G}(\mathbf{p})\mathbf{q}} - \mathbf{C}(\overline{\mathbf{q}})\left[\frac{\partial V_*}{\partial \mathbf{q}^T} + \left(\frac{\partial \boldsymbol{\Phi}_*}{\partial \mathbf{q}}\right)^T \boldsymbol{\lambda} - \mathbf{C}(\overline{\mathbf{q}})^T \boldsymbol{\gamma}\right] = \mathbf{0}. \tag{71}$$

In contrast to the continuous case (52) the two first terms do not cancel in general, because now the first two factors are based on the mean values $\overline{\mathbf{q}}$ and $\overline{\mathbf{p}}$ that are not necessarily orthonormal. Thus, the explicit expression for the $\boldsymbol{\gamma}$ vector in terms of $\mathbf{q}$ and $\mathbf{p}$ follows in the form

$$\boldsymbol{\gamma} = \boldsymbol{\gamma}_0 + \left[\mathbf{C}(\overline{\mathbf{q}})\mathbf{C}(\overline{\mathbf{q}})^T\right]^{-1} \mathbf{C}(\overline{\mathbf{q}})\left[\frac{\partial V_*}{\partial \mathbf{q}^T} + \left(\frac{\partial \boldsymbol{\Phi}_*}{\partial \mathbf{q}}\right)^T \boldsymbol{\lambda}\right], \tag{72}$$

where the term

$$\boldsymbol{\gamma}_0 = \left[\mathbf{C}(\overline{\mathbf{q}})\mathbf{C}(\overline{\mathbf{q}})^T\right]^{-1} \left[\mathbf{C}(\overline{\mathbf{q}})\mathbf{G}(\overline{\mathbf{p}})^T + \mathbf{C}(\overline{\mathbf{p}})\mathbf{G}(\overline{\mathbf{q}})^T\right] \mathbb{J}_0^{-1} \overline{\mathbf{G}(\mathbf{p})\mathbf{q}}. \tag{73}$$

accounts for the two terms associated with the homogeneous equations. It can be shown that this contribution is of order $\|\Delta\mathbf{q}\|\|\Delta\mathbf{p}\|$, and thereby of order $(\Delta t)^2$ relative to the other terms. However, the term $\boldsymbol{\gamma}_0$ must be included in the formulation to realize the full accuracy of the algorithm, as well as including energy and momentum conservation.

After elimination of $\boldsymbol{\gamma}$, the dynamic equation of motion (69) takes the form,

$$\Delta\mathbf{p} = -h\mathbf{G}(\overline{\mathbf{p}})^T\mathbb{J}_0^{-1}\overline{\mathbf{G}(\mathbf{p})\mathbf{q}} + h\mathbf{C}(\overline{\mathbf{q}})^T\boldsymbol{\gamma}_0 - h\left(\mathbf{I} - \mathbf{C}(\overline{\mathbf{q}})^T\left[\mathbf{C}(\overline{\mathbf{q}})\mathbf{C}(\overline{\mathbf{q}})^T\right]^{-1}\mathbf{C}(\overline{\mathbf{q}})\right)\left[\frac{\partial V_*}{\partial\mathbf{q}^T} + \left(\frac{\partial\boldsymbol{\Phi}_*}{\partial\mathbf{q}}\right)^T\boldsymbol{\lambda}\right]. \tag{74}$$

This constitutes the discrete equivalent to (56). In the discretized form the projection is based on the mean values $\mathbf{C}(\overline{\mathbf{q}})$, and this appears to preclude further reduction to the more compact rotation matrix form (59) of the continuous problem. Furthermore, it should be noted that while the equations associated with rotational motion includes a representation of rotating moment of inertia tensor $\mathbb{J}$ via the $\mathbf{G}$-matrices, the inertia effects associated with translation of the center of mass only contains the mass of the body m as a scalar factor. Typically this makes the rotational part of the motion the controlling factor for the numerical accuracy as illustrated in Section 5.2.

4.3. State-space algorithm

The kinematic equation (68), the dynamic equation (74) and the increment of the external constraints for the time step $\Delta t = t_{n+1} - t_n$ are solved simultaneously by Newton–Raphson iteration. The unknown variables are the current value of $[\mathbf{q}^T, \mathbf{p}^T]$ and the external Lagrange multipliers, $\boldsymbol{\lambda}^T$ associated with the current time interval. These are conveniently collected in the state vector

$$\mathbf{u} = \left[\mathbf{q}^T, \mathbf{p}^T, \boldsymbol{\lambda}^T\right]^T. \tag{75}$$

Similarly, the corresponding residual vector is arranged in the form

$$\mathbf{r} = \left[\mathbf{r}_q^T, \mathbf{r}_p^T, \mathbf{r}_\lambda^T\right]^T, \tag{76}$$

with elements defined by the discretized equations of motion and the external constraints as

$$\mathbf{r}_q = \Delta\mathbf{q} - h\mathbf{G}(\overline{\mathbf{q}})^T\mathbf{J}^{-1}\overline{\mathbf{G}(\mathbf{q})\mathbf{p}}, \tag{77a}$$

$$\mathbf{r}_p = \Delta\mathbf{p} + h\mathbf{G}(\overline{\mathbf{p}})^T\mathbf{J}^{-1}\overline{\mathbf{G}(\mathbf{p})\mathbf{q}} + h\left[\frac{\partial V_*}{\partial\mathbf{q}^T} + \left(\frac{\partial\boldsymbol{\Phi}_*}{\partial\mathbf{q}}\right)^T\boldsymbol{\lambda} - \mathbf{C}(\overline{\mathbf{q}})^T\boldsymbol{\gamma}\right], \tag{77b}$$

$$\mathbf{r}_\lambda = \frac{\partial\boldsymbol{\Phi}_*}{\partial\mathbf{q}}\Delta\mathbf{q}, \tag{77c}$$

with the Lagrange multipliers $\boldsymbol{\gamma}$ associated with the internal constraints are expressed in terms of $\mathbf{q}$ and $\mathbf{p}$ by (72).

Iterations based on the Newton–Raphson procedure amounts to considering the linearized equation for the residual $\mathbf{r}$ given by,

$$\mathbf{r} + \delta\mathbf{r} = \mathbf{r} + \left(\frac{\partial\mathbf{r}}{\partial\mathbf{q}}\delta\mathbf{q} + \frac{\partial\mathbf{r}}{\partial\mathbf{p}}\delta\mathbf{p} + \frac{\partial\mathbf{r}}{\partial\boldsymbol{\lambda}}\delta\boldsymbol{\lambda} + \cdots\right) = \mathbf{0}, \tag{78}$$

where the dots indicate higher order terms. The linearized increment $\delta\mathbf{r}$ is then determined in order to make the residual vanish. This corresponds to the system of equations

$$\mathbf{K}\delta\mathbf{u} = -\mathbf{r}, \tag{79}$$

with the elements of the tangential stiffness matrix defined by partial differentiation as

$$\mathbf{K}_{ij} = \partial\mathbf{r}_i/\partial\mathbf{u}_j. \tag{80}$$

Consistent expressions for the tangential stiffness are given by (A.2)–(A.5) in Appendix A. The iteration procedure is implemented with a convergence criterion specifying that the length of the residual vector must be less a prescribed value ε_r. It is convenient to define individual convergence criteria for each of the residual equation (77) reflecting the different lengths of the various vectors in (76). These are implemented as

$$\|\mathbf{r}_q\| \leqslant \varepsilon_r\|\mathbf{q}\|_0, \quad \|\mathbf{r}_p\| \leqslant \varepsilon_r\|\mathbf{p}\|_0 \tag{81}$$

and

$$\|\mathbf{r}_\lambda\| \leqslant \varepsilon_r. \tag{82}$$

The implementation of the algorithm for rigid body rotations is illustrated in pseudo-code format in Table 1. It has been noted previously that the Lagrange multipliers are associated with the particular interval of integration and do not have

Table 1
Conservative time integration algorithm.

(1)	Initial conditions: $\mathbf{u}_0 = [\mathbf{q}^T, \mathbf{p}^T, \mathbf{0}^T]_0^T$
(2)	Prediction step: $\mathbf{u} = \mathbf{u}_n$,
(3)	Residual calculation: $\mathbf{r} = \mathbf{r}(\mathbf{q}, \mathbf{p}, \lambda)$ from (77).
(4)	Update incremental rotation parameters: $\delta\mathbf{u} = -\mathbf{K}^{-1}\mathbf{r}$,with $\mathbf{K}$ from Appendix A. $\mathbf{u} = \mathbf{u} + \delta\mathbf{u}$, If $\|\mathbf{r}\| > \varepsilon_r$, repeat from (3).
(5)	Return to (2) for new time step, or stop.

any continuity requirements, hence the value $\lambda_0 = \mathbf{0}$ included in the initial conditions is a purely formal construct to establish the full vector $\mathbf{u}_n$ needed in the subsequent iteration procedure.

5. Numerical Examples

In this section two numerical examples are presented. The first example serves to illustrate the conservative properties of the algorithm in the absence of an external potential by considering free rotational motion of a rigid body. The second example generalizes the formulation also to include translational motion and the motion of a spinning top in a gravitational field with one point fixed is investigated for three different configurations. Additional examples involving multiple bodies connected by various types of hinges are presented in [25].

5.1. Free rotation of rigid body

The first example considers free rotation of a rigid body. The parameters are equivalent to those used in [21,26], corresponding to a box with side lengths $[1, 3, 2]$ and mass 12. This yields a principal moment of inertia tensor with respect to the center of mass given by $\boldsymbol{J} = \text{diag}[13, 5, 10]$. The motion is initiated by an angular velocity of $\boldsymbol{\Omega}_0 = [0.0, 0.05, 10]^T$, i.e rotation around the axis of intermediate moment of inertia with a small perturbation. This leads to unstable motion where the body is reversed at regular intervals as discussed in [21,26].

The discretized algorithm was derived by forming a finite increment of the augmented Hamiltonian, whereby conservation of energy in absence of approximation error is ensured. In the present example the kinetic energy $T = 500$ as well as the magnitude of the angular momentum vector $\|\boldsymbol{L}\|$ are conserved within an accuracy of 10^{-15} when an iteration tolerance of $\varepsilon_r = 10^{-8}$ is used. Similarly the kinematic constraint condition (22) as well as the displacement–momentum orthogonality relation (39) are satisfied within a very high accuracy for the present iteration tolerance. This is illustrated in Figs. 2(a) and 2(b) for the time step $h = 0.01$.

The second order accuracy of the present algorithm is illustrated in Fig. 3 in terms of the period error for different values of the non-dimensional time steps ωh, with $\omega = \|\boldsymbol{\Omega}_0\|$. The period error is obtained from Ω_3 relative to a reference period T evaluated for a fine discretization of $h = 10^{-6}$. For comparison, results obtained by the algorithm based on quaternions presented in [21], the energy–momentum scheme ALGO_C1 presented in [12] and the algorithm based on the Cayley representation of the rotation tensor from [26] are included. It is seen that all algorithms are second order accurate. However,

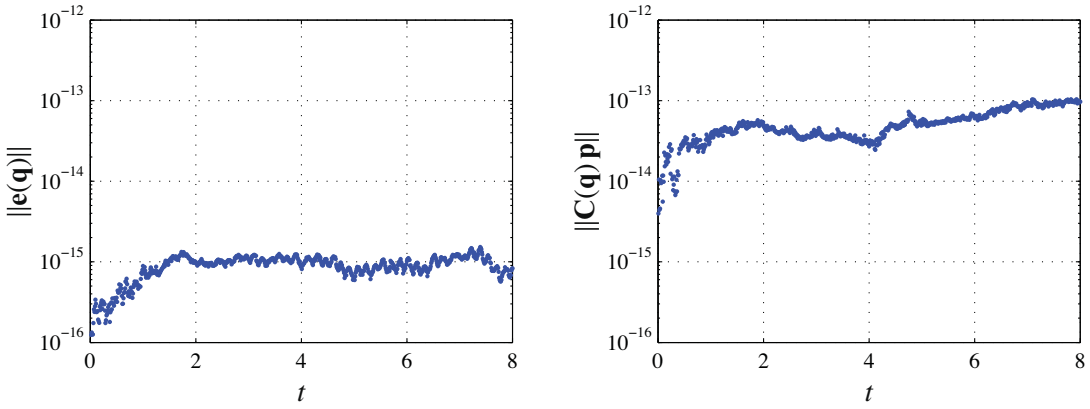

Fig. 2. Error on homogeneous constrains: (a) Kinematic constraint, (b) Orthogonality relation.

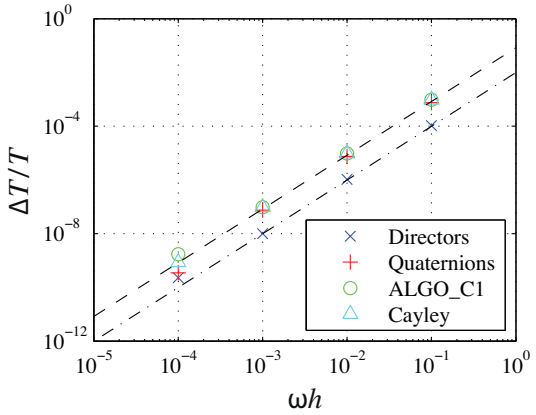

Fig. 3. Relative period error. $(\omega h)^2/12$ (– –), $(\omega h)^2/100$ (– · –).

while the accuracy of the benchmark algorithms roughly corresponds to the well-known asymptotic results for a single load component $\Delta T/T = (\omega h)^2/12$, see e.g. [24], the convergence constant of the present algorithm is changed from $1/12$ to about $1/100$. The number of iterations for convergence of the present algorithm was 4 in mean and 4 as maximum. For the quaternion algorithm these numbers were 3 and 3, while for the Cayley formulation they were 2.2 and 3.

5.2. Rotating top in gravitational field

In this example the motion of a spinning top in a gravitational field with one point fixed as illustrated in Fig. 4(a) is analyzed. The motion is conveniently expressed in terms of the angle of nutation θ, the angle of precession φ and the spin angle ψ.

The top is represented as a cone with dimensions equivalent to those used in [18], i.e height $a = 0.1$, radius $r = a/2$ and mass $m = \rho\pi r^2 a/3$. The mass density is $\rho = 2700$ and the center of gravity is located at a distance of $l = 3a/4$ along the local x_3-axis from the tip. The local moments of inertia are determined as

$$J_1 = J_2 = \frac{3}{80}m(4r^2 + a^2) + md^2, \quad J_3 = \frac{3}{10}mr^2,$$

where d denotes the distance from the origin of the base vector frame to the center of gravity. The top is located in a uniform gravitational field with acceleration $g = 9.81$ in the negative x_3-direction, hence the load potential takes the form

$$V(\mathbf{q}) = m\boldsymbol{g}^T(\boldsymbol{q}_0 + \boldsymbol{Q}\boldsymbol{x}_0^{\mathrm{cm}}).$$

Here, the gravitational vector is given as $\boldsymbol{g} = [0, 0, g]^T$, the deformation gradient tensor follow from (2) and $\boldsymbol{x}_0^{\mathrm{cm}}$ holds the local coordinates of the center of mass. The special case of a uniformly precessing top without nutation is considered. This requires that the initial angle of inclination θ_0, the angular velocity components $\dot\varphi$ and $\dot\psi$ satisfy the relation

$$\dot\psi = \frac{mgl}{J_3\dot\varphi} + \frac{J_2 - J_3}{J_3}\dot\varphi\cos(\theta_0),$$

see e.g. [20]. The initial conditions correspond to the those used in [18,21], i.e. a precession rate $\dot\varphi = 10$, an initial inclination angle $\theta_0 = \pi/3$ and the initial angular velocity vector

$$\boldsymbol{\Omega}_0 = [0, \dot\varphi\sin(\theta_0), \dot\psi + \dot\varphi\cos(\theta_0)]^T.$$

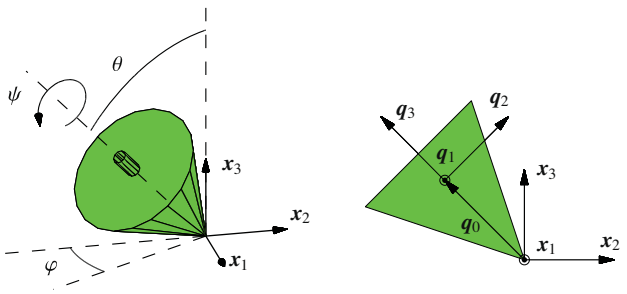

Fig. 4. Configuration of rotating top.

In order to illustrate the effect of including translational motion and holonomic constraints, three different configurations are considered:

Case 1 Purely rotational motion with the origin of the local body frame coinciding with the origin of the initial reference frame.

Case 2 Combined rotation and translation with the origin of the local body frame linked to the origin of the initial reference frame by a holonomic constraint,

$$\boldsymbol{\Phi}(\mathbf{q}) = \boldsymbol{q}_0 = \mathbf{0}.$$

Case 3 Combined rotation and translation with the origin of the local body frame located at the center of gravity, and with the distance to the origin of the initial reference frame fixed by a holonomic constraint,

$$\boldsymbol{\Phi}(\mathbf{q}) = \boldsymbol{q}_0 - l\boldsymbol{q}_3 = \mathbf{0}.$$

The x_1- and the x_3-component of the center of gravity for all the three cases are illustrated in Figs. 5(a) and 5(b) for a relatively large time step $h = 0.01$ corresponding to approximately 5 time steps per period $T = 2\pi/\|\boldsymbol{\Omega}_0\|$. It is seen that the algorithm predicts a significant period error, which leads to nutation due to violation of the steady precession condition. This issue was also observed and discussed in [21] for an algorithm based on quaternions. The effect is most pronounced for the cases 1 and 2 where the location of the center of mass is governed by the base vectors $\boldsymbol{q}_1, \boldsymbol{q}_2, \boldsymbol{q}_3$, which are determined with reduced accuracy compared to $\boldsymbol{q}_0$ as discussed in Section 4.2.

The numerical simulations have been performed using an iteration tolerance of 10^{-8}, and the conserved quantities, namely the total mechanical energy and the vertical component of the angular momentum l_3, are conserved well within this tolerance. The average as well as maximum number of iterations for convergence were 6, 6 and 7, respectively, for the three formulations.

The accuracy of the zero strain constraints (22) and the displacement-momentum orthogonality relation (39) are illustrated in Fig. 6. While the errors on the constraints in Fig. 6(a) are in the order of 10^{-15} for all three cases, a lower accuracy

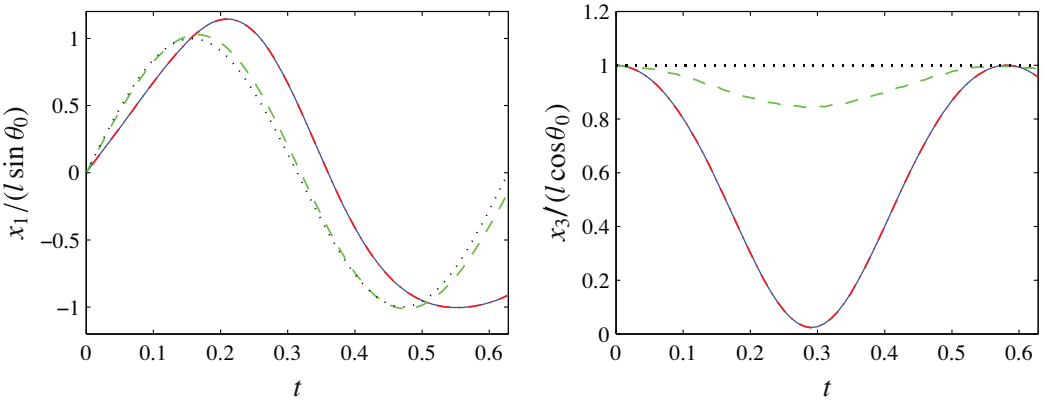

Fig. 5. Motion of center of mass for precessing top: (a) $x_1(t)$, (b) $x_3(t)$. Case 1 (—), Case 2 (-·-), Case 3 (- - -), analytical solution (···).

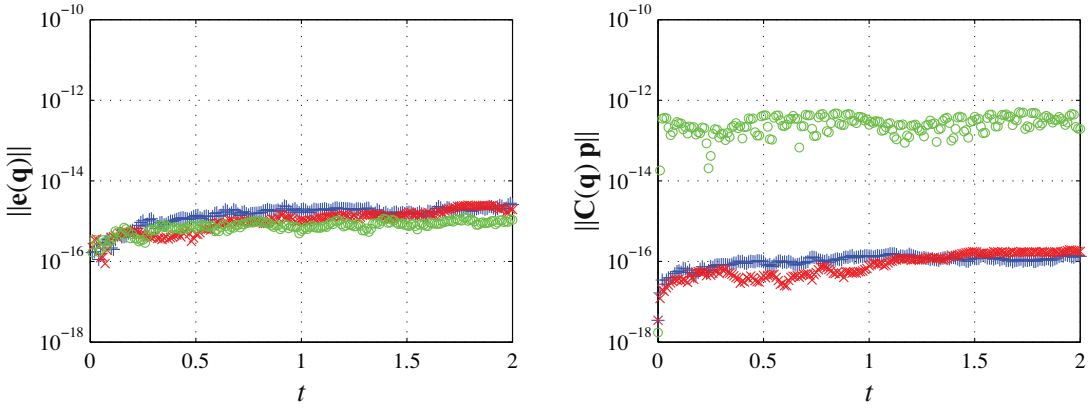

Fig. 6. Error on homogeneous constrains: (a) Kinematic constraint, (b) Orthogonality relation. Case 1 (+), Case 2 (×), Case 3 (○).

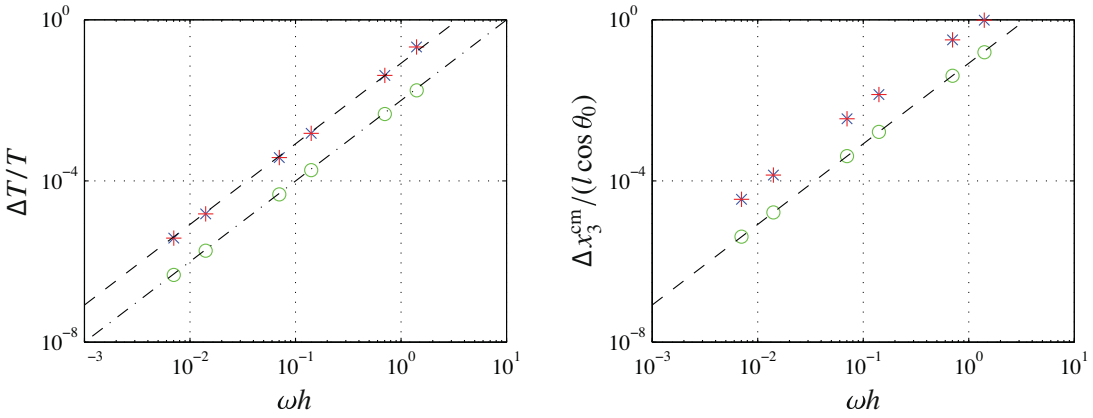

Fig. 7. Order of convergence: (a) Relative period error, (b) Relative nutation error. Case 1 (+), Case 2 (×), Case 3 (○), $(\omega h)^2/12$ (—), $(\omega h)^2/100$ (-·-).

is seen for the orthogonality relation in Fig. 6(b) in case 3, i.e. when the top exhibits both translational and rotation motion. For this case the orthogonality constraint is only satisfied within an accuracy of 10^{-12}. A closer inspection of each of the six orthogonality relations reveals that only the accuracy on the three relations associated with $\boldsymbol{q}_3$ are reduced, indicating that only these constraints are active in the present configuration. However, it should be noted that the error is still well below the iteration tolerance.

Finally, the second-order convergence of the algorithm in the non-trivial case where both an external potential and external constraints are included is illustrated in Fig. 7. Figure 7(a) illustrates the relative error on the vibration period $\Delta T/T$ evaluated via the x_1-component of the center of mass, while Fig. 7(b) shows the relative error on the x_3-component of the center of mass. The latter is a direct measure of the nutation illustrated in Fig. 5. In both figures the time increment is represented in non-dimensional form in terms of ωh, where ω is taken as $\|\boldsymbol{\Omega}_0\|$. As discussed above the particular high accuracy in C ase 3 is due to the fact that the location of the center of mass is determined solely in terms of the translational components $\boldsymbol{q}_0$, which are determined with full accuracy. Comparable results are obtained by reducing the time step by a factor three in the cases 1 and 2 corresponding to a shift of the time scale, whereby all points in Figs. 7(a) and 7(b) are aligned.

6. Conclusions

An energy and momentum conserving time integration algorithm for constrained rigid body motion, in which the rotational motion is represented via a convected set of orthonormal base vectors, has been developed. The equations of motion are derived from Hamilton's equation with three translational components plus nine base vector components as generalized coordinates. The formulation makes use of an augmented Hamiltonian where orthonormality constraints for the base vectors equivalent to vanishing of all Green strain components are included via Lagrange multipliers. However, a key feature of the formulation is that when the kinetic energy for rotational motion is formed via the instantaneous angular velocity, the Lagrange multipliers associated with the zero-strain constraints of the base vectors can be eliminated explicitly by using a set of displacement-momentum orthogonality relations. The effect of the Lagrange multipliers is then represented via a projection operator applied to the load potential gradient and the gradients of possible kinematic constraints, which subtracts their projections on the deformation modes from the unconstrained gradients. A discretized form of Hamilton's equations is identified by forming a finite increment of an augmented Hamiltonian energy function, whereby the conservation of energy and momentum is obtained by suitable combinations of mean values and increments in the finite derivatives of the Hamiltonian. Similarly, constraints are introduced in the form of finite increments, while the associated Lagrange multipliers are represented as constants in each time interval in order to reflect their role as the effective reaction forces needed for maintaining the constraints. This is in accordance with the physical interpretation of Lagrange multipliers on kinematic constraints as the corresponding reaction forces, and the association of the Lagrange multipliers with the incremental time interval enables local elimination.

Appendix A. Tangential Stiffness

In this appendix the explicit expression for the consistent tangential stiffness matrix used for Newton–Raphson iterations in Section 4 is given. For the actual implementation it may be convenient express the stiffness matrix (80) in a symmetric form. This can be accomplished by interchanging the equations associated with the increments of $\mathbf{q}$ and $\mathbf{p}$, respectively, and embedding the factor $h/2$ on $\boldsymbol{\lambda}$ in the system vector $\mathbf{u}$, whereby

$$\mathbf{K} = \begin{bmatrix} \mathbf{K}_{pq} & \mathbf{K}_{pp} & (\partial \boldsymbol{\Phi}_*/\partial \mathbf{q})^T \\ \mathbf{K}_{qq} & \mathbf{K}_{qp} & \mathbf{0} \\ \partial \boldsymbol{\Phi}_*/\partial \mathbf{q} & \mathbf{0} & \mathbf{0} \end{bmatrix}. \tag{A.1}$$

The non-zero sub-matrices follow from differentiation of the residual expressions in (77) as

$$\mathbf{K}_{qq} = \mathbf{I}_{12\times 12} - \frac{h}{2}\Big[\mathbb{G}(\bar{\mathbf{f}}) - \mathbf{G}(\bar{\mathbf{q}})^T \mathbb{J}_0^{-1} \mathbf{G}(\mathbf{p}_{n+1})\Big], \tag{A.2}$$

$$\mathbf{K}_{qp} = -\frac{h}{2}\mathbf{G}(\bar{\mathbf{q}})^T \mathbb{J}^{-1} \mathbf{G}(\mathbf{q}_{n+1}), \tag{A.3}$$

$$\mathbf{K}_{pq} = \frac{h}{2}\mathbf{G}(\bar{\mathbf{p}})^T \mathbb{J}_0^{-1} \mathbf{G}(\mathbf{p}_{n+1}) + h\frac{\partial^2 V_*}{\partial \mathbf{q}^T \partial \mathbf{q}} + h\frac{\partial}{\partial \mathbf{q}^T}\left[\left(\frac{\partial \boldsymbol{\Phi}_*}{\partial \mathbf{q}}\right)^T \boldsymbol{\lambda}\right] - \frac{h}{2}\left[\boldsymbol{\Gamma} + 2\mathbf{C}(\bar{\mathbf{q}})^T \frac{\partial \boldsymbol{\gamma}}{\partial \mathbf{q}}\right], \tag{A.4}$$

$$\mathbf{K}_{pp} = \mathbf{I}_{12\times 12} + \frac{h}{2}\Big[\mathbb{G}(\bar{\mathbf{g}}) - \mathbf{G}(\bar{\mathbf{p}})^T \mathbb{J}_0^{-1} \mathbf{G}(\mathbf{q}_{n+1})\Big] - h\mathbf{C}(\bar{\mathbf{q}})^T \frac{\partial \boldsymbol{\gamma}}{\partial \mathbf{p}}. \tag{A.5}$$

The derivatives of the Lagrange multipliers associated with the internal constraints follow by differentiation of (72) as

$$\begin{aligned} \frac{\partial \boldsymbol{\gamma}}{\partial \mathbf{q}} = -\frac{1}{2}\Big[\mathbf{C}(\bar{\mathbf{q}})\mathbf{C}(\bar{\mathbf{q}})^T\Big]^{-1}\Big\{ & \mathbf{C}\Big(\mathbf{C}(\bar{\mathbf{q}})^T\boldsymbol{\gamma}\Big) + \mathbf{C}(\bar{\mathbf{q}})\boldsymbol{\Gamma} - \mathbf{C}\Big(\frac{\partial V_*}{\partial \mathbf{q}^T}\Big) - \mathbf{C}(\bar{\mathbf{q}})\frac{\partial^2 V_*}{\partial \mathbf{q}^T\partial \mathbf{q}} - \mathbf{C}\left[\left(\frac{\partial \boldsymbol{\Phi}_*}{\partial \mathbf{q}}\right)^T\boldsymbol{\lambda}\right] - \mathbf{C}(\bar{\mathbf{q}})\frac{\partial}{\partial \mathbf{q}^T}\left[\left(\frac{\partial \boldsymbol{\Phi}_*}{\partial \mathbf{q}}\right)^T\boldsymbol{\lambda}\right] \\ & - \mathbf{C}\Big(\mathbf{G}(\bar{\mathbf{p}})^T\bar{\mathbf{g}}\Big) - \mathbf{C}(\bar{\mathbf{p}})\mathbb{G}(\bar{\mathbf{g}}) - \Big[\mathbf{C}(\bar{\mathbf{q}})\mathbf{G}(\bar{\mathbf{p}})^T + \mathbf{C}(\bar{\mathbf{p}})\mathbf{G}(\bar{\mathbf{q}})^T\Big]\mathbf{J}^{-1}\mathbf{G}(\mathbf{p}_{n+1})\Big\} \end{aligned} \tag{A.6}$$

and

$$\frac{\partial \boldsymbol{\gamma}}{\partial \mathbf{p}} = \frac{1}{2}\Big[\mathbf{C}(\bar{\mathbf{q}})\mathbf{C}(\bar{\mathbf{q}})^T\Big]^{-1}\Big\{\mathbf{C}(\bar{\mathbf{q}})\mathbb{G}(\bar{\mathbf{g}}) + \mathbf{C}\Big(\mathbf{G}(\bar{\mathbf{q}})^T\bar{\mathbf{g}}\Big) - \Big[\mathbf{C}(\bar{\mathbf{q}})\mathbf{G}(\bar{\mathbf{p}})^T + \mathbf{C}(\bar{\mathbf{p}})\mathbf{G}(\bar{\mathbf{q}})^T\Big]\mathbf{J}^{-1}\mathbf{G}(\mathbf{q}_{n+1})\Big\}, \tag{A.7}$$

where it is seen that the first six terms in (A.6) vanish in the case of free rotation. The expressions (A.2)–(A.5) make use of the intermediate variables

$$\bar{\mathbf{f}} = \mathbf{J}^{-1}\overline{\mathbf{G}(\mathbf{q})\mathbf{p}}, \quad \bar{\mathbf{g}} = \mathbf{J}^{-1}\overline{\mathbf{G}(\mathbf{p})\mathbf{q}}, \tag{A.8}$$

along with the matrix operators

$$\mathbb{G}(\bar{\mathbf{g}}) = \begin{bmatrix} \mathbf{0} & -\bar{g}_3\mathbf{I} & \bar{g}_2\mathbf{I} \\ \bar{g}_3\mathbf{I} & \mathbf{0} & -\bar{g}_1\mathbf{I} \\ -\bar{g}_2\mathbf{I} & \bar{g}_1\mathbf{I} & \mathbf{0} \end{bmatrix}, \quad \boldsymbol{\Gamma}(\boldsymbol{\gamma}) = \begin{bmatrix} \gamma_1\mathbf{I} & \gamma_6\mathbf{I} & \gamma_5\mathbf{I} \\ \gamma_6\mathbf{I} & \gamma_2\mathbf{I} & \gamma_4\mathbf{I} \\ \gamma_5\mathbf{I} & \gamma_4\mathbf{I} & \gamma_3\mathbf{I} \end{bmatrix}. \tag{A.9}$$

representing the derivatives of the products $\mathbf{G}(\mathbf{q})^T\bar{\mathbf{g}}$ and $\mathbf{C}(\mathbf{q})^T\boldsymbol{\gamma}$ with respect to the independent variables $\mathbf{q}$, respectively.

References

[1] J.G. Papastavridis, Maggi's equations of motion and the determination of constraint reactions, Journal of Guidance, Control, and Dynamics 13 (1990) 213–220.
[2] C. Liang, A differentiable null space method for constrained dynamic analysis, Journal of Mechanisms Transmissions and Automation in Design 109 (1987) 405–411.
[3] F.E. Udwadia, R.E. Kalaba, A new perspective on constrained motion, in: Proceedings of the Royal Society of London. Series A: Mathematical and Physical Sciences, vol. 439, 1992, pp. 407–410.
[4] J. Baumgarte, Stabilization of constraints and integrals of motion in dynamical systems, Computer Methods in Applied Mechanics and Engineering 1 (1972) 1–16.
[5] E. Bayo, J. García De Jalón, M.A. Serna, A modified Lagrangian formulation for the dynamic analysis of constrained mechanical systems, Computer Methods in Applied Mechanics and Engineering 71 (1988) 183–195.
[6] S. Yoon, R.M. Howe, D.T. Greenwood, Geometric elimination of constraint violations in numerical simulation of Lagrangian equations, Journal of Mechanical Design 116 (1994) 1058–1064.
[7] W. Blajer, Elimination of constraint violation and accuracy aspects in numerical simulation of multibody systems, Multibody System Dynamics 7 (2002) 265–284.
[8] Z. Terze, D. Lefeber, O. Muftić, Null space integration method for constrained multibody systems with no constraint violation, Multibody System Dynamics 6 (2001) 229–243.
[9] A. Laulusa, O.A. Bauchau, Review of classical approaches for constraint enforcement in multibody systems, Journal of Computational and Nonlinear Dynamics 3 (011004) (2008) 1–8.
[10] O.A. Bauchau, A. Laulusa, Review of contemporary approaches for constraint enforcement in multibody systems, Journal of Computational and Nonlinear Dynamics 3 (011005) (2008) 1–8.
[11] O.A. Bauchau, Flexible Multibody Dynamics, Springer, Dordrecht, 2011.
[12] J.C. Simo, K.K. Wong, Unconditionally stable algorithms for rigid body dynamics that exactly preserve energy and momentum, International Journal for Numerical Methods in Engineering 31 (1991) 19–52.
[13] J.C. Simo, N. Tarnow, The discrete energy-momentum method. Conserving algorithms for nonlinear elastodynamics, Zeitschrift für angewandte Mathematik und Physik 43 (1992) 757–792.

[14] O. Gonzalez, Exact energy and momentum conserving algorithms for general models in nonlinear elasticity, Computer Methods in Applied Mechanics and Engineering 190 (2000) 1763–1783.
[15] O.A. Bauchau, G. Damilano, N.J. Theron, Numerical integration of non-linear elastic multi-body systems, International Journal for Numerical Methods in Engineering 38 (1995) 2727–2751.
[16] E.V. Lens, A. Cardona, M. Géradin, Energy preserving time integration for constrained multibody systems, Multibody System Dynamics 11 (2004) 41–61.
[17] P. Betsch, The discrete null space method for the energy consistent integration of constrained mechanical systems. Part I: Holonomic constraints, Computer Methods in Applied Mechanics and Engineering 194 (2005) 5159–5190.
[18] P. Betsch, S. Leyendecker, The discrete null space method for the energy consistent integration of constrained mechanical systems. Part II: Multibody dynamics, International Journal for Numerical Methods in Engineering 67 (2006) 499–552.
[19] P. Betsch, P. Steinmann, Constrained integration of rigid body dynamics, Computer Methods in Applied Mechanics and Engineering 191 (2001) 467–488.
[20] H. Goldstein, C. Poole, J. Safko, Classical Mechanics, third ed., Addison Wesley, 2001.
[21] M.B. Nielsen, S. Krenk, Conservative integration of rigid body motion by quaternion parameters with implicit constraints, International Journal for Numerical Methods in Engineering 92 (2012) 734–752.
[22] C. Lanczos, The Variational Principles of Mechanics, fourth ed., Dover, New York, 1986.
[23] S. Krenk, The role of geometric stiffness in momentum and energy conserving time integration, International Journal for Numerical Methods in Engineering 71 (2007) 631–651.
[24] S. Krenk, Non-linear Modeling and Analysis of Solids and Structures, Cambridge University Press, Cambridge, UK, 2009.
[25] M.B. Nielsen, S. Krenk, Multibody motion in implicitly constrained director format with links via explicit constraints, in: Multibody Dynamics 2013, ECCOMAS Thematic Conference, Zagreb, Croatia.
[26] S. Krenk, A vector format for conservative time integration of rotations, in: Multibody Dynamics 2007, ECCOMAS Thematic Conference, Milan, Italy, pp. 1–12.

P5

Explicit free-floating beam element

M.B. Nielsen & S. Krenk

International Journal for Numerical Methods in Engineering,
Vol **98**:59–78, 2014.

INTERNATIONAL JOURNAL FOR NUMERICAL METHODS IN ENGINEERING
Int. J. Numer. Meth. Engng 2014; **98**:59–78
Published online 7 February 2014 in Wiley Online Library (wileyonlinelibrary.com). DOI: 10.1002/nme.4623

Explicit free-floating beam element

Martin B. Nielsen*,† and Steen Krenk

Department of Mechanical Engineering, Technical University of Denmark, DK-2800 Kgs. Lyngby, Denmark

SUMMARY

A two-node free-floating beam element capable of undergoing arbitrary large displacements and finite rotations is presented in explicit form. The configuration of the beam in three-dimensional space is represented by the global components of the position of the beam nodes and an associated set of convected base vectors (directors). The local constitutive stiffness is derived from the complementary energy of a set of six independent deformation modes, each corresponding to an equilibrium state of constant internal force or moment. The deformation modes are characterized by generalized strains, formed via scalar products of the element related vectors. This leads to a homogeneous quadratic strain definition in terms of the generalized displacements, whereby the elastic energy becomes at most bi-quadratic. Additionally, the use of independent equilibrium modes to set up the element stiffness avoids interpolation of kinematic variables, resulting in a locking-free formulation in terms of three explicit matrices. A set of classic benchmark examples illustrates excellent performance of the explicit beam element. Copyright © 2014 John Wiley & Sons, Ltd.

Received 11 September 2013; Revised 3 December 2013; Accepted 4 December 2013

KEY WORDS: explicit beam element; equilibrium modes; nonlinear beam element

1. INTRODUCTION

Large-displacement beam elements for efficient and accurate modeling of flexible slender structures has been the subject of a substantial number of papers. In particular, nonlinear beam theories in an initial frame of reference has been considered. A finite displacement beam theory was proposed by Reissner [1, 2] and used as basis for a computational approach by Simo and Vu-Quoc [3, 4]. This theory is often referred to as 'geometrically exact' as it coincides with the strain definitions in the Euler elastica, when shear and axial deformations are neglected, and is theoretically capable of accounting for finite rotations and for arbitrarily large deformation. The beam is commonly represented as a flexible curve with each material point associated with a cross-section, whose orientation is specified by a local set of base vectors (directors). This can be considered as a specific version of the theory for Cosserat rods [5]. The apparent simplicity and consistency of the underlying beam equations have led to the development of many different formulations; see, for example, [6–10]. However, as pointed out by Romero [11], the large number of formulations indicate that significant difficulties are associated with numerical discretization of the continuous equations. In particular, the interpolation of kinematic variables introduces the need for special measures in order to avoid locking phenomena caused by different interpolation of different strain components. Common approaches are the use of reduced integration [4] or the introduction of a hierarchical displacement interpolation where an additional center node is introduced locally at element level; see for example, [7].

Another aspect, initially highlighted by Crisfield and Jelenic [12], is the lack of frame indifference in many of the early formulations. This deficiency is closely related to the spatial interpolation of noncommuting finite rotations, for example, represented by the total or incremental form of rota-

*Correspondence to: Department of Mechanical Engineering, Technical University of Denmark, DK-2800 Kgs. Lyngby, Denmark.
†E-mail: mbni@mek.dtu.dk

tion pseudo-vectors [6, 7] or rotation increments [4]. This may lead to nonobjective discrete strain measures, even if the strain definition itself is objective. Additionally, it was illustrated in [12] that interpolation of incrementally updated rotations may lead to path-dependent solutions. A strain objective formulation was presented in [8], but with substantial increase in complexity. Alternative approaches that also preserve the objectivity of the strain measure by direct interpolation of the nine base vector components (directors) have been presented by Betsch and Steinmann [10, 13] and Romero and Armero [9].

To circumvent the issues associated with interpolation of finite rotations, so-called rotationless formulations such as the absolute nodal coordinate formulation have been developed; see for example, [14, 15]. In these formulations, inclinations, defined as the partial derivatives of the absolute nodal position vector rather than rotation variables, represent the orientation of the element. This permits the use of standard isoparametric interpolation, whereby a constant mass matrix is obtained. A drawback of these methods is that they suffer from a number of locking mechanisms due to the redundant representation of the kinematics [16]. Solutions accomplished by reformulation of the elastic forces exist, but at the expense of the some of the advantages and simplicity of the initial formulation. Furthermore, when position derivatives are used instead of rotations, representation of the curvature field requires the second derivatives, hence a lower accuracy is obtained compared to geometrically exact beam formulations [17].

A fundamentally different path was followed by Belytschko and co-workers [18, 19] who introduced the co-rotating formulation, in which the deformation of each element is considered with respect to a local element-based coordinate system. In this way, the overall large rigid body motion is accounted for by the co-rotating frame, while deformations are considered only within the local co-rotating frame, for example in the form of 'natural modes' presented by Argyris *et al*. [20], which identifies a set of independent discrete deformation modes. In this way, discrete interpolation of finite rotations is avoided, leading to an intrinsic objective description. Depending on the application, the local deformation can be modeled at various levels of sophistication ranging from linear small-deflection beam theory [21], over formulations including initial stress-based geometric stiffness [22], to relatively advanced formulations for beam–columns [23] and fully nonlinear flexibility-based beam elements by Neuhofer and Filippou [24, 25]. A recent formulation based on the co-rotational approach with inclusion of a second-order approximation for the local deformation has been presented in [26]. However, significant complexity is associated with deriving a consistent tangential stiffness accounting for finite rotation of the co-rotating frame. In particular, the task of obtaining a unique symmetric form requires special attention.

The present paper presents a free-floating beam element. The formulation combines the advantages of the co-rotating formulation with the consistency of the inertial frame approach. The key point is the use of global components of the position vector and the director vectors as generalized displacements, similar to Betsch and Steinmann [10] and Romero and Armero [9]. A set of generalized strains corresponding to each of the six deformation modes of the beam element is then defined in terms of scalar products of the global director components and the vector connecting the beam end points. The deformation modes characterized by the generalized element strains represent equilibrium states of the element, in which either an internal force or moment component is constant. The constitutive contribution to the element stiffness is then obtained from the complementary energy of the deformation modes, which provides a simple procedure for fairly general beams including pre-curvature [27] or nontrivial coupling effects [28]. In this paper, only straight beam elements are considered, and the external part of the geometric stiffness, associated with rotation of forces and moments at the element nodes, is included. Internal geometric stiffness effects from, for example, the normal force, could be included approximately in explicit form [23] or in a full iterative form [25]. However, as illustrated by the examples, the geometric stiffness effects are captured quite well by the simple external geometric stiffness formulation for element sizes that are sufficiently small relative to the corresponding buckling length scale. The present flexibility-based procedure for deriving the local stiffness properties avoids interpolation of kinematic variables and thereby circumvents the various locking phenomena associated with most kinematic representations. The generalized element strains defining the deformation modes are expressed by global vector components, and the formulation is therefore intrinsically objective and

DOI: 10.1002/nme

frame invariant. The tangential stiffness matrix is derived in explicit form from differentiation of the generalized force increments. The format has a certain resemblance to the co-rotating formulation but does not refer to any element-based local frame of reference. Furthermore, the formulation does not make use of finite rotations and leads directly to an explicit symmetric form of the global stiffness matrix.

The basic assumptions and the generalized displacements for the beam element are presented in Section 2. The generalized element strains with the static equilibrium modes are defined as quadratic forms of the generalized displacements in Section 3. The constitutive stiffness is obtained from the complementary energy of a set of six independent equilibrium modes in Section 4, while the full tangential stiffness matrix is given explicitly in Section 5. Finally, a solution algorithm for static analysis is summarized in Section 6, and numerical examples illustrating the numerical performance of the present free-floating beam element are presented in Section 7.

2. BEAM ELEMENT

A beam can be considered as a special case of a three-dimensional continuum in which one direction is much larger than the other two. Geometrically, it is therefore convenient to represent a beam as a curve segment $\mathbf{x}(s_0)$ where each material point $\mathbf{x}_0(s_0) = [x_1^0, x_2^0, x_3^0]^T$ is associated with a cross-section. The local deformation state at each cross-section can be represented by a set of local basis vectors $\mathbf{q}_1, \mathbf{q}_2, \mathbf{q}_3$, where subscripts 1 and 2 refer to the vectors spanning the plane of the cross-section, while subscript 3 refers to the normal to the cross-section plane. The global coordinates $\mathbf{x}(s_0)$ of a material point associated with the cross-section defined by the point $\mathbf{q}_0(s_0)$ on the beam axis can then be expressed in the form

$$\mathbf{x}(s_0) = \mathbf{q}_0(s_0) + \mathbf{R}(s_0)\mathbf{x}_0(s_0)\,, \tag{1}$$

where $\mathbf{q}_0(s_0)$ is the reference position of the local basis and $\mathbf{R}(s_0)$ is the transformation tensor between local and global components, defined as

$$\mathbf{R} = [\mathbf{q}_1, \mathbf{q}_2, \mathbf{q}_3]\,. \tag{2}$$

This is similar to the starting point for Cosserat rod theories; see, for example, [3, 5].

A common assumption for beam theories is to neglect the deformation in the cross-section plane. This implies that the vectors $\mathbf{q}_1$ and $\mathbf{q}_2$ representing the orientation of each cross-section must remain orthonormal. The third unit vector is defined as the normal to the cross-section given by $\mathbf{q}_3 = \mathbf{q}_1 \times \mathbf{q}_2$, and thus the triple $\{\mathbf{q}_1^T, \mathbf{q}_2^T, \mathbf{q}_3^T\}$ constitutes a local orthonormal basis that rotates with the cross-section as illustrated in Figure 1.

In the present formulation, a beam element in three-dimensional space is uniquely defined in terms of the position and orientation of the cross-sections at its end points with respect to a fixed

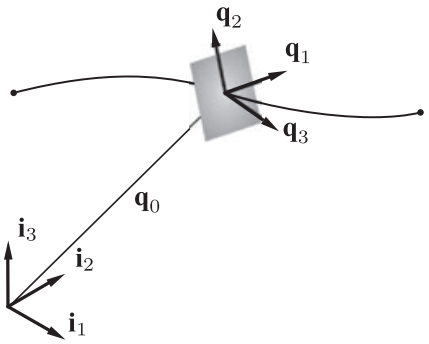

Figure 1. Beam representation as a curve with orthonormal directors.

DOI: 10.1002/nme

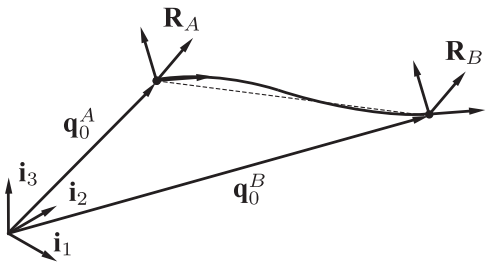

Figure 2. Configuration of beam element in the global frame of reference.

frame of reference $\{\mathbf{i}_1, \mathbf{i}_2, \mathbf{i}_3\}$ as illustrated in Figure 2. The global position of the beam end points A and B are represented by the vectors $\mathbf{q}_0^A$ and $\mathbf{q}_0^B$, while the orientation of the corresponding cross-sections is represented via the base vectors in the cross-section planes $\left[\mathbf{q}_1^T, \mathbf{q}_2^T\right]_A^T$ and $\left[\mathbf{q}_1^T, \mathbf{q}_2^T\right]_B^T$. The configuration of each node can therefore be described by the nodal displacement vectors

$$\mathbf{q}_A^T = \left[\mathbf{q}_0^T, \mathbf{q}_1^T, \mathbf{q}_2^T\right]_A , \qquad \mathbf{q}_B^T = \left[\mathbf{q}_0^T, \mathbf{q}_1^T, \mathbf{q}_2^T\right]_B . \tag{3}$$

In this representation, the configuration at each of the two element nodes is described by nine vector components. In the global analysis, constraints are introduced at each node, reducing the number of free parameters to 6.

The orthonormality conditions for the unit vectors $\mathbf{q}_1, \mathbf{q}_2$ are equivalent to enforcing vanishing in-plane Green strain components,

$$\mathbf{e}(\mathbf{q}) = \frac{1}{2}\begin{bmatrix} \mathbf{q}_1^T\mathbf{q}_1 - 1 \\ \mathbf{q}_2^T\mathbf{q}_2 - 1 \\ \mathbf{q}_1^T\mathbf{q}_2 + \mathbf{q}_2^T\mathbf{q}_1 \end{bmatrix} = \mathbf{0}. \tag{4}$$

The corresponding element constraint gradient matrix with respect to the local base vectors in the cross-section plane $\mathbf{q}_\alpha$ follows by a differentiation as

$$\mathbf{C}(\mathbf{q}_\alpha) = \frac{\partial \mathbf{e}}{\partial \mathbf{q}_\alpha} = \begin{bmatrix} \mathbf{0} & \mathbf{q}_1^T & \mathbf{0} \\ \mathbf{0} & \mathbf{0} & \mathbf{q}_2^T \\ \mathbf{0} & \mathbf{q}_2^T & \mathbf{q}_1^T \end{bmatrix} , \quad \alpha = 0, 1, 2, \tag{5}$$

with the block columns corresponding to differentiation with respect to the components of $\mathbf{q}_0$, $\mathbf{q}_1$, and $\mathbf{q}_2$, respectively. These conditions are imposed at nodes A and B via global constraints on a two- or three-director set at the nodes as discussed in Section 6.

It is convenient to introduce the notation

$$\mathbf{q}^T = \left[\mathbf{q}_A^T, \mathbf{q}_B^T\right] , \qquad \mathbf{g}^T = \left[\mathbf{g}_A^T, \mathbf{g}_B^T\right] , \tag{6}$$

for the full set of generalized displacements and conjugate forces associated with a single element AB. The internal energy is given by the elastic potential G, and the generalized forces are identified by considering a small change δG of the displacement state,

$$\delta G = \delta\mathbf{q}^T \frac{\partial G}{\partial \mathbf{q}^T} = \delta\mathbf{q}^T\mathbf{g} . \tag{7}$$

This defines the generalized forces conjugate to the displacements $\mathbf{q}$ in the form

$$\mathbf{g} = \frac{\partial G}{\partial \mathbf{q}^T} . \tag{8}$$

The differentiation is performed with respect to the 18 unconstrained displacements $\mathbf{q}$ corresponding to nine components at each of the element nodes. The constraints (4) are imposed subsequently as part of the global system of equations. The generalized force components representing the nodal forces appearing in the interaction between the elements are derived via differentiation of the internal elastic energy by use of (8).

DOI: 10.1002/nme

3. KINEMATIC RELATIONS

For an elastic beam element, the internal elastic energy G associated with elastic deformation can be fully represented via a set of generalized strain components, each defining a mode of deformation. Rigid body motion does not contribute to the elastic energy, and thus the number of generalized strains is smaller than the number of generalized displacements. The stiffness relations for the full set of generalized displacements can therefore be obtained via a reduced number of deformation modes combined with a transformation between the generalized strains and generalized displacements as illustrated in the subsequent sections.

In the present formulation, it is convenient to choose the deformation modes such that they each correspond to a set of end loads in equilibrium as illustrated in Figure 3. A similar approach is presented in [22] for co-rotating beam elements. However, a central point of the present formulation is that the deformation modes are expressed with respect to the global frame of reference, and the associated deformation components are obtained by simple scalar products of the global generalized displacement vectors. In this way, the introduction of an intermediate co-rotating coordinate system is avoided, giving two important features: no special attention is required for combining overall rotations associated with rigid body motion and local rotations of the deformation modes, and no special procedures are needed for establishing full symmetry of the co-rotational part of the tangential stiffness, usually constructed from extension and rigid body rotations alone.

The six equilibrium modes comprise three modes with a constant internal force component and three modes with a constant internal moment component as illustrated in Figure 3 for a straight beam element of length $2a$. The local directors in the undeformed element are given by the base vectors $\{\mathbf{q}_1^0, \mathbf{q}_2^0, \mathbf{q}_3^0\}$, with $\mathbf{q}_1^0, \mathbf{q}_2^0$ defining the cross-section planes.

The first two deformation modes correspond to a constant shear force Q_1 and Q_2, respectively, each generated by a force couple at the end sections. In order to create equilibrium, each of the two shear force states must be accompanied by end moments

$$M_\alpha^a = a\, \mathrm{e}_{\alpha\beta}\, Q_\beta \,, \tag{9}$$

where $\mathrm{e}_{\alpha\beta}$ is the permutation symbol, defined by $\mathrm{e}_{12} = -\mathrm{e}_{21} = 1$ and $\mathrm{e}_{11} = \mathrm{e}_{22} = 0$. The moments M_α^a act in the same direction at nodes A and B and generate an anti-symmetric bending moment distribution in the beam element. For a symmetric beam element, this corresponds to anti-symmetric curvature distributions with rotation angle $\frac{1}{2}\varphi_\alpha^a$ at nodes A and B as illustrated in Figure 3(a, b). The factor $\frac{1}{2}$ on the end rotations is introduced to obtain the simple product form $M_\alpha^a \varphi_\alpha^a$ for the associated external virtual work. In the hierarchy of deformation modes, the anti-symmetric bending

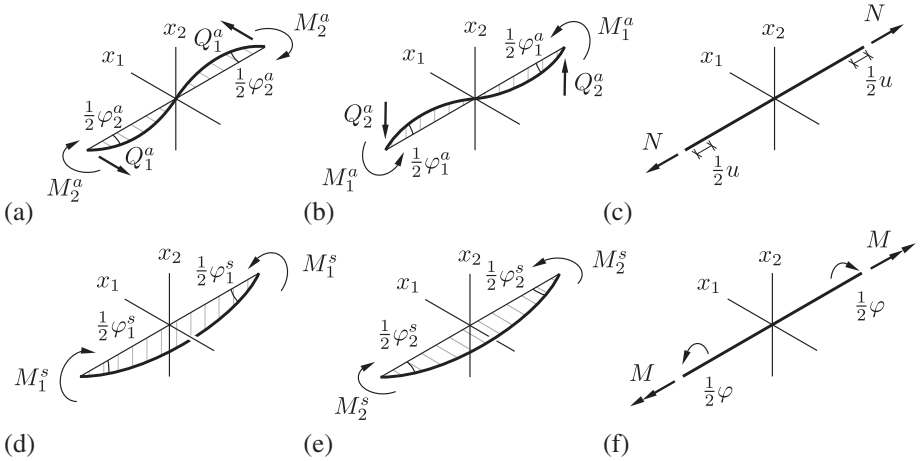

Figure 3. Deformation modes of beam element. (a) Constant shear force Q_1. (b) Constant shear force Q_2. (c) Constant normal force N. (d) Constant bending moment M_1. (e) Constant bending moment M_2. (f) Constant torsion moment M.

DOI: 10.1002/nme

modes are characterized by the constant shear forces Q_β, and it is convenient to introduce the associated conjugate displacements u_β. When using generalized stresses and the associated conjugate displacements, the corresponding work is expressed by a simple product. Thus, the external work of the anti-symmetric bending modes can be expressed either for the configuration in Figure 3 with rotation at nodes A and B, but without transverse displacement, or for the rotated element with opposite transverse displacements at A and B, but without rotation of these points. Rigid body motion does not influence the virtual work, and thus the virtual work can be expressed in two forms as

$$M^a_\alpha \, \varphi^a_\alpha = Q_\beta \, u_\beta \, . \tag{10}$$

Substitution of M^a_α from (9) into this relation results in conjugate transverse displacements given as

$$u_\beta = a \, \varphi^a_\alpha \, \mathrm{e}_{\alpha\beta} \, , \tag{11}$$

corresponding to the transverse displacement of node A relative to node B when the element is rotated to eliminate the end point of the rotations. The third mode corresponds to extension by the normal force N, generating the elongation u of the distance between the nodes. The first two of the constant moment modes consist of opposing bending moments M^s_α at nodes A and B, generating a constant and thereby symmetric bending moment distribution in the beam element. For a symmetric beam element, this corresponds to symmetric curvature distributions with rotation angle $\pm\frac{1}{2}\varphi^s_\alpha$ at nodes A and B as illustrated in Figure 3(c, d). The final constant moment mode corresponds to opposing torsion moments of magnitude M at A and B, generating a constant internal torsion moment M in the element and a total angle of twist φ. The generalized strains and conjugate stresses for the six equilibrium modes are conveniently collected in the vectors

$$\mathbf{v} = \left[u_1, u_2, u, \varphi^s_1, \varphi^s_2, \varphi\right]^T \quad , \quad \mathbf{t} = \left[Q_1, Q_2, N, M^s_1, M^s_2, M\right]^T \, , \tag{12}$$

whereby the external work takes the simple scalar product form $\mathbf{v}^T\mathbf{t}$.

While in principle large-displacement analysis of structures includes large deformations, the local deformations within an element are moderate given a sufficiently detailed discretization. In the present formulation, the generalized displacement components $\mathbf{q}$ account for arbitrarily large displacements and finite rotations of the nodes with respect to a global reference frame. These nodal generalized displacements are used to define generalized strains describing the equilibrium deformation modes of each element. The nonlinear kinematic relations describing the local deformations are sought in a homogenous quadratic form in the generalized displacements $\mathbf{q}$. For linear internal element properties, this leads to a bi-quadratic elastic energy potential, which is particularly suitable for designing a momentum and energy conserving time integration scheme in global form; see, for example, [29]. The examples in Section 7 indicate that the required number of the present simple elements is comparable to other more elaborate two-node elements and less than double for elements with interior nodes.

Generalized strains in quadratic form can be obtained by assuming that the angle φ_α between the cross-section normal $\mathbf{q}_3$ and the element reference vector $\Delta\mathbf{q}_0 = \mathbf{q}^B_0 - \mathbf{q}^A_0$ connecting nodes A and B is small, whereby $\sin\varphi_\alpha \simeq \varphi_\alpha$; see Figure 4. The rotation angle φ_α of a cross-section relative to the element reference vector $\Delta\mathbf{q}_0$ then follows by projecting the reference vector on to the unit vector $\mathbf{q}_\beta$ in the cross-section plane, whereby

$$\varphi_\alpha \simeq \frac{1}{2a}\Delta\mathbf{q}^T_0\mathbf{q}_\beta e_{\beta\alpha} \, . \tag{13}$$

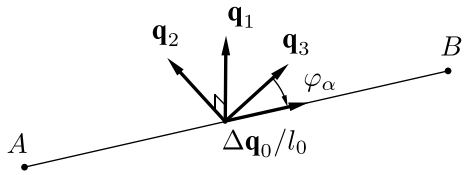

Figure 4. Local rotation by projection on beam reference axis.

DOI: 10.1002/nme

In the present formulation, a is assumed to be half the original length of the element, that is, without account of any local shortening effects due to bending. This is consistent with the assumption of the element as being initially straight, whereby the shortening due to bending becomes a higher-order effect. This may put certain restrictions on what can be represented by a single element, hence for some applications it may be convenient to extend the representation of the local deformation modes to a more sophisticated form accounting for nonlinear column effects, initial curvature, and so on; see for example [23, 25]. However, as illustrated in the examples in Section 7, the nonlinear geometric effects can be accurately captured by slightly increasing the number of elements, whereby the geometric stiffness effects are accounted for via the external contributions of the individual elements, essentially amounting to rotation of the forces at the nodes.

The generalized strain components (12) for the deformation modes are now expressed in terms of scalar products of the cross-section vectors $\mathbf{q}_\alpha$ at beam nodes A and B, and the element reference vector $\Delta\mathbf{q}_0$ by using the approximation (13). The angle of twist φ associated with the torsion mode is approximated by in-plane projections of the cross-section vectors $\mathbf{q}_\alpha$,

$$\varphi = \frac{1}{2}\left(\mathbf{q}_\alpha^A\right)^T \mathbf{q}_\beta^B \, e_{\beta\alpha} \,. \tag{14}$$

The rotation angles φ_α^s associated with symmetric bending follow as the difference between the local rotation angles evaluated at nodes A and B, whereby

$$\varphi_\alpha^s = \varphi_\alpha^B - \varphi_\alpha^A = \frac{1}{2a}\Delta\mathbf{q}_0^T\left(\mathbf{q}_\beta^B - \mathbf{q}_\beta^A\right) e_{\beta\alpha} \,. \tag{15}$$

Similarly, the anti-symmetric rotation angles φ_α^a can be identified as the sum of the local end-point angles, as

$$\varphi_\alpha^a = \varphi_\alpha^B + \varphi_\alpha^A = \frac{1}{2a}\Delta\mathbf{q}_0^T\left(\mathbf{q}_\beta^B + \mathbf{q}_\beta^A\right) e_{\beta\alpha} \,. \tag{16}$$

The equivalent transverse displacements u_β follow from substitution of this expression into (11),

$$u_\beta = -\frac{1}{2}\Delta\mathbf{q}_0^T\left(\mathbf{q}_\beta^B + \mathbf{q}_\beta^A\right) \,. \tag{17}$$

Finally, the Green strain ε is introduced as a measure for the axial extension the element, whereby the associated generalized strain component $u = 2a\varepsilon$ takes the form

$$u = \frac{1}{4a}\left(\Delta\mathbf{q}_0^T\Delta\mathbf{q}_0 - 4a^2\right) \,. \tag{18}$$

The relations (15)–(18) define the local generalized strains components $\mathbf{v}$ as quadratic forms of the global components of the generalized displacement components $\mathbf{q}$. The local strain components are obtained by scalar products of globally defined vectors, and they are therefore independent of a change of the global frame of reference. Thus, the generalized strains are invariant to finite rigid body motion. This is a crucial aspect of any finite displacement beam element, which has sometimes been violated; see for example [12] for a discussion on objectivity of strain measures.

4. LOCAL CONSTITUTIVE STIFFNESS

The constitutive stiffness associated with elastic deformation of the beam is conveniently derived from the complementary energy for the equilibrium modes defined in Figure 3. This leads to a simple procedure for obtaining the stiffness matrix for fairly general beam elements without the need for special measures for including shear deformation [27, 30]. Furthermore the locking problems, often encountered in low-order beam formulations due to inconsistent interpolation of rotations and displacements, are avoided.

DOI: 10.1002/nme

4.1. Elastic constitutive equations

For a linear elastic material, the internal energy is a quadratic form in the generalized strains $\mathbf{v}$. This can be expressed as

$$G(\mathbf{v}) = \frac{1}{2}\,\mathbf{v}^T\mathbf{A}\mathbf{v}\,, \tag{19}$$

with $\mathbf{A}$ representing the elastic stiffness associated with the generalized strains $\mathbf{v}$. The conjugate internal forces $\mathbf{t}$ then follow as the partial derivative of the internal energy with respect to the internal strains, whereby

$$\mathbf{t} = \frac{\partial G}{\partial \mathbf{v}^T} = \mathbf{A}\mathbf{v}\,. \tag{20}$$

In the present formulation, the generalized strains $\mathbf{v}$ and conjugate stresses $\mathbf{t}$ are defined by (12) associated with the deformation modes illustrated in Figure 3.

The relation between the global generalized forces $\mathbf{g}$ and the local internal stresses $\mathbf{t}$ from (20) is obtained by differentiation of the internal energy (8), as

$$\mathbf{g} = \left(\frac{\partial \mathbf{v}}{\partial \mathbf{q}}\right)^T \frac{\partial G}{\partial \mathbf{v}^T} = \left(\frac{\partial \mathbf{v}}{\partial \mathbf{q}}\right)^T \mathbf{t} = \mathbf{F}^T\mathbf{t}\,. \tag{21}$$

This identifies the transformation matrix between the local generalized stresses and global generalized forces in terms of the derivatives of their conjugate kinematic counterparts in the form

$$\mathbf{F} = \frac{\partial \mathbf{v}}{\partial \mathbf{q}}\,. \tag{22}$$

This transformation matrix serves to expand the reduced set of internal stresses to the full number of generalized forces similar to the transformation matrix used in [22, Chapter 5] in relation to a co-rotating formulation.

4.2. Complementary energy formulation

The constitutive properties of the beam element are contained in the stiffness matrix $\mathbf{A}$ associated with the deformation modes. A general form including the effect of shear deformation can be obtained from complementary energy via the flexibility matrix $\mathbf{A}^{-1}$ following the procedure described in [30]. The complementary energy is defined via a Legendre transform of the internal potential $G(\mathbf{v})$ as

$$G_c(\mathbf{t}) = \mathbf{v}^T\mathbf{t} - G(\mathbf{v}) = \frac{1}{2}\,\mathbf{t}^T\mathbf{A}^{-1}\,\mathbf{t}\,. \tag{23}$$

Each deformation mode corresponds to a state of constant internal force or moment, expressed in terms of the components in $\mathbf{t}$. For a general deformation state, the distribution of internal forces and moments is described by the components of the vectors $\mathbf{Q} = [Q_1, Q_2, Q_3]^T$ and $\mathbf{M} = [M_1, M_2, M_3]^T$. In elastic beam theory, these are related to the conjugate strain and curvature components $\boldsymbol{\gamma} = [\gamma_1, \gamma_2, \gamma_3]^T$ and $\boldsymbol{\kappa} = [\kappa_1, \kappa_2, \kappa_3]^T$, respectively, via a linear constitutive relation, which can be expressed in the flexibility or compliance format

$$\begin{bmatrix} \boldsymbol{\gamma} \\ \boldsymbol{\kappa} \end{bmatrix} = \begin{bmatrix}\, \mathbb{C} \,\end{bmatrix} \begin{bmatrix} \mathbf{Q} \\ \mathbf{M} \end{bmatrix}, \tag{24}$$

in terms of the symmetric 6×6 cross-section flexibility matrix $\mathbb{C}$. In the general case of an inhomogeneous anisotropic material, a full description of the deformation properties may require up to 21 independent flexibility components.

When the internal forces and strains have been defined as conjugate, the complementary energy per unit length of the beam follows in the form

$$G_s = \frac{1}{2}\begin{bmatrix}\mathbf{Q}^T, \mathbf{M}^T\end{bmatrix}\begin{bmatrix}\, \mathbb{C} \,\end{bmatrix}\begin{bmatrix} \mathbf{Q} \\ \mathbf{M} \end{bmatrix}. \tag{25}$$

DOI: 10.1002/nme

This form is particularly suitable for calculating the local constitutive element stiffness, as the distribution of the internal forces **Q** and moments **M** along the element is statically determinate and defined in simple terms from the equilibrium modes in Figure 3, independent of the cross-section properties of the beam element.

Let the axial position in the beam element of length $2a$ be represented by the normalized coordinate $\xi = [-1, 1]$. The distribution of internal forces can now be expressed in terms of the constant components, as

$$\begin{bmatrix} Q_1(\xi) \\ Q_2(\xi) \\ Q_3(\xi) \\ M_1(\xi) \\ M_2(\xi) \\ M_3(\xi) \end{bmatrix} = \begin{bmatrix} 1 & 0 & 0 & 0 & 0 & 0 \\ 0 & 1 & 0 & 0 & 0 & 0 \\ 0 & 0 & 1 & 0 & 0 & 0 \\ 0 & a\xi & 0 & 1 & 0 & 0 \\ -a\xi & 0 & 0 & 0 & 1 & 0 \\ 0 & 0 & 0 & 0 & 0 & 1 \end{bmatrix} \begin{bmatrix} Q_1 \\ Q_2 \\ N \\ M_1^s \\ M_2^s \\ M \end{bmatrix}, \tag{26}$$

or in the more compact form

$$\begin{bmatrix} \mathbf{Q}(\xi) \\ \mathbf{M}(\xi) \end{bmatrix} = \mathbf{T}(\xi)\,\mathbf{t}\,, \tag{27}$$

where the 6×6 transformation matrix $\mathbf{T}(\xi)$ is defined in (26). The flexibility matrix of the deformation modes can now be obtained by substitution of the relation (26) into the cross-section flexibility relation (25) followed by integration over the length of the element,

$$G_c(\mathbf{t}) = \int_0^{l_0} G_s(s_0)\,ds_0 = a\int_{-1}^{1} \frac{1}{2}\left[\mathbf{Q}(\xi)^T,\, \mathbf{M}(\xi)^T\right] \mathbb{C} \begin{bmatrix} \mathbf{Q}(\xi) \\ \mathbf{M}(\xi) \end{bmatrix} d\xi\,, \tag{28}$$

which identifies the flexibility matrix $\mathbf{A}^{-1}$ of the deformation modes by the integral

$$\mathbf{A}^{-1} = a\int_{-1}^{1} \mathbf{T}(\xi)^T \mathbb{C}\, \mathbf{T}(\xi)\, d\xi\,. \tag{29}$$

The stiffness matrix **A** for the deformation modes then follows from inversion of (29). In particular, for a constant flexibility matrix $\mathbb{C}$, for example for a prismatic beam, the ξ-terms accounting for the linearly varying anti-symmetric moment only contribute via quadratic terms, and thus it may be convenient to perform the integration in explicit form, whereby

$$\mathbf{A}^{-1} = 2a \begin{bmatrix} C_{11} + \frac{1}{3}a^2C_{55} & C_{12} - \frac{1}{3}a^2C_{54} & C_{13} & C_{14} & C_{15} & C_{16} \\ C_{21} - \frac{1}{3}a^2C_{45} & C_{11} + \frac{1}{3}a^2C_{44} & C_{23} & C_{24} & C_{25} & C_{26} \\ C_{31} & C_{32} & C_{33} & C_{34} & C_{35} & C_{36} \\ C_{41} & C_{42} & C_{43} & C_{44} & C_{45} & C_{46} \\ C_{51} & C_{52} & C_{53} & C_{54} & C_{55} & C_{56} \\ C_{61} & C_{62} & C_{63} & C_{64} & C_{65} & C_{66} \end{bmatrix}. \tag{30}$$

In particular, it is noted that the flexibility procedure for calculating the stiffness matrix yields a nonsingular format also for beams without shear flexibility. The procedure is easily extended to pre-twisted or curved beams; see for example [27, 28]. However, in the present paper, only straight homogeneous beams are considered, hence the stiffness matrix of the deformation modes takes the following uncoupled form:

$$\mathbf{A} = \frac{1}{2a} \begin{bmatrix} 3\psi_2 a^{-2} EI_2 & & & & & \\ & 3\psi_1 a^{-2} EI_1 & & & & \\ & & EA & & & \\ & & & EI_1 & & \\ & & & & EI_2 & \\ & & & & & GJ \end{bmatrix}, \tag{31}$$

DOI: 10.1002/nme

where EI_α represents the stiffness of the symmetric bending mode about the α-axis, GJ is the St. Venant torsional stiffness, and EA is the axial stiffness. The coefficients $3\psi_\alpha EI_\alpha$ are the bending stiffness of the anti-symmetric bending modes expressed via the shear flexibility parameter ψ_α defined as

$$\psi_\alpha = \frac{1}{1+\Phi_\alpha}, \quad \Phi_\alpha = \frac{3EI_\alpha}{a^2 GA_\beta}, \tag{32}$$

where α and β denote two different transverse axes. In the limit of vanishing shear flexibility $\Phi_\alpha = 0$, whereby the stiffness of the anti-symmetric bending modes in (31) is reduced to $3EI_\alpha$.

5. BEAM ELEMENT STIFFNESS MATRIX

In nonlinear analysis, the element stiffness matrix can be derived from the incremental form of the generalized force relation (21). This involves a change in the internal forces $\mathbf{t}$ as well as a change in the transformation matrix $\mathbf{F}$, as expressed by

$$d\mathbf{g} = \mathbf{F}^T d\mathbf{t} + d\mathbf{F}^T \mathbf{t}. \tag{33}$$

The first term represents the change in the internal force vector, associated with a change in deformation state via the local constitutive relation (20). The internal forces are functions of the generalized strains $\mathbf{v}$, hence the incremental change associated with a change in the generalized displacements $\mathbf{q}$ follows via the chain rule of differentiation as

$$d\mathbf{t} = d\mathbf{q}^T \frac{\partial \mathbf{t}}{\partial \mathbf{q}^T} = d\mathbf{q}^T \left[\left(\frac{\partial \mathbf{v}}{\partial \mathbf{q}} \right)^T \frac{\partial^2 G}{\partial \mathbf{v}^T \partial \mathbf{v}} \right] = d\mathbf{q}^T \left[\mathbf{F}^T \mathbf{A} \right], \tag{34}$$

with the transformation matrix $\mathbf{F}$ defined by (22) and the stiffness matrix $\mathbf{A}$ of the deformation modes, obtained as the inverse of the 6×6 flexibility matrix (29).

The second term in (33) is conveniently expressed in component form, as

$$d\mathbf{F}^T \mathbf{t} = d\mathbf{q}^T \left[\frac{\partial^2 v_k}{\partial \mathbf{q}^T \partial \mathbf{q}} t_k \right], \tag{35}$$

with summation over repeated subscripts $k = 1 \ldots 6$ associated with each of the internal stress components t_k. Upon substitution of the incremental relations (34) and (35) in (33), the increment of the global components of the element force vector is obtained in the form

$$d\mathbf{g} = \mathbf{K}\, d\mathbf{q}, \tag{36}$$

with the tangent stiffness matrix $\mathbf{K}$ given in the symmetric form

$$\mathbf{K} = \mathbf{F}^T \mathbf{A} \mathbf{F} + \frac{\partial^2 v_k}{\partial \mathbf{q}^T \partial \mathbf{q}} t_k = \mathbf{F}^T \mathbf{A} \mathbf{F} + \mathbf{K}_g. \tag{37}$$

The general form of this format is a characteristic of Lagrange type finite element formulations, with the first term expressing the constitutive changes of the internal stress state, transformed from local to global representation via the matrix $\mathbf{F}$, while the second term represents the geometric stiffness $\mathbf{K}_g$ due to rotation of the current stresses via the second derivatives of the generalized stress components v_k; see for example [22].

The constitutive stiffness matrix, represented as the first term in (37) is obtained by matrix multiplication between the local stiffness matrix $\mathbf{A}$, obtained via the inverse of the flexibility matrix (29), and the transformation matrix (22). The latter can be expressed in explicit form by differentiation of the quadratic kinematic relations (15)–(18), yielding

$$\mathbf{F}^T = \left(\frac{\partial \mathbf{v}}{\partial \mathbf{q}} \right)^T = \frac{1}{2a} \begin{bmatrix} 2a\bar{\mathbf{q}}_1 & 2a\bar{\mathbf{q}}_2 & -\Delta\mathbf{q}_0 & -\Delta\mathbf{q}_2 & \Delta\mathbf{q}_1 & \mathbf{0} \\ -a\Delta\mathbf{q}_0 & \mathbf{0} & \mathbf{0} & \mathbf{0} & \Delta\mathbf{q}_0 & a\mathbf{q}_2^B \\ \mathbf{0} & -a\Delta\mathbf{q}_0 & \mathbf{0} & -\Delta\mathbf{q}_0 & \mathbf{0} & -a\mathbf{q}_1^B \\ -2a\bar{\mathbf{q}}_1 & -2a\bar{\mathbf{q}}_2 & \Delta\mathbf{q}_0 & \Delta\mathbf{q}_2 & -\Delta\mathbf{q}_1 & \mathbf{0} \\ -a\Delta\mathbf{q}_0 & \mathbf{0} & \mathbf{0} & \mathbf{0} & -\Delta\mathbf{q}_0 & -a\mathbf{q}_2^A \\ \mathbf{0} & -a\Delta\mathbf{q}_0 & \mathbf{0} & \Delta\mathbf{q}_0 & \mathbf{0} & a\mathbf{q}_1^A \end{bmatrix}. \tag{38}$$

DOI: 10.1002/nme

Here, $\mathbf{F}$ is presented in transposed form for typographical reasons. Furthermore, the sum and the difference of the end point vectors have been introduced as $2\bar{\mathbf{q}}_\alpha = \mathbf{q}_\alpha^A + \mathbf{q}_\alpha^B$ and $\Delta\mathbf{q}_\alpha = \mathbf{q}_\alpha^B - \mathbf{q}_\alpha^A$, respectively.

The geometric element stiffness matrix is conveniently arranged in the block matrix format,

$$\mathbf{K}_g = \frac{\partial^2 v_k}{\partial \mathbf{q}^T \partial \mathbf{q}} t_k = \begin{bmatrix} \mathbf{K}_{11}^g & \mathbf{K}_{12}^g \\ \mathbf{K}_{21}^g & \mathbf{K}_{22}^g \end{bmatrix}. \tag{39}$$

The block matrices are then identified by differentiation of the generalized strain components v_k given by (14), (16) and (17), (18), whereby the geometric stiffness block matrices are found to be

$$\mathbf{K}_{11}^g = \frac{1}{2a} \begin{bmatrix} \mathbf{N} & -\mathbf{M}_2^s + \mathbf{M}_2^a & \mathbf{M}_1^s - \mathbf{M}_1^a \\ -\mathbf{M}_2^s + \mathbf{M}_2^a & \mathbf{0} & \mathbf{0} \\ \mathbf{M}_1^s - \mathbf{M}_1^a & \mathbf{0} & \mathbf{0} \end{bmatrix}, \tag{40}$$

$$\mathbf{K}_{22}^g = \frac{1}{2a} \begin{bmatrix} \mathbf{N} & -\mathbf{M}_2^s - \mathbf{M}_2^a & \mathbf{M}_1^s + \mathbf{M}_1^a \\ -\mathbf{M}_2^s - \mathbf{M}_2^a & \mathbf{0} & \mathbf{0} \\ \mathbf{M}_1^s + \mathbf{M}_1^a & \mathbf{0} & \mathbf{0} \end{bmatrix}, \tag{41}$$

$$\mathbf{K}_{12}^g = \mathbf{K}_{21}^{gT} = \frac{1}{2a} \begin{bmatrix} -\mathbf{N} & \mathbf{M}_2^s + \mathbf{M}_2^a & -\mathbf{M}_1^s - \mathbf{M}_1^a \\ \mathbf{M}_2^s - \mathbf{M}_2^a & \mathbf{0} & a\mathbf{M} \\ -\mathbf{M}_1^s + \mathbf{M}_1^a & -a\mathbf{M} & \mathbf{0} \end{bmatrix}. \tag{42}$$

These matrices have conveniently been expressed in terms of the symmetric moment M_α^s, the anti-symmetric moment M_α^a defined in terms of Q_β by (9), the torsion moment M, and the normal force N via the 3×3 unit matrix representations

$$\mathbf{M}_\alpha^s = M_\alpha^s \mathbf{I}, \qquad \mathbf{M}_\alpha^a = M_\alpha^a \mathbf{I}, \qquad \mathbf{M} = M\mathbf{I}, \qquad \mathbf{N} = N\mathbf{I}. \tag{43}$$

It is noted that the bending moment combinations correspond to the bending moments M_α^A and M_α^B at the element nodes. This explicit and compact form of the element matrices $\mathbf{A}$, $\mathbf{F}$, and $\mathbf{K}_g$ leads to a straightforward implementation as illustrated in the following.

6. SOLUTION ALGORITHM

In the present formulation, the equilibrium equations are derived from an extended potential $G_*(\mathbf{q})$, where the sum of the internal energy $G(\mathbf{q})$ and the work performed by external nodal forces $\mathbf{f}$ are supplemented by the kinematic zero strain constraints (4) associated with orthonormality of the cross-section directors. In the assembled model, the element base vectors $\mathbf{q}_\alpha$ are represented in terms of a set of base vectors associated with each node. The constraints are introduced via Lagrange multipliers $\boldsymbol{\lambda}$, and thus the extended potential can be expressed in the form

$$G_*(\mathbf{q}) = G(\mathbf{q}) + \mathbf{e}(\mathbf{q})^T \boldsymbol{\lambda} - \mathbf{q}^T \mathbf{f}. \tag{44}$$

Stationarity with respect to $\mathbf{q}$ and $\boldsymbol{\lambda}$ leads to the following set of nonlinear algebraic equations

$$\begin{aligned} \mathbf{g}(\mathbf{q}) + \mathbf{C}(\mathbf{q})^T \boldsymbol{\lambda} &= \mathbf{f}, \\ \mathbf{e}(\mathbf{q}) &= \mathbf{0}, \end{aligned} \tag{45}$$

where the first set defines the equilibrium equations, while the second set holds the constraint equations arranged in the form $\mathbf{e}^T = [\mathbf{e}_1^T, \mathbf{e}_2^T, \ldots, \mathbf{e}_n^T]$ for the nodes $1 \ldots n$. These equations can be solved iteratively by the Newton–Raphson method. The unknown variables of the problem, the generalized nodal displacements $\mathbf{q}$, and the Lagrange multipliers $\boldsymbol{\lambda}$ are conveniently collected in the vector $\mathbf{u} = [\mathbf{q}^T, \boldsymbol{\lambda}^T]^T$. The residual vector $\mathbf{r}$ representing the unbalance between internal forces and

DOI: 10.1002/nme

applied external load is formed as the difference between the left-hand and right-hand sides in (45), yielding

$$\mathbf{r} = \begin{bmatrix} \mathbf{f} - \mathbf{g}(\mathbf{q}) - \mathbf{C}(\mathbf{q})^T\boldsymbol{\lambda} \\ -\mathbf{e}(\mathbf{q}) \end{bmatrix}. \tag{46}$$

Equilibrium iterations are performed using the Newton–Raphson scheme, which essentially amounts to equating the linearized residual equation to zero, via the current residual vector $\mathbf{r}$ and the linearized increment $\delta\mathbf{r}$, as

$$\mathbf{r} + \delta\mathbf{r} = \mathbf{r} + \left(\frac{\partial \mathbf{r}}{\partial \mathbf{q}}\delta\mathbf{q} + \frac{\partial \mathbf{r}}{\partial \boldsymbol{\lambda}}\delta\boldsymbol{\lambda} + \ldots\right) = \mathbf{0}. \tag{47}$$

This can be arranged in the form of a set of linearized equations for the increments $\delta\mathbf{u}$,

$$\mathbf{K}\delta\mathbf{u} = \mathbf{r}, \tag{48}$$

where the tangential stiffness for the system is defined as the partial derivatives of the residual relation (46), as

$$\mathbf{K}_* = \frac{\partial \mathbf{r}}{\partial \mathbf{u}} = \begin{bmatrix} \mathbf{K} + \boldsymbol{\Lambda} & \mathbf{C}(\mathbf{q})^T \\ \mathbf{C}(\mathbf{q}) & \mathbf{0} \end{bmatrix}. \tag{49}$$

The element stiffness matrix is given in explicit form by (37) via the deformation gradient (22) and the geometric stiffness matrices (40), (41), and (42). The matrices $\mathbf{C}(\mathbf{q})$ and $\boldsymbol{\Lambda}(\boldsymbol{\lambda})$ are block diagonal matrices in the form

$$\mathbf{C}(\mathbf{q}) = \begin{bmatrix} \mathbf{C}_1 & & \\ & \ddots & \\ & & \mathbf{C}_n \end{bmatrix}, \quad \boldsymbol{\Lambda}(\boldsymbol{\lambda}) = \begin{bmatrix} \boldsymbol{\Lambda}_1 & & \\ & \ddots & \\ & & \boldsymbol{\Lambda}_n \end{bmatrix}, \tag{50}$$

in terms of the nodal contribution to the constraint derivatives $\mathbf{C}_j$.

The number of constraints depends on the problem. In a general three-dimensional problem, the constraint conditions $\mathbf{e}_j$ contain six conditions, each corresponding to a Green strain component.

Table I. Solution algorithm.

1)	Initial conditions	$\mathbf{u} = \left[\mathbf{q}_0^T, \mathbf{0}^T\right]^T$
2)	Flexibility matrix	$\mathbf{A}^{-1} = a\int_{-1}^{1} \mathbf{T}_\xi^T \mathbb{C}\, \mathbf{T}_\xi \, d\xi,$
3)	Increment load	$\mathbf{f} = \mathbf{f}_n + \Delta\mathbf{f}$
4)	Stress and internal forces:	
	Generalized strain	$\mathbf{v}$ from (15) to (18).
	Generalized stress	$\mathbf{t} = \mathbf{A}\mathbf{v}$.
	Strain gradient	$\mathbf{F} = \partial\mathbf{v}/\partial\mathbf{q}$
	Internal forces	$\mathbf{g} = \mathbf{F}^T\mathbf{t}$
5)	Residual calculation	$\mathbf{r} = \begin{bmatrix} \mathbf{f} - \mathbf{g} - \mathbf{C}(\mathbf{q})^T\boldsymbol{\lambda} \\ -\mathbf{e}(\mathbf{q}) \end{bmatrix}$
6)	Check global equilibrium	If $\|\mathbf{r}\| < \varepsilon_\mathrm{r}$, repeat from 3).
7)	Form tangent stiffness	$\mathbf{K} = \mathbf{F}^T\mathbf{A}\mathbf{F} + \dfrac{\partial^2 v_k}{\partial\mathbf{q}^T\partial\mathbf{q}} t_k$
		$\mathbf{K}_* = \begin{bmatrix} \mathbf{K} + \boldsymbol{\Lambda} & \mathbf{C}^T \\ \mathbf{C} & \mathbf{0} \end{bmatrix}$
8)	Solve global equations	$\delta\mathbf{u} = \mathbf{K}_*^{-1}\,\mathbf{r}$
		$\mathbf{u} = \mathbf{u} + \delta\mathbf{u}$
9)	Return to 3).	

DOI: 10.1002/nme

However, in the case of a two-dimensional initial geometry, only the three strain components indicated in (4), with gradient matrix $\mathbf{C}_j$ as given in (5), are needed. In the plane case, the Lagrange multiplier matrix $\boldsymbol{\Lambda}_j$ for node j appearing on the diagonal of the global stiffness matrix (49) takes the form

$$\boldsymbol{\Lambda}_j = \begin{bmatrix} \mathbf{0} & \mathbf{0} & \mathbf{0} \\ \mathbf{0} & \lambda_1\mathbf{I} & \lambda_3\mathbf{I} \\ \mathbf{0} & \lambda_3\mathbf{I} & \lambda_2\mathbf{I} \end{bmatrix}_j . \tag{51}$$

The introduction of support conditions, usually expressed as homogeneous nodal constrains, are easily implemented by eliminating the associated degrees of freedom. For the translational degrees of freedom, this task is trivial, while the procedure for preventing rotation about a fixed axis, for example, $\mathbf{q}_3$, amounts to eliminating the in-plane transverse component of one of the orthogonal vectors spanning the plane perpendicular to the axis of rotation, that is, either $\mathbf{q}_{12}$ or $\mathbf{q}_{21}$ and vice versa.

An implementation based on Newton–Raphson iterations is illustrated in Table I with a termination criterion requiring that the Euclidean norm of the residual vector (46) must be less than a prescribed value ε_r. Classic Newton–Raphson iterations are performed with a constant load increment within each equilibrium iteration; hence, these methods encounter problems at load maximum. In the following examples, the results for nonmonotonic changing loads have been obtained using the arc-length method in the form presented in [22].

7. REPRESENTATIVE NUMERICAL EXAMPLES

In this section, the numerical performance of the presented beam element is illustrated on a number of classic benchmark examples from the literature. The capability of handling large displacements and finite rotations is illustrated by plane as well as spatial problems.

7.1. Large deformation of cantilever

The first example considers large deformation of a cantilever subjected to a transverse force P at its free end as shown in Figure 5(a). The example has been considered by a number of authors for illustrating the influence of geometric stiffness for various beam formulations; see for example [22, 26, 31]. Parameters similar to the ones used in the latter two references have been used, that is, the cantilever is modeled as a beam with length $L = 2$, a rectangular cross-section with $h = b = 0.1$, and Young's modulus $E = 2.07 \times 10^{11}$. Vanishing shear and axial deformations have been enforced by increasing the associated stiffness coefficients by a factor of 10^5 for

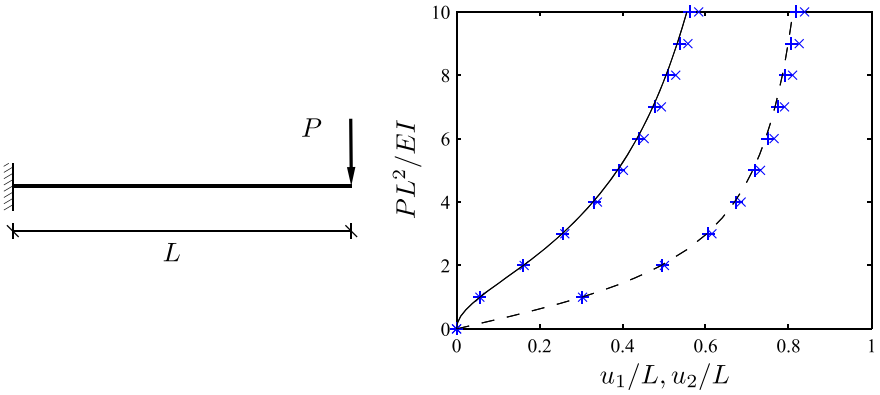

Figure 5. Cantilever with conservative end force. (a) Initial configuration. (b) Normalized load-displacement curves. (×) Four elements, (+) eight elements.

DOI: 10.1002/nme

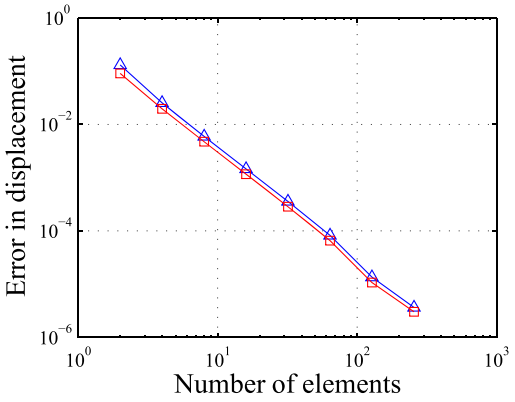

Figure 6. Convergence of tip displacements. (△) u_1 elements, (□) u_2.

comparison with an accurate elliptic integral solution based on inextensible elastica theory given by Mattiasson [32]. The load is described by the nondimensional parameter PL^2/EI and applied in 10 equal load steps leading to a final load of $PL^2/EI = 10$. Results for the nondimensional load and the nondimensional displacements u_1/L and u_2/L are illustrated in Figure 5(b) for two different discretizations corresponding to four and eight equal beam elements, respectively. The results are obtained with a relative tolerance of the residual of 10^{-6} leading to an average number of iterations around six. The elliptic integral solution [32] is plotted for comparison. It is seen that both models agree well with the analytical results, even at the final state where the horizontal displacement exceeds half the length of the beam. The deflections obtained using the four element discretization correspond to these numerical results within an accuracy of 2.5% and 2.0% for the horizontal and vertical deflections, respectively, while the error is reduced to below 0.6% and 0.5%, respectively, when increasing the number of elements to eight. The element exhibits second-order convergence as illustrated in Figure 6, which demonstrates a rather good performance, when considering the absence of local geometric stiffness within the individual elements.

7.2. Shallow angle frame

In this example, the shallow angle beam shown in Figure 7(a) is considered. The angle beam is loaded by a vertical downward load at the central node. A crucial feature of this example is the need for accounting for shortening due to bending. This is not included within the element in the present formulation, and thus it is necessary to use more than one element for each straight beam, whereby the shortening effect is represented by the finite displacements of the beam nodes. The solution

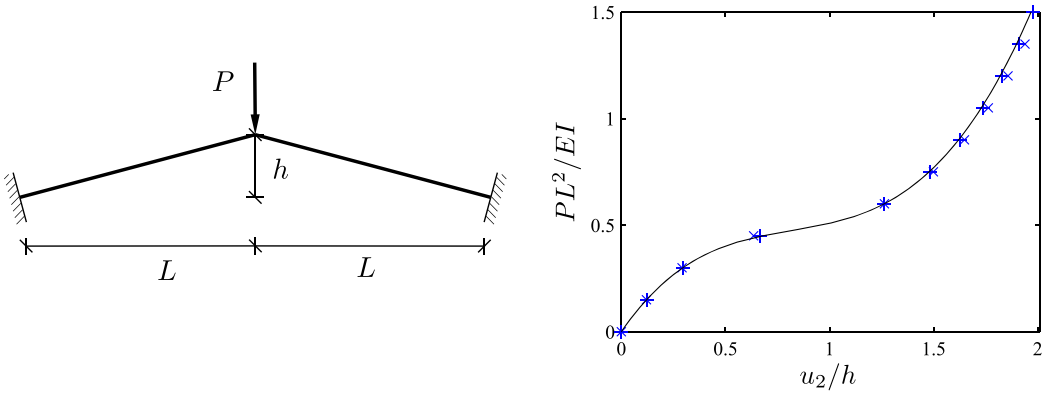

Figure 7. Angle beam with clamped supports. (a) Initial configuration. (b) Normalized load-displacement curve. (×) Five elements, (+) 10 elements, (—) reference solution obtained by using 50 elements.

DOI: 10.1002/nme

depends on the inclination h/b as well as the relative slenderness of the two beams, which may be expressed as $L_0^2 A/I$. Results for an inclination of $h/b = 0.024$ and a slenderness of $L_0^2 A/I = 3.0 \times 10^4$ are shown in Figure 7(b) in terms of the nondimensional vertical load PL^2/EI as a function of the vertical displacement of the center node u_2/L.

The results have been obtained for two models where each straight beam has been modeled using five and 10 identical elements, respectively. Approximate solutions can be obtained based on second-order theory according to Williams [33], or by using a more direct approach where each beam is considered as an inclined beam–column in a state of anti-symmetric bending; see, for example, [34]. However, both approaches involve linearization of the angles, and thus none of them represent the exact solution. Instead, comparison is performed with respect to a reference solution obtained by using 50 elements for each straight beam. The final load $P = 1.5EI/L^2$ is reached in 10 equal load steps using 4.7 and 4.8 Newton–Raphson iterations, respectively. It is seen that excellent agreement is found by using only five elements, which illustrate that the representation of local effects such as shortening due to bending can be obtained by using a moderate number of elements. In the formulation of Neuhofer and Filippou [25], the nonlinear deformation is included in a nonlinear kinematic field inside the element, leading to similar results when using five integration points within the element.

7.3. Buckling of clamped-hinged circular arch

Application of the present simple explicit beam formulation to a curved structure is now considered. A nonlinear analysis of the pre-buckling and post-buckling behavior of the clamped-hinged circular arch illustrated in Figure 8(a) is performed. Numerical results for this example have been presented by several authors for validating flexible beam formulations; see for example Simo and Vu-Quoc [4], Géradin and Cardona [35], Ibrahimbegovic [7], and Gerstmayr and Irschik [31]. Furthermore, inextendable elastica solutions for post-buckling of arches with various angles have been presented by DaDeppo and Schmidt [36]. Parameters similar to those in [7] have been used corresponding to an arch with radius $R = 100$ and an angle of $\phi = 215°$. The bending stiffness is $EI = 10^6$, while the axial and shear stiffness are $EA = GA = 10^2 EI$ in order to approximate the inextensible elastica solution.

Results for the normalized horizontal displacements u_1/R and the normalized vertical displacements u_2/R for varying load P, described via the nondimensional parameter $\lambda = PR^2/EI$, are shown in Figure 9. These have been obtained an arc-length solver with a hyperplane constraint for controlling the current displacements and load increments [22]. Furthermore, the deformed shape at load levels $\lambda_i = \{0.0, 4.0, 7.0, 8.8, -0.8, 0.8, 9.1\}$ corresponding to the ones presented in [4] are shown in Figure 8(b). Two different configurations based on 20 and 40 straight beam elements are considered. The behavior for both configurations agrees well with the results presented in [4, 35]

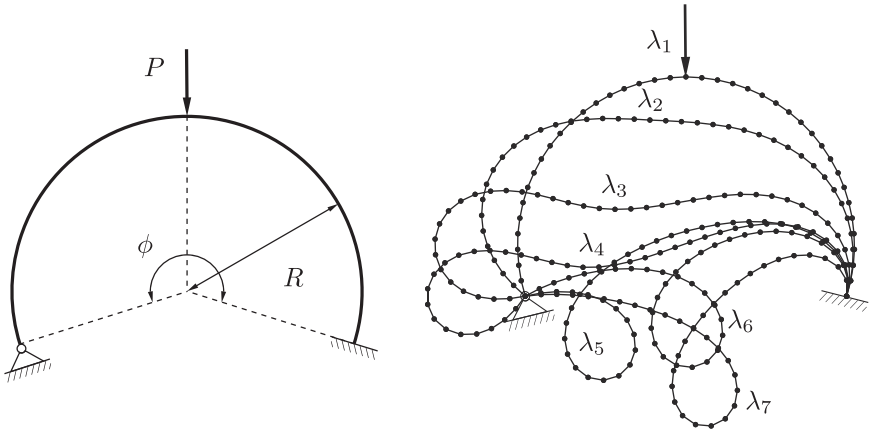

Figure 8. Clamped-hinged circular arch. (a) Initial configuration. (b) Deformed configuration at various load levels λ_i

DOI: 10.1002/nme

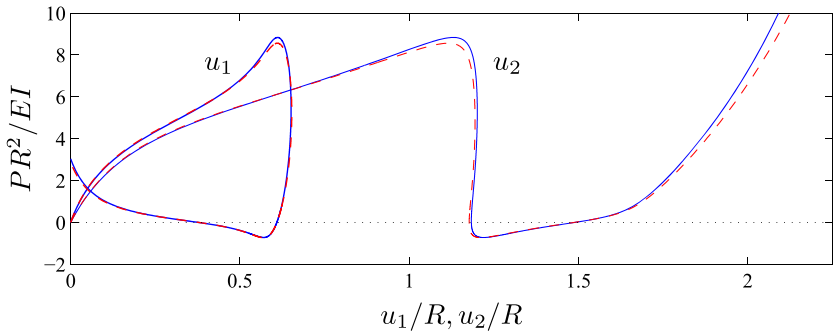

Figure 9. Normalized load-displacement curves for clamped-hinged circular arch. (—) 40 elements, (- - -) 20 elements.

where 40 linear elements have been used. The present 20 element discretization exhibits a slightly lower buckling load but still captures the overall behavior. The buckling load for the 40 element discretization has been found to 884, which is within an error of 1.5% of the value reported by da Deppo and Schmidt [36] of 897. A better accuracy for the 20 element discretization could be obtained with the present formulation by including pre-curvature as in [7].

7.4. Buckling of hinged angle frame

In this example, the buckling of the hinged frame illustrated in Figure 10 is considered. In essence, the buckling behavior is driven by a column instability of the vertical element, which can be interpreted as a spring-supported Euler column subjected to an eccentric vertical load at the top. The example has also been considered previously by several authors; see for example Simo and Vu-Quoc [4], Betsch and Steinmann [10], or Romero and Armero [9].

The parameters correspond to the ones used in [4], that is, a square frame with $h = b = 120$ subjected to a conservative vertical load P located at a horizontal distance of 24 from the frame corner. Each leg is modeled as a beam with a rectangular cross-section 2×3, Young's modulus $E = 7.2 \times 10^6$, and a Poisson's ratio $\nu = 0.3$. This corresponds to an axial stiffness $EA = 43.20 \times 10^6$, a shear stiffness $GA = 16.62 \times 10^6$, a bending stiffness $EI = 14.40 \times 10^6$, and a torsional stiffness $GJ = 11.08 \times 10^6$.

Results for the load–displacement curves are presented in Figure 11(a) and 11(b) for two different representations corresponding to five and 10 elements per leg. The post-buckling behavior has been traced using an arc-length solver with a hyperplane constraint for simultaneous control of the load

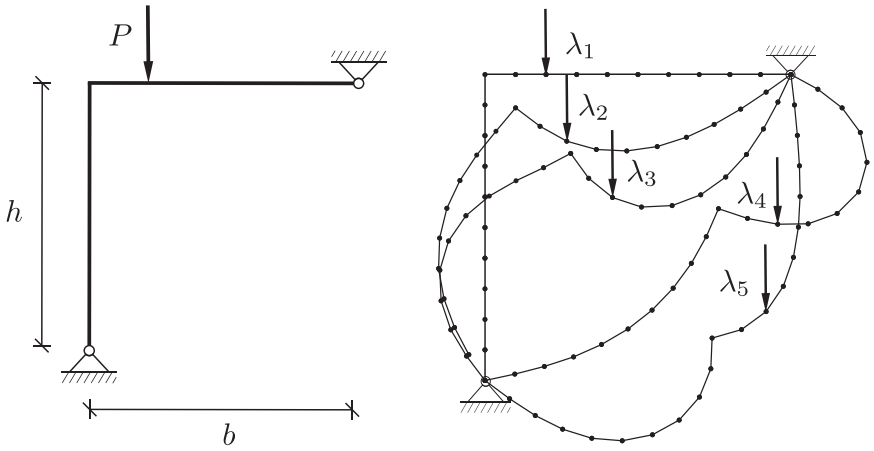

Figure 10. Buckling of hinged angle frame. (a) Initial configuration. (b) Deformed configuration at various load levels λ_i

DOI: 10.1002/nme

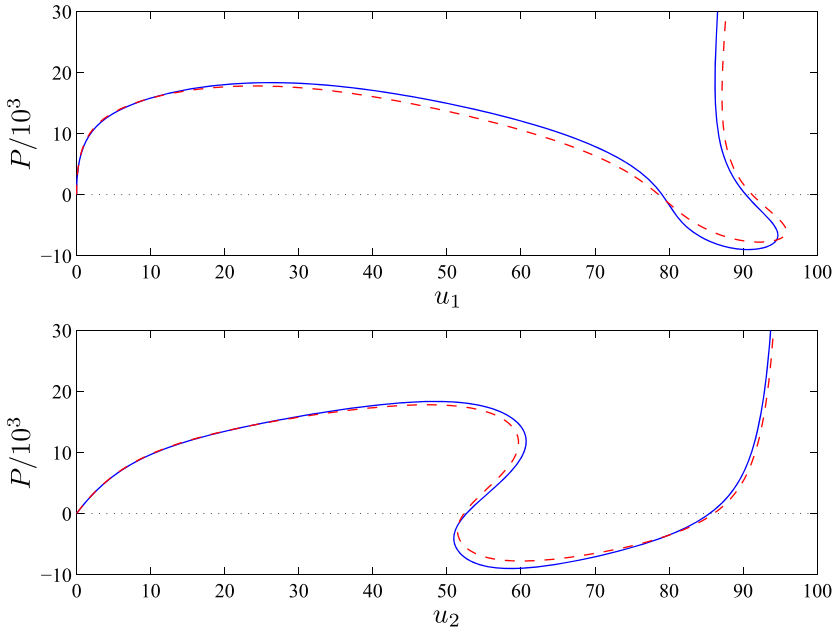

Figure 11. Load-displacement curves for hinged angle frame. (a) Horizontal displacement. (b) Vertical displacement. (—) 10 elements per leg, (- - -) five elements per leg.

and displacement increments; see, for example, [22]. It is seen that the response obtained by the present 10 element discretization for each leg is very similar to the ones presented in the references, while a slight difference is observed when each leg is discretized using only five elements. However, it should be noted that quadratic three-node elements have been used in all the references; hence, the present simple explicit formulation is fully competitive when the same number of nodes is used. Finally, the deformed configuration at certain load levels defined in terms of $\lambda_j = P/10^3$ are illustrated in Figure 10(b). The load levels are found as $\lambda_1 = 0.00$, $\lambda_2 = 15.05$, $\lambda_3 = 18.35$, $\lambda_4 = -8.98$, and $\lambda_1 = 20.75$, which agrees well with the results in [4, 10].

7.5. Three-dimensional deformation of curved cantilever

The last example illustrates the three-dimensional performance based on the 45-degree cantilever bend originally proposed by Bathe and Belourchi [37] and used for numerical validation of various beam formulations by a number of authors; see for example Simo and Vu-Quoc [4]. The example has furthermore been used to demonstrate path invariance of various beam formulations; see

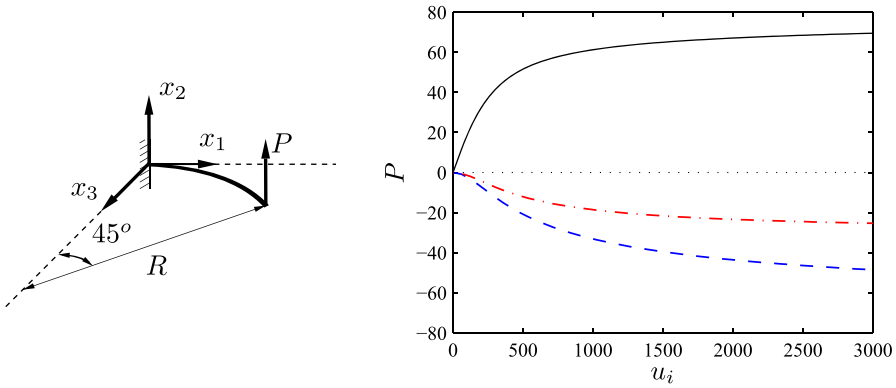

Figure 12. Cantilever 45-degree bend. (a) Initial configuration. (b) Load-displacement curves. (—) u_1, (- - -) u_2, (-·-) u_3.

DOI: 10.1002/nme

Table II. Tip position for curved cantilever beam (eight elements).

	x_1	x_2	x_3
Bathe and Belourch [37]	47.2	53.4	15.9
Simo and Vu-Quoc (GEBT) [4]	47.23	53.37	15.79
Cardona and Géradin (GEBT) [6]	47.04	53.50	15.55
Romero and Armero (GEBT) [11]	46.98	53.50	15.69
Crisfield (CR) [21]	46.84	53.71	15.61
Jonker and Meijaard (CR) [26]	46.94	53.64	15.64
Present explicit element	46.63	54.58	15.44

Jelenić and Crisfield [8] or Betsch and Steinmann [10]. However, the present formulation relies on an objective local deformation description via a set of deformation modes. Thus, the formulation avoids interpolation of incremental rotations and is path independent by construction.

The curved beam is modeled as a 45° section of a circle with radius $R = 100$ in the x_1-x_3 plane as illustrated in Figure 12(a). The beam has a unit square cross-section, and a Young's modulus and shear modulus of $E = 10^7$ and $G = E/2$, respectively. A conservative vertical load is applied at the tip in the x_2 direction. The tip displacement as a function of the applied load is illustrated in Figure 12 for a discretization of eight initially straight elements and corresponds closely to the results presented in [4]. Numerical results for the tip position are presented in Table II along with results from the original publication [37], formulations based on geometrically exact beam theory (GEBT) and co-rotating formulations (CR). A more extensive comparison can be found in [26]. It is seen that the present explicit formulation yields rather accurate results compared to the other approaches despite its simple kinematics and explicit form.

8. CONCLUSIONS

An explicit free-floating beam element with two nodes for analysis of three-dimensional structures is presented. Each node is represented by its position vector and a set of orthonormal base vectors. The beam stiffness matrix is obtained in global components in explicit form by combining a simple local representation in terms of equilibrium deformation modes with a corresponding set of nonlinear generalized strains, expressed explicitly via scalar products of the global position and base vectors associated with the two nodes of the element. In the present paper, the local stiffness associated with the equilibrium modes of deformation is assumed to be linear elastic and the element homogeneous, but extensions allowing for, for example, nonhomogeneous properties, geometric stiffness, and initial curvature within the local element representation are fully within the proposed format. The formulation is based on vector properties and does not make use of any representation of finite rotations. The formulation is frame invariant and valid for arbitrarily large displacements, with the only restriction being the assumption of moderate local deformation within the individual element. The global formulation is in terms of the position vector of each node and a corresponding set of orthonormal base vectors. For general beam structures with three-dimensional joints, three base vectors are required at each node, while structures that are initially plane only need two base vectors at each node. The rotation-free vector formulation leads to a redundant representation with three additional degrees of freedom for plane structures and six for general three-dimensional structures. The corresponding constraints take a very simple form corresponding to zero Green strain for the base vector sets at each node. The solution demonstrates the applicability of directly Newton–Raphson-based techniques, such as the arc-length method. A number of very large-displacement benchmark problems for simple beams and frames demonstrate that the present free-floating element formulation requires a similar number of elements, when compared to the formulations in the literature. This makes the element very competitive, as its global stiffness properties are defined in terms of three explicit matrices.

DOI: 10.1002/nme

REFERENCES

1. Reissner E. On one-dimensional finite-strain beam theory: the plane problem. *Zeitschrift für angewandte Mathematik und Physik* 1972; **23**:795–804.
2. Reissner E. Finite deformations of space-curved beams. *Zeitschrift für angewandte Mathematik und Physik* 1981; **32**:734–744.
3. Simo JC. A finite strain beam formulation. The three-dimensional dynamic problem. Part I. *Computer Methods in Applied Mechanics and Engineering* 1985; **49**:55–70.
4. Simo JC, Vu-Quoc L. A three-dimensional finite-strain rod model. Part II: Computational aspects. *Computer Methods in Applied Mechanics and Engineering* 1986; **58**:79–116.
5. Antman SS. *Nonlinear Problems of Elasticity* (2nd edn). Springer: Berlin, 2005.
6. Cardona A, Geradin M. A beam finite element non-linear theory with finite rotations. *International Journal for Numerical Methods in Engineering* 1988; **26**:2403–2438.
7. Ibrahimbegovic A. On finite element implementation of geometrically nonlinear Reissner's beam theory: Three-dimensional curved beam elements. *Computer Methods in Applied Mechanics and Engineering* 1995; **122**:11–26.
8. Jelenic G, Crisfield MA. Geometrically exact 3D beam theory: Implementation of a strain-invariant finite element for statics and dynamics. *Computer Methods in Applied Mechanics and Engineering* 1999; **171**:141–171.
9. Romero I, Armero F. An objective finite element approximation of the kinematics of geometrically exact rods and its use in the formulation of an energy-momentum conserving scheme in dynamics. *International Journal for Numerical Methods in Engineering* 2002; **54**:1683–1716.
10. Betsch P, Steinmann P. Frame-indifferent beam finite elements based upon the geometrically exact beam theory. *International Journal for Numerical Methods in Engineering* 2002; **54**:1775–1788.
11. Romero I. A comparison of finite elements for nonlinear beams: The absolute nodal coordinate and geometrically exact formulations. *Multibody System Dynamics* 2008; **20**:51–68.
12. Crisfield MA, Jelenic G. Objectivity of strain measures in the geometrically exact three-dimensional beam theory and its finite-element implementation. *Proceedings of the Royal Society of London. Series A: Mathematical, Physical and Engineering Sciences* 1999; **455**:1125–1147.
13. Betsch P, Steinmann P. Constrained dynamics of geometrically exact beams. *Computational Mechanics* 2003; **31**: 49–59.
14. Shabana AA, Hussein HA, Escalona JL. Application of the absolute nodal coordinate formulation to large rotation and large deformation problems. *Journal of Mechanical Design* 1998; **120**:188–195.
15. Shabana AA. Flexible multibody dynamics: Review of past and recent developments. *Multibody System Dynamics* 1997; **2**:189–222.
16. Gerstmayr J, Sugiyama H, Mikkola A. Review on the absolute nodal coordinate formulation for large deformation analysis of multibody systems. *Journal of Computational and Nonlinear Dynamics* 2013; **8**:031016–031016.
17. Bauchau OA, Han S, Mikkola A, Matikainen MK. Comparison of the absolute nodal coordinate and geometrically exact formulations for beams. *Multibody System Dynamics* 2013. DOI: 10.1007/s11044-013-9374-7.
18. Belytschko T, Hsieh BJ. Non-linear transient finite element analysis with convected co-ordinates. *International Journal for Numerical Methods in Engineering* 1973; **7**:255–271.
19. Belytschko T, Schwer L, Klein MJ. Large displacement, transient analysis of space frames. *International Journal for Numerical Methods in Engineering* 1977; **11**:65–84.
20. Argyris J, Balmer H, Doltsinis J, Dunne P, Haase M, Kleiber M, Malejannakis G, Mlejnek HP, Müller M, Scharpf D. Finite element method—the natural approach. *Computer Methods in Applied Mechanics and Engineering* 1979; **17–18**:1–106.
21. Crisfield MA. A consistent co-rotational formulation for non-linear, three-dimensional, beam-elements. *Computer Methods in Applied Mechanics and Engineering* 1990; **81**:131–150.
22. Krenk S. *Non-linear Modeling and Analysis of Solids and Structures*. Cambridge University Press: Cambridge, UK, 2009.
23. Krenk S, Vissing-Jørgensen C, Thesbjerg L. Efficient collapse analysis techniques for framed structures. *Computers & Structures* 1999; **72**:481–496.
24. Neuenhofer A, Filippou FC. Evaluation of nonlinear frame finite element models. *Journal of Structural Engineering* 1997; **123**:958–966.
25. Neuenhofer A, Filippou FC. Geometrically nonlinear flexibility-based frame finite element. *Journal of Structural Engineering* 1998; **124**:704–711.
26. Jonker JB, Meijaard JP. A geometrically non-linear formulation of a three-dimensional beam element for solving large deflection multibody system problems. *International Journal of Non-Linear Mechanics* 2013; **53**:63–74.
27. Krenk S. A general format for curved and non-homogeneous beam elements. *Computers & Structures* 1994; **50**: 449–454.
28. Krenk S. The torsion–extension coupling in pretwisted elastic beams. *International Journal of Solids and Structures* 1983; **19**:67–72.
29. Krenk S. The role of geometric stiffness in momentum and energy conserving time integration. *International Journal for Numerical Methods in Engineering* 2007; **71**:631–651.
30. Krenk S. *Element stiffness matrix for beams with general cross-section properties*, 2006. Department of Mechanical Engineering, Technical University of Denmark.
31. Gerstmayr J, Irschik H. On the correct representation of bending and axial deformation in the absolute nodal coordinate formulation with an elastic line approach. *Journal of Sound and Vibration* 2008; **318**:461–487.

32. Mattiasson K. Numerical results from large deflection beam and frame problems analysed by means of elliptic integrals. *International Journal for Numerical Methods in Engineering* 1981; **17**:145–153.
33. Williams FW. An approach to the non-linear behaviour of the members of a rigid jointed plane framework with finite deflections. *Quarterly Journal of Mechanics and Applied Mathematics* 1964; **17**:451–469.
34. Krenk S. *Mechanics and Analysis of Beams, Columns and Cables: A Modern Introduction to the Classic Theories*. Springer: Berlin, 2001.
35. Géradin M, Cardona A. *Flexible Multibody Dynamics: A Finite Element Approach*. Wiley: Chichester, UK, 2001.
36. DaDeppo DA, Schmidt R. Instability of clamped-hinged circular aches subjected to a point load. *Journal of Applied Mechanics* 1975; **42**:894–896.
37. Bathe KJ, Bolourchi S. Large displacement analysis of three-dimensional beam structures. *International Journal for Numerical Methods in Engineering* 1979; **14**:961–986.

DOI: 10.1002/nme

P6

Structural optimization of wind turbine rotor blades by multilevel sectional/multibody/3D-FEM analysis

C.L. Bottasso, F. Campagnolo, A. Croce, S. Dilli, F. Gualdoni, M.B. Nielsen

Multibody System Dynamics,
(In press)

Multibody Syst Dyn
DOI 10.1007/s11044-013-9394-3

Structural optimization of wind turbine rotor blades by multilevel sectional/multibody/3D-FEM analysis

C.L. Bottasso · F. Campagnolo · A. Croce · S. Dilli · F. Gualdoni · M.B. Nielsen

Received: 7 December 2012 / Accepted: 19 July 2013

Abstract The present work describes a method for the structural optimization of wind turbine rotor blades for given prescribed aerodynamic shape. The proposed approach operates at various description levels producing cost-minimizing solutions that satisfy desired design constraints at the finest modeling level. At first, a "coarse"-level constrained design optimization is performed by using a 1D spatial geometrically exact beam model for aero-servo-elastic multibody analysis and load calculation, integrated with a 2D FEM cross sectional model for stress/strain analysis, and the evaluation of the 1D model fully-populated cross sectional stiffness matrices. Next, a "fine"-level 3D FEM model is used for the refinement of the coarse-level solution. Improved results obtained at the level of the 3D model are utilized at the following coarse-level iteration through a heuristic modification of the design constraints. In addition, a buckling analysis is performed at the fine description level, which in turn affects the nonstructural blade mass. The updated constraint bounds and mass make their effects felt at the next coarse-level constrained design optimization, thereby closing the loop between the coarse and fine description levels. The multilevel optimization procedure is implemented in a computer program and it is demonstrated on the design of a multi-MW horizontal axis wind turbine rotor blade.

Keywords Wind turbine · Blade design · Multibody dynamics · CAD modeling · FE analysis · Aero-servo-elasticity · Multidisciplinary optimization

C.L. Bottasso (✉)
Wind Energy Institute, Technische Universität München, 85748 Garching b. München, Germany
e-mail: carlo.bottasso@tum.de

C.L. Bottasso · F. Campagnolo · A. Croce · S. Dilli · F. Gualdoni
Dipartimento di Scienze e Tecnologie Aerospaziali, Politecnico di Milano, 20156 Milano, Italy

M.B. Nielsen
Department of Mechanical Engineering, Technical University of Denmark, 2800 Kgs. Lyngby, Denmark

Published online: 30 August 2013

1 Introduction

The aerostructural design problem of wind turbine rotor blades concerns the definition of the optimal external aerodynamic shape and of the structural components of the blade that realize some desirable compromise among several figures of merit, including aerodynamic efficiency, weight, manufacturing costs, transportability, etc. All necessary trade-offs are usually considered and ultimately finalized within the more general problem of designing the whole wind turbine, where the goal is typically the minimization of the cost of energy.

This paper is concerned with the structural design of wind turbine rotor blades for given aerodynamic shape. Although this is only one aspect of the more general problem of designing a blade and a wind turbine, as mentioned above, it is nevertheless a highly complex and challenging task. In fact, the design should identify optimal structural layout, choice of materials and proper sizing of all structural members to ensure a cost-effective, safe and efficient operation throughout the lifetime of the machine. Given layout and materials, the sizing problem should be performed in such a way that all blade components (from webs, skin, and spar caps, to root bolting and all the way down to glued connections, reinforcements, etc.) can withstand extreme loads and the effects of fatigue due to deterministic cyclic and stochastic turbulent excitations. Furthermore, the blade should be designed in such a way to avoid resonant conditions, which would increase vibrations and fatigue, be stiff enough to avoid striking the tower even under extreme operating conditions, be flutter-free in all of its operating envelope including emergency conditions, and also free from local instabilities such as skin buckling, wrinkling, etc. The design should also be able to fully exploit the anisotropic properties of composite materials, for example, for inducing load mitigating couplings between blade bending and twisting [1]. Clearly, these goals should be met with the minimum possible cost, while satisfying all necessary manufacturing constraints.

The main challenge of this design problem comes from the need to marry the unsteady nature of loading in a wind turbine, which requires transient analyses, with the need to capture local effects such as stress concentrations and instabilities in complex 3D structures made with anisotropic composite materials. Transient analyses are routinely performed with beam-like models of the machine dynamics, coupled to suitable aerodynamic models and control laws that enable the simulation of the whole spectrum of unsteady operating conditions defining extreme loads and deflections, as well as fatigue. On the other hand, the verification of the local state of stress and strain and its stability are typically conducted with detailed 3D static finite element models, under loading conditions obtained from the ones computed with the transient models.

This two-stage analysis is typically performed "by hand": After a first coarse-level preliminary sizing performed using beam-like models, one performs a fine-level verification using 3D FEM and corrects any possible deficiency, for example, by increasing the thickness or lamination sequence of a component. Possibly, the result of the fine-level verification is used to update the coarse-level dynamic model and the process is iterated until convergence. Clearly, this procedure is time consuming and labor intensive. Furthermore, the design is not conducted as an integrated multilevel optimization, and might lead to suboptimal results since there is not a consistent way to reflect the results of the fine-level analysis into modifications of the coarse-level models.

The scope of the present paper is to improve on the current design method of rotor blades, by proposing a multilevel design procedure that conducts the design in a fully integrated and automated manner. The method includes 2D finite element models for the characterization and analysis of the blade cross sections, aero-servo-elastic multibody models for load calculation according to certification guidelines [2, 3], and detailed 3D finite element models for

detailed stress-strain, fatigue and buckling analysis. The design optimization is conducted by iterating among the various levels, so as to deliver a cost-minimizing design solution that also satisfies all desired design constraints at the finest description level, i.e., the detailed 3D model.

The design of wind turbine blades has been the subject of several investigations, and software packages are available that can support the process at the various necessary description levels. In the following, we review some of the relevant literature, first for preliminary coarse-level sizing and then for detailed fine-level verification, and we compare the state-of-the-art with the new integrated and multilevel procedures proposed here.

As previously stated, a coarse beam model is often sufficient for preliminary analysis as it is capable of providing fast and accurate results for primary parameters such as natural frequencies, deflections, loads, and the estimation of the overall dynamic behavior of the machine. At this stage, multibody procedures are routinely adopted, using geometrically exact beam formulations as in [4] and as in the nonlinear finite-element-based multibody dynamics wind turbine simulation code `Cp-Lambda` (Code for Performance, Loads, Aero-Elasticity by Multi-Body Dynamic Analysis) [5, 6] used here, or with Timoschenko beam elements as in [7]; modal representations of the flexible elements are also in widespread use, as in the wind turbine aero-elastic codes `FAST` [8] and `GH-Bladed` [9].

The use of such tools for preliminary design of rotor blades has been described in a few publications. In particular, the codes `RotorOpt` [10, 11] and `FOCUS6` [12] implement integrated design environments. A suite of design tools is described in [13], providing the facilities for preliminary blade design, although the various software modules do not appear to be integrated in a unified optimization framework. Recently, the multidisciplinary wind turbine design code `Cp-Max` (Code for Performance Maximization) was described in [14]. In that work, the structural blade design problem is formulated as a constrained optimization based on a two-level modeling system. The first level is represented by a parametric aero-servo-elastic multibody model, while the second level by 2D finite element parametric models of the blade cross sections. The integration of the two models allows for the synthesis of a beam given its cross sections, and for the evaluation of the sectional loading given the beam one, which are the two crucial steps of the design problem. In fact, from the sectional models, fully-populated stiffness matrices are computed using the code `ANBA` (Anisotropic Beam Analysis), based on the anisotropic beam theory formulated in [21]. The stiffness matrices obtained in this way are used for defining geometrically exact shear and torsion-deformable beams [19] in `Cp-Lambda`. On the other hand, recovery relations provided by `ANBA` allow for the computation of local sectional stresses and strains based on internal stress resultants computed with `Cp-Lambda`.

The formulation described in [14] enables the structural optimization of rotor blades through the integration of 2D cross sectional analysis and 1D spatial beam models. Although that paper mentioned the link towards a detailed fine-level 3D FEM verification of the design, the formulation lacked the ability to close the loop from fine-level analysis back to coarse-level representation, which is the only way one can generate a design that is optimal and constraint satisfying at the finest description level. This loop closure capability is described in the present work, and has been incorporated in an updated version of the `Cp-Max` software.

Several tools have been developed for the detailed structural analysis of wind turbine blades, typically developed in the form of pre- and post-processing software interfaced with commercial FE solvers. For example, `NUMAD` [15] serves as a preprocessor for the commercial FE software `ANSYS`. Given an externally generated CAD model, the code produces a mid-thickness model of the blade, meshes it using shell elements, and lets the user define all

necessary material properties, loading and boundary conditions for the required analyses. Similarly, FOCUS6 is also capable of generating detailed structural models of rotor blades using lay-up shell elements, while NSE-blade-mesher [16] exploits a combined solid and shell element mesh in connection with the FE solver ABAQUS. This code was used for confirming the bending and twisting behavior of a blade predicted by sectional analysis in [17], while a full structural multicriteria optimization for a given aerodynamic shape is performed in [18] by utilizing a parametric FE model using ANSYS.

Here, a new tool is described for the automatic generation and analysis of 3D FE structural blade models. First, a detailed CAD model is generated in terms of NURBS (Non-Uniform Rational B-Splines) surfaces directly from the blade geometry obtained at the coarse description level. Next, the CAD model is associated with material properties, boundary as well as extreme and fatigue loading conditions, and meshed into shell or solid elements to enable the execution of the necessary analyses.

Static deflection and fatigue analyses are conducted on the fine-level 3D model, with the goal of verifying the satisfaction of the stress, strain, and fatigue constraints, since the 3D model can represent effects that sectional and beam models cannot capture. Furthermore, a nonlinear buckling analysis is performed under the maximum tip deflection loads.

A heuristic approach is used for incorporating the effects of the 3D FEM level analyses back into the coarse-level model. This way, new 2D sectional models are generated, which in turn define a new 1D spatial beam model, and the complete process is repeated. Typically, very few iterations between the coarse and fine levels are necessary for convergence.

Through the new procedure described herein, a multilevel optimization is used to determine cost-minimizing design solutions that satisfy all desired constraints at the finest description level within reasonable computational costs. In particular, the loop closure between fine 3D FEM static and coarse multibody dynamic and cross sectional models is the main contribution of the present paper, and it has not been described before to the authors' knowledge.

The paper is organized as follows. At first, the general principles of the multilevel optimization procedure are described in Sect. 2.1 and the algorithmic organization of the code is illustrated in Sect. 2.2. Next, a detailed description is given in Sect. 3 of the various tasks that implement the automated CAD and FE model generation procedures and associated FE analyses, starting with a brief discussion of the relevant modeling aspects in Sect. 3.1. The description of the CAD model generation of the various components of the blade follows in Sect. 3.2, and the generation of the FE model is given in Sect. 3.3. This modeling task is conducted in two different manners tailored to the subsequent meshing, as described in Sect. 3.3.1, which is performed using either layered composite shells or solid elements. The correct orientation of the anisotropic material properties is addressed in Sect. 3.3.2, while the conversion of the relevant envelope load cases from the coarse description level into representative loading conditions for the 3D FE model is described in Sect. 3.3.3. Finally, the fine-level analyses are discussed in Sect. 3.4. The paper is complemented by Sect. 4, where the capabilities of the proposed integrated multilevel optimization procedures are illustrated on the structural design of a blade for a 2MW horizontal axis wind turbine.

2 Multilevel structural optimization of wind turbine rotor blades

2.1 Overview of multilevel optimization

Figure 1 illustrates the proposed multilevel constrained structural design optimization of wind turbine rotor blades, which is briefly described here below.

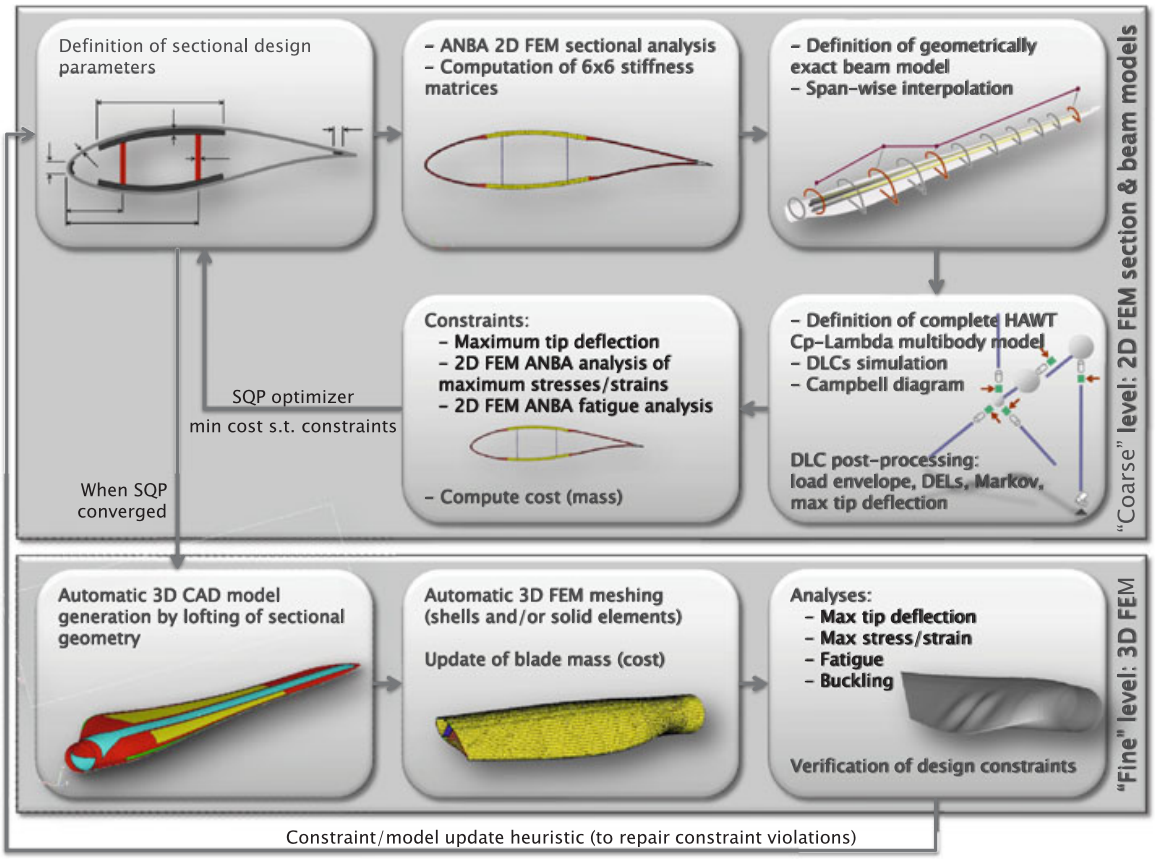

Fig. 1 Multilevel structural blade optimization for given aerodynamic shape

As a starting point for the optimization, an initial definition of the blade structural configuration and associated material properties is required. Next, the primary design variables are defined at selected span-wise sections, typically including the thicknesses of skin, shear webs, and spar caps as well as the area of the leading and trailing edge reinforcements; intermediate values along the blade span are interpolated using shape functions.

Based on this and all other necessary input data, a complete aero-servo-elastic model of the machine is developed using the wind turbine simulation code `Cp-Lambda`. All entities in the model are described using Cartesian coordinates in a single inertial frame, and constraints are enforced using Lagrange multipliers. Blades are described using a geometrically exact shear and torsion deformable beam model [19], which can represent arbitrarily large three dimensional rotations and displacements; spatial discretization is obtained using an isoparametric formulation, resulting in a nonlinear full finite element method. Time integration of the resulting differential algebraic multibody equations of motion in index-3 form is performed using a nonlinearly unconditionally stable energy decaying integration scheme [20]. The code supports static and transient analyses as well as the computation of frequencies and mode shapes about deformed equilibrium configurations.

Each blade is described in terms of cross sectional properties computed at user-selected span-wise stations; for the computation of transient loads the number of sections is of the order of one-hundred, while in the optimization loop defining the blade properties a few tens of sections are usually sufficient. Sectional stiffness matrices accounting for all possible structural couplings are computed using the code `ANBA` [21], based on either 2D finite element meshes or equivalent panels. In the latter case, which is the one considered here, each section is meshed with a number of panels ranging between one-hundred and one-hundred

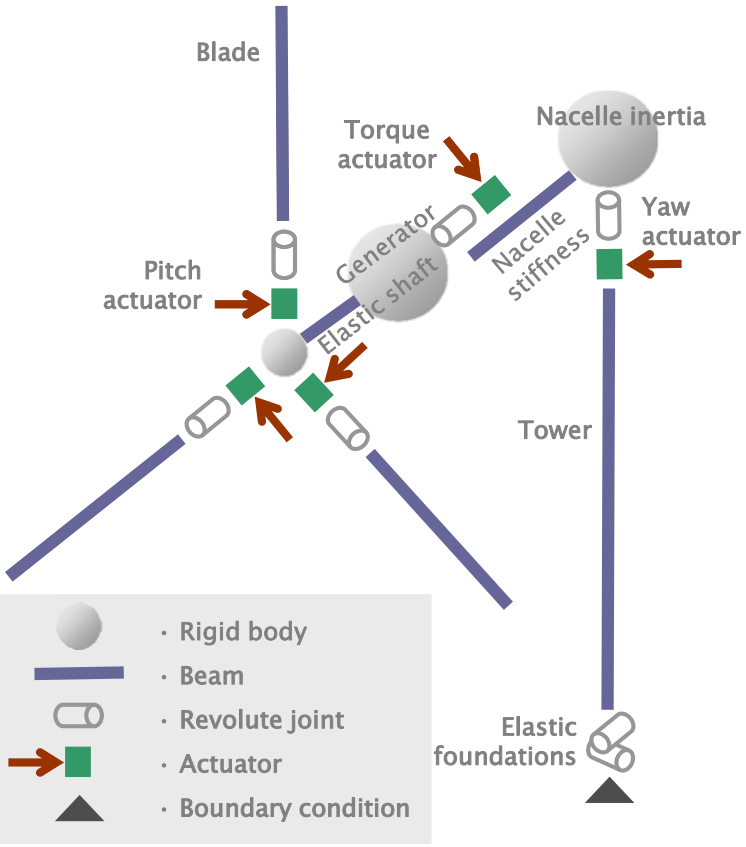

Fig. 2 Topological representation of wind turbine multibody model

and fifty, depending on the local geometry. Each blade is finally modeled as a geometrically exact beam, using a number of cubic elements between twenty and thirty.

The aerodynamic loads computation is based on classical Blade Element Momentum (BEM) theory. Blades are associated to lifting lines described by three-dimensional twisted curves, and aerodynamic loads are then computed on the basis of local flow characteristics and local airfoil aerodynamic coefficients, stored in look-up tables [14].

The topological description of the wind turbine multibody model is reported in Fig. 2. The turbine flexible bodies—i.e. the blades, tower and drive train—are modeled by beam elements, while rigid bodies are used to model the inertial properties of the hub, generator and nacelle. Revolute joints are used for the pitch and rotor degrees of freedom, and are connected to the outputs of their relevant actuator models, while the tower foundation characteristics are modeled with torsional springs and dampers.

The model is supplemented by a regulation strategy and a collective-pitch/torque controller based on a speed-scheduled linear quadratic regulator (LQR) [22], capable of controlling the machine over its entire operating envelope.

With the closed-loop aero-servo-elastic model, transient design load cases (DLCs) are simulated that include turbulent wind cases, extreme gusts, and a variety of fault conditions, according to [2, 3]. Automatic procedures manage the post-processing of all generated results, to define a generalized load envelope. Sectional load envelopes are extracted as matrices containing values of the maximum and minimum internal stress resultants. In the present work, a generalized load envelope is defined that also includes the time histories of turbulent loads due to DLC 1.2 [2], used for the determination of fatigue damage, as well as the loads associated with the maximum tip deflection. The determination of the latter loading condition is formulated as an optimization problem that looks for a set of equivalent static loads that, together with gravitational and inertial loads associated with the operational conditions

at the time when the maximum tip deflection occurs, closely match the actual deflections and internal stress distribution [14].

Using the generalized load envelope, for each instantiation of the blade design one can compute all relevant design quantities, such as maximum tip deflection, stress, and strain states at selected verification points in a number of span-wise sections through recovery relations provided by `ANBA`, and the level of fatigue-induced damage at the same verification spots. These quantities are then enforced as inequality constraint conditions for the optimization problem.

The code also computes the Campbell diagram of the machine, so that constraint conditions ensuring a resonant-free design can be included in the optimization. Furthermore, one can also include additional constraints on the unknown design parameters, such as bounds on the span-wise ply tapering rates or on the relative position between sectional center of gravity and pitch axis.

In this work, the merit function of the optimization problem is represented by the total mass of the blade. This quantity is computed based on the spatial and sectional configuration of the blade and also includes nonstructural masses due to surface coating, foam core, resin take-up, etc. Here, it is implicitly assumed that mass is well correlated with cost; the choice of mass as the merit function is also due to the fact that reliable cost models are not available in the public domain.

The constrained multi-disciplinary optimization is run until convergence using the sequential quadratic programming (SQP) method implemented in the `fmincon` routine of the `Matlab` software [23]. In order to reduce the computational cost, the optimization is run for a frozen load envelope; once the cost optimization converges, a new aero-servo-elastic wind turbine model is generated following the previously described steps and the relevant analyses are repeated for updating the generalized load envelope. The optimization is repeated until no more changes in the load envelope and the design are detected, which typically takes very few iterations. This procedure minimizes the number of evaluations of the generalized load envelope so as to reduce the computational cost [14].

From the computed blade geometry, the code automatically generates a 3D CAD model, which precisely accounts for all components of the blade (shear webs, web core, flanges, spar caps, leading and trailing edge reinforcement, internal skin, skin core and external skin) as well as their associated material properties and laminate characteristics (see Sect. 3). The meshing of the blade is performed with the commercial preprocessing software `HyperMesh` [24], which provides macro-based facilities for automatic mesh generation using either shell or solid elements and the subsequent export of the model data in the form of input files compatible with various commercial FE solvers.

The 3D FE model provides the framework for a fine-level verification of the design constraint inequalities associated with admissible stresses, strains, deflections, and fatigue damage, as the detailed model reveals effects that may have been overlooked by the coarse quasi-3D model composed of 1D spatial beam and 2D cross sectional models. For example, local stress concentrations at the beginning and end of the spar caps or at regions with rapidly changing geometry in the span-wise direction cannot be correctly represented by beam models, since in these cases the very hypotheses underlying beam theories are violated. In case constraint violations are detected at the fine-level, the coarse optimization loop is repeated with constraint bounds that are tightened proportionally to the violation amount; coarse and fine-level iterations are repeated until an optimal design that satisfies the constraint conditions at the finest description level is obtained.

In addition, the 3D model can be used for designing secondary structural components, as for example the thickness of the skin core through a linearized buckling analysis. This in

turn affects the nonstructural mass of the blade model leading to an improved estimate for the cost function. This mass change affects the coarse-level analysis, that is then repeated until convergence; this is usually accomplished in a few iterations as illustrated in Sect. 4.3.

2.2 Algorithmic organization of multi-level optimization

The multilevel optimization for minimum blade weight that was sketched in the previous pages, can be more precisely expressed in the following algorithmic form:

$$\textbf{Function } \left(\boldsymbol{p}_s^*, w^*\right) = \texttt{MinBladeWeight}(\boldsymbol{p}_a, \boldsymbol{p}_s, D, \Gamma_s): \tag{1a}$$

$$(\boldsymbol{E}) = \texttt{LoadEnvelope}(\boldsymbol{p}_a, \boldsymbol{p}_s, D), \tag{1b}$$

$$\textbf{do} \tag{1c}$$

$$(\boldsymbol{p}_{s1}, \boldsymbol{p}_{s2}) = \boldsymbol{p}_s, \tag{1d}$$

$$\left(\boldsymbol{p}_{s1}^*, w_1^*\right) = \texttt{MinWeightBladeFrozenLoads}(\boldsymbol{p}_a, \boldsymbol{p}_{s1}, D, \boldsymbol{E}, \Gamma_s), \tag{1e}$$

$$(M) = \texttt{3DCADAndFEMeshGeneration}\left(\boldsymbol{p}_a, \boldsymbol{p}_{s1}^* \cup \boldsymbol{p}_{s2}, \boldsymbol{E}\right), \tag{1f}$$

$$\left(\boldsymbol{p}_{s2}^*, w_2^*, \Gamma_s'\right) = \texttt{3DFEAnalysis}(M, \boldsymbol{p}_{s2}, D, \boldsymbol{E}, \Gamma_s), \tag{1g}$$

$$\boldsymbol{p}_s^* = \boldsymbol{p}_{s1}^* \cup \boldsymbol{p}_{s2}^*, \tag{1h}$$

$$\left(\boldsymbol{E}'\right) = \texttt{LoadEnvelope}\left(\boldsymbol{p}_a, \boldsymbol{p}_s^*, D\right), \tag{1i}$$

$$\Delta p_{s1} = \left\| \boldsymbol{p}_{s1}^* - \boldsymbol{p}_{s1} \right\|, \qquad \Delta \boldsymbol{E} = \left\| \boldsymbol{E}' - \boldsymbol{E} \right\|, \tag{1j}$$

$$\boldsymbol{p}_s = \boldsymbol{p}_s^*, \qquad \boldsymbol{E} = \boldsymbol{E}', \qquad \Gamma_s = \Gamma_s', \tag{1k}$$

$$\textbf{while } (\Delta p_{s1} \geq \text{tol}_{p_{s1}} \textbf{ and } \Delta \boldsymbol{E} \geq \text{tol}_E). \tag{1l}$$

Here, and in the following, functions are indicated with the notation

$$(O) = \texttt{FunctionName}(I), \tag{2}$$

where I indicates a list of input variables, while O a list of output ones.

In (1a), the mass optimization function takes as input the known and given parameters $\boldsymbol{p}_a$ describing the aerodynamic shape of the blade, the unknown structural parameters $\boldsymbol{p}_s$, the additional data structure D and list of constraint bounds Γ_s, and returns the optimal values of structural parameters $\boldsymbol{p}_s^*$ and corresponding blade weight w^*.

Unknowns $\boldsymbol{p}_s$ are partitioned into primary structural variables $\boldsymbol{p}_{s1}$, which are designed during the coarse optimization, and secondary structural variables $\boldsymbol{p}_{s2}$, such as the skin core thickness that can only be analyzed in the 3D FE model. List D contains all relevant data describing the characteristics of the machine

$$D = \{P_r, V_{\text{in}}, V_{\text{out}}, R, H, \text{AF}, C, v_{\text{tip}_{\max}}, L_{\text{DLC}}, \ldots\}, \tag{3}$$

which, among others, include rated power P_r, range between cut-in V_{in} and cut-out V_{out} wind speeds, rotor radius R, tower height H, list of airfoil data $\text{AF} = \{\ldots, \text{AF}_i, \ldots\}$, wind turbine class C [2], maximum admissible tip speed to limit noise emissions and list $L_{\text{DLC}} = \{\ldots, \text{DLC}i.j, \ldots\}$ containing all DLCs according to [2, 3] used for blade sizing. Finally,

Γ_s is a vector of constraint parameters used for enforcing the design inequalities during structural optimization, defined as

$$\Gamma_s = \left(\boldsymbol{\sigma}_{\text{adm}}, \boldsymbol{\epsilon}_{\text{adm}}, \boldsymbol{\delta}_{\text{tip,max}}, [\omega_L, \omega_U], \ldots\right)^T, \tag{4}$$

where $\boldsymbol{\sigma}_{\text{adm}}$ and $\boldsymbol{\epsilon}_{\text{adm}}$ denote the admissible magnitudes for stress and strain components, $\boldsymbol{\delta}_{\text{tip,max}}$ is the maximum admissible tip deflection and the interval $[\omega_L, \omega_U]$ represents bounds for the placement of selected natural frequencies.

The coarse-level optimization for the primary structural design variables, $\boldsymbol{p}_{s1}$, is performed using the quasi-3D beam model in (1e), as illustrated by the "coarse" level block in Fig. 1. Next, the 3D CAD model is created and its mesh M is generated in (1f), as described later on in Sect. 3. Finally, the refined structural analysis in terms of the 3D FE model is performed in (1g), which yields updated values of the secondary design variables, $\boldsymbol{p}_{s2}$, and of the design inequality parameters, Γ_s. These three steps are shown in the "fine" level block of Fig. 1.

As pointed out in [14], the recalculation of the full load envelope $\boldsymbol{E}$ for each change in the structural design variables may imply a considerable computational cost. Therefore, the coarse (1e) and fine (1g) level steps are conducted considering the load envelope $\boldsymbol{E}$ as frozen. However, it should be emphasized that the effects of the design on the load envelope is recovered by the iteration in (1c–1l), so that the procedure has the sole effect of reducing the computational cost, but does not affect the results.

The coarse-level constrained optimization (1e), which is solved using the SQP algorithm, takes the form

$$\textbf{Function } \left(\boldsymbol{p}_s^*, w^*\right) = \texttt{MinWeightBladeFrozenLoads}(\boldsymbol{p}_a, \boldsymbol{p}_s, D, \boldsymbol{E}) : \tag{5a}$$

$$\boldsymbol{p}_s^* = \min_{\boldsymbol{p}_s} W(\boldsymbol{p}_s, D) \quad \left(\text{and } w^* = \arg\min_{\boldsymbol{p}_s} W\right), \tag{5b}$$

$$\text{s.t.:} \quad \boldsymbol{g}_s(\boldsymbol{p}_s) \leq \boldsymbol{0}, \tag{5c}$$

$$\boldsymbol{\omega}(\boldsymbol{p}_s, D) \in [\boldsymbol{\omega}_L, \boldsymbol{\omega}_U], \tag{5d}$$

$$\boldsymbol{\sigma}(\boldsymbol{p}_s, \boldsymbol{E}, D) \leq \boldsymbol{\sigma}_{\text{adm}}, \tag{5e}$$

$$\boldsymbol{\epsilon}(\boldsymbol{p}_s, \boldsymbol{E}, D) \leq \boldsymbol{\epsilon}_{\text{adm}}, \tag{5f}$$

$$\boldsymbol{d}(\boldsymbol{p}_s, \boldsymbol{E}, D) \leq 1, \tag{5g}$$

$$\boldsymbol{\delta}_{\text{tip}_{\text{max}}}(\boldsymbol{p}_s, \boldsymbol{E}, D) \leq \boldsymbol{\delta}_{\text{tip}_{\text{adm}}}. \tag{5h}$$

The design constraint inequalities for this problem involve the following conditions:

- (5c): requirements on the unknown structural parameters, such as for example limits on the span-wise ply tapering rates.
- (5d): the placement of significant natural frequencies to lie within a desired interval $[\omega_L, \omega_U]$ in order to avoid resonant conditions. This could be a requirement for the first flap-wise blade eigenfrequency to lie above the three-per-rev frequency at the rated rotor speed, or a requirement for a suitable gap between two consecutive blade frequencies.
- (5e), (5f): bounds on stress and strain components $\boldsymbol{\sigma}$ and $\boldsymbol{\epsilon}$, respectively, at a selected number of points on cross sections of interest, in order so ensure sufficient structural strength according to [2, 3].

– (5g): criterion on fatigue induced damage in turbulent wind conditions DLC 1.2 [2]. Damage d_{σ_r} at a point on a cross section due to a single stress component σ_r is computed according to [2], while a multiaxial damage index d is computed according to [25, 26] as

$$d = d_{\sigma_1}^{2/m} + d_{\sigma_1}^{2/m} - (d_{\sigma_1} d_{\sigma_2})^{1/m} + d_{\sigma_6}^{2/m}, \tag{6}$$

where m denotes the inverse slope of the S-N curve and indices 1, 2, and 6 refer to the longitudinal, transverse, and shear stress components, respectively. The damage indices d for each verification point on each cross section are collected in a vector $\boldsymbol{d}$ and are all bounded to unity.
– (5h): a limit on the maximum blade tip deflection throughout all time histories of all DLCs.

The fine-level analysis (1g) can be stated in the following algorithmic form:

$$\textbf{Function } \left(\boldsymbol{p}_{s2}^*, w_2^*, \Gamma_s'\right) = \texttt{3DFEAnalysis}(M, \boldsymbol{p}_{s2}, D, \boldsymbol{E}, \Gamma_s): \tag{7a}$$

$$\left(\boldsymbol{p}_{s2}^*, w_2^*\right) = \texttt{MinSecondaryWeight}(M, D, \boldsymbol{E}), \tag{7b}$$

$$\Gamma_s' = \texttt{ConstraintVerificationAndUpdate}(M, D, \boldsymbol{E}, \Gamma_s), \tag{7c}$$

and comprises of two main steps.

The first, (7b), concerns the design of secondary structural parameters, in this case represented by the skin core thickness with respect to local buckling. This problem yields the optimal values of the secondary variables $\boldsymbol{p}_{s2}^*$, as well as an improved estimate for the blade mass $w^* = w_1^* + w_2^*$. The buckling analysis in itself can be formulated as the following constrained optimization:

$$\textbf{Function } \left(\boldsymbol{p}_{s2}^*, w_2^*\right) = \texttt{MinSecondaryWeight}(M, D, \boldsymbol{E}): \tag{8a}$$

$$\boldsymbol{p}_{s2}^* = \min_{\boldsymbol{p}_{s2}} W_2(M, D) \quad \left(\text{and } w_2^* = \arg\min_{\boldsymbol{p}_{s2}} W_2\right), \tag{8b}$$

$$\text{s.t.:} \quad \boldsymbol{\lambda}(M, D, \boldsymbol{E}) \geq 1, \tag{8c}$$

where $\boldsymbol{\lambda}$ are the eigenvalues of the linearized buckling problem associated with the loading conditions stored in the generalized envelope $\boldsymbol{E}$. Further details on the solution of this problem are given in Sect. 3.4.4.

The second step, (7c), concerns the verification of the design constraint conditions on the 3D FE model through static, modal and fatigue analyses. If constraint violations are detected, updated constraint bounds Γ_s' are generated, that will in turn affect the next solution of problem (1e). The design constraint that are verified at this level are:

– Placement of natural frequencies, corresponding to the coarse-level inequalities (5d).
– Bounds on stress and strain components, corresponding to the coarse-level inequalities (5e) and (5f).
– Fatigue induced damage constraints, corresponding to the coarse-level inequalities (5g).
– Maximum blade tip deflection, corresponding to the coarse-level inequality (5h).

If the verification of the constraint conditions on the fine-level model performed in (7c) reveals that some design inequalities are not satisfied, a heuristic approach is applied in which the constraints are modified proportionally to the violation amount. Assume that a condition for maximum stress $\sigma_{\max,2D}$ is satisfied at a given section $\sigma_{\max,2D} < \sigma_{\text{adm}}$ at the

end of the ith coarse-level optimization, but it is violated when the fine-level 3D analysis is performed, i.e. $\sigma_{\max,3D} > \sigma_{\text{adm}}$. Then the admissible stress for the $(i+1)$th iteration is modified as

$$\sigma_{\text{adm}}^{(i+1)} = s_\sigma \, \sigma_{\text{adm}}^{(i)}, \tag{9}$$

where $s_\sigma = \sigma_{\max,3D}/\sigma_{\max,2D}$. This way, a more stringent constraint condition is imposed at the next coarse-level iteration. It may be expected that the stress ratio between the quasi-3D and the 3D analyses is almost constant for moderate variations of the structural element sizes. Therefore, the present approach may be used for refining the coarse-level analysis according to the results from the fine-level solution. The other constraint parameters Γ_s are handled in a similar way, so that the full set of constraint limits may be updated as

$$\Gamma_s' = \boldsymbol{S}\Gamma_s, \tag{10}$$

where $\boldsymbol{S}$ is a diagonal matrix containing the constraint limit modification factors $s_{(\cdot)}$ for each of the constraint conditions.

3 CAD modeling, FE generation and analysis

Crucial to the success of the present automated optimization procedure is the construction of a robust and reliable finite element model. For a complex structure such as a wind turbine blade this requires several steps, which can be summarized as:

- Parametric definition of each blade component, either in terms of its bounding surfaces or of the laminate mid-planes, as described in Sect. 3.2.
- Generation of a complete FE model, described in Sect. 3.3, which in turn requires:
  - Mesh generation, including both the 3D blade discretization using either shell or solid elements and the discretization of 2D cross sections for sectional analysis in terms of panel or surface elements, as described in Sect. 3.3.1.
  - Assignment of element properties, including the laminate ply stacking sequences and associated thicknesses, material parameters, and fiber orientations, as detailed in Sect. 3.3.2.
  - Conversion of the 1D spatial beam model loading conditions into equivalent conditions for the 3D FE model, as described in Sect. 3.3.3.
- FE analysis and post-processing of the results for the verification of the relevant design conditions, as detailed in Sect. 3.4.

In this work, the CAD model generation, as well as the assignment of the associated material properties and loading conditions, is based on the information from the coarse-level optimizer, and it is performed in `Matlab`. The FE mesh generation is performed using the batch meshing facilities of `HyperMesh`, where the required scripts are generated in `Matlab`. Finally, `Matlab` scripts handle the batch submission of the various analyses performed using `MSC Nastran` [27], as well as their post-processing.

3.1 Modeling aspects

The way in which the FE modeling of wind turbine blades is conducted may have a significant influence on the procedures used for generating the CAD geometry. The most frequently used technique for blade modeling is based on layered shell elements [12, 15], which

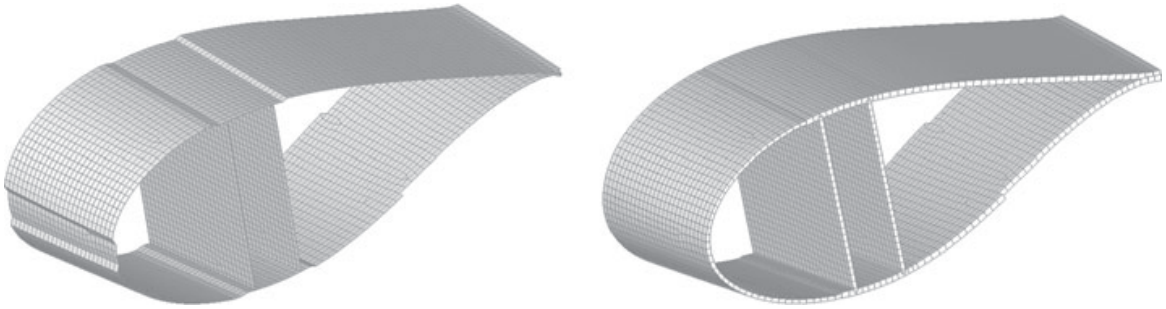

(a) Mid-thickness shell elements (b) Solid elements

Fig. 3 Two possible FEM models of rotor blades

are commonly available in commercial FE solvers. Most implementations provide the possibility of specifying the extent of the elements in terms of offsets from a reference surface other than its mid-thickness. This is particularly convenient when dealing with wind turbine blades, as the elements can be specified with respect to the exterior surface defined by the shape of the airfoils. Since the external shape is smooth, the generation of the necessary CAD model is not particularly complicated.

However, a possible drawback of the offset technique is that it may result in the erroneous prediction of the torsional behavior of the blade [30]. This problem is of particular concern since torsion affects loading through changes in the angle of attack, as for example explicitly exploited for load mitigation in bend-twist coupled rotor blades [1]. Recent improved shell formulations circumvent this problem, as for example element `SHELL281` [32] or the pre-integrated matrix input [33] available for `ANSYS`.

Otherwise, one can generate a mid-thickness CAD model of the blade, as done manually in [31]. The construction of the geometry using mid-thickness surfaces, illustrated in Fig. 3(a) at left, is in general rather cumbersome, since thickness variations lead to step changes between contiguous mid-thickness surfaces.

Alternatively, solid elements can be used for building the mesh, as shown in Fig. 3(b) at right. These are particularly suitable for capturing interlaminar stresses, for delamination and debonding analysis. However, the use of solid elements may complicate the CAD generation, since both the external and internal surfaces must be defined, which may be cumbersome to do in the various transition zones of a blade. Furthermore, one should pay specific attention to the accurate definition of the material property orientation [34]. While procedures for associating the correct material orientation to models composed of shell elements are rather well established (e.g., by direct projection of a user-defined material reference vector on the element [35]), the case of complex models composed of solid elements requires special attention as individual local coordinate systems must be defined for each element in the mesh.

For generality, the present implementation supports all approaches mentioned above, so that one may generate mid-thickness or exterior surface shells with offsets, or, alternatively, solid element meshes. It further includes 2D sectional meshing capabilities, based on either panel or 2D surface elements, to be used for sectional analysis in `ANBA`.

3.2 CAD model

The generation of a complete CAD surface model for shell meshing is accomplished as follows.

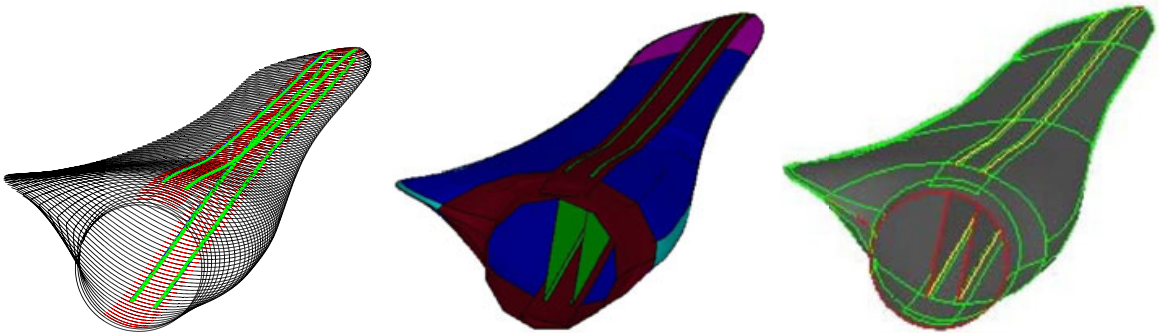

(a) Interpolation of airfoil data points

(b) NURBS surfaces

(c) Partitioning in simple subsurfaces

Fig. 4 Selected steps in the generation of the CAD model of a wind turbine blade

A number of cross sections, typically of the order of one hundred, are obtained by thickness-interpolation of the generating airfoil data points, using their span-wise chord and twist distributions. Chordwise spline interpolations are used for parameterizing the airfoils from their data points, and nodes define the location of the boundaries of the projections of the various blade elements (spar caps, shear webs, etc.) onto the external blade surface, as illustrated in Fig. 4(a).

For mid-thickness CAD generation, an inward projection along the local normal is performed using the thickness information associated with each blade element. This way, steps at the boundaries between elements with different thicknesses are generated. The thickness data accounts for span-wise variations, as computed by the coarse-level optimization, as well as user-defined chord-wise variations; the latter ones are used to avoid modeling errors associated with the overlapping of inner skin/core, which are likely to occur near the trailing edge [17].

From the chordwise interpolations of the airfoils or their mid-thickness projections, collocation data points are obtained with sufficient sampling resolution (typically of the order of one thousand points per cross section) to allow for an accurate surface parameterization, which is obtained by using NURBS [36] on each surface describing a blade component projection. In the present implementation, only nonrational surfaces are utilized, whose weights are equal to unity, and control points are obtained by least squares from collocation points. Collocation parameters for chord-wise interpolation are obtained using the centripetal method [37], while span-wise collocation parameters follow by averaging of the parameters determined at two consecutive sections. Once all collocation parameters are obtained, knot vectors are computed by using the average method suggested by de Boor [36]. An illustration of the resulting surface model is given in Fig. 4(b) for the case of mid-thickness representation.

For the construction of a solid mesh, the external blade surfaces are first generated as described above. Next, the various surfaces are further partitioned into simpler subsurfaces, as illustrated in Fig. 4(c). Partitioning is performed such that, by extruding inward each external subsurface along the local thickness direction, one can obtain the associated facing internal subsurface; this will allow for the generation of the solid mesh by means of a similar through-the-thickness extrusion of a surface mesh, as explained later on. Contact areas between two surfaces, as at the glued connections between shear webs and spar caps, are also used for the partitioning, so as to ensure conforming discretizations during meshing.

The information associated with the parametric NURBS representation of the resulting model is finally exported in IGES (Initial Graphics Exchange Specification) format towards `HyperMesh` for subsequent meshing.

The present approach, which tries to generate an accurate geometric model before meshing, differs significantly from the lofting of predefined cross sectional meshes used for example in [17], and presents several advantages. In fact, using this approach the shape of the internal skin as well as the transitions between zones with varying thickness along the span of the blade are precisely reconstructed. This is particularly important since these regions must be accurately modeled [3], and it may be particularly useful in areas of rapid span-wise variations as the one between root and max chord span.

3.3 FE model

3.3.1 Mesh generation

The generation of an unstructured mostly quadrilateral shell mesh is obtained by using `HyperMesh` on the exterior or mid-thickness surface CAD model; a limited number of triangular elements is generally obtained close to corners and in a few difficult spots. The meshing algorithm ensures the conformity of the resulting grid across edges bounding the various subsurfaces of the model.

An unstructured mostly hexahedral solid mesh is obtained by first quad meshing the external subsurface of each individual blade component as for the shell case, projecting the mesh onto the opposite internal surface, optionally defining through-the-thickness discretizations by the same projection, and finally connecting the resulting surface grids into a solid one. Since the initial surface meshes are conforming, the final solid grid is also guaranteed to be conforming.

The surface meshing and extrusion procedure is illustrated in Fig. 5 for a span-wise portion of the spar cap; notice that the external surface has been divided into several stripes in the chord-wise direction, to account for the glued connections with the shear webs. A span-wise portion of the resulting complete solid mesh is illustrated in Fig. 6(a), and details of the trailing edge with its reinforcement strip and the thickness variation of the core is shown in Fig. 6(b).

For sectional analysis, one can generate either a panel mesh, i.e. a discretization of the mid-thickness line in 1D elements, or a 2D mesh, i.e., a grid of quad or tria elements that discretize the various components of the cross section. The first option was used in the examples of the present paper, although the second is also implemented in the code and

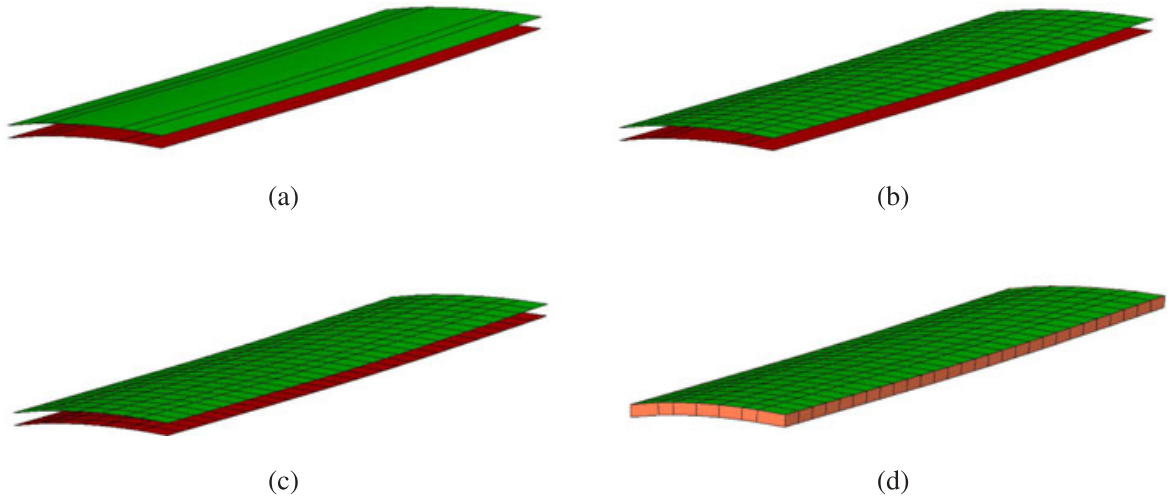

Fig. 5 Surface meshing and extrusion procedure

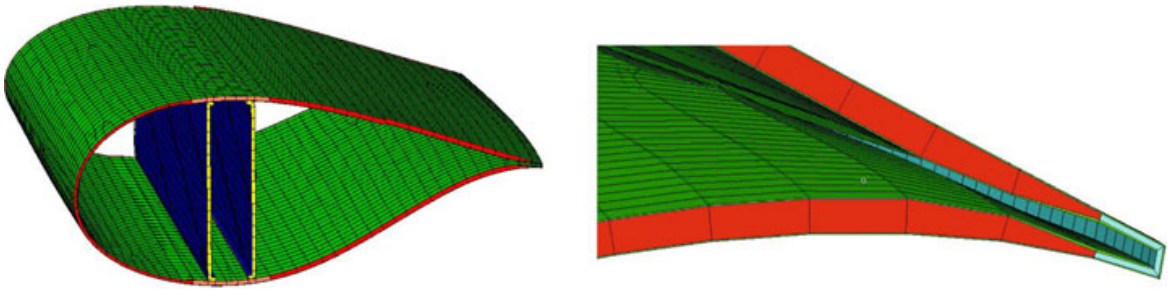

(a) (b)

Fig. 6 Span-wise portion of solid mesh and trailing edge detail

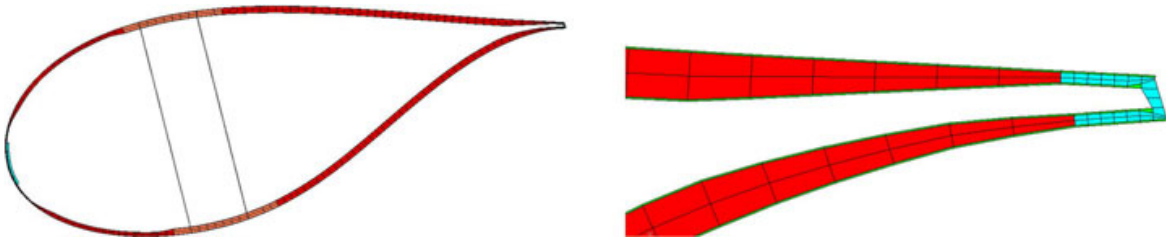

(a) (b)

Fig. 7 2D mesh for cross sectional analysis

provides for a higher definition evaluation of the state of stress of the cross section, possibly including also the interlaminar stresses.

For the panel case, meshing of the mid-thickness sectional line model is straightforward. For the 2D case, the external lines are first projected inward by using the local normals; this way defining the bounding lines of the various blade component cross sections. The external line mesh is then extruded inwards, possibly realizing multiple through-the-thickness subdivisions, accounting for the local thickness information available at each cross section; connection of the external and extruded line meshes generates the cross sectional surface grid.

A 2D cross sectional mesh and a close-up view of the trailing edge area are illustrated in Figs. 7(a) and 7(b), respectively.

3.3.2 Material properties

Material properties, including the orientation of the fibers with respect to the pitch axis, are associated with the various entities of the CAD model during its definition.

Once the mesh has been generated, the definition of the material properties of each mesh element is obtained as follows. At first, the centroid of each element is computed; if the element is of the 3D type, its centroid is projected onto the master CAD face of that blade component. At that CAD face location, a local material reference frame is defined that has a unit vector in the direction of the fibers and a second unit vector along the local normal, computed from the NURBS surface parameterization. The orthotropic material properties of the element are then readily obtained by transforming into the local reference frame of that same element.

For shell meshes, the procedures support either the generation of single layer equivalent composite laminates or of layer-by-layer representations. The latter approach is particular

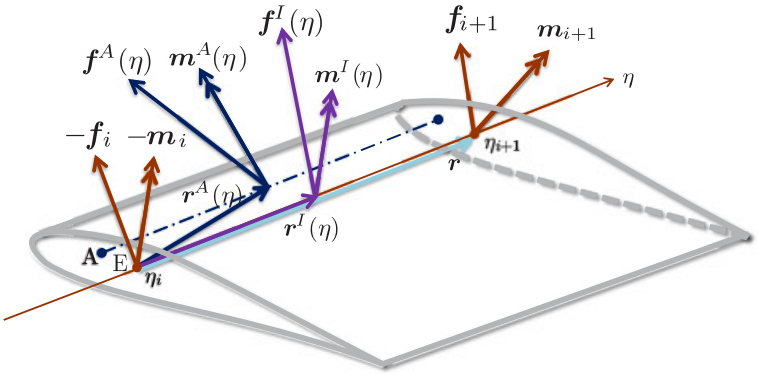

Fig. 8 Recovery of inertial loads from sectional internal stress resultants and aerodynamic loads

convenient for modeling very thin layers, such as the skin coating that would result in elements with very high aspect ratios. Even though such details of the blade design may seem to be of minor importance from the structural point of view, they can indeed have a significant influence on the estimation of the total mass (up to $4 \div 5$ %), with a consequent possible effect on the blade dynamic properties.

3.3.3 Equivalent loading conditions

In order to perform all relevant analyses on the fine-level FE model, appropriate loading and boundary conditions must be generated from the results of the coarse-level multibody simulations; these include loads inducing extreme stress and strain values, loads associated with maximum tip deflections, as well as time histories of the turbulent loads cases for the evaluation of fatigue damage. For each of these loading conditions, span-wise distributions of the internal stress resultants and of the aerodynamic forces are readily available from the multibody simulations. The computation of equivalent loading conditions for the FE model is here performed by distinguishing between aerodynamic and inertial loads. This way, realistic loading conditions for the blade can be established, e.g., by limiting the application of the aerodynamic loads to the external skin nodes.

Span-wise distributions of inertial loads are recovered by enforcing the equilibrium of a blade portion. With reference to Fig. 8, consider a blade segment $\eta \in [\eta_i, \eta_{i+1}]$, where $\eta \in [0, 1]$ is the span-wise nondimensional coordinate running along the beam reference line passing through the sectional point E. The internal stress resultants on the $(i+1)$th section is $\boldsymbol{f}_{i+1}$, and the moment resultant about E is $\boldsymbol{m}_{i+1}$, while the ones on the ith section negative face are $-\boldsymbol{f}_i$ and $-\boldsymbol{m}_i$, respectively. At the span-wise station η, per-unit-span aerodynamic forces $\boldsymbol{f}^A(\eta)$ and moments $\boldsymbol{m}^A(\eta)$ are applied at the aerodynamic reference line passing through the sectional point A, which is at a distance $\boldsymbol{r}^A(\eta)$ from point E on the ith section. Similarly, per-unit-span inertial forces $\boldsymbol{f}^I(\eta)$ and moments $\boldsymbol{m}^I(\eta)$ are applied at the beam reference line, which is at a distance $\boldsymbol{r}^I(\eta)$ from point E on the ith section.

The force and moment (about E) equilibrium conditions for the blade segment write

$$-\boldsymbol{f}_i + \boldsymbol{f}_{i+1} + \int_{\eta_i}^{\eta_{i+1}} \left(\boldsymbol{f}^A + \boldsymbol{f}^I\right) \mathrm{d}\eta = 0, \tag{11a}$$

$$-\boldsymbol{m}_i + \boldsymbol{m}_{i+1} + \int_{\eta_i}^{\eta_{i+1}} \left(\boldsymbol{m}^A + \boldsymbol{m}^I + \boldsymbol{r}^A \times \boldsymbol{f}^A + \boldsymbol{r}^I \times \boldsymbol{f}^I\right) \mathrm{d}\eta + \boldsymbol{r} \times \boldsymbol{f}_{i+1} = 0. \tag{11b}$$

By using a trapezoidal approximation for the span-wise integrals, one obtains

$$\int_{\eta_i}^{\eta_{i+1}} \boldsymbol{f}^I \,\mathrm{d}\eta \approx \frac{\eta_{i+1} - \eta_i}{2} \left(\boldsymbol{f}_i^I + \boldsymbol{f}_{i+1}^I\right), \tag{12}$$

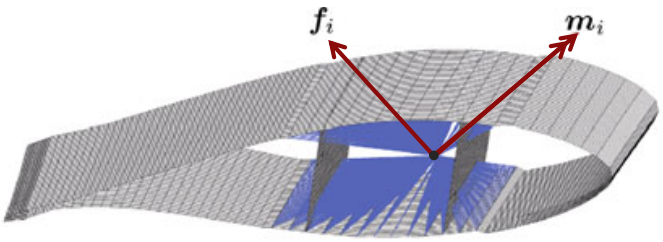

Fig. 9 Load application to spar caps nodes using the RBE3 element

where $\boldsymbol{f}_i^I$ and $\boldsymbol{f}_{i+1}^I$ are sectional inertial forces. By inserting (12) into (11a), starting from the blade tip, one may compute each sectional inertial force $\boldsymbol{f}_i^I$ based on the sectional resultants and aerodynamic loads. Similarly, from (11b) one may compute each sectional inertial moment $\boldsymbol{m}_i^I$.

Once sectional loads have been recovered as explained, they are applied to the blade structure by means of RBE3 interpolation elements provided in the commercial FE solver MSC Nastran [27]. Different sets of nodes can be associated with different interpolation elements, each one in turn associated with a different set of forces and moments. This way aerodynamic loads can be applied to the sole skin nodes, while inertial loads can be applied to all sectional nodes; alternatively, combined loads can be applied to the spar cap nodes, as shown in Fig. 9. In all cases, forces are distributed to each node considering local user defined weighting factors, while moments are applied as sum of equilibrated forces on dependent nodes, as explained in [29]. An example of the application of loads to the spar cap of a shell 3D model is reported in Fig. 9.

A more realistic way of representing aerodynamic loads would be to reconstruct the chord-wise pressure distribution, for example using assumed shapes from experimental measurements or from suitable numerical models such as Xfoil [28]. This feature will be included in future releases of the code.

3.4 Analysis

The automatically generated 3D FE model enables the detailed fine-level verification of the various constraint inequalities associated with the overall optimization problem. Furthermore, it can be used for designing secondary structural parts such as the skin core thickness by means of a linearized buckling analysis. In the present section, the assumptions and procedures for these various analyses are described.

3.4.1 Static analysis

Static analyses are performed for the verification of the constraint inequalities associated with the max/min allowable stresses/strains and the maximum tip deflection, with the aim of revealing possible effects not captured by the beam model.

For each user-defined verification section, the max/min stress/strain loading conditions are readily identified by scanning all DLCs of interest [14], and using the sectional recovery relations provided by ANBA. Next, the corresponding equivalent loading conditions are first computed as described in Sect. 3.3.3 from the coarse-level analysis, and then applied to the 3D FE model. Similarly, by scanning all DLCs, the maximum tip deflection condition is identified and translated into an equivalent loading condition.

Geometric and material linear static analyses are performed in MSC Nastran, and the relevant results in terms of strains, stresses and displacements are processed in Matlab

to detect possible violations of the constraint conditions. It was verified that, for the examples developed in the present work, the use of geometrically nonlinear analyses, as opposed to the present linear ones, yield only negligible differences, although this might not be the case for the future projected very long and slender next generation wind turbine blades.

3.4.2 Modal analysis

During coarse optimization, a design accommodating desired dynamic properties can be obtained by specifying suitable constraints for significant natural frequencies of the blade, as described in Sect. 2.2. Such constraints are typically expressed for the rotating blade at rated RPM. The inertial effects associated with blade rotation are taken into account in the `Cp-Lambda` modal analysis by first performing a nonlinear static analysis subjected to a loading condition including the inertial effects of rotational motion, and then by performing a modal analysis about the resulting deformed configuration, accounting for the centrifugal stiffness term.

A similar procedure could be used for performing the modal analysis on the 3D FE model [27]. However, while coarse-level constraints are enforced for the rotating frequencies, the fine-level verification of the frequency conditions is performed here for simplicity as a standard nonrotating modal analysis about the blade undeformed configuration. In particular, ratios between corresponding nonrotating frequencies, computed on the coarse-level beam and fine-level FE models, are used as indicators of the disagreement between the two representations. This is a reasonable assumption, since both models are sophisticated enough to precisely account for inertia-related changes of frequencies, and thus the ratios between nonrotating frequencies are expected to change in a similar fashion. Furthermore, rotational effects on frequencies are typically rather limited for wind turbine rotor blades.

3.4.3 Fatigue analysis

Similarly to the coarse-level optimization procedure [14], the fine-level evaluation of damage caused by loads in turbulent wind conditions (DLC 1.2 [2]) is only conducted for a limited set of critical points at user-defined verification sections. Such critical points are identified during coarse optimization as the sectional spots where the multiaxial damage index d of Eq. (6) exceeds a specified threshold.

The stress time histories necessary for evaluating the damage index are conveniently computed by exploiting the linear superposition of static unit load cases applied to the FE model with load histories obtained from the beam model (see e.g. [38]). At each verification point, a static force or moment (in the case of shells) of unit magnitude is applied, and the full stress time history follows as

$$\sigma_i(t) = \sum_j P_j(t) \frac{\sigma_{i,j}}{P_{j,\mathrm{FEA}}}, \tag{13}$$

where $P_j(t)$ denotes a load history obtained by a multibody transient simulation, $P_{j,\mathrm{FEA}}$ the applied unit load, and σ_i is the static stress resultant at point i for load case j. This procedure reduces the computational cost necessary for the evaluation of the full stress time history on the comprehensive 3D FE model. The remaining steps required for the computation of the damage index follow the same procedure used at the coarse analysis level, using rain-flow counting and the associated Markov matrices.

3.4.4 Buckling analysis

An additional feature only provided by a full 3D FE model is the capability of performing a linearized buckling analysis, which can be used for designing secondary structural elements, such as the skin and web core thicknesses. It is important to include the sizing of secondary components in the design process, because the distribution of the associated structural material has a significant influence on the nonstructural mass, which in turn affects the dynamic behavior of the blade by changing its natural frequencies.

Prior to the FE analysis, an initial distribution of the core material and thickness for skin and webs can be estimated by the following two step procedure, based on simplified design formulas:

1. Choice of material. Appropriate stiffness properties for the core material are estimated such that local buckling (or wrinkling) is avoided, as this may cause fractures in the core or delamination. Following [39], this is accomplished by comparing the computed extreme compressive stress to the following critical stress:

$$\sigma_{\text{adm,wrinkling}} = 0.5\sqrt[3]{G_{\text{core}} E_{\text{core}} E_{\text{skin}}}, \tag{14}$$

   where G and E denote the shear and Young's moduli, respectively.
2. Thickness sizing. For the skin and web panels, the critical buckling stress $\sigma_{\text{adm,buck}}$ and shear $\tau_{\text{adm,buck}}$ are computed using the following equations:

$$\sigma_{\text{adm,buck}} = \frac{\pi^2}{t_{\text{panel}} b^2} K_{\text{c}} \sqrt{D_{11} D_{22}}, \tag{15a}$$

$$\tau_{\text{adm,buck}} = \frac{\pi^2}{t_{\text{panel}} b^2} K_{\text{s}} \sqrt[4]{D_{11} D_{22}^3}, \tag{15b}$$

   where t_{panel} is the skin or web panel thickness, b is the panel edge width, D_{11} and D_{22} are the diagonal components of the out-of-plane bending stiffness matrix of the sandwich panels computed with classical laminate theory. Finally, K_{c} and K_{s} are buckling factors accounting for several properties of a sandwich structure, like its ortotrophy, curvature and out-of-plane shear flexibility, as well as for the way the longitudinal stress is distributed along the plate edge. For further details about the computation of the buckling factors, see [40].

   At several stations along the blade span, the skin core is sized by imposing the constraint $\lambda_s \geq 1$, where λ_s is the skin buckling load factor, computed by solving the following equation:

$$\lambda_s \left(\frac{\sigma}{\sigma_{\text{adm,buck}}} \right) + \lambda_s^2 \left(\frac{\tau}{\tau_{\text{adm,buck}}} \right)^2 = 1, \tag{16}$$

   which takes into account stress-shear interactions [41]. Similarly, the web core is sized constraining $\lambda_w \geq 1$, where λ_w is the solution of

$$\lambda_w^2 \left(\left(\frac{\sigma}{\sigma_{\text{adm,buck}}} \right)^2 + \left(\frac{\tau}{\tau_{\text{adm,buck}}} \right)^2 \right) = 1. \tag{17}$$

Subsequently in the design process, at the fine verification level and similarly to the case of the primary structural variables described in Sect. 2.2, the core thickness of a region where

buckling occurs is increased by an amount proportional to the exceedance of the constraint condition $\lambda \leq 1$, where λ is the buckling eigenvalue associated with the applied load.

In the present implementation, the linear buckling analysis is performed using the loading condition that results in the maximum tip deflection of the blade, as this results in severe compressive loads on the suction side of the blade. Alternatively, loads associated with the extreme values of compressive stresses at relevant sections could be identified from the load envelope and used for the buckling analysis.

4 Applications and results

4.1 Baseline wind turbine

In this section, the performance of the developed multilevel optimization procedures is illustrated with respect to a Class-IIIA 2MW HAWT with a 45 m rotor radius. The structural layout of the blade is a stressed-shell configuration with single upper and lower spar caps confined within two planar shear webs, normal to the maximum chord line. The primary structural design parameters $\boldsymbol{p}_{s1}$ are defined as the common thickness of the two shear webs, the common thickness of the upper and lower spar caps and the thickness of the external blade shell. These quantities are represented by span-wise linear interpolations of corresponding nodal unknowns located at $\eta = 0, 0.01, 0.03, 0.10, 0.195, 0.20, 0.25, 0.4, 0.5, 0.6, 0.75, 0.8, 0.98$, and 1, resulting in a total number of primary structural design parameters equal to 53. A typical blade section is reported in Fig. 10.

The main blade structural components are reported in Table 1. The blade is made of six different material types, whose mechanical properties are summarized in Table 2. Non-structural masses are accounted for with both span-wise and chord-wise proportional quantities. A first estimate of the secondary design parameters, represented by the skin core thickness, is obtained using the preliminary design formulas described in Sect. 3.4.

The coarse minimum weight structural sizing is based on DLCs 1.2, 1.4, 1.5, 1.6, 1.7, 2.2, 2.3, and 6.1 [2]. The design constraints include: placement of the first and second blade natural frequencies with at least 12 % and 20 % gaps, respectively, with the three-per-rev harmonic, a maximum blade tip deflection of $\delta_{\text{tip}_{\text{adm}}} = 5$ m, max/min allowable stresses/strains and fatigue constraints (see Eqs. (5a)–(5h)).

The frequency placement and max tip deflection constraints are active at convergence, and thus the design is driven by the blade flap bending stiffness. In addition, fatigue constraints are active in the skin between 10 % and 40 % span, where the largest chords occur, while constraints associated with stresses/strains are far from their respective limits. For this

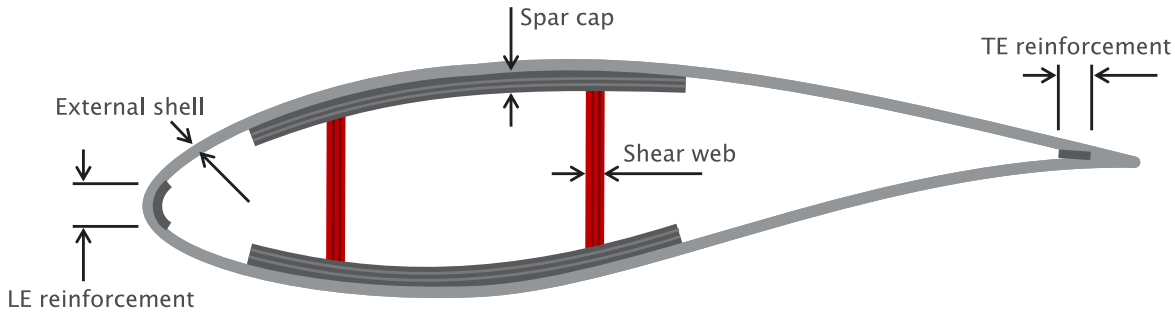

Fig. 10 Primary structural design parameters on a typical section

Table 1 Structural configuration

Component	Starting section (% span)	Ending section (% span)	Material type
Skin	0	100	Stitched triaxial −45/0/+45 fiberglass
Spar caps	3	97.8	Unidirectional fiberglass
Shear webs	10	97.8	Stitched biaxial −45/+45 fiberglass
Trailing and leading edge reinforcements	10	80	Unidirectional fiberglass
Skin core	10	97.8	T500 Foam
Web core	10	97.8	T400 Foam

Table 2 Material properties

Material type	Longitudinal Young's modulus [MPa]	Transversal Young's modulus [MPa]	Shear modulus [MPa]
Stitched triaxial −45/0/+45 fiberglass	28,500	10,300	6400
Unidirectional fiberglass	38,200	8600	3500
Stitched biaxial −45/+45 fiberglass	9700	9700	10,900
T500 foam	93	93	40
T400 foam	65	65	28

reason, static analyses performed at the fine level are limited to the loading condition that results in the maximum tip deflection.

Two different 3D models are generated using either mid-thickness shell elements or solid elements. For the shell model, the blade is discretized by isoparametric linear triangular and quadrilateral elements with layered composite properties. The solid model is based on isoparametric linear prismatic and hexahedral solid elements. For both models, the characteristic element side lengths are about 5 cm. All loads are applied to the spar caps using `RBE3` elements.

At first, possible differences between the coarse-level model and the detailed 3D models are investigated by performing modal, static, fatigue, and buckling analyses. Next, bounds are updated for the constraints that fail verification, and the effects of loop closure on a subsequent coarse-level iteration are illustrated.

4.2 First multilevel iteration

4.2.1 Modal analysis

Table 3 reports the first flap-wise and edge-wise blade natural frequencies obtained with the 3D mid-thickness shell, 3D solid, and beam `Cp-Lambda/ANBA` models. The associated vibration modes are visualized in Fig. 11.

It is noted that the first flap-wise natural frequency agrees well for all models. On the other hand, the matching is not as good for the edge-wise mode, since the frequency pre-

Table 3 Comparison of the two lowest blade natural frequencies

	Shell	Solid	Cp-Lambda/ANBA
$\omega_{1,\text{flap}}$ [Hz]	0.8552	0.8533	0.8568
$\omega_{1,\text{edge}}$ [Hz]	1.0120	1.0076	1.0560

(a) First flap-wise vibration mode (b) First edge-wise vibration mode

Fig. 11 The two lowest blade vibration modes

dicted by the beam model is about 4 % higher than the 3D ones. In the coarse-level optimization, this frequency is constrained to have a 20 % margin with respect to the three-per-rev harmonic, and the constraint is active at convergence. To account for this, the constraint bound for this frequency is increased by 4 % for the next coarse-level design iteration.

4.2.2 Static analysis

A static analysis for the load case corresponding to the maximum blade deflection is conducted next. A comparison of the flap- and edge-wise blade deflections obtained with the beam and 3D FE models reveals that all agree very well within a 0.02 % margin.

On the other hand, as expected, the stress distribution shows much larger differences. Figures 12(a) and 12(b) plot the span-wise distribution of maximum stresses in the fiber direction of skin and caps, respectively.

Figure 13 shows the skin-wise distribution of the longitudinal stress at 10 % of blade span, plotted as a function of the nondimensional coordinate $0 \leq s \leq 1$. The importance of 3D effects in this blade region is particularly clear if one looks at the shell and solid models stress distributions and compares them to the beam one.

Significant relative differences are apparent at the root region, and in particular at the beginning of webs, leading and trailing edge reinforcements. The cause for these discrepancies is due to the simultaneous presence of rapid transitions in the local geometry and a low skin thickness. The latter exhibits a rapid variation in the first 10 % span, becoming only 1/20 of the root thickness. The figures show that peaks arise exactly at the boundary region of the spar caps and the transition of the skin core, a complex region illustrated in Fig. 14.

In summary, the investigation of static loading conditions clearly illustrates the need for a detailed 3D FE analysis in order to obtain reliable estimates of the stress field over the whole blade. While a beam model in general provides reasonable results for most of the blade span, it is however unable to describe the detailed stress field at critical three dimensional and rapidly varying regions.

4.2.3 Fatigue analysis

A fatigue analysis as described in Sect. 3.4 is performed using the mid-thickness shell model. Results for the fatigue damage index evaluated according to the multiaxial criterion

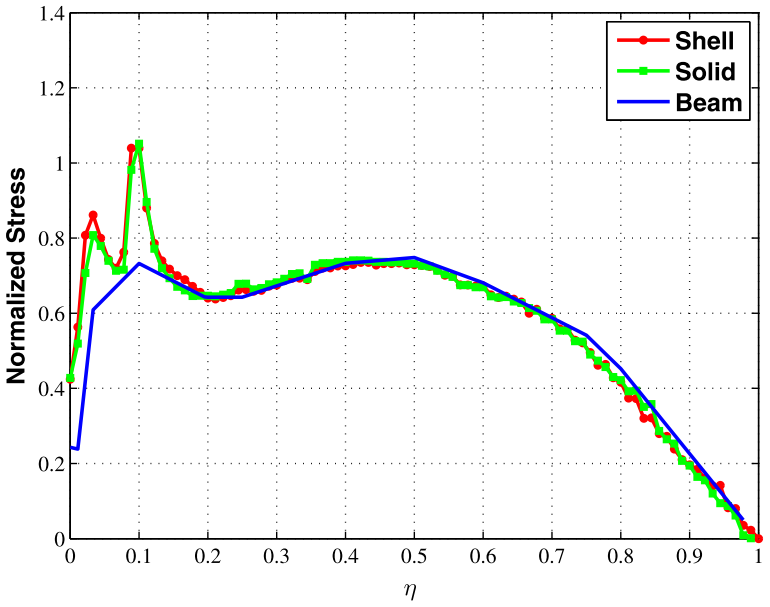

(a) Maximum stress $\sigma_{1,\max}$ in skin

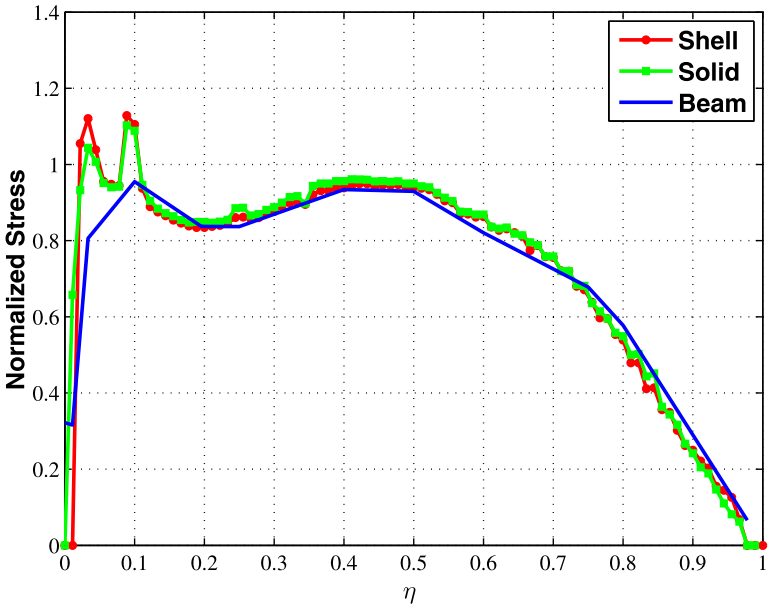

(b) Maximum stress $\sigma_{1,\max}$ in spar caps

Fig. 12 Normalized maximum stresses in fiber direction

of Eq. (6) at selected span-wise sections are illustrated in Fig. 15(a), along with comparable results obtained on the beam model.

It appears that the detailed 3D mid-thickness shell model predicts a significant peak at 10 % span, violating the fatigue constraint. Similarly to the static analysis case, the peak is grossly underestimated by the coarse-level beam model.

Figure 15(b) plots the fatigue damage parameter in the skin at the most critical region, within a margin of 100 mm around 10 % span. Fatigue damage is computed at points distributed along the airfoil, and plotted as a function of the curvilinear coordinate s. Similarly to the span-wise results, the 3D FE model predicts higher damage coefficients than the beam model, while both indicate the trailing edge region ($s = 0$ and $s = 1$) of the blade as the most exposed to fatigue.

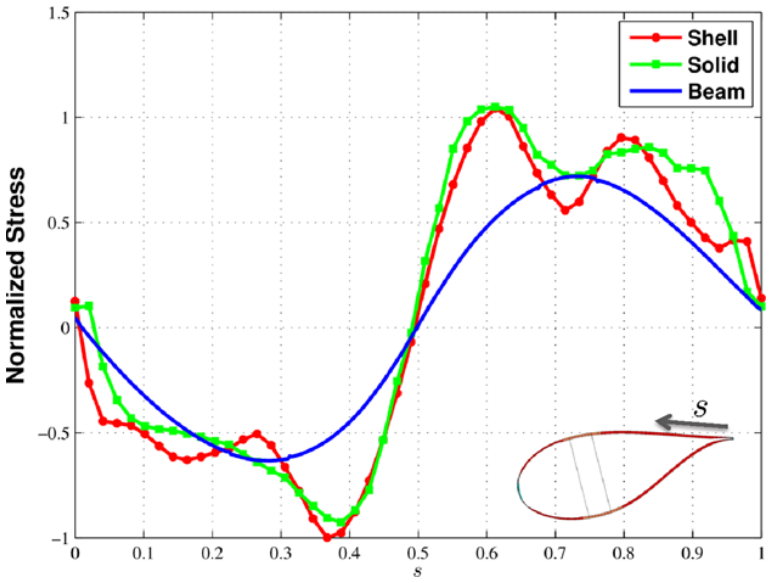

Fig. 13 Normalized stress in the skin at the span-wise station $\eta = 0.10$, vs. curvilinear coordinate s

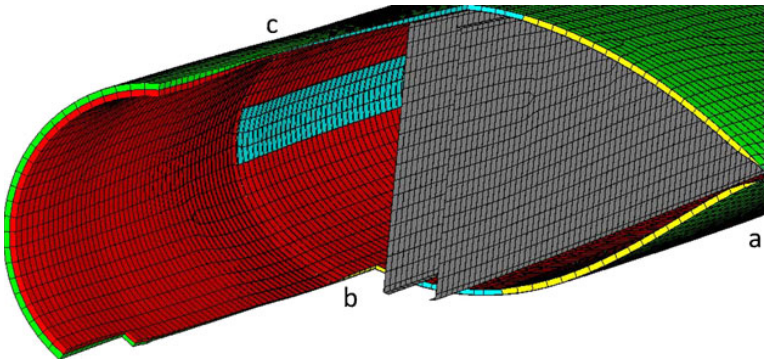

Fig. 14 Detail of the blade root: (**a**) trailing edge transition, (**b**) beginning of skin core, (**c**) beginning of spar caps

4.2.4 Linear buckling analysis

Finally, a linearized buckling analysis of the 3D FE model is conducted by subjecting the blade to the loading condition of maximum tip displacement.

The first two buckling modes are shown in Figs. 16(a) and 16(b). The first mode is localized near the blade root, while the second at the maximum chord region. Only the first mode is critical for the applied loading condition ($\lambda \leq 1$), and the instability is caused by the high compressive stresses that are generated around 10 % span.

To correct for this, the structural capacity at this region would need to be increased. This can be done by using procedure (8a)–(8c), which would increase the skin core thickness. However, it should be noted that the same region of the blade failed the verification of the fatigue constraints. The update of the associated constraint bounds will induce, at the next coarse-level optimization, a modification of the primary structural parameters that will also induce a local strengthening of the structure. As a side effect, this might results in a sufficient buckling resistance for the original core thickness. In light of this observation, it was decided to avoid the update of the secondary design parameters, and wait for the result of the next coarse design iteration.

4.3 Closure of multilevel optimization loop

The closure of the loop between the coarse-fine analyses and back is illustrated by performing a second iteration. After the first iteration, the fine-level FE results identified the following critical aspects:

Fig. 15 Damage index at selected verification points

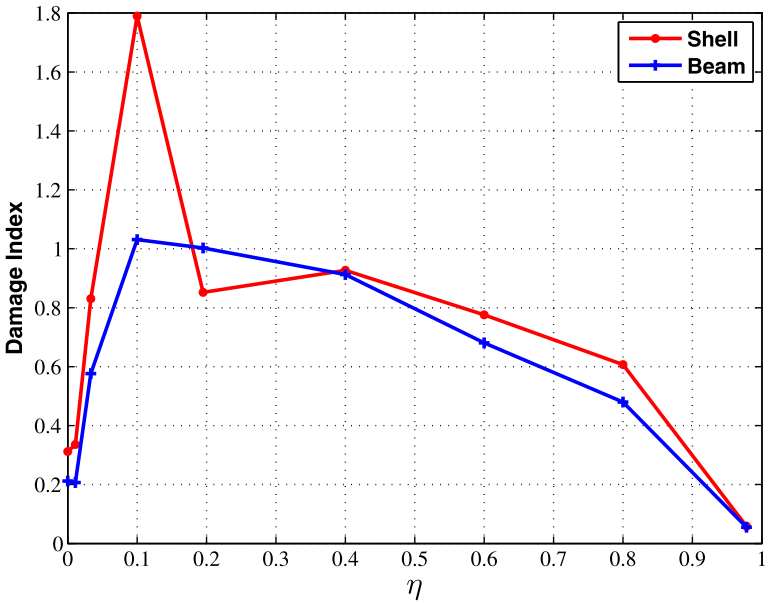

(a) Damage index vs. blade span

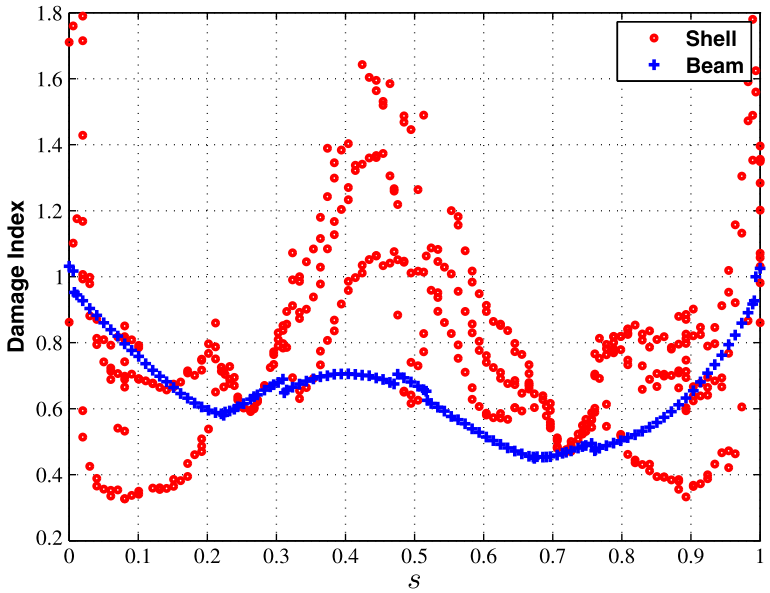

(b) Damage index at $\eta = 0.10$ span section, vs. curvilinear coordinate s

– The natural frequency spacing constraint is violated, as the 3D model edge-wise frequency is approximately 4 % lower than the one predicted by the coarse-level beam model.
– Significant stress concentrations are present at the initiation sections of spar caps, shear webs, and trailing and leading edge reinforcements, around 3 % and 10 % span.
– Fatigue constraints are violated at 10 % span due to the same stress concentrations, with a fatigue damage index exceeding 1.8.
– The thickness of the blade skin core around 10 % span is not sufficient to resist local buckling.

These results are used for tightening some of the constraint conditions for the next coarse iteration, which become:

$$\omega_{1,\text{edge}} \geq 1.04 \cdot 1.20 \cdot 3P, \tag{18a}$$

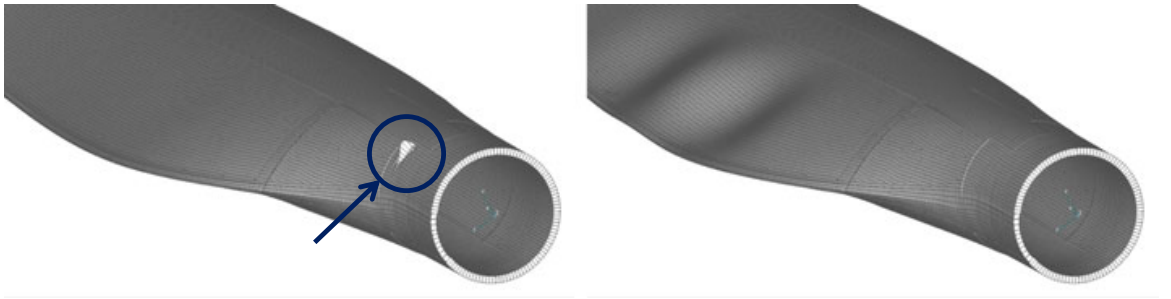

(a) First buckling mode, $\lambda_{\text{Shell}} = \lambda_{\text{Solid}} = 0.8$ (b) Second buckling mode, $\lambda_{\text{Shell}} = 3.6$, $\lambda_{\text{Solid}} = 3.4$

Fig. 16 Close-up view of first two buckling modes

$$d(\boldsymbol{p}_s, D)_{10\ \%\text{skin}} \leq 1/1.8. \tag{18b}$$

The first condition modifies the edge-wise frequency spacing constraint, while the second corrects the fatigue condition at 10 % span. Since stress peaks do not exceed allowables, no specific action is taken. For buckling, no action is taken in order to see if the strengthening induced by the tighter fatigue constraint is capable of fixing the problem.

The geometrical changes caused by the updated constraints are illustrated in Figs. 17(a) and 17(b).

The trailing edge reinforcement has been significantly increased. This change is driven by the need for an increased edge-wise bending stiffness, required for the satisfaction of the modified frequency constraint condition, and the fine 3D edge-wise frequency now satisfies the 20 % margin with the three-per-rev harmonic.

The skin thickness in the critical region at 10 % span has been increased from 5 % to 10 % of the root thickness, so as to satisfy the more stringent fatigue constraint condition. This has in turn increased the total blade mass by about 1.2 %.

The direct effect of increased skin thickness on the fatigue damage index computed on the fine 3D model is illustrated in Fig. 18. The figure shows that the previous peak at 10 % span is lowered to just below unity, indicating that the design now satisfies the fatigue requirement at the fine level.

Furthermore, as illustrated in Fig. 19(a), the previously identified skin stress concentrations are lowered in the critical region. In particular, the skin thickness increase at 10 % span eliminates the stress peak at that same location, whereas the peak at 3 % span, i.e., at the beginning of the spar caps, is only slightly reduced. Changes in the skin geometry affect also the spar cap stresses, which are similarly lowered as illustrated in Fig. 19(b).

Finally, the increased skin thickness has an indirect effect on the buckling capacity. In fact, the lowest buckling eigenvalue is now increased from 0.8 to 2.08, implying that the improved design exhibits sufficient buckling strength so that, in this particular case, a skin core thickness increase by the secondary design loop proves not to be necessary.

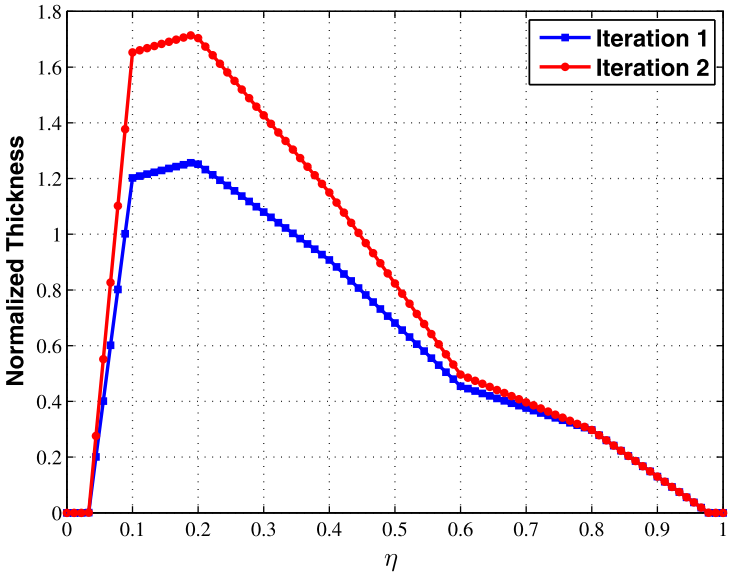

(a) Trailing edge reinforcement

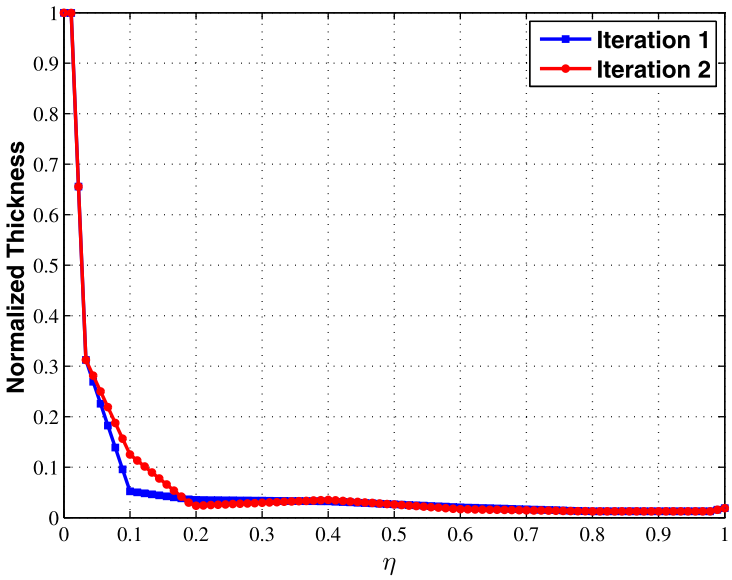

(b) Skin thickness

Fig. 17 Normalized thicknesses of blade components

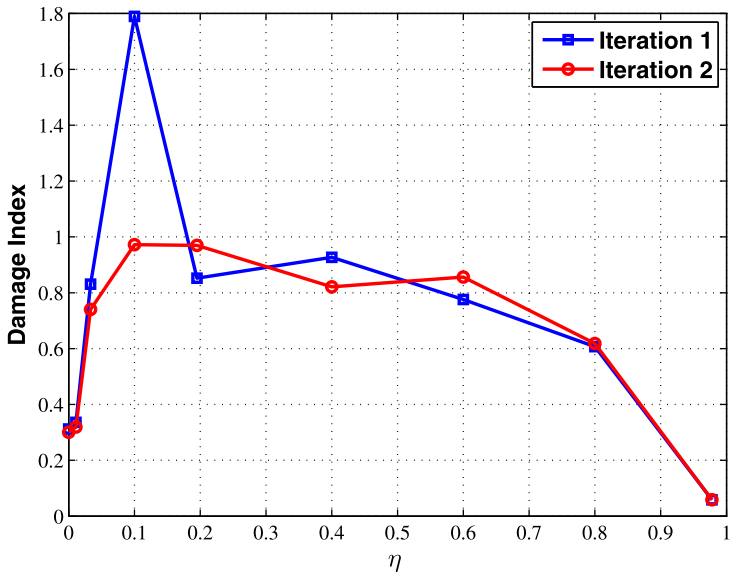

Fig. 18 Damage index at selected sections along blade span

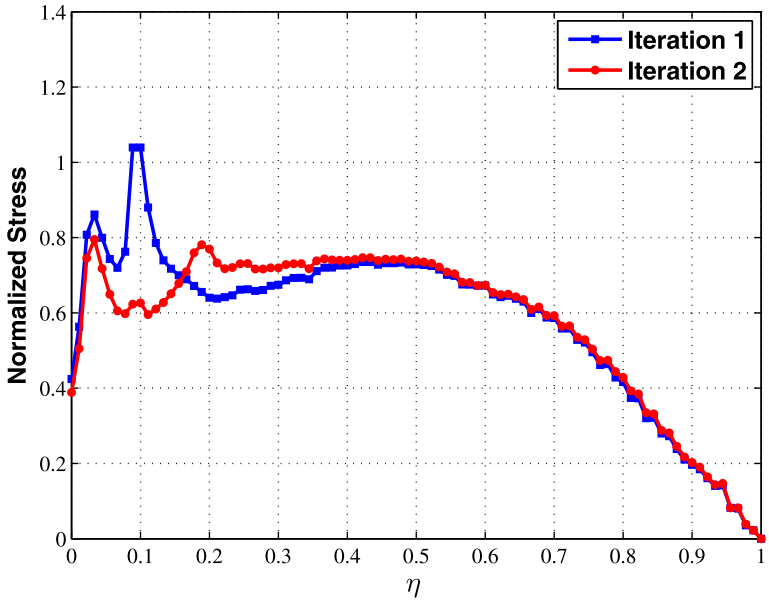

(a) Maximum stress $\sigma_{1,\max}$ in skin

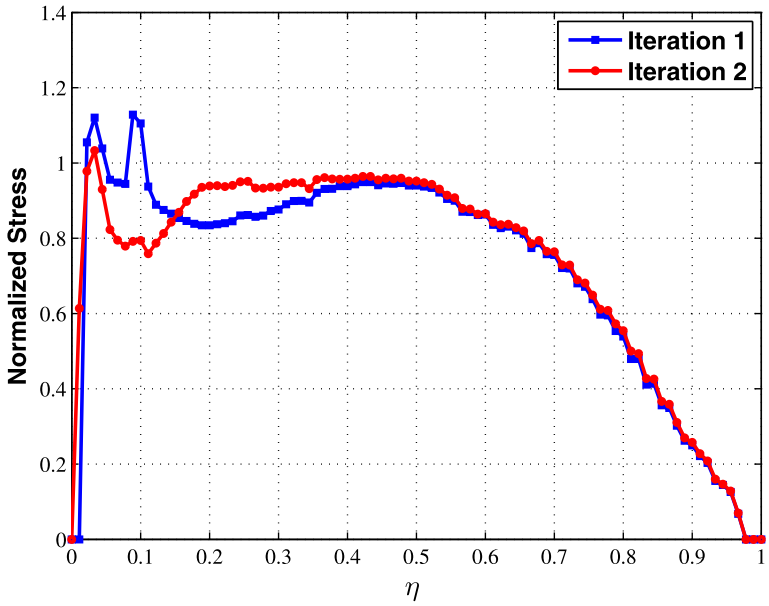

(b) Maximum stress $\sigma_{1,\max}$ in spar caps

Fig. 19 Normalized maximum stresses in fiber direction

5 Conclusions

In this paper, we have presented a multilevel optimization method for wind turbine rotor blades, that operates at different description levels to generate a cost-minimizing solution satisfying a number of design requirements expressed as inequality constraints.

The highlights of the proposed approach can be summarized as follows:

– Determination of the complete load envelope, including fatigue loads, by multibody aero-servo-elastic simulations conducted according to certification guidelines.
– Multidisciplinary optimization by iteration between a multibody model and cross sectional 2D models, which provide the synthesis of fully populated stiffness matrices and the computation of sectional stresses and strains.

– Automatic generation of detailed 3D NURBS-based CAD model, accounting for all principal structural components, using either shell (with or without offsets) or solid descriptions.
– Automatic meshing of the models, including association of properties for anisotropic composite layered materials and loading conditions from the multibody aero-servo-elastic analyses.
– Complete reanalysis of the blade at the fine 3D FE description level, and verification of the satisfaction of the design constraints, including buckling.
– Heuristic update of the design constraints, based on the results of the fine-level reanalysis, and loop closure that enables successive coarse-level iterations until convergence.

The procedure was demonstrated on a 2MW wind turbine. After a first coarse-level optimization, detailed stress and fatigue analyses conducted on the fine-level 3D model revealed significant stress concentrations between the root and the maximum chord regions. These effects were not captured by the coarse-level beam model, which is blind to highly three-dimensional variations and abrupt changes in the stress field. Furthermore, the modal analysis of the 3D model showed the violation of a frequency constraint condition, while the buckling analysis highlighted the presence of skin instability under the maximum tip deflection loading condition. By tightening the respective constraint bounds for the subsequent coarse-level iteration, it was shown that convergence can be obtained very rapidly by iterating between the coarse and fine levels.

Although the skills of an experienced analyst is irreplaceable when conducting the design of complex engineering systems such as a wind turbine blade, the proposed highly automated design tools are believed to be able to streamline the design process and help in the exploration of the design space, relieving the burden of the most complex and error-prone tasks and allowing the user to focus on the understanding of the various design tradeoffs to come to the best possible solution.

References

1. Bottasso, C.L., Campagnolo, F., Croce, A., Tibaldi, C.: Optimization-based study of bend-twist coupled rotor blades for passive and integrated passive/active load alleviation. Wind Energy. doi:10.1002/we.1543 (2012)
2. Wind Turbines. Part 1. Design Requirements, 3rd edn. International Standard IEC 61400-1 (2005)
3. Guideline for the Certification of Wind Turbines, edn. 2010. Germanischer Lloyd Industrial Services GmbH, Renewables Certification, Brooktorkai 10, 20457 Hamburg, Germany (2010)
4. Lee, D., Hodges, D.H., Patil, M.J.: Multi-flexible-body dynamic analysis of horizontal axis wind turbines. Wind Energy **5**, 281–300 (2002)
5. Bauchau, O.A., Bottasso, C.L., Nikishkov, Y.G.: Modeling rotorcraft dynamics with finite element multibody procedures. Math. Comput. Model. **33**, 1113–1137 (2001)
6. Bottasso, C.L., Croce, A.: `Cp-Lambda`: User's Manual. Dipartimento di Ingegneria Aerospaziale, Politecnico di Milano (2006–2013)
7. Larsen, T.J., Hansen, A.M.: How 2 `HAWC2`: The User's Manual. Risø report Risø-R-1597(ver. 3-1)(EN), Risø National Laboratory, Roskilde, Denmark (2007)
8. Jonkman, J.M., Buhl, M.L. Jr: `FAST` User's Guide. Technical report NREL/EL-500-38230, National Renewable Energy Laboratory, Colorado, USA (2005)
9. `Bladed`. GL Garrad Hassan, St. Vincent's Works, Silverthorne Lane, Bristol. www.gl-garradhassan.com
10. `RotorOpt` perfects rotor design. LM Glasfiber, News Letter, September, p. 5 (2007)
11. Fuglsang, L.: Integrated design of turbine rotors. In: European Wind Energy Conference and Exhibition (EWEC), Brussels, Belgium, 31 March–3 April (2008)

12. Duineveld, N.P.: Structure and Possibilities of the FOCUS Design Package. Dutch Wind Workshops. TU Delft, Delft (2008)
13. Jonkman, J.: NREL structural and aeroelastic codes. In: 2008 Wind Turbine Workshop, Sandia National Laboratories, Albuquerque, NM, USA, 12–14 May (2008)
14. Bottasso, C.L., Campagnolo, F., Croce, A.: Multi-disciplinary constrained optimization of wind turbines. Multibody Syst. Dyn. **27**, 21–53 (2012)
15. Laird, D.L.: NUMAD User's Manual—Numerical Manufactoring and Design Tool. Sandia report SAND2001-2375, Wind Energy Technology, Sandia National Laboratories (2001)
16. Hoyt, D.M., Graesser, D.: Rapid FEA of wind turbine blades—summary of NSE composites' structural analysis capabilities for blade NSE bladeMesher in-house software. NSE Composites, 1101 North Northlake Way, Suite 4, Seattle, WA 98103, May (2008)
17. Ashwill, T.: Sweep-Twist Adaptive Rotor Blade: Final Project Report. Sandia report SAND2009-8037, Sandia National Laboratories, Albuquerque, NM, USA (2010)
18. Jureczko, M., Pawlak, M., Mężyk, A.: Optimisation of wind turbine blades. J. Mater. Process. Technol. **167**, 463–471 (2005)
19. Bauchau, O.A.: Flexible Multibody Dynamics. Solid Mechanics and Its Applications, vol. 176. Springer, Berlin (2011)
20. Bauchau, O.A., Bottasso, C.L., Trainelli, L.: Robust integration schemes for flexible multibody systems. Comput. Methods Appl. Mech. Eng. **192**, 395–420 (2003)
21. Giavotto, V., Borri, M., Mantegazza, P., Ghiringhelli, G.: Anisotropic beam theory and applications. Comput. Struct. **16**, 403–413 (1983)
22. Bottasso, C.L., Croce, A., Nam, Y., Riboldi, C.E.D.: Power curve tracking in the presence of a tip speed constraint. Renew. Energy **40**, 1–12 (2012)
23. Matlab. The MathWorks Inc., 3 Apple Hill Drive, Natick, MA 01760-2098, USA. www.mathworks.com
24. HyperMesh. Altair Engineering, 1820 Big River Rd., Troy, MI 48082, USA. www.altair.com
25. Philippidis, T.P., Vassilopoulos, A.P.: Complex stress state effect on fatigue life of GRP laminates. Part I. Experimental. Int. J. Fatigue **24**, 813–823 (2002)
26. Philippidis, T.P., Vassilopoulos, A.P.: Complex stress state effect on fatigue life of GRP laminates. Part II. Theoretical formulation. Int. J. Fatigue **24**, 825–830 (2002)
27. MD/MSC NASTRAN 2010: Quick Reference Guide. MSC Software (2010)
28. Drela, M., Youngren, H.: Xfoil: Subsonic Airfoil Development System. web.mit.edu/drela/Public/web/xfoil
29. MD/MSC NASTRAN 2011: Linear Static Analysis User's Guide. MSC Software (2011)
30. Laird, D., Montoya, F., Malcolm, D.J.: Finite element modeling of wind turbine blades. In: Proceedings of AIAA/ASME Wind Energy Symposium, AIAA-2005-0.195, Reno, Nevada, USA, pp. 9–17 (2005)
31. Berry, D.: Design of 9-Meter Carbon-Fiberglass Prototype Blades: CX-100 and TX-100. Sandia report SAND2007-0201, Sandia National Laboratories, Albuquerque, NM, USA (2007)
32. Resor, B.: Integrated design and analysis at Sandia. In: 2010 Sandia Wind Turbine Blade Workshop, Sandia National Laboratories, Albuquerque, NM, USA (2010)
33. Federov, V.A., Dimitrov, N., Berggren, C., Krenk, S., Branner, K., Berring, P.: Investigation of structural behaviour due to bend-twist couplings in wind turbine blades. In: Proceedings of International Conference on Composite Materials (ICCM-17), Edinburgh, Scotland, 27–31 July (2009)
34. Chen, J., Hallett, S., Wisnom, M.R.: Modelling complex geometry using solid finite element meshes with correct composite material orientations. Comput. Struct. **88**, 602–609 (2010)
35. MSC NASTRAN: Element Reference Manual. MSC Software (2010)
36. Piegl, L., Tiller, W.: The NURBS Book. Monographs and Visual Communications, 2nd edn. Springer, New York (1996)
37. Lee, E.T.Y.: Choosing nodes in parametric curve interpolation. Comput. Aided Des. **21**, 363–370 (1989)
38. Bishop, N.W.M., Sherratt, F.: Finite Element Based Fatigue Calculations. National Agency for Finite Element Methods & Standards (NAFEMS), Great Britain (2000)
39. Sullins, R.T., Smith, G.W., Spier, E.E.: Manual for Structural Stability Analysis of Sandwich Plates and Shells. NASA contractor report, NASA CR-1457, Washington DC, USA, December (1969)
40. Lindenburg, C., de Winkel, G.D.: Buckling load prediction tools for rotor blades. ECN-C-05-103 (2005)
41. Bruhn, E.F.: Analysis and Design of Flight Vehicle Structures, 2nd edn. Jacobs Pub. (1973)

DTU Mechanical Engineering
Section of Solid Mechanics
Technical University of Denmark

Nils Koppels Allé, Bld. 404
DK- 2800 Kgs. Lyngby
Denmark
Phone (+45) 4525 4250
Fax (+45) 4593 1475
www.mek.dtu.dk
ISBN: 978-87-7475-373-5

DCAMM
Danish Center for Applied Mathematics and Mechanics

Nils Koppels Allé, Bld. 404
DK-2800 Kgs. Lyngby
Denmark
Phone (+45) 4525 4250
Fax (+45) 4593 1475
www.dcamm.dk
ISSN: 0903-1685